The formation and characterisation of micro- and nanostructured surfaces through combinations of top-down and bottom-up fabrication methodologies.

by

Simon J. Leigh

A thesis submitted to

The University of Birmingham

for the degree of

DOCTOR OF PHILOSOPHY

School of Chemistry
College of Engineering and Physical Sciences
The University of Birmingham
October 2009

This thesis is dedicated to my parents who have tirelessly given me their support throughout the course of my academic career so far

Abstract

The research presented in this thesis explores work on micro and nanoscale patterning and structuring, towards 3D patterning of surfaces. The undertaking of such work is key to the advancement in areas such as microelectronics, nanotechnology and device and sensor fabrication.

Chapter 1 (*Nanotechnology: Introduction to Small Technology*) presents an introduction to the background of the thesis research and information on the concepts and techniques used throughout the thesis.

The first experimental chapter, **Chapter 2** (*Laying the Molecular Foundations*) explores the patterning of monomolecular self-assembled-monolayers (instead of conventional polymeric resists) with electron beam lithography to form chemical patterns on gold surfaces. The chemical patterns on the surface then direct the self-assembly of gold nanoparticles with complementary chemistry.

Chapter 3 (*From the Foundations Upwards*) utilises the self-assembling ability of the nanoparticles from the previous chapter and explores how they can be incorporated into a multilayer structure on a surface. This multilayer assembly is achieved by the layer-by-layer deposition methodology in conjunction with a charged polyelectrolyte. The layer-by-layer deposition process is followed with three different characterization techniques and the results compared. The chapter also examines other routes to directly patterning the layer-by-layer assembled structures such as photolithography and microfluidics**.**

Chapter 4 (*Printing and Scratching*) explores the versatility of the nanoparticles and polyelectrolytes (from Chapter 3) towards alternative deposition techniques; in this case, a standard consumer-grade inkjet printer is used to deposit the materials to surfaces. Futhermore, an Atomic Force Microscope is then used to define patterns and structures in the printed structures.

Chapter 5 (*Corrugations and Collagen*) introduces the recovery and transfer of micro/nanostructured gold surfaces from gold-coated CD-R disks to silicon substrates as a route for producing cheap, structured gold substrates. The previous chapters examine methods to control the location of materials on surfaces, the corrugated gold substrates fabricated for this chapter are used to demonstrate that the actual orientation of materials themselves can also be controlled. In this case, the naturally occurring, fibrous and bio-technologically interesting material collagen is oriented on a surface by simply rotating the surface in a suspension of collagen in a novel device fabricated for these experiments.

The final experimental chapter, **Chapter 6** (*DNA based Foundations and Walls*) uses surface chemical modification to immobilise synthetic hairpin oligonucleotides carrying a photolabile group, on a silicon surface. Once immobilised on a surface, the oligonucleotides are patterned using photolithography to leave exposed single strands, which, through the specific assembly properties of DNA, are used to direct the spatially specific assembly of complementary strands carrying molecular dye or nanoparticle labels. This hybrid system shows that self-assembly processes found in nature can be combined with chemical modification of surfaces and oligonucleotide strands to also form 3D dimensional structured surfaces.

Acknowledgments

There are many people who I would like to thank for their help and support both during the researching and writing-up of this thesis.

First of all, I would like to thank Professor Jon. A. Preece for allowing me to undertake my PhD studies with him. His help, support, guidance and enthusiasm proved invaluable throughout the course of my PhD and provided me with many skills and experiences I will take forward into the rest of my career. Many thanks must also go to members of the Preece group past and present, namely, Dr Sara Diegoli, Dr Parvez Iqbal, Dr Mayandithevar Manickam, Dr Coen van der Brom, Scott Charlesworth, Dr Paula Mendes, Paul Yeung & Rachael Manton. Special thanks also go to Dr Christopher Hamlett and Dr James Bowen whose friendship, advice and humor helped me to succeed through the course of my PhD.

My research would also not have been possible without the many collaborators whom I worked with during my research. In light of this, I would like to thank, Dr Alex Robinson (Physics, University of Birmingham), Dr Ramon Eritja & Brendan Manning (IRB, Barcelona), Dr Jose Prieto (UPM, Madrid, Spain), Dr Dave Tunnicliffe (BAE Systems) and Dr Dave Tune (9D Technologies). I am also grateful to Steve Evans (School of Physics and Astronomy, University of Leeds) for the use of the X-ray photoelectron spectrometer and Graham Leggett (School of Chemistry, University of Sheffield) for the use of their laser and thermal evaporator.

I would also like to thank Dr Stuart Hosfield, my A-level chemistry teacher, his enthusiasm for the subject and his amusing anecdotes of his time spent at University were one of the main driving forces behind me pursuing both a degree and PhD in chemistry.

Thanks also go to my girlfriend Emma, for in her words being ‘totally awesome’, supporting me and encouraging me through my PhD and the writing up of my thesis.

Finally, I would like to thank my parents, Ann and Cliff and my family for their continued love and support, which was also crucial to me succeeding in my PhD research.

Contents

List of illustrations & tables

Chapter 1

Figure 1.6. Digramatic representation of XRL experiment setup.

Figure 1.7. Diagram of microcontact printing process; **a)** a solid, topographically patterned master surface is fabricated; **b)** PDMS is cast on the master surface, allowed to solidify then removed; **c)** the PDMS stamp is inked with a chemical 'ink'; **d)** a clean surface (in this case Au); **e)** the inked stamp is then brought into contact with the clean surface; and **f)** the 'ink' is transferred to the substrate.

Figure 1.8. Diagram of the DPN process, molecules are transferred from the AFM tip to the substrate surface through the water meniscus.

Figure 1.9. Diagram showing the process of nanografting; **a)** a complete SAM is **b)** shaved away in the presence of a secondary SAM molecule which **c)** selectively replaces the original SAM in the regions which were shaved.

Figure 1.10. Diagrammatic representation of water contact angle on a solid surface.

Figure 1.11. Diagram demonstrating process contact angle measurement of a drop of liquid on a solid surface.

Figure 1.13. Diagrammatic representation of ellipsometer setup.

Figure 1.14. Diagram demonstrating the operation of an AFM.

Figure 1.15. Diagrammatic representation of photoelectron ejection process.

Chapter 2

Figure 2.1. Simulation of distribution and number of backscattered electrons at 30,000 and 90,000 μC/cm^2 made using CASINO electron modelling software.

Scheme 2.1. Structure of of NPPTMS and the analogous thiol-terminated molecule, NPHT.

Figure 2.2. Time-resolved XPS spectra of the N 1s peak of a NO_2 terminated SAM on a silicon substrate.

Figure 2.3. Model of electron induced processes in NBT molecule. A monolayer of NBT is irradiated by electrons and generates amino (NH_2) end groups while the underlying aromatic monolayer is dehydrogenated and cross linked.

Scheme 2.2. Scheme showing the experimental procedures adopted.

Figure 2.4. XPS survey spectra of NPHT SAM on Au surface.

Figure 2.5. a) optical microscopy image of large-scale features after immersion in Au-NPs; and **b)** magnified region (**step 2)**.

Figure 2.6. SEM images of NPHT SAM **a)** after EBL exposure over a range of doses **(**5 000 – 125 000 μC/cm^2); and **b)** after immersion into Au-NPs **(step 2)**.

Figure 2.7 a) summarised SEM images of Au-NPs attached to NPHT SAM exposed at a range of electron doses; **b)** resultant graph showing electron dose vs attachment of Au-NPs **(step 2)**.

Figure 2.8. Figure depicting '*snap-on*' and '*snap-off*' points in AFM adhesion force mapping.

Figure 2.9. AFM adhesion force maps in air; **a)** approach (*snap-on*); **b)** retract (*snap-off*); & **c)** adhesion force response of region across exposed and un-exposed areas of sample.

Figure 2.9. (step 3) Diagram showing the linear feature sizes examined, **type A** (*500 nm wide, 400 nm gap*) and **type B** (*250 nm wide, 550 nm gap*).

Figure 2.10. Diagram showing the areas exposed to the primary incident electron beam (red areas), **type A** (*500 nm wide, 400 nm gap*) and **type B** (*250 nm wide, 550 nm gap*) (**step 3**).

Figure 2.11. a) SEM images of **type A** & **B** features fabricated at increasing electron dose and after immersion in Au-NPs; **b)** Graph depicting the percentage increase (broadening) in line-widths of features after deposition of Au-NPs, ■ **type A** and ▲ **type B** (**step 3**).

Figure 2.12. SEM image of **type A** feature, *inset*, magnified region of a single 500 nm wide feature **(step 3)**.

Figure 2.12. (step 3) Diagram showing the linear feature sizes examined, **type C** (*500 nm wide, 1000 nm gap*) and **type D** (*250 nm wide, 1000 nm gap*).

Figure 2.13. Diagram showing the areas exposed to the primary incident electron beam (red areas), **type C** (*500 nm wide, 1000 nm gap*) and **type D** (*250 nm wide, 1000 nm gap*) (**step 3**).

Figure 2.14. Surface coverage analysis from AFM images of Au-NPs and C-Au-NPs deposited on a 4-ATP SAM.

Figure 2.15. Graphs showing the 'actual' width of; **a)** 500 nm lines (**type C**); and **b)** 250 nm lines (**type D**) of C-Au-NPs with 1000 nm gap, measured by AFM, plotted against electron dosage of underlying SAM. Region A shows feature broadening with electron dose, while region B shows pattern inversion.

Figure 2.15. SEM image of 250 nm wide C-Au-NP lines exposed at 45 000 $\mu C/cm^2$ (**type D**), *inset*, magnified region of 250 nm wide feature showing non-specific adsorption either side of the feature.

Figure 2.16. SEM image of inverted type D features exposed at 90 000 $\mu C/cm^2$, with no attachment of C-Au-NPs in regions of the primary electron dose of the SAM but attachment in the inter-feature gaps, *inset*, magnified region showing 250 nm wide feature free of C-Au-NPs (**step 4**).

Figure 2.18. a,b & c) AFM adhesion force maps of inverted pattern regions after immersion in C-Au-NPs (**step 4**).

Figure 2.19. Diagram depicting the electron dose related behaviour of NPHT SAMs.

Chapter 3

Scheme 3.1. Scheme showing the way in which LBL films are sequentially built-up.

Figure 3.1. a) Topographical AFM image of PEM line arrays with (PDDA/ $PSS)_3$PAH layers and **b)** its corresponding height profile.

Figure 3.2. Figure demonstrating the optical properties of gold nanoparticles.

Figure 3.3. Photo of a simple microfluidic mixer device made from polystyrene

Scheme 3.2. Experimental scheme for sequential PDAC/Au-NP deposition process

Scheme 3.3. Experimental scheme for sequential PDAC/Au-NP deposition process after photolithographic pre-patterning of underlying substrate.

Scheme 3.4. Experimental scheme for sequential PDAC/Au-NP deposition process via microfluidics after T-Au-NP surface patterning & derivatisation with NH_2 terminated thiol SAM.

Scheme 3.5. Chemical structure of PDAC, n=100-200 kDa.

Figure 3.4. Photograph of the solution cell fabricated for the measurement

Figure 3.5. Time vs thickness data for deposition of PDAC on silicon surface examined with *in-situ* spectroscopic ellipsometry (**step 1**).

Figure 3.6. AFM tapping mode height images of PDAC/Au-NP sequential deposition on glass.

Figure 3.7. Model showing the sequential build-up of Au-NPs on the substrate surface.

Figure 3.8. Results of a visual count of the number of Au-NPs per 500 nm^2 for each bilayer from AFM images.

Figure 3.9. UV-vis spectrophotometry graphs for 1, 2 and 3 bilayer PDAC/Au-NP films on glass substrates (**steps 2, 3 & 4 respectively**).

Scheme 3.6. Schematic representation of UV-vis experiment.

Figure 3.10. Graph showing the number of nanoparticles per 500 nm^2 calculated from UV-vis results.

Figure 3.11. Schematic representation and specifications of the cantilevers used as supplied by the manufacturer.

Figure 3.12. Tapping mode images of cantilevers after addition of each PDAC/Au-NP bilayer.

Table 3.1. Data obtained from PDAC/Au-NP mass adsorption experiments.

Figure 3.13. Graph showing the number of Au-NPs per 500 nm^2 estimated from mass adsorption experiments.

Table 3.2. Average values for the number of nanoparticles deposited per 500 nm^2 obtained from UV-vis estimation, direct counting with AFM and AFM cantilever mass adsorption experiments.

Figure 3.14. Optical microscopy of remaining negative pattern from a TEM grid after resist exposure and removal (**step 7**).

Figure 3.15. a) Optical microscopy image of $(PDAC/Au\text{-}NP)_1$ features (darker regions) after removal of the underlying photoresist with inset schematic of TEM grid mask; **b)** zoomed in image of patterned region (**step 10**).

Figure 3.16. UV-vis spectra of $(PDAC/Au\text{-}NP)_1$ sample on glass before and after immersion in photoresist remover (**step 9**).

Figure 3.17. a) AFM tapping mode images of $(PDAC/Au\text{-}NP)_1$ features after photoresist removal, magnified regions; **b)** with and **c)** without aggregated nanoparticle structures; and **d)** line section across image a).

Figure 3.18. Diagram of microfluidic wafer layout.

Figure 3.19. Photograph and markings for positions of TEM grids on silicon wafer (**step 12**).

Figure 3.20. Optical microscopy images of **a)** surface of silicon wafer after patterning through TEM grid mask with 244 nm laser and rinsing with chloroform, **b)** magnified region (**step 13**).

Figure 3.21. a) Silicon wafer after microfluidic lid bonding and **b)** the complete wafer after fitting of microfluidic ports (**step 14**).

Figure 3.22. Optical microscopy images of two regions of the surface of silicon wafer after microfluidic lid bonding (**step 14**).

Figure 3.23. Optical microscopy images of inspection windows of microfluidics wafer; **a)** before addition of any liquids; **b)** after deposition of 4-ATP; **c)** after deposition of 1 layer Au-NPs; **d)** after further deposition of a $(PDAC/Au\text{-}NP)_1$ layer ;and **e)** after deposition of $(PDAC/Au\text{-}NP)_2$ layers.

Chapter 4

Scheme 4.1. a) Schematic diagram of magnification of an inkjet printed image; and **b)** photograph of a section of business card and magnified image showing dried inkjet printed droplets.

Figure 4.1. Schematic of a thermally activated Canon impulse jet printhead.

Figure 4.2. a) Optical microscope image of patterned carbon nanotube catalyst dot pitch 20 μm; **b)** and **c)** SEM image of multi wall carbon nanotubes grown at the patterned area.

Figure 4.3. Light microscopy images of printed collagen patterns, including a ring and a circle, prior to cell seeding at **a)** x40 **b)** x100 and **c)** a circular pattern at x40 magnifications.

Figure 4.4. Diagrammatic representation of nanoindentation, nanoscratching, and nanoshaving fabrication processes from side views and top views: **a)** nanoindentation is the local deformation of a material formed by indenting the surface; **b)** nanoscratching is the extended formation of an abrasion on the surface of a material; and **c)** nanoshaving is the removal of material from the surface of a material.

Figure 4.5. AFM image of a furrow scratched into polyimide; *inset,* cross-section of feature.

Scheme 4.2. Schematic representation of work carried out.

Table 4.1. Operating Specifications for Canon Pixma ip5300 Inkjet Printer

Figure 4.6. Photograph of the adapted CD carriage for printing directly to standard microscope slides with highlighted area for microscope slide placement.

Scheme 4.4. Chemical structure of Trifluoropropylsilane, TFPS.

Figure 4.7. Digital photographs showing the contact angle of a 2µl droplet of PDAC on **a)** clean glass surface (<5^{o}); and **b)** hydrophobised glass surface (~80^{o}).

Scheme 4.3. Chemical structure of PDAC, n=100,000 – 200,000 MW.

Table 4.2. Optical microscopy images of the varying film morphologies of PDAC inkjet printed at various densities per unit area (all images same scale) and mass of material deposited at each density (*calculated through weighing of substrate before and after printing*) on hydrophilic surfaces.

Figure 4.8. Optical microscopy images of inkjet printed PDAC regions on hydrophilic glass surfaces.

Figure 4.9. Optical microscopy images and size analysis of PDAC islands printed at 1Y density on both hydrophilic and hydrophobised surfaces.

Figure 4.10. Diagrammatic representation of PDAC droplet with **a)** hydrophilic surface; and **b)** hydrophobic surface

Figure 4.11. Digital photograph of Au-NPs printed to absorbant photographic paper in order to visualise their characteristic red colouration after 20 printing runs.

Figure 4.12. Photograph showing Au-NP aggregation (dark purple colouration) in the nozzle of an ink cartridge.

Figure 4.13. a) Optical microscopy images of inkjet printed PDAC features during immersion in a solution of C-Au-NPs; and **b)** graph showing the blue pixel count of the resultant PDAC/C-Au-NP features as a function of time.

Figure 4.14. Optical microscopy of PDAC templated features on clean glass and hydrophobised glass surfaces after deposition of C-Au-NPs.

Figure 4.15. Comparison of 1Y PDAC feature sizes on clean glass and hydrophobised glass surfaces after immersion in C-Au-NPs.

Figure 4.16. AFM **a)** *height, amplitude* and *phase* images of area after nanscratching process; and **b)** section analysis showing apparent height from top of (PDAC/C-Au-NP) to bottom of scratched feature.

Figure 4.17. a) Large-scale optical microscopy image of AFM scratched regions of inkjet printed PDAC and solution deposited C-Au-NP film under increasing load *(or decreasing vertical deflection settings)*; **b)** close-up image of highlighted region (image a) of AFM scratched squares with highlighted region of material build-up.

Figure 4.18. Representative optical microscopy images of the circular island PDAC/C-Au-NP features both before and after AFM scratching procedures.

Figure 4.19. Colour transmitted-light optical microscopy image confirming the removal of the C-Au-NPs from the centre of the IJP templated features, *inset,* magnified region.

Chapter 5

Figure 5.8. Diagram showing setup for measuring the speed of rotation.

Figure 5.9. Graph showing the measured rotation speeds achieved at the motor supply voltages.

Figure 5.10. Optical microscopy image of collagen fibres aligned in the direction of the flow of the suspension over the surface.

Figure 5.11. SEM images of **a)** a collagen fibre on a corrugated Au surface; **b)** the end of a collagen fibre where the smaller composite fibres and fibrils have spread on the surface; **c)** a close-up of a collagen fibre showing the composite fibres and fibrils.

Figure 5.12. Diagram showing the way in which collagen is proposed to attach to surface.

Figure 5.13. AFM contact mode image of collagen fibril aligned in the direction of the Au corrugations, *inset,* magnified region of fibril crossing surface valley.

Figure 5.14. AFM contact **(a, b, c, *left*)** and deflection **(a, b, c, *right*)** images of collagen fibrils aligned at 90^0 on corrugated Au surfaces.

Figure 5.15. Diagram depicting the measurements taken with AFM to determine the deformations exhibited by the collagen fibres over the corrugated surface.

Figure 5.16. Graphs depicting the relationship between **a)** the fibril lengths to fibril diameter; **b)** fibril diameter to deformation distance; and **c)** fibril length to deformation distance.

Chapter 6

Figure 6.1. Comparison of some available methods for patterning DNA on surfaces, soft-lithography using PDMS stamps, surface lithographic pre-patterning and the method presented here of photo-patterning the DNA molecules themselves.

Scheme 6.1. Experimental scheme.

Figure 6.2. Tapping mode AFM image of SiO_2 surface after cleaning and –OH functionalisation (**-OH, substrate a**).

Figure 6.3. Tapping mode AFM image of SiO_2 after APTMS SAM functionalisation (**-NH_2, substrate b**).

Table 6.1. Water contact angles, thickness and RMS roughness of functionalised silicon surfaces.

Figure 6.4. N (1s) X-ray photoelectron spectra of substrates a-d.

Figure 6.5. Tapping mode AFM image of SiO_2 surface functionalised with isothiocianate groups (**-SCN, substrate c**).

Figure 6.6. Tapping mode AFM image of surface functionalised with oligonucleotide A, (**-OLIGO, substrate d**).

Scheme 6.2. Photocleavage of the hairpin oligonucleotide A carrying the 2-nitrobenzyl group (DMT, dimethoxytrityl group).

Figure 6.7. AFM tapping mode image of surface after photolysis and rinsing with single oligonucleotide strand (**-SINGLE, substrate f**).

Figure 6.8. Figure showing **i)** the presence of the hairpin loop, **ii)** the removal of the hairpin loop, revealing the single stranded oligonucleotide and **iii)** self-coiling and/or collapse of the resultant single-stranded oligonucleotide.

Figure 6.9. Assessment of intramolecular versus intermolecular duplex formation by photolysis and subsequent hybridization. Two silicon surfaces were functionalised with hairpin oligonucleotide A. One surface was not photolyzed with UV light **a)** while the other was photolyzed **b)**. Hybridization with the complementary oligonucleotide labelled with rhodamine showed a more intense fluorescence at the photolyzed surface **b)**. *Inset*, are the average fluorescence intensities of the unphotolyzed / photolyzed surfaces in arbitrary units (a.u.).

Figure 6.10. AFM tapping mode image of surface after hybridisation with complementary strand B carrying rhodamine label (**-RHODAMINE, substrate g**).

Figure 6.11. AFM tapping mode image of surface after hybridisation with complementary strand B carrying gold nanoparticle label (**-AuNP, substrate h**).

Figure 6.12. **a)** Fluorescence image after photo-patterning and hybridization with complementary sequence B labelled with rhodamine (substrate g) (step 7), *inset:* Image of the calibration mask used in the photolysis. **b)** Optical microscopy image after photo-patterning and hybridization with complementary sequence B labelled with 10 nm gold nanoparticles (substrate h) (step 8). *inset:* Image of the calibration mask used in the photolysis. The visible lines are areas that were masked during photolysis and hence have no nanoparticles attached. Photography obtained with a stereomicroscope with lateral illumination.

List of Common Acronyms Used

4-ATP	**4-aminothiophenol**
AFM	**Atomic Force Microscopy**
APTMS	**Aminopropyltrimethoxysilane**
EBL	**Electron Beam Lithography**
IJP	**Inkjet Printing**
LBL	**Layer-by-layer**
OTS	**Octadecyltrichlorosilane**
PDAC	**Poly-diallyldimethylammonium chloride**
SAM	**Self-assembled Monolayer**
SEM	**Scanning Electron Microscopy**
SNOM	**Scanning Near-field Optical Microscopy**
TFPS	**Trifluoropropylsilane**
XRL	**X-ray Lithography**

Chapter 1

Small Foundations in Big Science:

The Formation and Characterisation of Micro and Nanostructured Surfaces.

Chapter 1 is reproduced in parts from an article entitled:

'Engineering Nanostructures at Surfaces Using Nanolithography' by Sara Diegoli, Christopher A. E. Hamlett, Simon. J. Leigh, Paula. M. Mendes and Jon. A. Preece, in *Proceedings of the IMECH E Part G Journal of Aerospace Engineering*, **2007**, *221*, 589

Abstract

This chapter provides an introduction into the background of micro and nanostructured surfaces. Micro and nanostructured surfaces have important functions in both nature and the technology we use every day. An introduction to techniques used to fabricate and characterise these surfaces is also presented. An overview of the scope of nanostructured surfaces is followed by considerations of lithographic methods, irradiative methods and mechanical methods for top-down nanostructuring of surfaces which is then followed by an overview of bottom-up approaches to nanostructuring surfaces. Surface characterisation techniques are described in detail and evaluated.

1.1 Micro/nanostructures and surfaces

1.1.1 Microstructures and microstructured surfaces

Microstructures are generally classed as structures with length scales between 1-100 μm. Microstructured surfaces are therefore surfaces that contain features within this size regime.[1] Many of the objects around us exhibit microstructuring, even living cells can be classed as microstructures.[2] One of the main places where such structures and architectures are commonplace is within the microelectronics industry.

1.1.2 Microelectronics

Microelectronics is a subfield of electronics. Microelectronics, as the name suggests, is related to the study, manufacture and fabrication, of electronic components with micrometre-scale features.[3] Most microelectronic devices are made from semiconductor materials and many components of normal electronic design are available in microelectronic equivalent: transistors, capacitors, inductors, resistors and diodes. The microelectronics industry has been at the forefront of developing new fabrication technologies in order to miniaturise computer components and devices for many years.

1.1.3 Moore's Law

In 1965, Gordon Moore (co-founder of Intel) observed a trend that has driven the growth of the microelectronics industry for the past 40 years.[4] He observed that the number of transistors (the most important feature of a silicon chip) per integrated circuit was doubling every 12 months (figure 1.1).

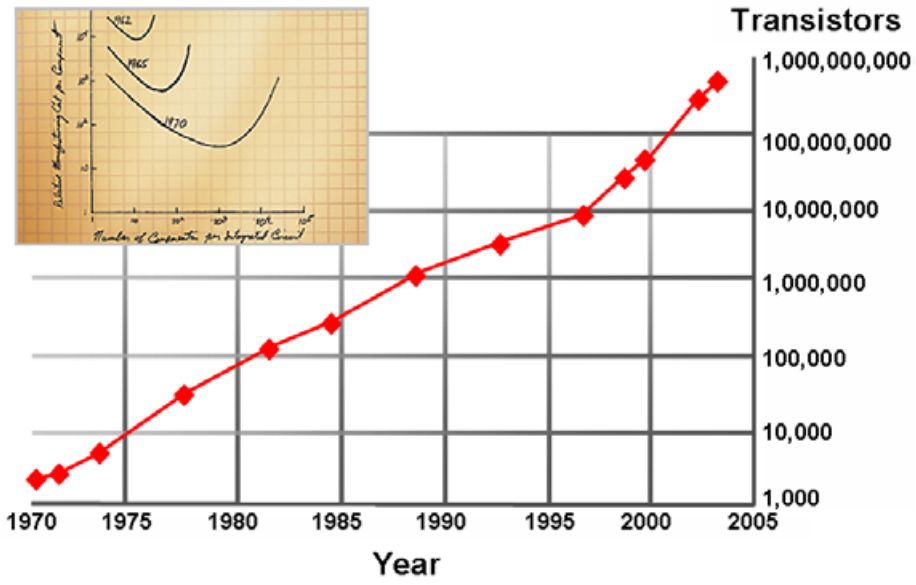

Figure 1.1. Moore's law predicts increase in transistors per unit area *vs* time, *inset* Moore's' original graph.[4]

Since this prediction, the microelectronics industry has been roughly following this trend. However, we are now at the point where if we desire to continue with this trend for miniaturisation, new fabrication methods are needed, as we reach the limits of our current manufacturing technology.[5] In the drive to reach these goals the microelectronics industry has evolved to become the nanoelectronics industry, where structures with nanoscale dimensions are becoming regularly and easily achievable.

1.2 Top-down fabrication

Top-down fabrication has been the mainstay for creating micro-scale structures for the past 50 years and is still used today for producing nano-scale electronic structures.[6] The approach can be likened to an artist carving a sculpture from a single piece of wood and is a subtractive approach (scheme 1.1).

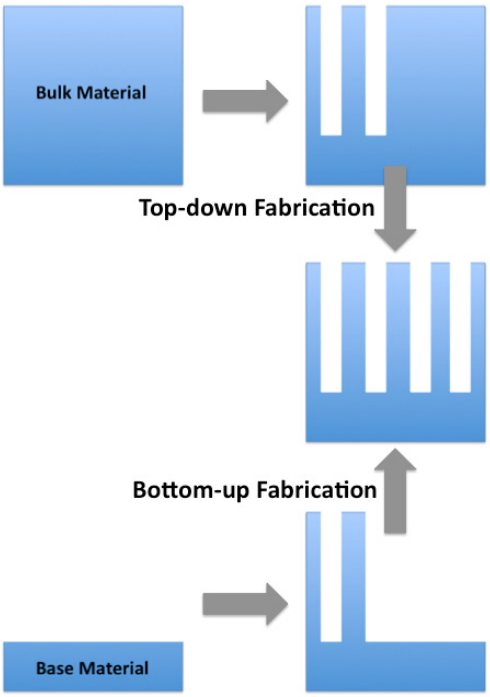

Scheme 1.1. Schematic of top-down fabrication process, showing removal of material to reach final structure and bottom-up fabrication process showing addition of material to reach the final structure.

Top-down fabrication has allowed the microelectronics industry to produce 65 nm transistors, with chips due for production containing features of 45 and 25 nm.[7] However, photolithography, the process used to make these structures is reaching fundamental limits in terms of the miniaturisation that is achieved.[8]

1.3 Bottom-up fabrication

Bottom-up fabrication can take advantage of inherent structural motifs in molecular building blocks, allowing them to self-assemble in a precise manner into the desired structure[9, 10] (scheme 1.1). The bottom up approach encompasses such things as dendrimer formation[11, 12] supramolecular chemistry[13] and nanomaterial synthesis. Fabricating nanoscale structures and architectures on surfaces has been the subject of intense interest and investigation in the last several years,[14] with much

focus on the bottom-up routes for fabrication, as these routes represent some of the ultimate fabrication limits that are achieved.

1.4 Nanotechnology

Nanotechnology is an interdisciplinary research area, concerned with the fabrication of structures,[15] electronic devices,[16] optical,[17] chemical[18] and biological sensors[19] with dimensions from 1 to 100 nm (1 nm = 1 x 10^{-9} m). With an ever increasing demand from consumers and industry alike for miniaturisation of microelectronic devices, new and novel methods for fabrication of nanostructured architectures are required. Richard Feynman predicted in his famous speech in 1959,[20] that miniaturisation would reach such a degree that it might be possible to store information at atomic levels, or how it might be possible to build molecular sized machines. These predictions have paved the way for research that has lead us to the point where Richard Feynmans visions are being realised.

1.4.1 Nanostructures & nanostructured surfaces

Nanostructures are generally classed as structures with length scales between 1-100 nm. In just a few years, exploring nanostructured materials has become a new theme common to many disciplines of science and engineering.[21] The recent surge of interest in these nanostructured systems stems from the novel physical and chemical properties that arise upon size reduction.[22] Structured materials on the nanometre scale can lead to improved, and sometimes novel properties with emerging applications ranging from functional devices to advanced chemical and biological sensors.[23] Significant advances made in nanomaterials research, together with improved lithographic fabrication strategies[24] have led to dramatic enhancements in the creation of complex and well-defined nanostructures on surfaces. Control of

matter on the nanoscale already plays an important role in scientific disciplines as diverse as physics, chemistry, materials science, biology, medicine, and engineering.[25-27] Nanostructures are low-dimensionality material systems that can possess many novel properties[28-31] that are fundamentally different from those displayed by the bulk materials. When nanostructures are engineered into functional materials, these systems benefit from the unique properties exhibited by the nanostructures. High-performance electronic[32] and optoelectronic devices,[33] specific chemical and biological sensors[34, 35] and tools for biological[36] and quantum mechanical[37, 38] research are just some of the potential application for nanostructured materials. Major advances in nanoscience and nanotechnology have enabled the development of synthetic techniques and new tools for manipulating, fabricating and characterizing nanostructured materials. Molecular surface science has greatly contributed to the advancement of nanofabrication technology by providing ideal platforms for engineering surfaces on a molecular level.[39–44] For instance, self-assembled monolayers (SAMs), (section 1.4.2.2) which form spontaneously by the adsorption of an active surfactant onto a solid surface, possess important properties of self-organization and adaptability to a number of technologically relevant surface substrates. The properties of a SAM (thickness, structure, surface energy, and stability) can be easily controlled and specific functionalities can also be introduced into the building blocks. SAMs of thiols on gold[45] and triethoxysilanes on silicon dioxide[46] are examples of two widely used techniques to modify the surface properties of metallic and inorganic substrates. The variety of methods[47–51] available to characterise SAMs and other functionalised surfaces on the nanoscale has grown in step with the ability to create sophisticated, patterned surfaces. Scanning probe techniques, such as scanning-tunnelling microscopy (STM)[52], atomic force microscopy (AFM, section 1.6.3)[53] and scanning near-field optical microscopy[54] are

very important analytical tools that are capable of imaging surfaces down to the nanometre scale. Aside from their use in nanoscale topographical imaging,[55] scanning probe microscopes have been widely employed in nanolithography.[56] Furthermore, lithographic techniques developed for the semiconductor industry, such as electron beam lithography (EBL, section 1.5.1.2.2) and X-ray lithography (XRL, section 1.5.1.2.3), have been combined with advanced surface chemistry techniques to develop new nanofabrication protocols.

1.4.2 Concepts and materials for nanostructure fabrication

Current research strategies are aimed at integrating top-down and bottom-up methodologies to achieve useable nanostructures in a fashion that allows for straightforward fabrication and the possibility of mass scale production. Some of the major concepts and materials used are explained below.

1.4.2.1 Self-assembly

Self-assembly[57] can be defined as the assembly of molecules or atoms into organised structures, *via* covalent and non-covalent bonds.[58, 59] There are two types of molecular self-assembly, *intra*molecular self-assembly and *inter*molecular self-assembly. Intramolecular self-assembling molecules are often complex polymers with the ability to assemble from a random coil conformation into a well-defined stable structure such as protein secondary and tertiary structures.[60] Intermolecular self-assembly is the ability of molecules to form supramolecular assemblies (quaternary structures) (figure 1.2).[61]

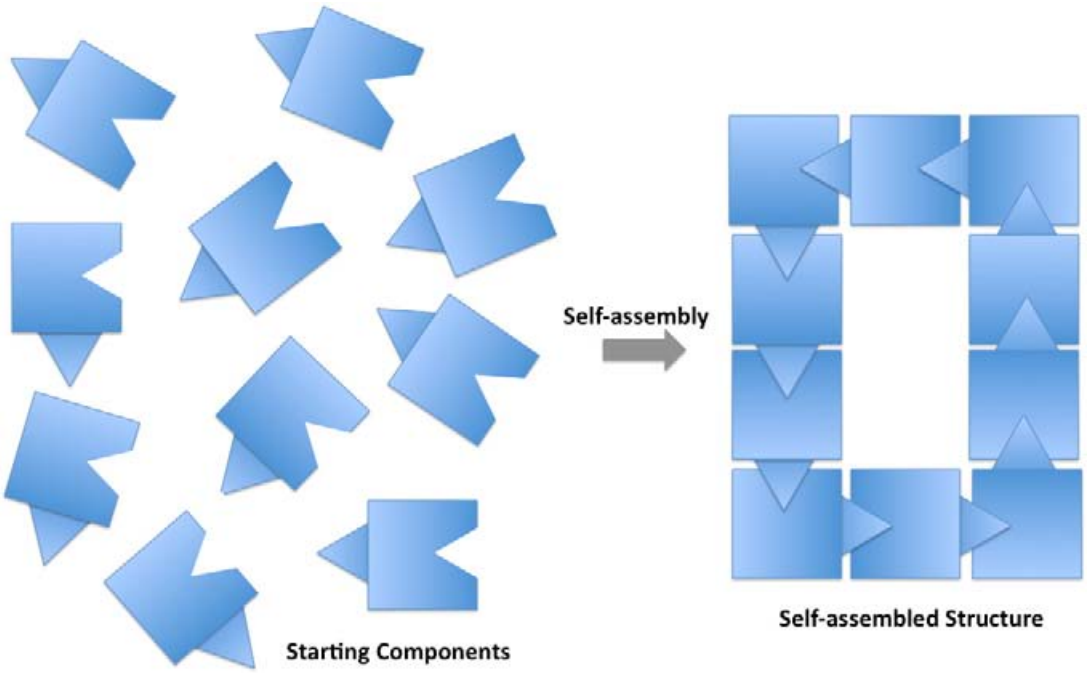

Figure 1.2. Diagram depicting self-assembly of components into a final structure.

A simple example of intermolecular self-assembly is the formation of a micelle by surfactant molecules in solution.[62] The term, self-assembly can also be applied to the process of nanoscale components such as colloids and polymers into larger architectures.[63]

1.4.2.2 Self-assembled monolayers (SAMs)

SAMs are relatively ordered assemblies of organic molecules[64, 65] one molecule thick, attached to a solid substrate. The formation of a SAM involves taking an organic molecule that has a headgroup with a specific affinity for a certain bulk substrate (e.g. gold, glass, silicon) and allowing a layer of these molecules to chemisorb to the surface from solution or the vapour phase (figure 1.3). A common example of a well ordered SAM is alkane thiols on gold.[66] A clean Au substrate is immersed in a solution of alkanethiolates which weakly physisorb onto the substrate allowing the S-containing head group to chemisorb on the substrate surface forming

an Au-S bond. As more alkanethiolate molecules adsorb on the surface, islands of surfactant molecules form as a result of attractive intermolecular van der Waals forces which continue to grow until the substrate surface is covered by a layer of surfactants of monomolecular thickness. In order to minimise the free energy of the system, and to maximise intramolecular van der Waals forces between molecular chains, the surfactant molecules tilt at an angle which is commonly ~30 ° to the surface of the substrate. The initial stage of thiol SAM formation (both physisorption and chemisorption) usually takes minutes or less at 0.1-10 mM thiol concentration in a solvent.[67] More ordering of the assembly can take place over days or months, with thiol molecules taking on their characteristic tilt on gold surfaces,[68] depending on the molecules involved. The chemistry of the alkanethiolate backbone has a major influence on the rate of SAM formation,[69] highlighted by the fact that alkanethiols with a long chain alkyl backbone form SAMs at a faster rate than those consisting of a shorter alkyl backbone.[70] This difference in the rate of SAM formation is due to the attractive van der Waals forces between adjacent molecules increasing as a function of chain length.

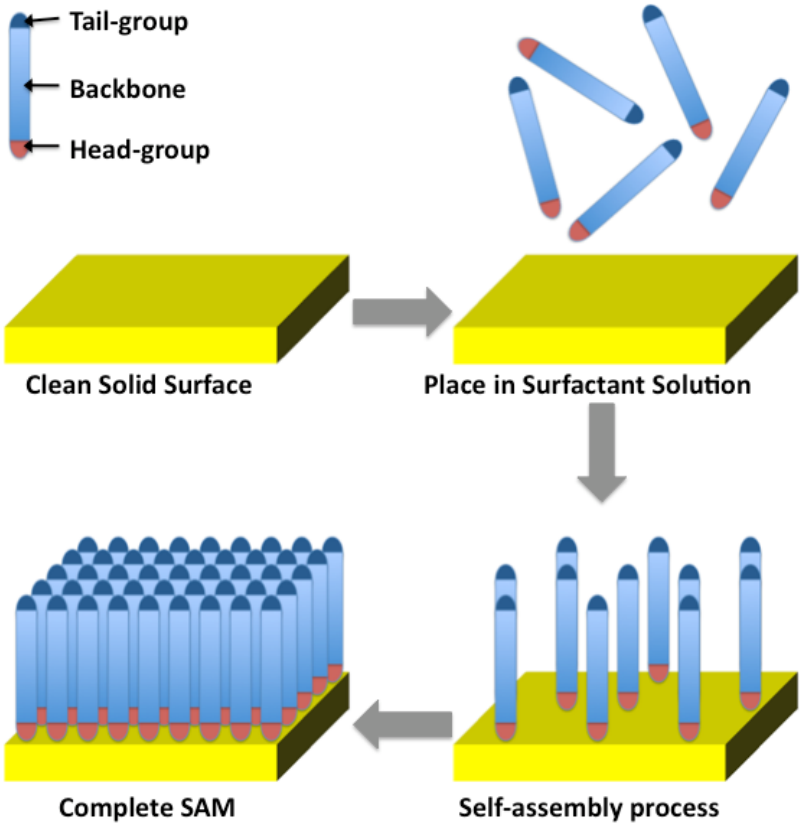

Figure 1.3. Schematic representation of generic SAM formation process.

A variety of other self-assembled monolayers can be formed on solid substrates. Organosilane molecules on silicon oxide[71-75] surfaces are another well known example of a SAM system which potentially offer greater technical relevance to electronics than alkyl thiol assembly on metals, as silicon is the base material of choice for the microelectronics industry.[76] Organosilane SAMs are thought to be amorphous in nature, with defects present at the surface. Organosilane SAMs on silicon are more difficult to form[77, 78] than thiols on Au, because the water required to promote the chemisorption of the molecules to the surface, also promotes the formation of oligomeric siloxanes in solution. These oligomers then physisorb to the surface, forming ill-defined surfaces.[79, 80] The full mechanism of organosilane monolayer formation is not fully understood, but studies with OTS,[81-83] suggest the following:

- **Surface adsorption:** a monolayer of the monomer ($RSi(OR')_3$ where R' = methyl or ethyl group) is physisorbed to the surface.[84]
- **Hydration:** $RSi(OR')_3$ is hydrolysed to $RSi(OH)_3$ by the inherent hydrogen bonded water layer present at the SiO_2 surface.
- **Silanisation:** a chemical reaction covalently links the silanes together and anchors them to the surface by dehydration.[85]
- **Cross-linking:** silane molecules cross-link.

Silane SAM formation has also been shown to be highly dependent on formation conditions such as deposition temperature,[86] solvent choice and silane concentration and amount of water present,[87] with initial cross-linking and bonding to the surface taking up to an hour at room temperature.[88]

SAMs in general, remain high priorities for research,[89-91] as they allow one to modify metal and semi-conductor surfaces with chemically well-defined ultrathin organic films in a relatively easy and reliable manner.[92]

1.4.3 Nanoscale materials

Most molecular systems can be classed as nanoscale materials as they have length scales on the order of nanometres. Examples of other commonly used nanoscale materials are nanoparticles,[93] (along with nanotubes[94] and nanorods[95]) polymers,[96] polyelectrolytes[97] and even DNA oligonucleotides.[98] The nanoscale components related to this thesis are introduced below.

1.4.3.1 Metal nanoparticles

Metal nanoparticles have attracted much attention in recent years.[99-101] as they have some interesting properties[102] that make them attractive for use in catalysis,[103] electronics,[104] optics,[105] and biotechnology.[106-107] L. B. Hunt in his article entitled 'The true story of the Purple of Cassius' published in 1976 said that the literature on gold, glass and ceramics has attributed Andrew Cassius the credit for discovering the the purple preparation of colloidal gold with stannous hydroxide some 300 years previously.[108] The process is still used today to produce enamel colours from pink to maroon but was known of as far back as the 1600's. One of the first scientific papers examining the properties of gold nanoparticles was written in 1857 by Michael Faraday who was fascinated by the ruby red colour of colloidal gold and how it interacted with light.[109] Faraday concluded that the ruby red fluid was gold dispersed in the liquid in a finely divided metallic form not visible in the microscopes of the day. The ruby red colour he observed is attributable to a narrow absorption band of the particles at 520 nm.

The term 'colloid' used to describe a mixture where one substance is evenly dispersed in another, was coined by T. H. Graham in 1861.[110] Since these early studies, gold nanoparticles have been found to be versatile building blocks for nanoscale materials, structures and devices[111] due to their highly conducting nature. Nanoparticle solutions can be considered as metal atom clusters[112] surrounded by an absorbed stabilising agent to prevent aggregation, and are classed as colloidal dispersions.[113] The stabilising agents on the surface of the nanoparticles are usually organic molecules which may or may not carry a charge.[114] The optical properties of gold nanoparticles are discussed in subsequent chapters.

1.4.3.2 Polyelectrolytes

Polyelectrolytes are polymers whose repeating units bear an electrolyte group, which dissociates in aqueous solutions making the polymers charged.[115] Like polymers, polyelectrolytes solutions are often viscous. Charged molecular chains, commonly present in soft matter systems, play a fundamental role in determining structure, stability and the interactions of various molecular assemblies.[116] The unique properties are being exploited in a wide range of technological and industrial fields.[117] One of the major natural occurrences of polyelectrolytes is biology and biochemistry.[118] Many biological molecules are polyelectrolytes, for instance, polypeptides and DNA are polyelectrolytes.[119]

1.4.3.3 DNA oligoncleotides

An oligonucleotide is a short nucleic acid polymer, typically with twenty or fewer bases. Although they can be formed by bond cleavage of longer segments, they are now more commonly synthesised by polymerizing individual nucleotide precursors.[120] Automated synthesizers allow the synthesis of oligonucleotides up to 160 to 200 bases. The length of the oligonucleotide is usually denoted by "mer" (from Greek meros, "part"). For example, a fragment of 25 bases would be called a 25-mer. Because oligonucleotides readily bind to their respective complementary nucleotide, they are often used as probes for detecting DNA or RNA.[121] Examples of procedures that use oligonucleotides include DNA microarrays.[122] Oligonucleotides composed of DNA (oligodeoxyribonucleotides) are often used in the polymerase chain reaction, a procedure that can greatly amplify almost any small piece of DNA.[123]

1.6 Nanostructure and nanostructured surface fabrication

The common techniques for nanostructuring surfaces can be loosely grouped into three main types; *irradiative methods*, *soft lithographies and mechanical methods*, Each specific fabrication type has its own inherent advantages, disadvantages and resolution. Careful choice of an appropriate fabrication technique is key in forming functional nanostructured surfaces.

1.5.1 Lithographic methods

Lithography (from the greek terms *lithos*, meaning stone & *grapho*, meaning to write) when applied to the formation of structured surfaces traditionally refers to a process where a material is deposited on a surface then patterned through irradiative exposure. More recently, lithography has become an umbrella term for processes creating patterns on surfaces through a variety of methodologies, such as *irradiative* and *soft lithographies.*

1.5.1.2 Irradiative methods

1.5.1.2.1 Photo/optical-lithography

(N.B. Work carried out using photolithography is presented in chapter 3)

UV-visible light is a valuable tool for the preparation of topographically and chemically patterned surfaces. Conventional photolithographic processes use visible and UV light to pattern a thin film of resist spin-coated to a substrate surface.[124] The minimum feature sizes obtained with photolithography can vary depending on the process used, but are on the order of 50-100 of nanometres using a deep-UV light source. Upon exposure to the light source the resist molecules either undergo photoinitiated polymerization and cross-linking (negative photoresist) or

photoinitiated degradation (positive photoresist) depending on the type of resist used.[125] Patterns are achieved by passing the light through a photomask before it reaches the resist layer. This mask either allows light to pass or blocks light in specific regions, leading to transfer of the specific shape to the resist layer. The resists used in conventional photolithography are normally polymers in spin-coated layers of up to tens of microns.[126] Once a resist pattern is achieved on the sample surface, the pattern can be transferred to the bulk material of the sample through an etching step,[127] where the areas free from resist are etched away, whereas the regions covered with resist exhibit a slower etch response (figure 1.4).[128]

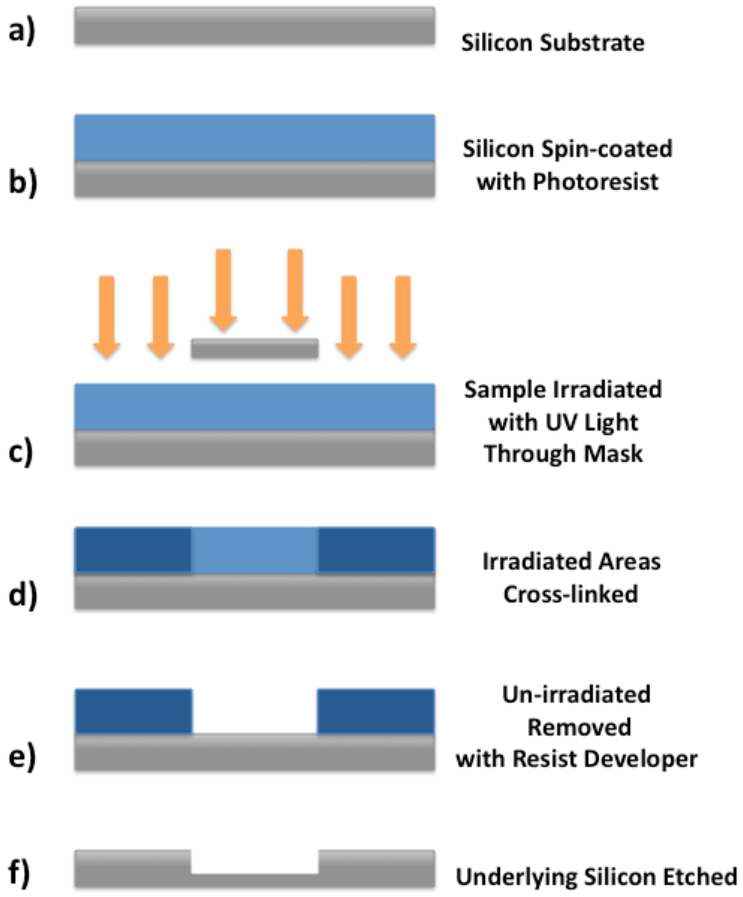

Figure 1.4. Diagrammatic representation of negative photolithography process; **a)** a clean silicon substrate; **b)** a layer of resist spin-coated onto the silicon substrate; **c)** substrate irradiated with UV light; **d)** irradiated areas of resist are cross-linked, **e)** un-

irradiated areas of resist are removed with developer; and **f)** the whole substrate is etched to transfer pattern to underlying silicon.

Different combinations of resist and etch materials, along with resist layer thicknesses lead to differing aspect ratios between regions with and without resist.[129] Photolithography is still used as a mainstream technology throughout the world for structuring and patterning materials, especially within the microelectronics industry with the advent of techniques such as deep UV (DUV) photolithography.[130] The major fabrication limit of photolithography is the fundamental physics behind the process itself, inadequate depth of focus as resolution is increased and diffraction effects.[131] It is possible to improve the depth of focus at a given resolution by decreasing the wavelength of the light used and to a certain extent, this method has proved very successful.[132] However, when the wavelength of the light used is decreased, the light becomes more damaging to the optics and the samples used. For short wavelength light, another problem is that most materials are highly absorbing in this region, meaning that patterning thick resist layers becomes impossible, leading to poor etch aspect ratios.[133]

More recently, the same process has been used to pattern layers of individual molecules (SAMs) chemically bound to surfaces.[134] Exposure of SAMs to short wavelength light (244 nm) initiates highly specific photoreactions, which proceed with very different mechanisms in the case of thiol- and organosilane-based SAMs. Nevertheless, all the photoinduced processes lead to complete or partial removal of the SAM in the irradiated areas. It is known that in these Au-S SAM systems the thiolates-Au bond (R−S−Au) can be oxidized by irradiation with UV light affording sulphonate species ($R-SO_2O-Au$) which are more weakly bound to the Au compared with the original thiols. This simple photochemistry can be used for the preparation of

chemically patterned surfaces by removing the sulphonate from the irradiated areas or displacing it with a second thiol. These patterns can be exploited as masks to etch features in the underlying substrate or further modified to guide the self-organization of nanomaterials, overcoming the problems encountered when using conventional resist systems.[135]

1.5.1.2.2 Patterning with electrons

(N.B. Work carried out using electron beam lithography is presented in chapter 2)

A finely focused beam of electrons can be deflected accurately and precisely over a surface. When the surface is coated with a radiation sensitive polymeric material, the electron beam can be used to write patterns at high resolution. The first experimental electron beam writing systems were designed to take advantage of the high resolution capabilities in the late sixties.[136, 137] Electron beams can be focused to a few nanometers in diameter and rapidly deflected either electromagnetically or electrostatically, such that the EBL process can be used to pattern features down to a few nanometres in size. In practice the smallest features achieved are usually on the order of tens of nanometres unless EBL is carried out in controlled conditions environments. Electrons possess both particle and wave properties and have a wavelength on the order of a few tenths of an angstrom, and therefore their resolution is not limited by diffraction considerations. The resolution of electron beam lithography is limited by forward scattering of the electrons in the resist layer and back scattering from the underlying substrate. (figure 1.5)

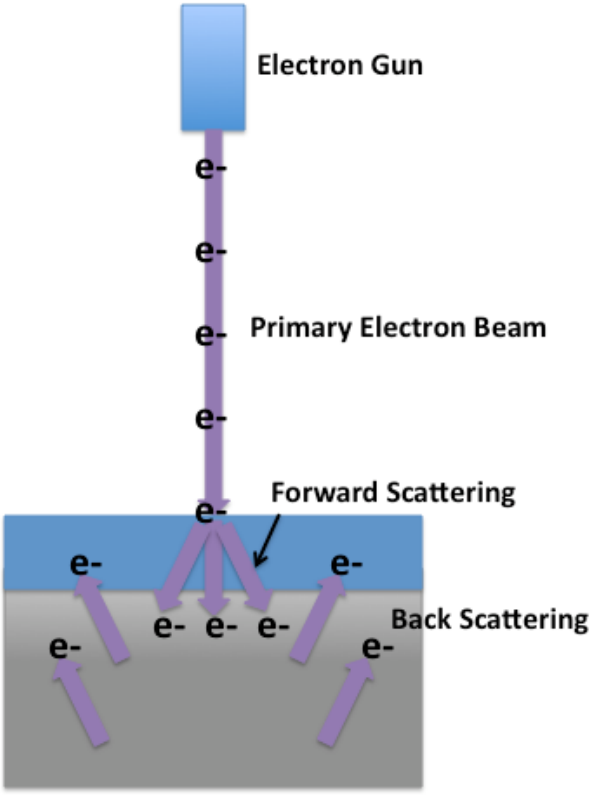

Figure 1.5. Diagram showing the process occurring during electron exposure of a resist covered substrate.

When an electron beam enters a polymer film or any solid material, the electron loses energy via elastic and inelastic collisions known collectively as electron scattering. Elastic collisions result only in a change of direction of the electrons, whereas inelastic collisions lead to energy loss. These scattering processes lead to a broadening of the beam, *i.e.* the electrons spread out as they penetrate the solid producing a transverse or lateral electron flux normal to the incident beam direction, and cause exposure of the resist at points remote from the point of initial electron incidence, which in turn results in developed resist images wider than expected.[138] The magnitude of electron scattering depends on the atomic number and density of both the resist and substrate, as well as the velocity of the electrons or the accelerating voltage. Exposure of the resist by the forward and backscattered electrons depends on the beam energy, film thickness and substrate atomic number. As the beam energy

increases, the energy loss per unit path length and scattering cross-sections decreases. Thus, the lateral transport of the forward scattered electrons and the energy dissipated per electron decrease while the lateral extent of the backscattered electrons increases due to the increased electron range. As the resist film thickness increases, the cumulative effect of the small angle collisions by the forward scattered electrons increases. Thus, the area exposed by the scattered electrons at the resist- substrate interface is larger in thick films than in thin films. Proper exposure requires that the electron range in the polymer film be greater than the film thickness in order to ensure exposure of the resist at the interface. One down-side to EBL is that it is a serial process, in that each individual feature is 'written' one after another, making fabrication times considerably longer than photolithography which is a parallel process. EBL resists such as PMMA (polymethylmethacrylate) are often the same resists used for deep UV photolithography and even X-ray lithography (scheme 1.2).

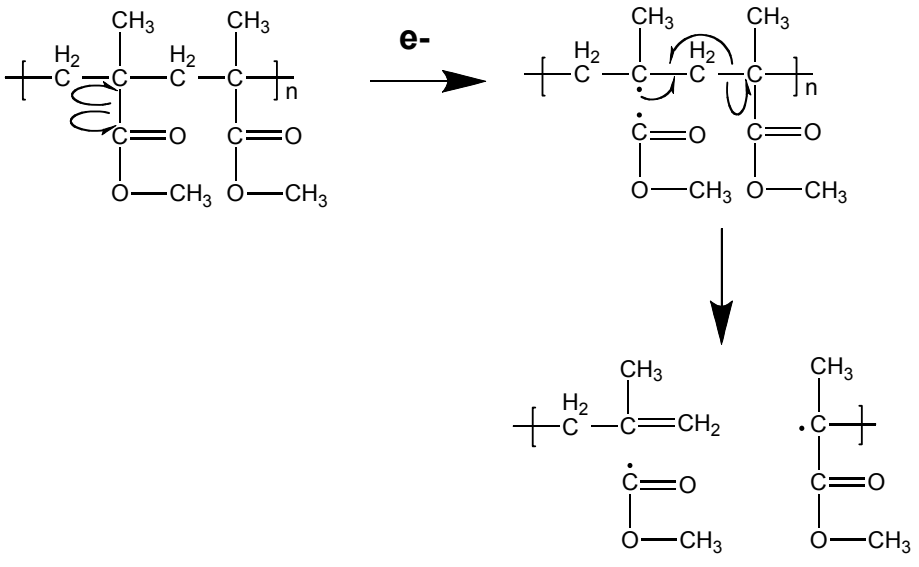

Scheme 1.2. Scheme depicting the break-up of PMMA (positive tone resist) on exposure to electrons.

E-beam induced modification of thiol- and silane- based SAMs has also been the subject of intense research. It has emerged that e-beam exposure leads to loss of orientational and conformational order in the monolayer and scission of covalent bonds that induce dehydrogenation and cross-linking in the molecular film.[139-144] It has also been reported that exposure of aliphatic SAMs to high e-beam doses leads to the transformation of the monolayer to a hydrogen depleted, unsaturated, graphitic residue.[145-149]

1.5.1.2.3 Patterning with X-rays

X-rays with wavelengths in the range of 0.04 to 0.5 nm represent another alternative radiation source with potential for high-resolution pattern replication into polymeric resist materials. X-ray lithography was invented in the early 1970's and is a highly viable sub 0.25 micron lithographic technique.[150] The use of X-rays in semiconductor fabrication was first suggested by H. I. Smith.[151] The essential elements in X-ray lithography include a mask consisting of a pattern made with an X-ray absorbing material, an X-ray source of sufficient brightness and an X-ray sensitive resist material[152] (figure 1.6).

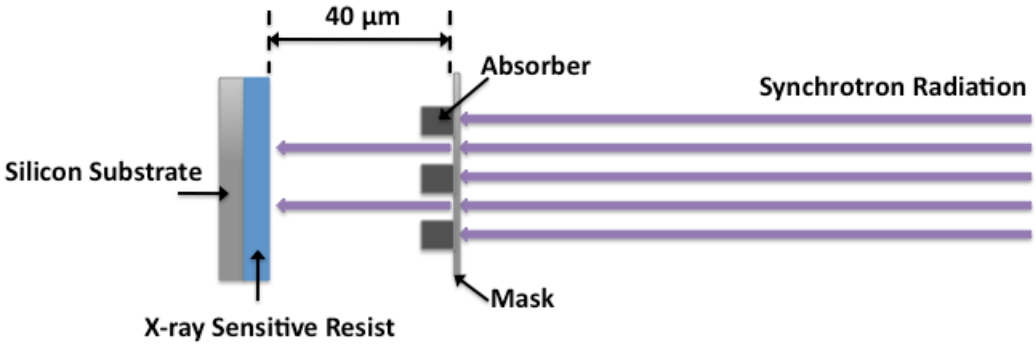

Figure 1.6. Diagrammatic representation of XRL experiment setup.

There are two mainstream types of X-ray radiation sources: (i) electron impact and (ii) synchrotron sources. Conventional electron impact sources produce a broad spectrum of X-rays, centered about a characteristic line of the material, which are

generated by bombardment of a suitable target material by a high-energy electron beam. The synchrotron or storage ring produces a broad spectrum of radiation stemming from energy loss of electrons in motion at relativistic energies. This radiation is characterized by an intense, continuous spectral distribution from the infrared to the long wavelength X-ray region. It is highly collimated and confined near the orbital plane of the circulating electrons, thereby requiring spreading in the vertical direction by moving the mask and wafer combination with constant speed through the fan of synchrotron radiation. Synchrotrons offer the advantage of high power output. Absorption of an X-ray photon results in the formation of a photoelectron which undergoes elastic and inelastic collisions within the absorbing material producing secondary electrons which are responsible for the chemical reactions in the resist film. The range of the primary photoelectrons is on the order of 100-200 nm.

X-ray lithography has seen an increase in use due to the greater availability of powerful and reliable X-ray sources (such as synchrotrons), but still remains a research and prototyping tool due to the costs and mask fabrication requirements. X-ray lithography is normally used as a parallel process, in that all the patterns are formed in one step through irradiation through a mask.[153] As well as being useful for patterning 'conventional' type polymeric resists, X-ray lithography has also been demonstrated with ultrathin molecular resist materials such as SAMs.[154] A more in-depth discussion of X-ray lithography with conventional polymeric resist materials can be found elsewhere.[155] X-ray lithography can be used with conventional polymeric resist systems to make high-resolution patterns on the order of tens of nanometres.[156, 157]

1.5.1.3 Soft lithographies

The term '*soft lithography*' encompasses the technologies of microcontact printing (μCP)[158], replica molding (REM),[159] microtransfer molding (μTM),[160] micromolding in capillaries (MIMIC)[161] and solvent-assisted micromolding (SAMIM).[162]

1.5.1.3.1 Microcontact printing

Microcontact printing (μCP)[163] developed by the Whitesides group[164] at Harvard University, is the replication of a pre-defined pattern from a stamp to a substrate via diffusion of a molecular 'ink' from the stamp to the substrate (figure 1.7).[165]

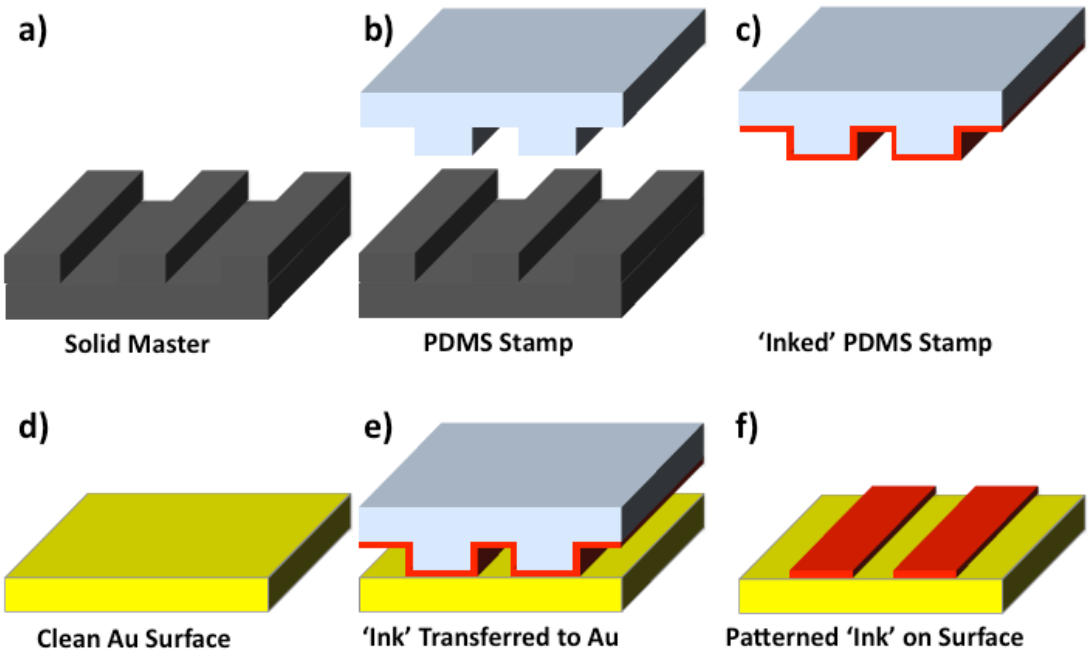

Figure 1.7. Diagram of microcontact printing process; **a)** a solid, topographically patterned master surface is fabricated; **b)** PDMS is cast on the master surface, allowed to solidify then removed; **c)** the PDMS stamp is inked with a chemical 'ink'; **d)** a clean surface (in this case Au); **e)** the inked stamp is then brought into contact with the clean surface; and **f)** the 'ink' is transferred to the substrate.

Microcontact printing represents a cheap, facile method of creating chemical patterns with sub-micron lateral features over cm^2 areas. The term 'microcontact printing' is often used even for examples of the technique which yield sub 100-nm features but more recently these examples are termed 'nanocontact printing[166] in the literature. The simplest use of microcontact printing is often for the patterning of gold surfaces with thiols[167] in which, a stamp (figure 1.7b) is used to apply a thiol to certain areas of a bare gold surface (figure 1.7 c, d, e & f). The thiol can then be used as an etch resist on thin gold films, protecting the coated areas from chemical etching, while the uncoated gold areas are removed to leave a structured gold film. Alternatively, after the transfer is complete, the gold substrate may be briefly dipped into a solution of a second thiol (known as backfilling), which fills the remaining bare areas and if suitable second thiols are chosen, marked contrasts in properties such as hydrophilicity or binding of proteins particles and polymers[168] may be achieved. Minimum feature sizes achievable using microcontact printing have so-far been in the region of 50 nm.[169]

1.5.1.3.2 Dip-pen nanolithography

Dip pen nanolithography (DPN) is a technique based upon scanning probe lithography. DPN involves the use of an atomic force microscope tip to transfer molecules from the AFM tip to a surface that it is brought into contact with (figure 1.8).[170] The minimal feature sizes obtainable with DPN can be on the order of 20 nanometres.

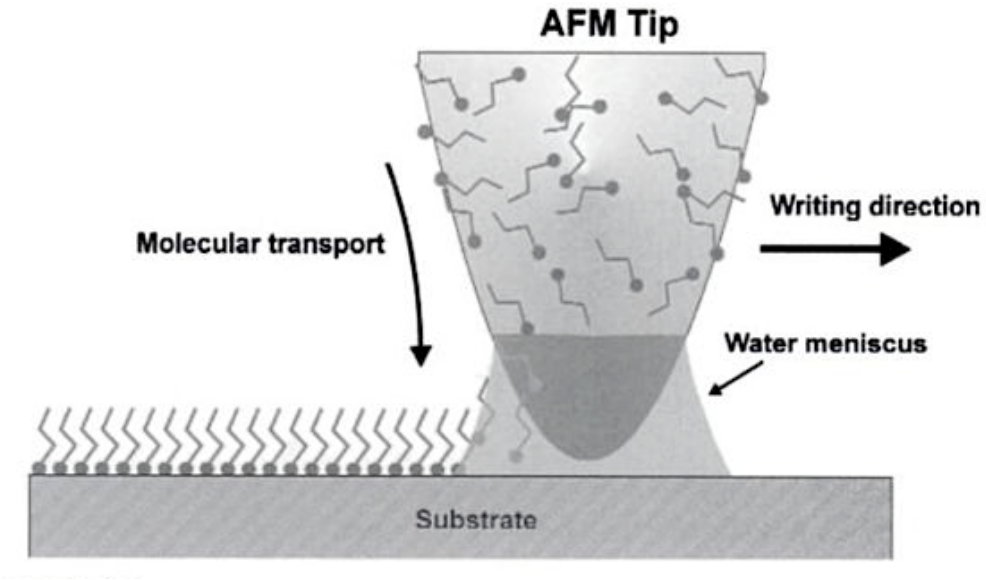

Figure 1.8. Diagram of the DPN process, molecules are transferred from the AFM tip to the substrate surface through the water meniscus.[171]

The vehicle for deposition can include pyramidal scanning probe microscope tips, hollow tips, and even tips on thermally actuated cantilevers.[172] Recent advances have demonstrated massively parallel patterning using two-dimensional arrays of 55,000 tips.[173] Applications of this technology currently range through chemistry, materials science, and the life sciences, and include such work as ultra high density biological nanoarrays, additive photomask repair, and brand protection for pharmaceuticals.[174] The transfer of a molecular 'ink' from a coated AFM tip to a substrate was first reported by Jaschke and Butt in 1995.[175] The technique was further developed by a research group at Northwestern University led by Chad Mirkin who also introduced the term DPN.

1.5.2 Mechanical methods

Mechanical methods of surface structuring encompass methods such as nanomanipulation, nanoindentation and nanoshaving. Nanoindentation, nanoscratching and nanoshaving will be discussed in Chapter 4. Nanografting, which is an extension of nanoshaving will discussed here. Based on AFM and STM tools, these patterning techniques enable the manipulation, damage or removal of structures at the atomic level. Mechanical methods, such as nanoshaving, closely mimic methods currently employed for fabrication of structures and devices on the macroscale, such as the use of a lathe to 'shave' down a bulk material into the desired shape. Not only nanoshaving, but also nanoindentation and nanoscratching have originated from nanotribology studies of friction and adhesion of materials to surfaces.[176]

1.5.2.1 Nanomanipulation

Nanomanipulation experiments can represent the absolute limit of fabrication, where individual atoms are placed into the desired pattern or structure on a material surface. Nanomanipulation operations usually are one of two types.[177] The first type involves deposition of a nanoscale species or atom on a surface, and then the use of either an AFM or STM to manoeuvre/push the species into position. The second type of operation involves deposition of a species on a temporary location using standard deposition techniques and then picking up of the species and moving it to its new location. This is usually accomplished by means of manipulating the tip/sample bias of a STM. Structure formation by nanomanipulation processes is at present very time consuming, with no equipment specifically designed for the purpose, hence such experiments are at present mostly confined to research and prototyping. Species and the resolution of assembled species can range from nanoparticles[178] right through to

individual atoms.[179] The iconic experiment in the development of such techniques was carried out in 1990 by Eigler and Schweizer[180] where xenon atoms were manipulated on a Ni(110) surface in a manner such as to write 'IBM' with the xenon atoms. Also, stadium-type quantum corrals have been assembled by depositing a close line of Fe atoms on a Cu(111) surface.[181] Nanomanipulation techniques are continually being developed and they provide a route to the ultimate limit of fabrication.

1.5.2.2 Nanografting

The technique of nanografting is usually (but not exclusively) utilized on surfaces modified with SAMs (figure 1.9a) and is achieved by nanoshaving in the presence of a second replacement surfactant molecule with a greater affinity for the surface than the molecule being removed by the AFM tip (figure 1.9b).[182] Therefore, once the mature SAM is removed from the desired area by the AFM tip it will be replaced with the new incoming SAM (figure 1.9c). Nanografting allows for the formation of positive and negative patterns via tailoring of the incoming surfactant molecule lengths. In order to successfully perform a nanografting operation, there are certain requirements that SAMs should meet.

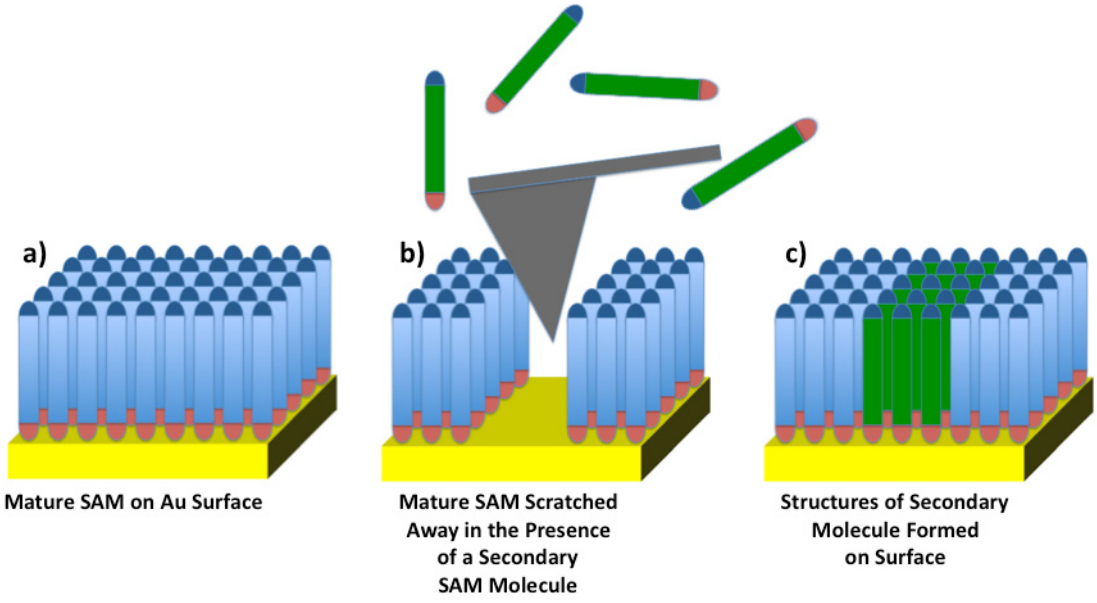

Figure 1.9. Diagram showing the process of nanografting; **a)** a complete SAM is **b)** shaved away in the presence of a secondary SAM molecule, which **c)** selectively replaces the original SAM in the regions which were shaved.

The SAMs must be readily removable with the force generated by the AFM tip, but more importantly, the SAMs must form on the surface of the substrate being used in a quick and precise manner. It is for these reasons that thiol SAMs on gold are usually the system of choice for nanografting experiments, due to the way in which thiols rapidly form homogenous monolayers on exposed gold surfaces and formation of the Au-S bond is reversible in solution.

1.6 Nanostructure and nanostructured surface characterisation

1.6.1 Surface contact angle analysis

The contact angle is the angle at which a liquid/vapor interface meets a solid surface. The contact angle is specific for any given system and is determined by the interactions across the three interfaces. The contact angle thus directly provides information on the interaction energy between the surface and the liquid. Most often,

the concept is illustrated with a small liquid droplet resting on a flat horizontal solid surface with the shape of the droplet determined by the Young Relation.[183] The contact angle plays the role of a boundary condition. The contact angle is not limited to a liquid/vapour interface and is equally applicable to the interface of two liquids or two vapours (figure 1.10).

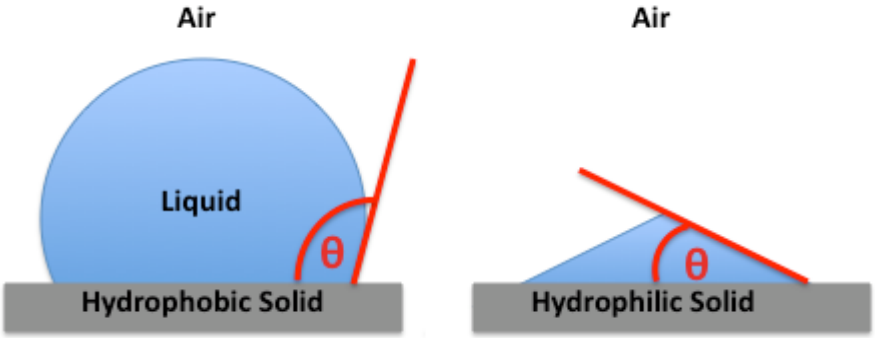

Figure 1.10. Diagrammatic representation of water contact angle on a solid surface.

If we consider a liquid drop on a solid surface; if the liquid is very strongly attracted to the solid surface (for example water on a strongly hydrophilic solid) the droplet will completely spread on the solid surface and the contact angle will thus be close to 0°. Less strongly hydrophilic solids will have a contact angle up to 90°. On many highly hydrophilic surfaces, water droplets will exhibit contact angles in the range of 0° to 30°. If the solid surface is hydrophobic, the contact angle will be larger than 90°. On highly hydrophobic surfaces the surfaces have water contact angles as high as 150° or even nearly 180°. On these highly hydrophobic surfaces, water droplets simply rest on the surface, without wetting the surface to any significant extent. These surfaces are termed superhydrophobic and can be obtained on fluorinated (*Teflon-like coatings*)[184] or appropriately micropatterned surfaces (*Lotus effect*).[185] The theoretical description of contact arises from the consideration of a thermodynamic equilibrium between the three phases (figure 1.11): the liquid phase of the droplet (L), the solid phase of the substrate (S), and the gas/vapor phase of the

ambient (V) (which will be a mixture of ambient atmosphere and an equilibrium concentration of the liquid vapor).

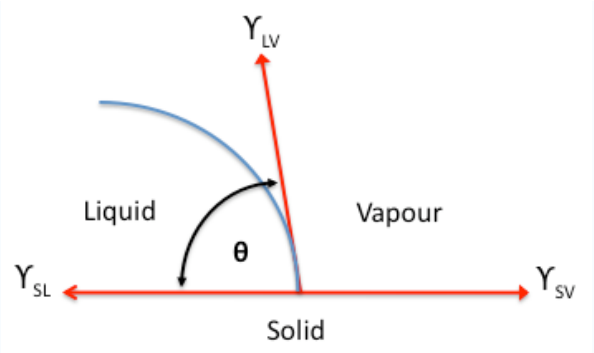

Figure 1.11. Diagram demonstrating process contact angle measurement of a drop of liquid on a solid surface.

The V phase could also be another (immiscible) liquid phase. At equilibrium, the chemical potential in the three phases should be equal. It is convenient to frame the discussion in terms of the interfacial energies. We denote the solid-vapor interfacial energy as γ_{SV}, the solid-liquid interfacial energy as γ_{SL} and the liquid-vapor energy (i.e. the surface tension) as simply γ, we can write an equation that must be satisfied in equilibrium (known as the Young Equation):

$$0 = \gamma_{SV} - \gamma_{SL} - \gamma\cos\theta_C \qquad \textbf{equation 1.1}$$

where θ_C is the equilibrium contact angle. The Young equation assumes a perfectly flat surface, and in many cases surface roughness and impurities cause a deviation in the equilibrium contact angle from the contact angle predicted by Young's equation. Even in a perfectly smooth surface a drop will assume a wide spectrum of contact angles between the highest (*advancing*) contact angle, θ_A, and the lowest (*receding*) contact angle, θ_R.

1.6.1.1 Contact angle measurement methods

1.6.1.1.1 The static sessile drop method

In the sessile drop method, the contact angle is measured by a contact angle goniometer using an optical system to capture the profile of a pure liquid on a solid substrate. The angle formed between the liquid/solid interface and the liquid/vapor interface is the contact angle. Older systems used a microscope optical system with a back-light. Current-generation systems employ high-resolution cameras and software to capture and analyze the contact angle.

1.6.1.1.2 The dynamic sessile drop method

The dynamic sessile drop is similar to the static sessile drop but requires the volume of the drop to be modified dynamically. A droplet is placed on a surface with the delivery needle still within the droplet. Liquid is then added to the droplet which causes the position of the interface between liquid/air/surface to move position. The angle exhibited by the droplet during this phase is called the advancing angle. Once the maximum droplet volume has been obtained, liquid is removed from the droplet causing the droplet to decrease in volume, at the critical point where the angle remains constant and the position of the three-phase boundary retracts across the surface, the average receding angle is achieved.

1.6.1.1.3 Dynamic Wilhelmy method

This is a method for calculating average advancing and receding contact angles on solids of uniform geometry. Both sides of the solid must have the same properties. Wetting force on the solid is measured as the solid is immersed in or withdrawn from a liquid of known surface tension.

1.6.1.1.3 Single-fiber Wilhelmy method

This is the dynamic Wilhelmy method applied to single fibers to measure advancing and receding contact angles.

1.6.1.1.4 Powder contact angle method

Powder contact angle analysis enables measurement of average contact angle and sorption speed for powders and other porous materials. Change of weight as a function of time is measured.

1.6.2 Spectroscopic ellipsometry

Spectroscopic ellipsometry is a sensitive optical technique for determining the properties of surfaces and thin films.[186] The technique of ellipsometry uses elliptically polarized light, giving rise to the name *'ellipsometry'*. The shape and orientation of the ellipse depends on the angle of incidence, the direction of the polarization of the incident light, and the reflection properties of the surface. We can measure the polarization of the reflected light with a quarter-wave plate followed by an analyzer; the orientations of the quarter-wave plate and the analyzer are varied until no light passes though the analyzer. From these orientations and the direction of polarization of the incident light we can calculate the relative phase change, and the relative amplitude change, introduced by reflection from the surface. An overview of the ellipsometry instrument is presented in figure 1.13.

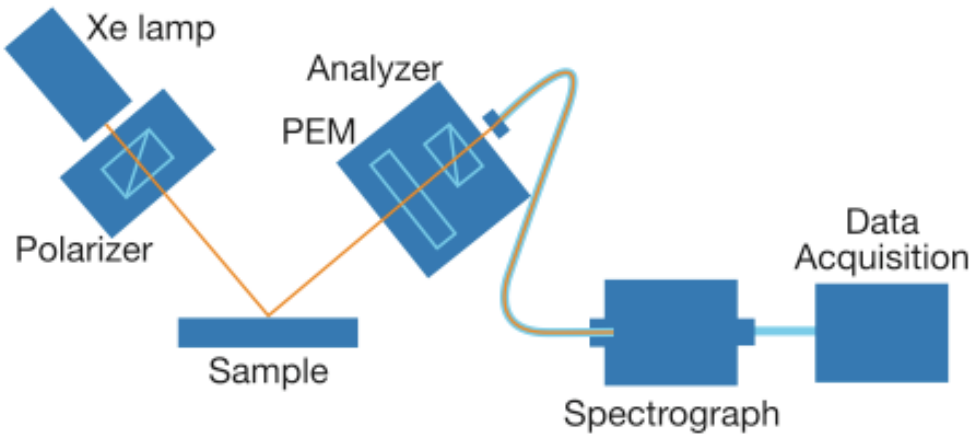

Figure 1.13. Diagrammatic representation of ellipsometer setup.

An ellipsometer measures the changes in the polarization state of light when it is reflected from a sample. If the sample undergoes a change, for example a thin film on the surface changes its thickness, then its reflection properties will also change. Measuring these changes in the reflection properties can allow us to deduce the actual change in the film's thickness. Since the general polarization state of polarized light reflected from a surface is elliptical, the term ellipsometer is used. The most important application of ellipsometry is to study thin films. In the context of ellipsometry, a thin film is one that ranges from essentially zero thickness to several thousand Angstroms, although this range can be extended in some cases.[187] The sensitivity of an ellipsometer is such that a change if film thickness of a few Angstroms is usually easy to detect. Ellipsometry measures the change in polarisation, as well as the intensity, upon reflection from a surface. Linearly polarised light, when reflected from an surface, will change its state to elliptically polarised. Viewed end on the electric vector of the light, E, appears to describe an ellipse.

1.6.3 Atomic Force Microscopy (AFM)

The Atomic Force Microscope (AFM) was invented by Binnig, Quate and Gerber in 1985, and is one of the foremost tools for the characterisation and manipulation of matter at the nanoscale.[188] The principles behind AFM operation are very simple. The AFM consists of a cantilever (probe) with a sharp tip at its end that is used to scan the specimen surface (figure 1.14).

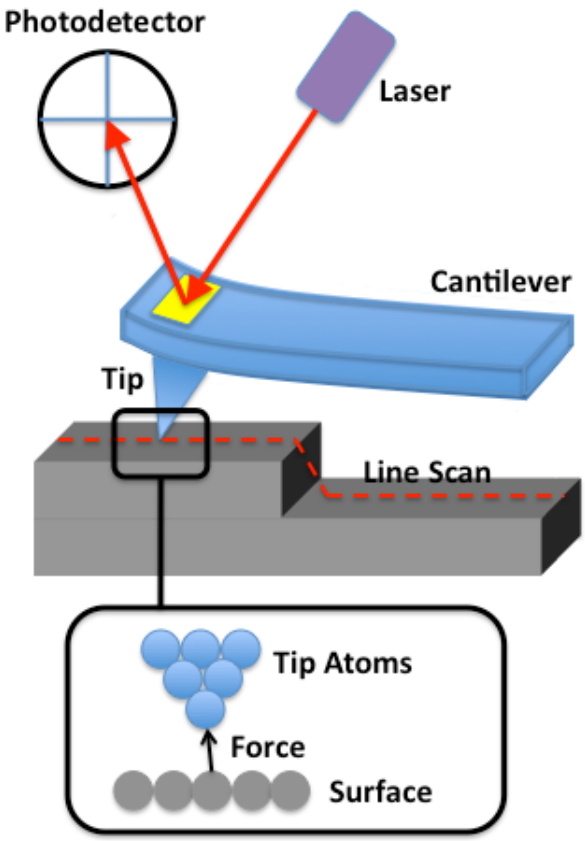

Figure 1.14. Diagram demonstrating the operation of an AFM.

The probe is typically made from silicon or silicon nitride with a tip radius of curvature on the order of nanometers. When the tip is brought into close proximity of a sample surface, the Van der Waals force between the tip and the sample leads to a deflection of the cantilever described by Hooke's law.[189] Typically, the tip deflection is measured using a laser spot reflected from the top of the cantilever onto an array of photodiodes. AFM measurements can be performed in two different modes and these

are contact or tapping mode. Contact mode involves the tip and the substrate being kept in constant contact and the tip being rastered across the surface with the resultant deflection of the cantilever monitored by the position of the laser on the photodiode. During tapping mode AFM the cantilever is vibrated close to its resonant frequency and the change of oscillation of the cantilever is detected upon interaction between the tip and surface.

1.6.4 X-ray Photoelectron Spectroscopy (XPS)

XPS is a method for determining the chemical composition of a materials' surface and involves the irradiation of the sample with X-rays.[190] XPS can be used to measure:

- The elemental composition of the surface (*top 1–10 nm*)
- The empirical formula of pure materials
- The elements that contaminate a surface
- The chemical or electronic state of each element in the surface
- The uniformity of elemental composition across the top surface (*i.e, line profiling or mapping*)

The X-rays, with energy *hv*, interact with the surface atoms by exciting core electrons within the atoms. If the electrons are excited enough, to overcome the electron binding energy within their atomic orbital (EB), they are ejected from the atom in the form of a photoelectron with energy (EK) (figure 1.15).

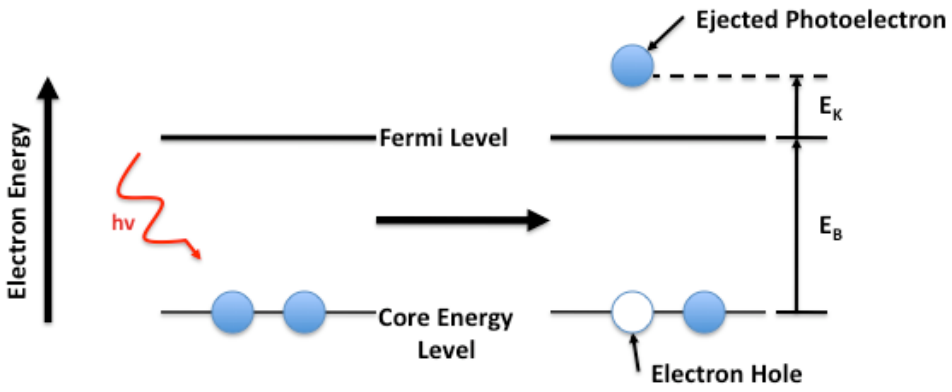

Figure 1.15. Diagrammatic representation of photoelectron ejection process.

The energies of the photoelectrons are measured and a spectrum of photoelectron energies is recorded. The electron binding energy is dependant on the chemical environment of the electron, thus the electron binding energy is characteristic of the electronic orbital and element in which it exists. Knowledge of the kinetic energy of the ejected photoelectron and the energy of the incident X-ray radiation upon the sample allows the electron binding energy to be determined by use of **equation 2**.

$$EK = hv - EB \qquad \textbf{equation 1.2}$$

A typical XPS spectrum is presented as a plot of the number of electrons detected (sometimes per unit time) (Y-axis) versus the binding energy of the electrons detected (X-axis). Because XPS's are not equally sensitive to all ejected electrons, count values achieved have to be scaled using an atomic sensitivity factor so as to allow comparison of compositions of elements on the same sample.[191]

1.6.5 Scanning Electron Microscopy (SEM)

SEM is an imaging technique that images the sample surface by scanning it with a high-energy beam of electrons in a raster scan pattern.[192] The electrons interact with the atoms that make up the sample producing signals that contain information

about the sample's surface topography, composition and other properties such as electrical conductivity. The types of signals produced by an SEM include secondary (SE) and back scattered (BE) electrons, characteristic X-rays, light (cathodoluminescence), specimen current and transmitted electrons. Non-conductive samples are normally coated with a conductive layer such as carbon or gold in order to allow the samples to be imaged successfully. SEM can be used to image surface features down to the nanoscale routinely.

1.7 References

1) Gleiter, H., **Nanostructured Materials: Basic Concepts and Microstructure**, *Acta. Materialia.*, **2000**, *48*, 1-29.

2) Yu, P., McKinnon, J. J., Christensen, C. R., Christensen, D. A., Marinkovic, N. S and Miller, L. M., **Chemical Imaging of Microstructures of Plant Tissues within Cellular Dimension using Synchrotron Infrared Microspectroscopy**, *J. Agric. Food. Chem.*, **2003**, 51, 6062-6067.

3) **Microelectronics**, Whitaker, J. C., **2005**, CRC Press.

4) http://www.intel.com/technology/mooreslaw/ - Accessed 20/09/09.

5) **Resolution Enhancement Techniques in Optical Lithography**, Wong, A. K-K., **2001**, SPIE Press.

6) **Into the Nano Ear: Moore's Law Beyond Planar Silicon CMOS**, Huff, H., **2008**, Springer.

7) http://www.intel.com/pressroom/archive/releases/ 20070918corp_a.htm?iid=tech_arch_32nm+body_pressrelease - Accessed 20/09/09.

8) **Nanoscale Devices: Fabrication, Functionalization and Accessibility from the Macroscopic World**, Cerofolini, G., **2009**, Springer.

9) Lewis. P. A., Donhauser. Z. J., Mantooth. B. A., Smith. R. K., Bumm. L. A., Kelly. K. F. and Weiss. P.S., **Control and Placement of Molecules *via* Self-assembly**, *Nanotechnology*, **2001**, *12*, 231-237.

10) Sastry. M., **Assembling Nanoparticles and Biomacromolecules using Electrostatic Interactions**, *Pure. Appl. Chem.*, **2002**. *74*, 9, 1621-1630.

11) Pericet-Camara. R., Papastavrou. G. and Borkovec, M., **Atomic Force Microscopy Study of the Adsorption and Electrostatic Self-Organization of Poly(amidoamine) Dendrimers on Mica**, *Langmuir*, **2004,** *20*, 3264-3270.

12) Wang. S.-T., Yan, J. and Chen, L., **Formation of Gold Nanoparticles and Self-assembly into Dimer and Trimer Aggregates**, *Mat. Letters*, **2005**, *59*, 1383-1386.

13) **Supramolecular Interactions at Functional Self-assembled Monolayers on Gold**, Beulen, M., **1999**, ISBN 90 365 1316 2.

14) Lu, W. and Lieber, C. M., **Nanoelectronics from the Bottom-up**, *Nature*, **2007**, *6*, 841-850.

15) Megelski, S., Stephens, J. S., Chase, D. B. and Rabolt, J. F., **Micro- and Nanostructured Surface Morphology on Electrospun Polymer Fibers**, *Macromolecules*, **2002**, *35*, 8456-8466.

16) Kim, J., Akinaga, H., Atoda, N, and Tominaga, J., **Nanoelectronic Devices with Reactively Fabricated Semiconductor**, *Appl. Phys. Lett.*, **2002**, *80*, 2764-2766.

17) Mcfarland, A. D. and van Duyne, R. P., **Single Silver Nanoparticles as Real-time Optical Sensors with Zeptomole Sensitivity**, *Nano. Letts.*, **2003**, *3*, 1057-1062.

18) Kong, J., Franklin, N. R., Zhou, C., Chapline, M. G., Peng, S., Cho, K. and Dai, H., **Nanotube Molecular Wires as Chemical Sensors**, *Science*, **2000**, *287*, 622-625.

19) Sotiropoulou, S. and Chaniotakis, N. A., **Carbon Nanotube Array-Based Biosensor**, *Anal. Bioanal. Chem.*, **2003**, *375*, 103-105.

20) Feynmann. R. P., **"Theres Plenty of Room at the Bottom"**, *Eng. Sci,* **1960.**

21) **Nanostructured Materials: Processing, Properties and Applications**, Koch, C., **2002**, Taylor & Francis.

22) Schuster, A., Lakshmanan, R., Ponton, J. and Sefiane, K., **Modelling a Novel Miniaturised Reactor/Separator System**, *J. Chem. Tech. Biotech.*, **2003**, *78*, 342-346.

23) Sotiropoulou, S., Gavalas, S. V., Vamvakaki, V. and Chaniotakis, N. A., **Novel Carbon Materials in Biosensor Systems,** *Biosens. Bioelec.,* **2003**, *18*, 211-215.

24) Rothschild, M, Bloomstein, T. M., Curtin, J. E., Downs, D. K., Fedynyshyn, T. H., Hardy, D. E., Kunz, R. R., Liberman, V., Sedlacek, J. H. C. and R. S. Uttaro, **157 nm: Deepest Ultraviolet Yet**, *J. Vac. Sci. Technol. B.*, **1999**, *17*, 3262-3266.

25) Kullaba, K and Manners, I., **Polyferrocenylsilanes: Metal-containing Polymers for Materials Science, Self-assembly and Nanostructure Applications**, *Macromol. Rapid. Commun.*, **2001**, *22*, 711-724.

26) Aggeli, A., Nyrkova, I. A., Bell, M., Harding, R., Carrick, L., McLeish, T. C. B., Semenov, A. N. and Boden, N., **Hierarchical Self-assembly of Chiral Rod-like Molecules as a Model for Peptide β-sheet Tapes, Ribbons, Fibrils, and Fibers,** *PNAS*, **2001**, *98*, 11857-11862.

27) Smith, L. A. and Ma, P. X., **Nano-fibrous Scaffolds for Tissue Engineering**, *Coll. Surf. B: Biointerfaces,* **2004**, 39, 125-131.

28) Long, D. L., Burkholder, E. and Cronin, L., **Polyoxometalate Clusters, Nanostructures and Materials: From Self-assembly to Designer Materials and Devices**, *Chem. Soc. Rev.*, **2007**, *36*, 105-121.

29) Jurgens, D., Greiner, A., Stutzle, R., Habenicht, A., Sligte, E. T. and Oberthaler, M. K., **Quantum Features in Atomic Nanofabrication using Exactly Resonant Standing Waves**, *Phys. Rev. Lett.*, **2004**, *93*, 237402.1-237402.4.

30) Ulbrich, T. C., Makarov, D., Hu, G., Guhr, I. L., Suess, D., Schrefl, T. and Albrecht, M., **Magnetization Reversal in a Novel Gradient Nanomaterial**, *Phys. Rev. Lett.*, **2006**, *96*, 077202.1-077202.4.

31) Sun, C. Q., **Size Dependence of Nanostructures: Impact of Bond Order Deficiency**, *Prog. Solid State Chem.*, **2007**, *35*, 1-159.

32) Mendes, P. M., Flood, A. H., and Stoddart, J. F., **Nanoelectronic Devices from Self-organized Molecular Switches**, *Appl. Phys. A, Mater. Sci. Process.*, **2005**, *80*, 1197-1209.

33) Fang, X. S. and Zhang, L. D., **One-dimensional (1D) ZnS Nanomaterials and Nanostructures**, *J. Mater. Sci. Technol.*, **2006**, *22*, 721-736.

34) Cui, Y., Wei, Q. Q., Park, H. K. and Lieber, C. M., **Nanowire Nanosensors for Highly Sensitive and Selective Detection of Biological and Chemical Species**, *Science*, **2001**, *293*, 1289-1292.

35) Zheng, G. F., Patolsky, F., Cui, Y., Wang, W. U. and Lieber, C. M., **Multiplexed Electrical Detection of Cancer Markers with Nanowire Sensor Arrays**, *Nat. Biotechnol.*, **2005**, *23*, 1294-1301.

36) Christman, K. L., Enriquez-Rios, V. D. and Maynard, H. D., **Nanopatterning Proteins and Peptides**, *Soft Mater.*, **2006**, *2*, 928-939.

37) Sun, C. Q., **Size Dependence of Nanostructures: Impact of Bond Order Deficiency**, *Prog. Solid State Chem.*, **2007**, 35, 1-159.

38) Pfund, A., Shorubalko, I., Leturcq, R., Borgstrom, M. T., Gramm, F., Muller, E. and Ensslin, K., **Fabrication of Semiconductor Nanowires for Electronic Transport Measurements**, *Chimia*, **2006**, *60*, A729-A734.

39) Sagiv, J., **Organized Monolayers by Adsorption .1. Formation and Structure of Oleophobic Mixed Monolayers on Solid-surfaces**, *J. Am. Chem. Soc.*, **1980**, *102*, 92-98.

40) Gun, J., Iscovici, R. and Sagiv, J., **On the Formation and Structure of Self-Assembling Monolayers. 2. A Comparative-study of Langmuir–Blodgett and Adsorbed Films using Ellipsometry and IR Reflection Absorption-Spectroscopy**, *J. Colloid Interface Sci.*, **1984,** *101*, 201-213.

41) Maoz, R. and Sagiv, J., **On the Formation and Structure of Self-assembling Monolayers. 1. A Comparative ATR-Wettability study of Langmuir–Blodgett and Adsorbed Films on Flat Substrates and Glass Microbeads**, *J. Colloid Interface Sci.*, **1984**, *100*, 465-496.

42) Netzer, L. and Sagiv, J., **A New Approach to Construction of Artificial Monolayer Assemblies**, *J. Am. Chem. Soc.*, **1983**, *105*, 674-676.

43) Netzer, L., Iscovici, R. and Sagiv, J., **Adsorbed Monolayers Versus Langmuir–Blodgett monolayers Why and How: 1. from Monolayer to Multilayer, by Adsorption**, *J. Am. Chem. Soc.*, **1983**, *99*, 235-241.

44) Nuzzo, R. G. and Allara, D. L., **Adsorption of Bifunctional Organic Disulfides on Gold Surfaces**, *J. Am. Chem. Soc.*, **1983**, *105*, 4481-4483.

45) Schreiber, F., **Self-assembled Monolayers: from 'Simple' Model Systems to Biofunctionalized Interfaces**, *J. Phys. Condens. Mater.*, **2004**, *16*, R881-R900.

46) Onclin, S., Ravoo, B. J. and Reinhoudt, D. N., **Engineering Silicon Oxide Surfaces using Self-assembled Monolayers**, *Angew. Chem., Int. Ed.*, **2005**, *44*, 6282-6304.

47) Fadley, C. S., Baird, R. J., Siekhaus, W., Novakov, T., and Bergstro, S. A. **Surface Analysis and Angular Distributions in X-ray Photoelectron-Spectroscopy**, *J. Electron Spectrosc. Relat. Phenom.*, **1974,** *4*, 93-137.

48) **Surface Analysis by Auger and X-ray Photoelectron Spectroscopy**, Briggs, D. and Grant, J. T., **2003**, SurfaceSpectra Ltd and IM Publications.

49) Alsnielsen, J., Jacquemain, D., Kjaer, K., Leveiller, F., Lahav, M. and Leiserowitz, L., **Principles and Applications of Grazing-incidence X-ray and Neutron-scattering from Ordered Molecular Monolayers at the Air-water-Interface**, *Phys. Rep. Rev. Sec. Phys. Lett.*, **1994**, *246*, 252-313.

50) Good, R. J., **Contact-angle, Wetting, and Adhesion–A Critical Review**, *J. Adhes. Sci. Technol.*, **1992**, *6*, 1269-1302.

51) McCrackin, F. L., Passaglia, E., Stromberg, R. R., and Steinber, H. **Measurement of Thickness and Refractive Index of Very Thin Films and Optical Properties of Surfaces by Ellipsometry**, *J. Res. Nat. Bur. Stand.*, **1963**, *A67*, 363-377.

52) Binnig, G., Rohrer, H., Gerber, C. and Weibel, E., **Surface Studies by Scanning Tunneling Microscopy**, *Phys. Rev. Lett.*, **1982**, *49*, 57-61.

53) Binnig, G., Quate, C. F. and Gerber, C., **Atomic Force Microscopy**, *Phys. Rev. Lett.*, **1986**, 56, 930-933.

54) Pohl, D. W., Fischer, U. C., Durig, U. T., **Scanning Near-Field Optical Microscopy (SNOM)**, *J. Microsc.*, **1988**, *152*, 853-861.

55) Uchihashi, T., Ishida, T., Koomiyama, M., Ashino, M., Sugawara, Y., Mizutani, W., Yokoyama, K., Morita, S., Tokumoto, H. and Ishikawa, M., **High-Resolution Imaging of Organic Monolayers using Noncontact AFM**, *Appl. Surf. Sci.*, **2000**, *157*, 244-250.

56) Fontaine, P. A., Dubois, E. and Stievenard, D., **Characterization of Scanning Tunneling Microscopy and Atomic Force Microscopy-based Techniques for Nanolithography on Hydrogen-passivated Silicon**, *J. Appl. Phys.*, **1998**, *84*, 1776.

57) Huie. J. C., **Guided Molecular Self-assembly: A Review of Recent Efforts**, *Smart. Mater. Struct.*, **2003**, *12*, 264-271.

58) Feldheim. D. L. and Keating. C. D., **Self-assembly of Single Electron Transistors and Related Devices**, *Chem. Soc. Rev*., **1998**, *27*, 1.

59) Schreiber. F., **Structure and Growth of Self-assembling Monolayers**, *Progress in Surface Science*, **2000**, *65*, 151-257.

60) **Prediction of Protein Structure and Principles of Protein Conformation**, Fasman, G. D., **1989**, Springer.

61) Decher. G., Hong. J. D. and Schmitt. J., **Buildup of Ultrathin Multilayer Films by a Self-assembly process: III. Consecutively Alternating Adsorption of Anionic and Cationic Polyelectrolytes on Charged Surfaces**, *Thin Solid Films*, **1992**, *210/211*, 831-835.

62) Israelachvili, J. N., Mitchell, D. J. and Ninham, B. W., **Theory of Self-assembly of Hydrocarbon Amphiphiles into Micelles and Bilayers**, *J. Chem. Soc., Faraday Trans. 2*, 1976, 72, 1525-1568.

63) Elemans, J. A. A. W., Rowan, A. E. and Nolte, R. J. M., **Mastering Molecular Matter. Supramolecular Architectures by Hierarchical Self-assembly**, *J. Mater. Chem.*, **2003**, *13*, 2661-2670.

64) Bethell, D., Brust, M., Schiffrin, D. J. and Kiely, C., **From Monolayers to Nanostructured Materials: An Organic Chemists View**, *J. Electroanal Chem*, **1996**, *409*, 137-143.

65) **An Introduction To Ultrathin Organic Films: From Langmuir--blodgett to Self-assembly**, Ulman, A., **1991**, Academic Press.

66) Bright. R. M., Musik, M. D. and Natan, M. J., **Preparation and Characterization of Ag Colloid Monolayers**, *Langmuir*, **1998**, *14*, 5695-5701.

67) Love, J. C., Estroff, L. A., Kriebel, J. K., Nuzzo, R. G. and Whitesides, G. M., **Self-assembled Monolayers of Thiolates on Metals as a Form of Nanotechnology**, *Chem. Rev.,* **2005,** 105, 1103-1169.

68) Yourdshahyan, Y. and Rappe, A. M., **Structure and Energetics of Alkanethiol Adsorption on the Au(111) Surface,** *J. Chem. Phys.*, **2002**, *117*, 825-833.

69) Schreiber, F., **Structure and Growth of Self-assembling Monolayers**, *Prog. Surf. Sci.* **2000**, 65, 151-25.

70) Bain, C. D., Troughton, E. B., Tao, Y. T., Evall, J., Whitesides, G. M. and Nuzzo, R. G., **Formation of Monolayer Films by the Spontaneous Assembly of Organic Thiols from Solution onto Gold**, *J. Am. Chem. Soc.,* **1989,** 111, 321-335.

71) **'Silane Coupling Agents- Connecting Across Boundaries'**, Gelest Inc, http://www.gelest.com/Library/.

72) Kajiyama, T., Kojio, K. and Tanaka, K, **Aggregation States and Molecular Motion of Polymer Ultrathin Films Prepared at the Air/water Interface**, *Adv. Coll. Int. Sci*., **2004**, *111,* 159-179.

73) Zhu. X. Y. and Major, R. C., **Two-Step Approach to the Formation of Organic Monolayers on the Silicon Oxide Surface**, *Langmuir*, **2001**, *17*, 5576-5580.

74) Angst. D. L. and Simmons. G. W., **Moisture Absorption Characteristics of Organosiloxane Self-assembled Monolayers**, *Langmuir*, **1991**, *7*, 2236-2242.

75) Sugimura, H., Hozumi, A., Kameyama, T. and Taka, O., **Organosilane Self-assembled Monolayers Formed at the Vapour/solid Interface,** *Surf. Inter. Anal.*, **2002**, *34*, 550-554.

76) **Microelectronic Materials**, Grovener, C., **1989**, CRC Press.

77) Parikh, A. N., Liedberg, B., Atre, S. V., Ho, M. and Allara, D. L, **Correlation of Molecular Organization and Substrate Wettability in the Self-Assembly of n-Alkylsiloxane Monolayers**, *J. Phys. Chem*., **1995***, 99*, 9996-10008.

78) Mendes, P. M., Belloni, M., Ashworth, M., Hardy, C., Nikitin, K., Fitzmaurice, D., Critchley, K., Evans, S. and Preece, J., **Reduction of an Aromatic Nitro-Group- Containing Thin Film on SiO_2 to an Aromatic Amine Film**, *Chem. Phys. Chem*., **2003**, *4*, 8, 884-889.

79) Fadeev, A. Y. and McCarthy, T. J., **Self-Assembly Is Not the Only Reaction Possible between Alkyltrichlorosilanes and Surfaces: Monomolecular and Oligomeric Covalently Attached Layers of Dichloro- and Trichloroalkylsilanes on Silicon**, *Langmuir*, **2000**, *16*, 7268-7274.

80) Resch. R., Grasserbauer, M., Friedbacher, G., Vallant, Th., Brunner, H., Mayer, U. and Hoffmann. H., **In-situ and Ex-situ AFM Investigations of the Formation of Octadecylsiloxane Monolayers**, *Appl. Surf. Sci*, **1999**, *140*, 168-175.

81) Balgar, T., Bautista, R., Hartmann, N. and Hasselbrink, E, **An AFM Study of the Growth Kinetics of the Self-assembled Octadecylsiloxane monolayer on Oxidized Silicon**, *Surf. Sci*, **2003**, *532-535*, 963-969.

82) Tripp, C. P. and Hair, M. L, **An Infrared Study of the Reaction of Octadecyltrichlorosilane with Silica**, *Langmuir*, **1992**, *8*, 1120-1126.

83) Rye, R., Nelson, G. C. and Dugger, M. T., **Mechanistic Aspects of Alkylchlorosilane Coupling Reactions**, *Langmuir*, **1997**, *13*, 2965-2972.

84) Resch, R., Grasserbauer, M., Friedbacher, G., Vallant, Th., Brunner, H., Mayer, U. and Hoffmann, H., **In-situ and Ex-situ AFM Investigations of the Formation of Octadecylsiloxane Monolayers,** *Appl. Surf. Sci*, **1999**, *140*, 168.

85) Riegler, J. E., and LeGrange, J. D, **Observation of a Monolayer Phase Transition on the Meniscus in a Langmuir-Blodgett Transfer Configuration**, *Phys. Rev. Lett*., **1988**, *61*, 2492-2495.

86) Schwartz, D. K., **Mechanisms And Kinetics Of Self-Assembled Monolayer Formation**, Annual Review of Physical Chemistry, **2001**, *52*, 107-137.

87) Foisner, J., Glaser, A., Kattner, J., Hoffmann, H., Friedbacher, G., **Atomic Force Microscopy Investigation of the Growth of Different Alkylsiloxane Monolayers from Highly Concentrated Solutions**, *Langmuir*, **2005**, *19*, 3741-3746.

88) Diegoli, S., Mendes, P. M., Baguley, E. R., Leigh, S. J., Iqbal, P., Garcia Diaz, Y. R., Begum, S., Critchley, K., Hammond, G. D., Evans, S. D., Attwood, D., Jones, I. P. and Preece, J. A., **pH-Dependent Gold Nanoparticle Self-Organization on Functionalized Si/SiO_2 Surfaces**, *J. Exp. Nano. Sci.*, **2006**, *1*, 333-353.

89) Calistri-Yeh, M., Kramer, E. J., Sharma, R., Zhao, W., Rafailovich, M. H., Sokolov, J. and Brock, J. D., **Thermal Stability of Self-Assembled Monolayers from Alkylchlorosilanes**, *Langmuir*, **1996**, *12,* 2747-2755.

90) Zharnikov, M., Kuller, A., Shaporenko, A., Schmidt, E. and Eck, W, **Aromatic Self-Assembled Monolayers on Hydrogenated Silicon**, *Langmuir*, **2003**, *19*, 4682-4689.

91) Flink, S., van Veggel, F. C. J. M. and Reinhoudt. D. N., **Sensor Functionalities in Self-Assembled Monolayers**, *Adv. Mat*, **2000**, *12*, 18, 1315-1328.

92) Flink, S., van Veggel, F. C. J. M. and Reinhoudt, D. N., **Functionalization of Self-assembled Monolayers on Glass and Oxidized Silicon Wafers by Surface Reactions**, *J. Phys. Org. Chem*., **2001**, *14*, 407-415.

93) Shipway, A, N., Katz, E. and Willner, I., **Nanoparticle Arrays on Surfaces for Electronic, Optical, and Sensor Applications**, *Chem. Phys. Chem.*, **2000**, *1*, 18-52.

94) Wang, J., **Carbon-Nanotube Based Electrochemical Biosensors: A Review**, *Electroanal.*, **2005**, *17*, 7-14.

95) Pérez-Juste, J., Pastoriza-Santos, I., Liz-Marzán, L. M. and Mulvaney, P., **Gold nanorods: Synthesis, Characterization and Applications**, *Coord. Chem. Rev.*, **2005**, *249*, 1870-1901.

96) Zhao, B. and Brittain, W. J., **Polymer Brushes: Surface-immobilized Macromolecules**, *Prog Polym. Sci.*, **2000**, *25*, 677-710.

97) Ober, C. K. and Wegner, G., **Polyelectrolyte-Surfactant Complexes in the Solid State: Facile Building Blocks for Self-organizing Materials**, *Adv. Mater.*, **1997**, *9*, 17-31.

98) Pividori, M. I., Merkoçi, A. and Alegre, S., **Electrochemical Genosensor Design: Immobilisation of Oligonucleotides onto Transducer Surfaces and Detection Methods**, *Biosensors and Bioelectronics,* **2000**, *15*, 291-303.

99) Brust, M., Walker, M., Bethell, D., Schiffrin, D. J., Whyman, R., **Synthesis of Thiol-derivatised Gold Nanoparticles in a Two-phase Liquid–liquid System**, *Chem. Comm*., **1994**, *7,* 801-802.

100) Capek, I., **Preparation of Metal Nanoparticles in Water-in-oil (w/o) Microemulsions**, *Adv. Coll. Int. Sci.*, **2004**, *110,* 49-74.

101) Bognold, G., **The Use of Surface-active Agents in the Preparation and Assembly of Quantum-sized Nanoparticles**, *Adv. Coll. Int. Sci.*, **2003***, 106*, 169.

102) Eustis, S. and El-Sayed, M. A., **Why Gold Nanoparticles are More Precious than Pretty Gold: Noble Metal Surface Plasmon Resonance and its Enhancement of the Radiative and Nonradiative Properties of Nanocrystals of Different Shapes**, *Chem.Soc.Rev.*, **2006**, *35*, 209-217.

103) Crooks, R. M., Zhao, M., Sun, Li., Chechik, V. and, Yeung, L. K., **Dendrimer-Encapsulated Metal Nanoparticles: Synthesis, Characterization, and Applications to Catalysis**, *Acc. Chem. Res.,* **2001**, *34*, 181-190.

104) Paul, S., Pearson, C., Molloy, A., Cousins, M. A., Green, M., Kolliopoulou, S., Dimitrakis, P., Normand, P., Tsoukalas, D. and, Petty, M. C., **Langmuir−Blodgett Film Deposition of Metallic Nanoparticles and Their Application to Electronic Memory Structures**, *Nano. Letts.,* **2003**, *3*, 533-536.

105) Doremus. R. H., **Optical Properties of Small Gold Particles**, *J. Chem. Phys*., **1964**, *40*, 2389-2397.

106) Hainfeld, J. F., Slatkin. D. N., Focella. T. M., **Gold Nanoparticles: A New X-ray Contrast Agent**, *British Journal of Radiology*, **2006**, *79,* 248-253.

107) Hussain, I., Brust. M., Papworth. A. J. and Cooper. A. I., **Preparation of Acrylate-Stabilized Gold and Silver Hydrosols and Gold−Polymer Composite Film**, *Langmuir*, **2003**, *19*, 4831-4835.

108) Hunt, L. B. **The True Story of the Purple of Cassius. The Birth of Gold-based Glass and Enamel Colours**, *Gold Bull.*, **1976**, *9*, 134..

109) Faraday, M., **Experimental Relations of Gold(and Other Metals) to Light**, *Philos. Trans. R. Soc. London.,* **1857**, *147*, 145..

110) Graham, T. H., **Liquid diffusion applied to analysis**, *Philos. Trans. R. Soc. London.,* **1861**, *151*, 183.

111) Bethel, D., Schiffrin, D. J., Kiely. D. and Brust, M., **From Monolayers to Nanostructured Materials: An Organic Chemists View**, *J. Electroanal Chem*, **1996**, *409*, 137-143.

112) Leudtke, W. D. and Landman, U., **Structure, Dynamics, and Thermodynamics of Passivated Gold Nanocrystallites and Their Assemblies**, *J. Phys. Chem*., **1996**, *100,* 13323-13329.

113) **Fondations of Colloid Science, 2nd Edition**, Hunter, R.J, **2001,** Oxford University Press.

114) Caruso, F., **Nanoengineering of Particle Surfaces**, *Adv. Mater.*, **2001**, *13*, 11-22.

115) **Physical Chemistry of Polyelectrolytes**, Radeva, T., **2001**, CRC Press.

116) **Polyelectrolyes with Defined Molecular Architecture**, Schmidt, M., **2004**, Springer.

117) Ambade, A. V., Sandanaraj, B. S., Klaikherd,A. and Thayumanavan, S., **Fluorescent Polyelectrolytes as Protein Sensors**, *Polymer International*, **2007**, *56*, 474-481.

118) Zhang, J., Senger, B., Vautier, D., Picart, C., Schaaf, P., Voegel, J-C. and Lavalle, P., **Natural Polyelectrolyte Films based on Layer-by layer Deposition of Collagen and Hyaluronic Acid**, *Biomaterials*, **2005**, *26*, 3353-3361.

119) Anderson, C. F., and Record, Jr, M. T., **Polyelectrolyte Theories and Their Applications to DNA**, *Ann. Rev. Phys. Chem.*, **1982**, *33*, 191-222.

120) Goodchild, J., **Conjugates of Oligonucleotides and Modified Oligonucleotides: A Review of their Synthesis and Properties**, *Bioconjugate Chem.*, **1990**, *1*, 165-180.

121) Mascini, M., Palchetti, I. and Marrazza, G., **DNA Electrochemical Biosensors**, *Fresenius' Journal of Analytical Chemistry*, **2001**, *369*, 15-22.

122) Stoughton, R. B., **Applications Of DNA Microarrays in Biology**, *Ann. Rev. Biochem.*, **2005**, *74*, 53-82.

123) Marks, J. D., Tristem, M., Karpas, A. and Winter, G., **Oligonucleotide Primers for Polymerase Chain Reaction Amplification of Human Immunoglobulin Variable Genes and Design of Family-specific Oligonucleotide Probes**, *Eur. J. Immun.,* **1991**, *21*, 985-991.

124) Lorenz, H., Despont, M., Fahrni, N., LaBianca, N., Renaud, P. and Vettiger, P., **SU-8: A Low-cost Negative Resist for MEMS**, *J. Micromech. Microeng.,* **1997**, *7*, 121-124.

125) **Fundamentals of Microfabrication: The Science of Miniaturization**, Madou, M. J., **2002**, CRC Press.

126) **MEMs: Design and Fabrication, The MEMs Handbook Second Edition series**, Gad-el-Hak, M., **2006**, CRC Press.

127) **Microlithography Fundamentals in Semiconductor Devices and Fabrication**, Nonogaki, S., Ueno, T. and Ito, T., **1998**, CRC Press.

128) **Fundamentals of Microfabrication: The Science of Miniaturization**, Madou, M. J., **2002**, CRC Press, p2.

129) van Delft, F. C. M. J. M. and Weterings, J. P., **Hydrogen Silsesquioxane/novolak Bilayer Resist for High Aspect Ratio Nanoscale Electron-beam Lithography**, *J. Vac. Sci. Technol. B.*, **2000**, 18, 3419-3423.

130) **Field Guide to Optical Lithography**, Mack, C. A., **2006**, SPIE Press.

131) **The Physics of Sub-micron Lithography**, Valiev, K. A., **1992**, Plenum Press.

132) Yoshiaki, M., Takashi, O., Tatsuo, T. and Kyozo, S., **Deep-UV Photolithography**, *Japanese Journal of Applied Physics,* **1978**, *17*, 541-550.

133) Reichmanis, E., Nalamasu, O., Houlihan, F. M., Wallow, T. I., Timko, A. G., Cirelli, R., Dabbagh, G., Hutton, R. S., Novembre, A. E. and Smith, B. W., **Resist Design Concepts for 193 nm Lithography: Opportunities for innovation and invention**, *J. Vac. Sci. Technol. B.*, **1997**, *15*, 2528-2533.

134) Sun, S. Q., Mendes, P., Critchley, K., Diegoli, S., Hanwell, M., Evans, S. D., Leggett, G. J., Preece, J. A. and Richardson, T. H., **Fabrication of Gold Micro- and Nanostructures by Photolithographic Exposure of Thiol-Stabilized Gold Nanoparticles**, *Nano. Lett.*, **2006**, *6*, 345-350.

135) Sun, S. Q., Chong, K. S. L., and Leggett, G. J., **Photopatterning of Self-Assembled Monolayers at 244 nm and Applications to the Fabrication of Functional Microstructures and Nanostructures**, *Nanotechnology*, **2005**, 16, 1798-1808.

136) **Handbook of Microlithography, Micromachining and Microfabrication**, Rai-Choudhury, P., **1997**, IET.

137) **Handbook of Semiconductor Manufacturing Technology**, Nishi, Y. and Doering, R., **2000**, CRC Press, p573.

138) **Electron-beam Technology in Microelectronic Fabrication**, Brewer, G. R. and Ballantyne, J. P., **1980**, Academic Press.

139) Muller, H. U., Zharnikov, M., Volkel, B., Schertel, A., Harder, P., and Grunze, M., **Low-energy Electron-induced Damage in Hexadecanethiolate Monolayers**. *J. Phys. Chem. B*, **1998**, *102*, 7949-7959.

140) Rowntree, P., Dugal, P. C., Hunting, D. and Sanche, L., **Electron Stimulated Desorption of H-4 from Chemisorbed Molecular Monolayers**, *J. Phys. Chem.*, **1996**, *100*, 4546-4550.

141) Seshadri, K., Froyd, K., Parikh, A. N., Allara, D. L., Lercel, M. J. and Craighead, H. G., **Electron-beam-induced Damage in Self-assembled Monolayers**, *J. Phys. Chem.*, **1996**, *100*, 15900-15909.

142) Volkel, B., Golzhauser, A., Muller, H. U., David, C. and Grunze, M., **Influence of Secondary Electrons in Proximal Probe Lithography**, *J. Vac. Sci. Technol. B*, **1997**, 15, 2877-2881.

143) Zharnikov, M., Geyer, W., Golzhauser, A., Frey, S. and Grunze, M., **Modification of Alkanethiolate Monolayers on Au-substrate by Low Energy Electron Irradiation: Alkyl chains and the S/Au interface**, *PCCP*, **1999**, *1*, 3163-3171.

144) Baer, D. R., Engelhard, M. H., Schulte, D. W., Guenther, D. E., Wang, L. Q. and Rieke, P. C, **Electron-Beam Effects on $(CH_2)_{17}$ Self-assembled Monolayer SiO_2 /Si Specimens**, *J. Vac. Sci. Technol. A*, **1994**, *12*, 2478-2485.

145) Rieke, P. C., Baer, D. R., Fryxell, G. E., Engelhard, M. H. and Porter, M. S., **Beam Damage of Self-assembled Monolayers**, *J. Vac. Sci. Technol. A, Vac. Surf. Films*, **1993**, *11*, 2292-2297.

146) Hutt, D. A. and Leggett, G. J., **Static Secondary Ion Mass Spectrometry Studies of Self-assembled Monolayers: Electron Beam Degradation of Alkanethiols on Gold**, *J. Mat. Chem.*, **1999**, *9*, 923-928.

147) Seshadri, K., Froyd, K., Parikh, A. N. and Allara, D. L., **Electron-Beam-Induced Damage in Self-Assembled Monolayers**, *J. Phys. Chem.*, **1996**, *100* 5900-15909.

148) Rieke, P. C., Tarasevich, B. J., Wood, L.L., Engelhard, M. H., Baer, D. R., Fryxell, G. E., John, C. M., Laken, D. A. and Jaehnig, M. C., **Spatially Resolved Mineral Deposition on Patterned Self-Assembled Monolayers**, *Langmuir*, **1994**, *10,* 619-622.

149) Zhou, C., Jones, J. C., Trionfi, A., Hsu, J. W. P. and Walker, A. V., **Electron Beam-Induced Damage of Alkanethiolate Self-Assembled Monolayers Adsorbed on GaAs (001): A Static SIMS Investigation**, *J. Phys. Chem. C*, Article ASAP, DOI: 10.1021/jp905612p.

150) **Microelectronic Materials and Processes**, Levy, R. A., **1989**, Springer.

151) Spears, D. L. and Smith, H. I., **High-resolution Pattern Replication using Soft X rays**, *Electr. Lett.*, **1972**, 8, 102-104.

152) **Handbook of Nanophase and Nanostructured Materials: Volume III: Materials Systems and Applications**, Wang, Z. L. and Liu, Y., **2002**, Springer, p287.

153) Bogdanov, A. L. and Peredkov, S. S., **Use of SU-8 Photoresist for Very High Aspect Ratio X-ray Lithography**, *Microelec. Eng.,* **2005**, *53,* 493-496.

154) Diegoli, S., Hamlett, C. A. E., Leigh, S. J., Mendes, P. M. and Preece, J. A., **Engineering Nanostructures at Surfaces**, *Proc. Inst. Mech. Eng. Part G J. Aerosp. Eng.,* **2007**, *221*, 589-629.

155) Smith, H. I. and Flanders, D. C., **X-ray lithography --- A Review and Assessment of Future Applications**, *J. Vac. Sci. Technol.*, **1980**, *17*, 533-535.

156) Chao, W., Harteneck, B. D., Liddle, J. A., Anderson, E. H. and Attwood, D. T., **Soft X-ray Microscopy at a Spatial Resolution Better than 15 nm**, *Nature*, **2005**, *435*, 1210-1213.

157) Cuisin, C., Chelnokov, A., Lourtioz, J.-M., Decanini, D. and Chen, Y., **Submicrometer Resolution Yablonovite Templates Fabricated by X-ray Lithography**, *Appl. Phys. Lett.*, **2000**, *77*, 770-772.

158) Oscarsson, S., Pavlovic, E. and Quist, A. P., **Recent Advances in Microcontact Printing**, *Anal. Bioanal. Chem.*, **2005**, *381*, 591-600.

159) Xia, Y., Kim, E., Zhao, X-M., Rogers, J. A., Prentiss, M. and Whitesides, G. M., **Complex Optical Surfaces Formed by Replica Molding Against Elastomeric Masters**, *Science,* **1996**, *273*, 347-349.

160) Zhao. X-M., Xia, Y. and Whitesides, G. M., **Fabrication of Three-Dimensional Microstructures: Microtransfer Molding**, *Adv. Mater.,* **1996**, *8*, 837-840.

161) Kim. E., Xia. Y. and Whitesides, G. M., **Making Polymeric Microstuctures: Capillary Micromolding**, *Nature,* **1995**, 376, 581-584.

162) Kim, E., Xia, Y., Zhao. X-M. and Whitesides. G. M., **Solvent-assisted Microcontact Molding: A Convenient Method for Fabricating Three-Dimensional Structures on Surfaces of Polymers**, *Adv. Mater.,* **1997** ,*9*, 651-654.

163) Mrksich, M. and Whitesides, G. M., **Patterning Self-assembled Monolayers using Microcontact Printing: A New Technology for Biosensors?**, *Trends in Biotechnology,* **1995**, *13,* 228-235.

164) Wilbur, J. L., Kumar, A., Biebuyck, H. A., Kim, E. and Whitesides, G. M., **Microcontact Printing of Self-assembled Monolayers: Applications in Microfabrication**, *Nanotechnology*,**1996**, *7*, 452-457.

165) **Introduction to Microelectromechanical Systems Engineering**, Maluf, N. and Williams, K., **2004**, Artech House, p66.

166) Li, H-W., Muir, B. V. O., Fichet, G. and Huck**,** W. T. S., **Nanocontact Printing: A Route to Sub-50-nm-Scale Chemical and Biological Patterning,** *Langmuir,* **2003**, *19*, 1963-1965.

167) Libioulle, L., Bietsch, A., Schmid, H., Michel, B. and Delamarche, E., **Contact-Inking Stamps for Microcontact Printing of Alkanethiols on Gold**, *Langmuir,* **1999**, *15*, 300-304.

168) Liang, Z., Rackaitis, M., Li, K., Manias, E. and Wang, Q., **Micropatterning of Conducting Polymer Thin Films on Reactive Self-assembled Monolayers**, *Chem. Mater*., **2003**, *15*, 2699-2701.

169) Zhang, H., Elghanian, R., Amro, N. A., Disawal, S. and Eby, R., **Dip Pen Nanolithography Stamp Tip**, *Nano Letts*, **2004,** *4,* 1649-1655.

170) Piner, R. D., Zhu, J., Xu, F., Hong, S. and Mirkin, C. A., **"Dip-Pen" Nanolithography**, *Science,* **1999**, *283*, 661-663.

171) **Nanotechnology: A Gentle Introduction to the Next Big Idea**, Ratner, D., **2003**, Prentice Hall PTR, p45.

172) Wang, B. D., Zou, X., Chung, J., Mirkin, C. A. and Chang, L., **Design, Fabrication, and Characterization of Thermally Actuated Probe Arrays for Dip Pen Nanolithography**, *IEEE Journal of Microelectromechanical Systems*., **2004**, *13*, 594-602.

173) Wang, Y., Mirkin, C. A. and Park, S-J., **Nanofabrication Beyond Electronics**, *ACS Nano,* **2009**, *3*, 1049-1056.

174) Weiss, P. S., **A Conversation with Prof. Chad Mirkin: Nanomaterials Architect**, *ACS Nano,* **2009**, *3*, 1310-1317.

175) Jaschke, M. and Butt, H-J., **Deposition of Organic Material by the Tip of a Scanning Force Microscope**, *Langmuir*, **1995**, *11*, 1061-1064.

176) Robinson, G. M. and Jackson, M. J., **A Review of Micro and Nanomachining from a Materials Perspective**, *J. Mater. Process. Technol.*, **2005**, *167*, 316-337.

177) Fahlbusch, S., Mazerolle, S., Breguet, J. M., Steinecker, A., Agnus, J., Perez, R. and Michler, J., **Nanomanipulation in a Scanning Electron Microscope**, *J. Mater. Process. Technol.*, **2005**, *167*, 371-382.

178) Hansen, L. T., Kuhle, A., Sorensen, A. H., Bohr, J. and Lindelof, P. E., **A Technique for Positioning Nanoparticles using an Atomic Force Microscope**, *Nanotechnology*, **1998**, *9*, 337-342

179) Crommie, M. F., Lutz, C. P., Eigler, D. M. and Heller, E. J., **Quantum Corrals**, *Physica D.*, **1995**, *83*, 98-108.

180) Eigler, D. M. and Schweizer, E. K., **Positioning Single Atoms with a Scanning Tunneling Microscope**, *Nature*, **1990**, *344*, 524-526.

181) Stepanyuk, V. S., Niebergall, L., Hergert, W. and Bruno, P., ***Ab initio* Study of Mirages and Magnetic Interactions in Quantum Corrals,** *Phys. Rev. Lett.*, **2005**, 94, 187201-187205.

182) Xu, S. and Liu, G. Y., **Nanometer-scale Fabrication by Simultaneous Nanoshaving and Molecular Self-assembly**. *Langmuir*, **1997**, *13*, 127-129.

183) Schwartz, L.W. and Garoff, S., **Contact Angle Hysteresis on Heterogeneous Surfaces,** *Langmuir*, **1985**, *1*, 219-230.

184) Smith, B. K., Sniegowski, J. J., LaVigne, G. and Brown, C., **Thin Teflon-like Films for Eliminating Adhesion in Released Polysilicon Microstructures**, *Sensors and Actuators A: Physical*, **1998**, *70*,159-163

185) Marmur, A., **The Lotus Effect: Superhydrophobicity and Metastability,** *Langmuir*, **2004**, *20*, 3517-3519.

186) **Spectroscopic Ellipsometry and Reflectometry, A Users Guide**, Tomkins, H. G., **1999**, Wiley.

187) **Handbook of Ellipsometry**, Tomkins, H. G., **2005**, Springer.

188) **Atomic Force Microscopy, Biomedical Methods and Applications,** Braga, P. C. and Ricci, D., **2004**, Humana Press.

189) **Springer Handbook of Nanotechnology,** Bhushan, B., **2006**, Springer.

190) **Surface analysis of polymers by XPS and static SIMS**, Briggs, D., **1998**, Cambridge University Press.

191) **Practical Surface Analysis: Auger and X-ray photoelectron spectroscopy**, Briggs, D. and Seah, M. P., **1990**, Wiley.

192) **Scanning Electron Microscopy and X-ray Microanalysis**, Goldstein, J., Newbury, D. E., Joy, D. C., Echlin, P., Lyman, C. E., Lifshin, E. and Sawyer, L, **2003**, Springer.

Chapter 2

Laying the Molecular Foundations:

Electron Beam Lithography Induced Chemical Conversion of NO_2 Terminated SAMs to NH_2 Terminated SAMs on Au Surfaces and Subsequent Site-Specific Deposition of Au Nanoparticles

Chapter 2 is reproduced from an article entitled:

'Examination of the factors affecting the direct-write electron beam patterning of self-assembled monolayers and subsequent attachment of gold nanoparticles on gold surfaces' by Simon. J. Leigh, Alex. P.G. Robinson, Jose. L. Prieto, James. Bowen and Jon. A. Preece, in preparation.

Abstract

Electron beam lithography is a high resolution lithographic technique for nanostructuring surfaces. This chapter details the use of electron beam lithography to induce the chemical conversion of the surface groups of aromatic NO_2 terminated thiol SAMs on Au surfaces to aromatic NH_2 groups, subsequently leading to the site specific deposition of Au nanoparticles to form nanostructured surfaces. The response of the SAM over a range of electron doses for the lithography process is characterised and related to feature quality and attachment of nanoparticles.

2.1 Introduction

Lithographic patterning of surfaces has been the mainstay of the microelectronics/integrated circuit industry for many years.[1] However, conventional

photolithography has many limitations, making its future use for formation of nanostructured surfaces impractical and unlikely *(see more in-depth discussion in Chapter 1, Section 1.5.1.2.1)*. Currently, techniques such as electron beam lithography (EBL), X-ray lithography (XRL)[2] or scanning near-field optical (SNOM) lithography[3] are seen to provide routes for fabrication beyond the limitations of photolithography. These new lithographic techniques can often be used much like conventional lithographies, in that a pattern is defined in a resist layer, which is then developed and used as an etch mask, with the pattern transferred to the underlying material. While providing increased resolution over photolithography, such fabrication is still a wholly top-down process. The key to achieving maximum resolution and controllability for defining nanostructured surfaces is to integrate bottom-up methodologies, with key components spontaneously self-assembling to top-down lithographically patterned surfaces. The controlled, precise, yet facile fabrication of 3D nanostructures is an area of major interest for the nanoscience and nanotechnology community.[4] In response to this goal, the use of a combination of bottom-up and top-down processes has been employed, exploiting the desirable characteristics of each technique.[5-8] When applied to systems involving a modification of the chemical nature of components to influence the assembly of nanoscale components, such a combination of techniques has been termed '*Precision chemical engineering'*. [9] With respect to the work presented here, the approach involves the formation of ultrathin films or self-assembled monolayers (SAMs) on metal,[10] semiconductor[11] and insulator surfaces,[12] followed by subsequent chemical modification with a precision lithographic technique and immobilisation of particulates on the modified surfaces to form 3D nanostructures.[13-15] Soft lithographic techniques such as microcontact printing (μCP) can also lead to the formation of patterned surfaces which can then be further derivatised with polymers through surface initiated polymerisation reactions.[16]

2.1.1 Electron beam lithography (EBL)

One lithographic technique that provides the most realistic short-term possibilities for fabrication beyond the current limits of optical (photo-) lithography is EBL,[17] which can be used for creating high resolution (sub 10 nm) patterns on surfaces.[18,19] The first EBL instruments, based on scanning electron microscopes (SEMs) were developed in the late 1960s. Shortly thereafter, the discovery that the common polymer PMMA (polymethyl methacrylate) made an excellent e-beam resist lead to more extensive use of the technique.[20] In brief, the technique consists of scanning a focussed beam of electrons across a surface, usually covered in a film of resist that is sensitive to electrons. The EBL system can be controlled so as to deliver a well-defined dose of electrons per unit area, making EBL fabrication highly reproducible. Currently, EBL is principally used in support of the integrated circuit industry, where it has three niche uses.[21,22] The first of these uses is in mask making, typically for the chrome-on-glass masks used by optical lithography processes. The second application for EBL is in direct-write processing for advanced prototyping of integrated circuits and manufacture of small volume speciality products. Finally, EBL is becoming more frequently used in research into the scaling limits of integrated circuits and studies of quantum effects and other novel physics phenomena at nanoscale dimensions.[23] The high resolution of the features that can be fabricated with EBL makes the technique ideal for probing the possibilities of forming viable nanostructured surfaces for post-optical lithography, where smaller features are required.

Traditionally, in developing a new resist for EBL, there are several issues that need to be addressed, such as resist contrast, post exposure dissolution, dose sensitivity, and resolution.[24,25] These issues need to be examined and addressed in developing any EBL fabrication system so as to achieve maximum resolution and

flexibility. Existing polymeric resist systems also suffer from resolution problems and poor etch durability.[21] In conventional EBL the resolution achievable is limited by the large size of the molecules in the polymeric resist and secondary electron processes such as forward scattering and the proximity effect. However, these effects can be minimized by the use of small molecules such as SAMs as a 'pseudo-resist'.[26]

2.1.2 Considerations and commonly occurring effects during EBL that lead to the proximity effect

The proximity effect is the phenomenon that the electron exposure dose distribution, and hence the pattern achieved, is wider than the scanned pattern, due to the interactions of the primary beam electrons with the resist and substrate. This effect leads to the resist outside the scanned pattern to receive a non-zero dose.

2.1.2.1 Forward scattering

As electrons penetrate a conventional resist, a fraction of them will undergo small angle scattering events, which can significantly broaden the beam profile towards the bottom of the resist layer. The increase in effective beam diameter (*in nm*) due to forward scattering can be given empirically by the formula $d_f=0.9(R_f/V_b)^{1.5}$, where R_f is the resist thickness in nm and V_b, the beam voltage in kV. The degree of forward scattering that occurs can be minimised by reducing the resist thickness and utilising a high accelerating voltage.[27]

2.1.2.2 Backscattering & backscattered electrons (BEs)

As the electrons continue to penetrate the 'resist' and into the substrate, some will experience large angle scattering events. These BEs may return through the resist at a significant distance from the primary dose site, causing additional resist

exposure.[28] This backscattering is a major contributing factor to the electron beam proximity effect. The range the electrons travel in the substrate depends on both the energy of the primary electrons and type of substrate. The fraction of the electrons that are backscattered, *n*, is roughly independent of the beam energy,[29] however it is dependent on the substrate material, with low atomic number materials giving less backscattering. Typical values of *n* range from 0.17 for silicon to 0.50 for tungsten and gold.[30] As the primary electron dose is increased, the number of backscattered electrons also increases (figure 2.1).

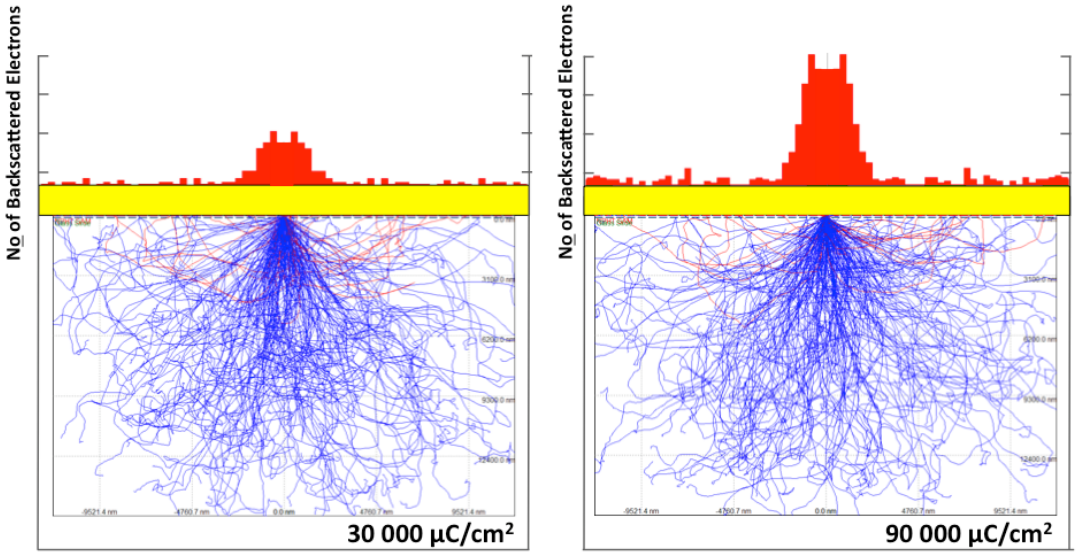

Figure 2.1. Simulation of distribution and number of backscattered electrons at 30,000 and 90,000 µC/cm^2 made using CASINO electron modelling software.

2.1.2.3 Secondary electrons (SEs)

As the primary electrons slow down, much of their energy is dissipated in the form of SEs.[31] In conventional EBL, these SEs are responsible for the bulk of the actual resist exposure process. Since their range in the resist is only a few nm, they contribute little to the proximity effect. Instead, the net result can be seen as a pattern resolution greater than the minimum beam diameter, which accounts for the minimum

practical beam resolution (~10-20 nm) of most modern high-resolution EBL systems.[32]

2.1.2.4 The proximity effect

The overall result of the previously discussed factors is that the electron dose delivered to the sample is not exactly confined to the patterns that are written by the EBL tool, resulting in pattern specific variations in feature size and linewidth from the resist outside the scanned pattern receiving a non-zero electron dose.[33] This effect is collectively known as the proximity effect. In conventional EBL, where normal polymeric resists are used, the proximity effect can lead to either *over* or *under exposure* of features. The proximity effect is also exacerbated by the production of close packed or nested features, where the exposure of one feature can lead to broadening or secondary exposure effects in a neighbouring feature.[34]

2.1.3 Molecular materials - ultrathin films and pseudo-resists

The key to overcoming effects such as the proximity effect and detrimental etching effects (such as under etching) is to develop high performance resists and etches or pseudo resist systems that utilise irradiation to carry out chemical conversions in the pseudo-resist that can be further derivatised or added to with nanoscale species such as nanoparticles (which have potential applications in the areas of electronics,[35,36] photonics,[37] sensors[38] and catalysis[39]) without the need for developing and etching steps. Such systems have key advantages over conventional polymeric resists, which often show poor etch durability and self-limiting resolution due to their size.[40] One of the key ways to form ultrathin films is through the formation of self-assembled monolayers (SAMs). The self-assembling nature of SAMs means that a regular, reproducible monomolecular layer can normally be

formed in a facile manner, without the need to follow rigorous formation and developing protocols.[41] The use of such monomolecular thin films negates the effects of forward scattering on the system, however, the processes that create secondary and backscattered electrons in the substrate are still problematic. Hence, characterisation of new systems is essential to discover the limits of the fabrication that can be carried out before the proximity effect becomes a limiting factor.

2.1.4 Energetic irradiation induced chemical reduction of nitro groups to amines

The literature has shown that it is possible to reduce the surface aromatic–NO_2 group of a self-assembled monolayer to that of an NH_2 group using EBL and X-ray irradiation.[9, 42-45] Mendes *et al.*[43] utilised the molecule NPPTMS, which, when immobilised on SiO_2 surfaces was shown to respond to doses of electrons and X-rays which induce the chemical conversion of the NO_2 terminal group to an NH_2 terminal group (scheme 2.1).

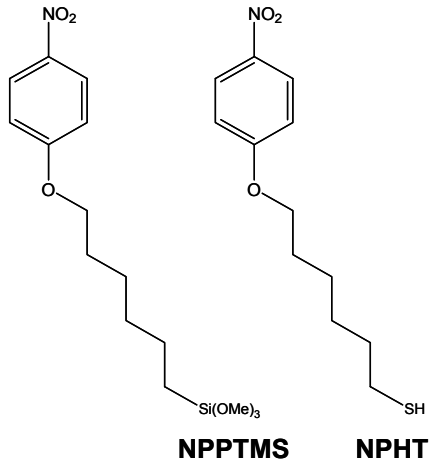

Scheme 2.1. Structure of of NPPTMS[43] and the analogous thiol-terminated molecule, NPHT.

By using X-rays to carry out the conversion process, the chemical change on the surface can concomitantly be analysed by analysis of the XPS spectra (figure 2.2). This method for spatially selective conversion of the terminal groups of the SAM provides a contrast in chemical functionality on the substrate surface, which can be exploited to influence the assembly of nanoscale materials such as nanoparticles.[43] This molecular system was shown to provide high-resolution features when exposed to a beam of electrons.

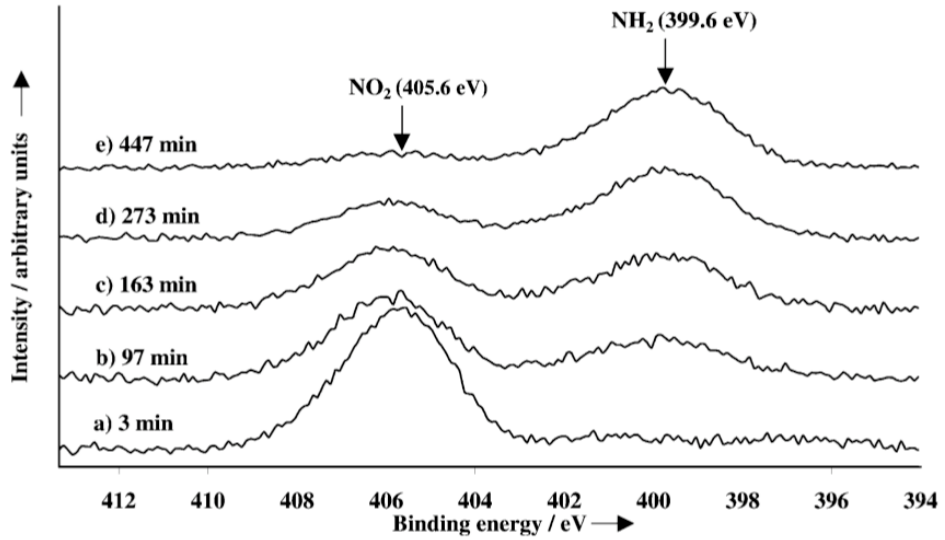

Figure 2.2. Time-resolved XPS spectra of the N 1s peak of a NO_2 terminated SAM on a silicon substrate.[43]

However, the ability of silane molecules to easily polymerise and form multilayers in the presence of excess moisture instead, as opposed to SAMs on surfaces, meant that reproducibility of the silane SAM formation process was sometimes poor, limiting the resolution. SAMs have also been shown to spontaneously form between gold surfaces and sulphur containing molecules,[46] leading to reproducible monomolecular layer formation compared to silane SAM formation and conventional resist spin-coating.

2.1.5 NO_2 to NH_2 conversion mechanism

E-beam irradiation can either induce removal, crosslinking, damage or modification of an internal and/or terminal functional group of SAMs.[47] Such systems can then be used in a second stage as general templates to direct the assembly of nanoscale components, to either unirradiated or the irradiated regions to create three-dimensional nanostructured surfaces.[48] Until recently, most work on e-beam irradiation of SAMs was focussed on simple aliphatic and aromatic SAMs with lateral dimensions down to 5 nm having been fabricated.[49] E-beam irradiation of aliphatic SAMs has been shown to cause the loss of orientational and conformational order,[50, 51] (which has been exploited as a mechanism for forming mixed SAMs[52]) partial dehydrogenation,[53] formation of C=C bonds,[54] appearance of oxygenated functional groups and partial desorption of the film fragments.[55] Regarding aromatic SAMs, electron irradiation induces primarily C-H bond scissions in the aromatic unit, with subsequent cross-linking between the neighbouring aromatic moieties. Structures with a lateral size below 20 nm have been fabricated. The increased etch resistance of electron irradiated SAMs makes them a negative tone resist for lithographic applications whereas aliphatic SAMs, where electron-induced damage dominated over crosslinking, can be used as positive tone resists.[56] Beyond the principal differences between aliphatic and aromatic SAMs, the molecular orientation and packing density have also been seen to affect the extent of the irradiation induced modification.[57] The mechanism for the electron beam and X-ray induced conversion of NO_2 to NH_2 is beginning to be better understood and investigations in the literature suggest the mechanism reproduced below (figure 2.3).

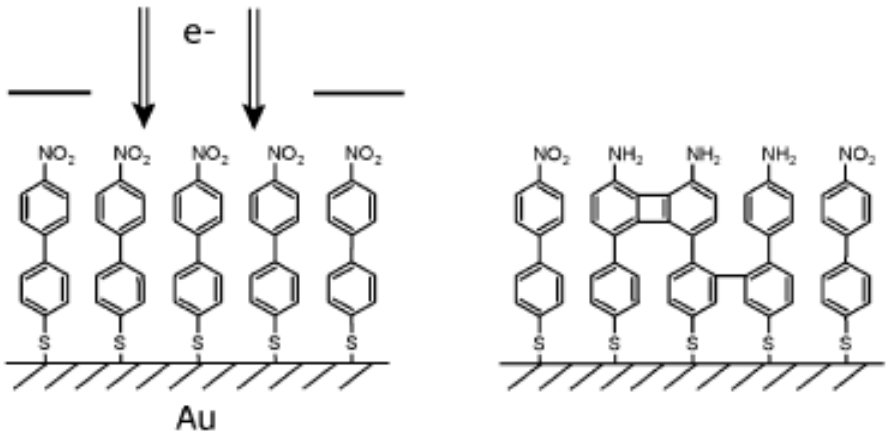

Figure 2.3. Model of electron induced processes in NBT molecule. A monolayer of NBT is irradiated by electrons and generates amino (NH_2) end groups while the underlying aromatic monolayer is dehydrogenated and cross linked.[58]

Grunze *et al,*[42-45] first demonstrated the possibility for the EBL induced reduction, by exposing a SAM of 4'-nitro-1,1'-biphenyl-4-thiol on an Au surface. The periphery –NO_2 moieties were converted to the respective –NH_2 moieties allowing generation of 1 μm down to 10 nm wide lines, thus using the SAM as a pseudo-resist. Fourier Transform Infrared (FTIR) studies revealed a more rigid structure in the exposed regions compared to the unexposed areas. Electrons resultant from the irradiation step are thought to locally convert the terminal nitro groups to amino groups,[45] while concomitantly the aromatic layer is dehydrogenated and cross linked.[58, 59] The released hydrogen is transferred to the nitrogen. Chemical reduction of NO_2 terminated films would normally be performed by immersing the substrate in a solution of a catalytic hydrogen transfer agent such as $SnCl_2$ in anhydrous EtOH for 3 h at 50^{o}C. This is followed by sonication successively in 5 M HCl, 1 mM EDTA (ethylenediaminetetraacetic acid) and anhydrous $CHCl_3$.[44] Studies by Iqbal *et al.*[60] using X-ray lithography have confirmed the conversion of the terminal NO_2 groups and also shown that the presence of the aromatic group is required to carry out the conversion process with molecules containing only aliphatic groups not undergoing

the X-ray induced NO_2 to NH_2 conversion process, but rather appearing to have the NO_2 group selectively cleaved from the SAM. With e-beam induced conversion, it is believed that the electrons responsible for the conversion process are not the incident primary electron dose, but the resultant secondary electrons arising from electron scattering processes.[61] With this lithographic approach, SAMs have been successfully used to fabricate patterns with lateral sizes below 10 nm.[62, 63]

2.2 Aims and objectives

Previous literature has shown many electron doses (and beam energies) that can be used for carrying out the NO_2 to NH_2 conversion process. However, a systematic study on such behaviour has been lacking. As well as being a factor pertaining to the response of the molecule, due to the ultrathin nature of the SAMs, the scattering characteristics, resultant from the underlying surface (which differ for different surface materials) play a major role in the response of the SAM to the e-beam dose, in that different amounts of scattered electrons will remain in the local vicinity to the primary dose region depending on the substrate. The aim of the work presented in this chapter is to carry out a systematic study of the electron dose vs response behaviour of an aromatic-NO_2 terminated SAM (NPHT) on gold surfaces (**step 1**), which will then be used to promote the site-specific deposition of gold nanoparticles through their known affinity for NH_2 terminated surfaces (**step 2**).[43,64] The effect of the feature sizes and inter-feature gaps on the required electron dose and nanoparticulate species will also be examined (**step 3**), along with the effect of high electron dose exposure (**step 4**).

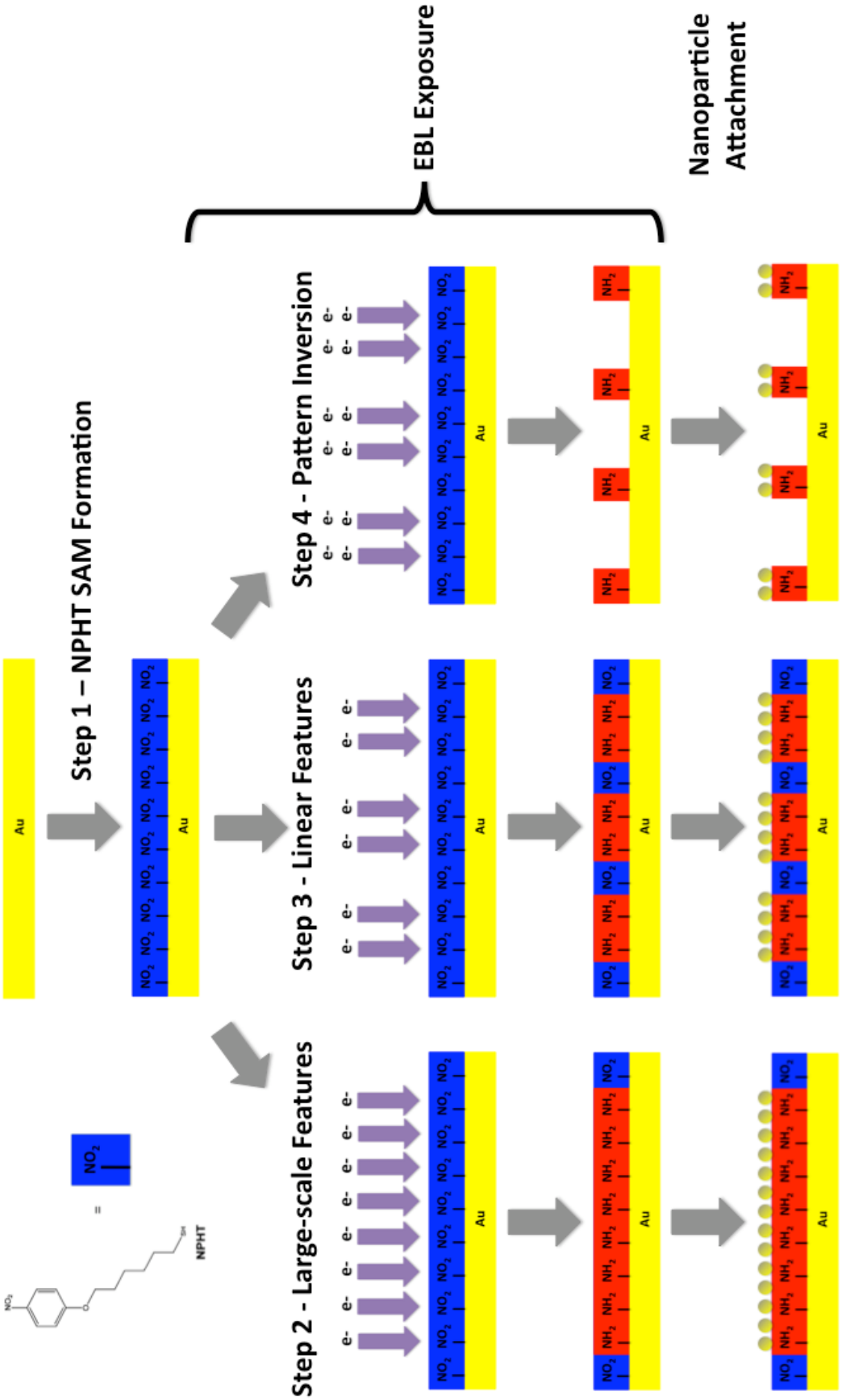

Scheme 2.2. Scheme showing the experimental procedures adopted.

2.3 Results and discussion

2.3.1 Research methodology

Initially, NPHT SAMs will be formed on planar Au surfaces (**scheme 2.2, step 1**). The first task will then be to examine the electron dose required to carry out patterning of large-scale features on NPHT SAMs (**scheme 2.2, step 2**) and then move to examining the required electron dose for creating linear features on NPHT SAMs (**scheme 2.2, step 3**). Finally, the use of high electron doses to induce pattern inversion on SAMs will be investigated (**scheme 2.2, step 4**).

2.3.2 NPHT SAM formation (step 1)

NPHT SAMs were formed over 24 hrs from an ethanolic solution. The NPHT SAMs had an ellipsometric thicknesses of 1.36 $\pm$ 0.19 nm, in good agreement with the estimated value (1.5 nm, Chem3D Software), taking into account the characteristic tilt angle of SAMs of this type.[65] Water contact angles of NPHT SAMs ($\theta_a = 67 \pm 1^o$, $\theta_r = 45 \pm 1^o$) also agreed with literature values ($\theta_a = 64^o$) for aromatic-NO_2 terminated SAMs on gold surfaces.[65] The elemental composition of the monolayers was determined by XPS (figure 2.4). The elements C, N, O, S and Au were monitored in the spectra. The XPS survey spectrum confirmed the presence of peaks at binding energies; 284, 400, 531 and 162 eV which are indicative of the presence of C, N, O and S, respectively[66] and agreed with the previously reported data (figure 2.4).[67]

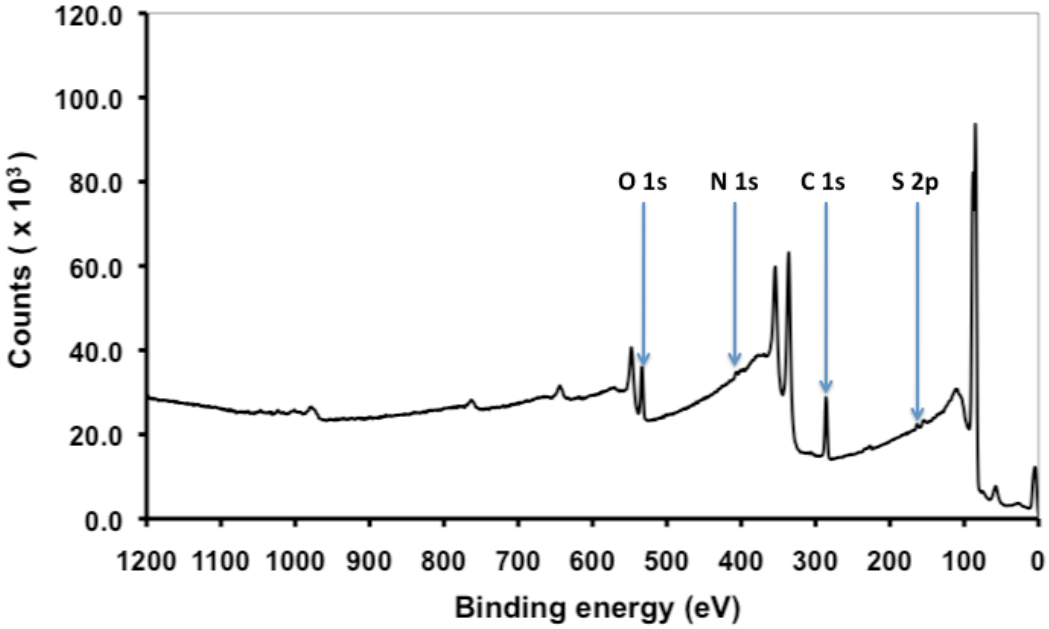

Figure 2.4. XPS survey spectra of NPHT SAM on Au surface.

2.3.3 Large-scale feature electron dosage characterisation (step 2)

To initially assess the effect of electron dosage on the reduction of NO_2 to NH_2 in the NPHT SAM, a grid pattern of 120 μm x 120 μm, 200 μm spaced squares was exposed to a beam energy of 50 keV to a range of increasing electron dosages (5 000 – 125 000 μC/cm^2, figure 2.5). The total fabrication time for the grid was approximately 14 hours. After exposure, the sample was imaged utilising the SEM capabilities of the EBL instrument, and subsequently immersed into a solution of citrate passivated Au-NPs. After the immersion into the Au-NPs the sample was initially imaged with optical microscopy (figure 2.5). The optical microscopy images revealed a contrast between the exposed regions and the unexposed regions. The sample was then re-imaged by SEM, with the before and after immersion images presented in figure 2.6a and figure 2.6b respectively.

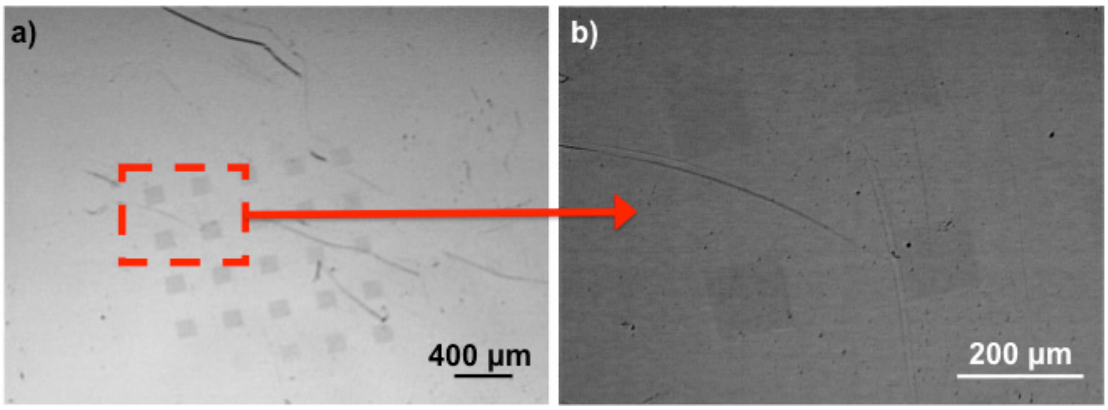

Figure 2.5. a) optical microscopy image of large-scale features after immersion in Au-NPs; and **b)** magnified region (**step 2**).

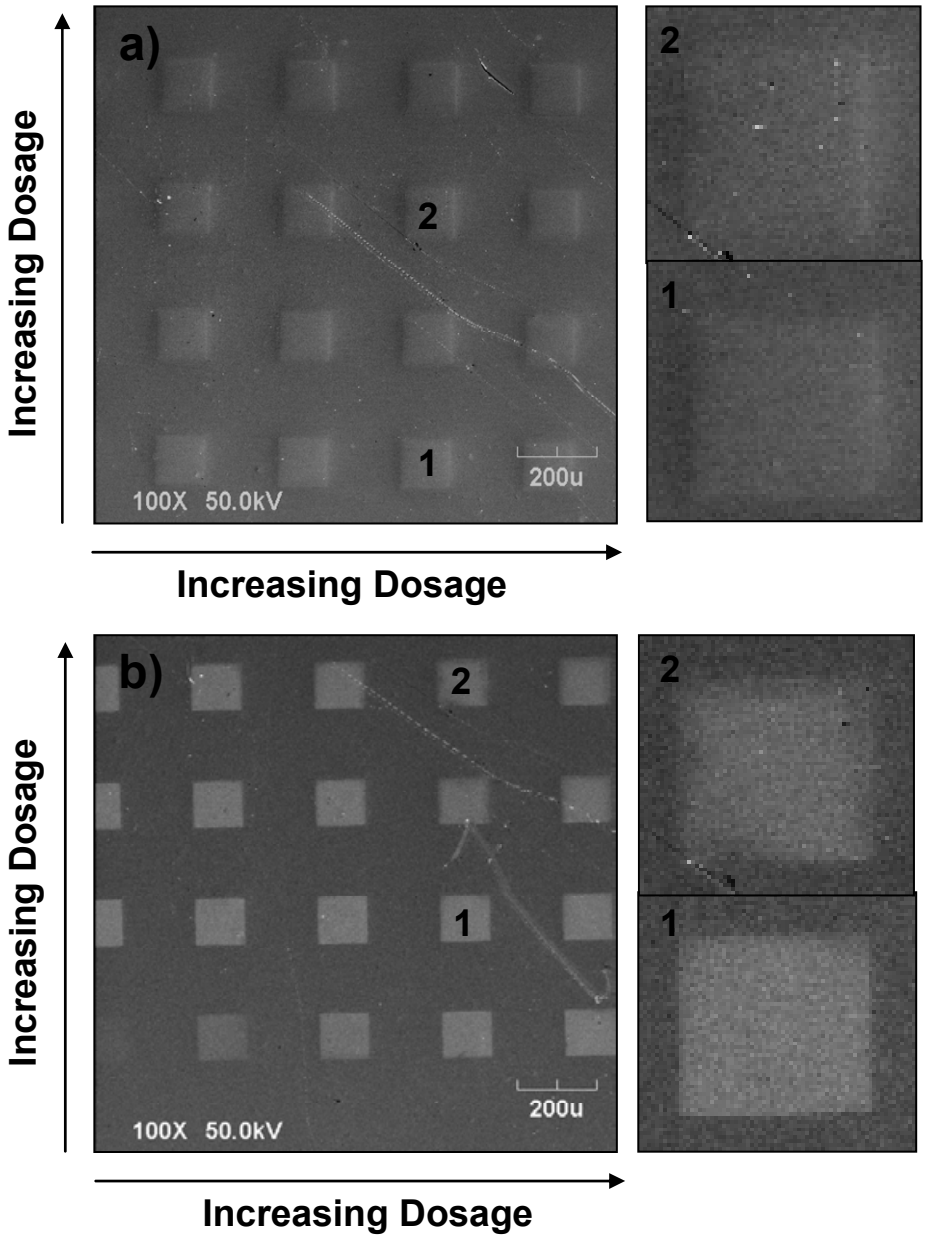

Figure 2.6. SEM images of NPHT SAM **a)** after EBL exposure over a range of doses **(**5 000 – 125 000 μC/cm^2); and **b)** after subsequent immersion into Au-NPs (**step 2**).

A clear contrast in appearance is seen between the surfaces before (figure 2.6a) and after immersion (figure 2.6b) in the Au-NP solution. After the immersion, the image contrast between the exposed regions and surrounding SAM is much brighter, indicative of Au-NPs being adsorbed to the electron exposed region. It should be noted that although in figure 2.6a all the squares appear to have similar

contrast with respect to the surrounding regions, in-fact they were fabricated at increasing electron dosages, with the bottom-left square of image B fabricated at a dose of 5 000 μC/cm^2 and then increasing in increments of 5 000 μC/cm^2 left to right and increasing bottom to top. The gradient in the observed contrast is clearly seen in figure 2.6b, after immersion in the Au-NPs dispersion, with the bottom left square (5 000 μC/cm^2) showing a low contrast, indicative of a low degree of Au-NP attachment. The electron dose controlled absorption of Au-NPs is quantified in figure 2.7 as an average particle count of 6 areas. The squares in the top right corner of figure 2.6b appear to have a poor edge resolution with the characteristic shadowing effects normally observed after high dose EBL.[35] The inset magnified sections of the SEM images (figure 2.6b 1 & 2) confirm this loss of edge resolution as the electron dose is increased, which cannot be observed before Au-NP attachment. As can be seen from the summarised SEM images in figure 2.7a and corresponding graph of nanoparticle attachment (figure 2.7b), it can be deduced that the optimal dosage for the conversion of the NO_2 group to an NH_2 group and subsequent attachment of Au-NPs to features of this size is around 30,000 μC/cm^2.

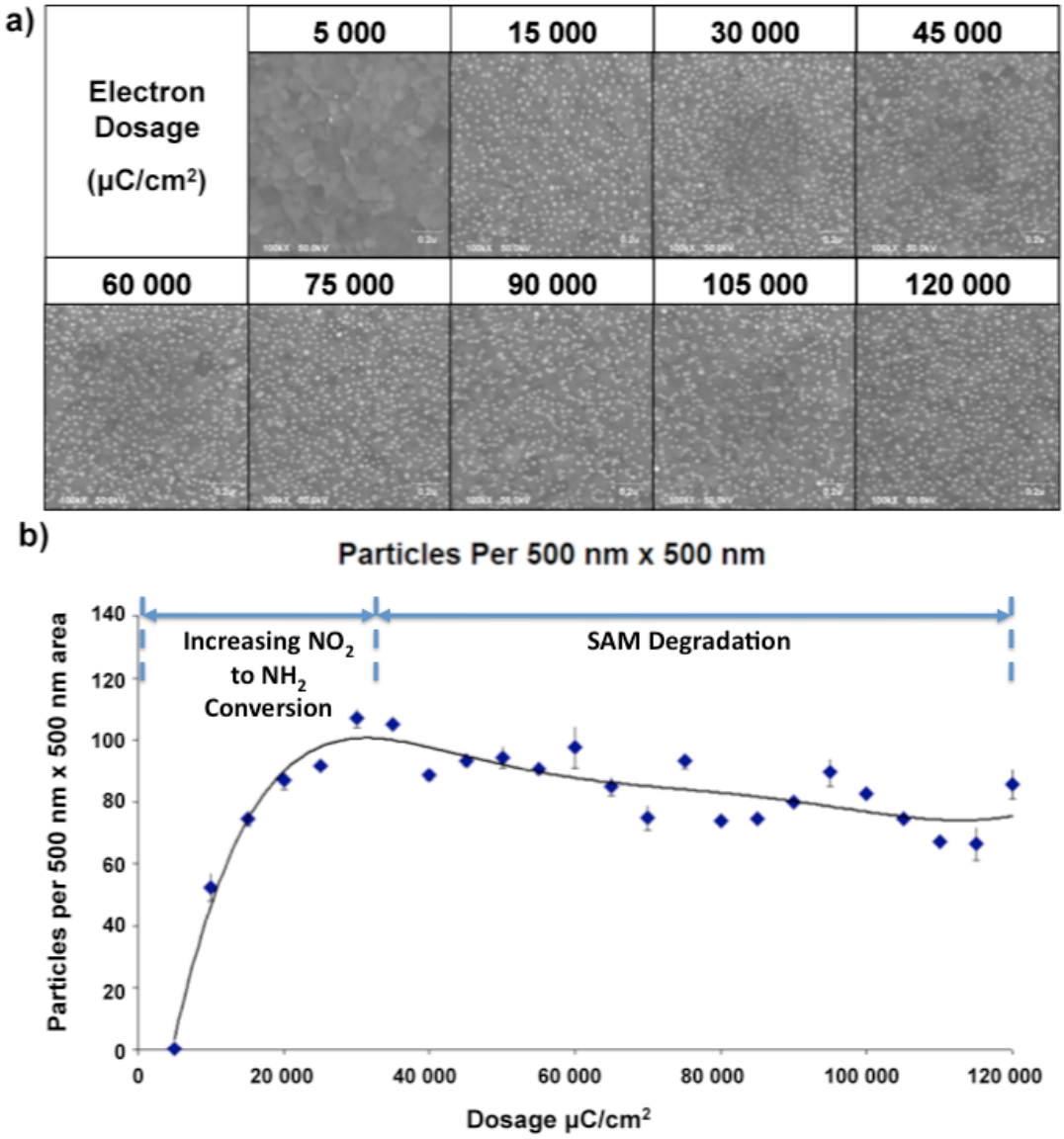

Figure 2.7 a) summarised SEM images of Au-NPs attached to NPHT SAM exposed at a range of electron doses; **b)** resultant graph showing electron dose vs attachment of Au-NPs **(step 2)**.

The shape of the EBL electron dose vs nanoparticle adsorption graph mimics that of the response of a conventional negative EBL resist to increasing electron dose, where exposure at a certain dose leads to a rapid change in the retained film thickness and higher doses can lead to a decrease in the retained film thickness.[59, 68, 69] At electron doses above those affording maximum nanoparticle attachment, the amount

of nanoparticle attachment decreases, possibly indicating degradation of the SAM due to the increased amount of secondary electrons present.

The rationale for the attachment of the Au-NPs is that the surface NO_2 groups of the NPHT become reduced upon electron beam exposure and are converted to NH_2 groups. It is believed that the reduction of the nitro group to an amino group is carried out not by the primary incident electrons, but by secondary low energy electrons emitted from the surface.[21, 43] The NH_2 groups, when immersed in the acidic Au-NP solution become protonated, forming NH_3^+ groups, which are able to bind to negatively charged, citrate-stabilised (COO^-) Au-NPs. The effect of increasing the primary electron dose is to increase the number of BE and hence increase the number of secondary electrons.

The electron dose of 30 000 $\mu C/cm^2$ observed to yield the greatest proportion of Au-NP attachment and is comparable to the dose of 35 000 $\mu C/cm^2$ reported to be required to carry out the large-scale nitro reduction on a biphenyl based $-NO_2$ terminated SAM on Au.[45] Similar experiments to those presented here have shown that EBL with subsequent attachment of gold nanoparticles can be seen with an analogous silane molecule (NPPTMS) on silicon.[43] It is hypothesised that the difference in the EBL dose behaviour between SAMs on gold and silicon is related to the differing film thicknesses and electron scattering characteristics of the two underlying surfaces, requiring a higher dose for the gold surface.[21,70]

2.3.3.1 AFM adhesion force mapping of EBL exposed samples

AFM adhesion force mapping was carried out to gain insight into the adhesive response of the SAM samples after EBL fabrication, but before immersion in Au-NPs. AFM adhesion force mapping involves bringing the tip of an AFM into close proximity to the surface of interest until the attractive forces between the AFM tip and

the surface cause the cantilever to deflect towards the surface (the so-called *'snap-on'* point). The tip is then retracted slowly until it breaks contact with the surface and springs back upwards (the so-called *'snap-off'* point)(figure 2.8).

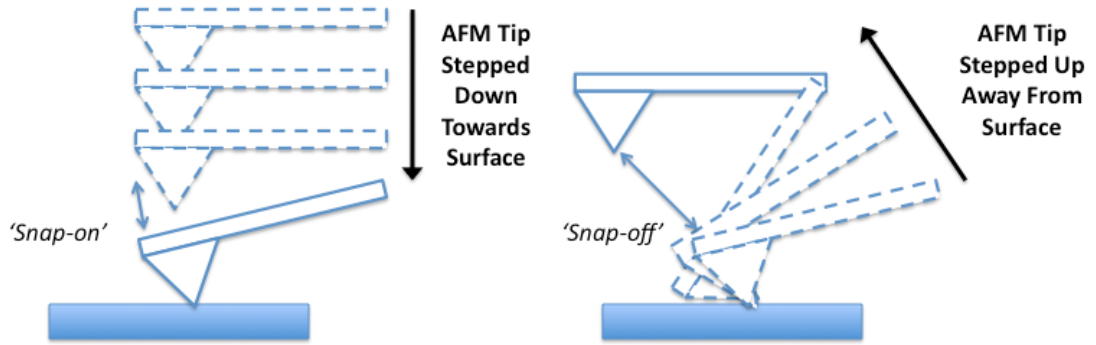

Figure 2.8. Figure depicting '*snap-on*' and '*snap-off*' points in AFM adhesion force mapping.

A more complete discussion of the principles behind adhesion force mapping can be found here.[71] Initial AFM tapping mode imaging of EBL patterned regions after EBL exposure revealed no contrast between the exposed and unexposed regions with either, height, amplitude or phase imaging. Operating the AFM in force mapping mode over the same area with the same standard tapping mode AFM tip revealed contrast between the EBL exposed and unexposed regions on both the approach and retraction of the AFM tip to/from the sample surface (figure 2.9).

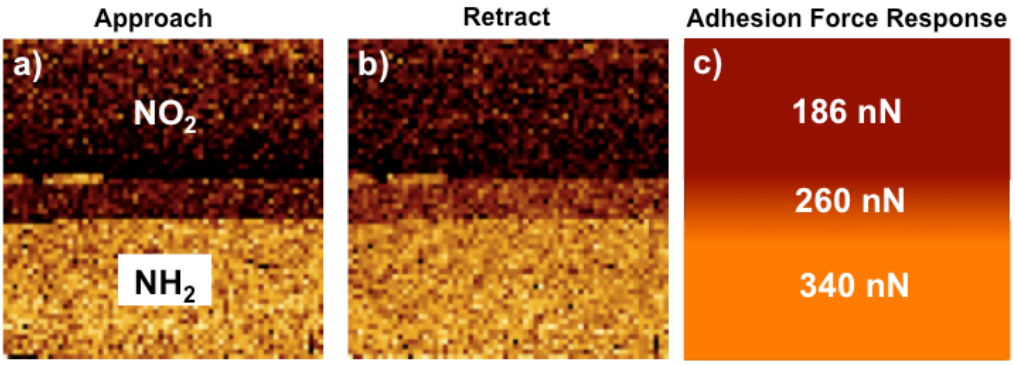

Figure 2.9. AFM adhesion force maps in air; **a)** approach (*snap-on*); **b)** retract (*snap-off*); & **c)** adhesion force response of region across exposed and un-exposed areas of sample.

After determination of the deflection sensitivity of the cantilever and calibration of the spring constant, the average adhesive force upon tip retraction (*'snap-off'*) of each region was calculated. The NH_2 terminated regions exhibited an adhesive force of approximately 340 nN, which corresponds well to literature values for NH_2 terminated SAMs on Au surfaces (340 nN).[72] The NO_2 terminated regions of the sample exhibited an adhesive force of approximately 186 nN, a lower value than for the NH_2 regions, presumably because there is a reduced interaction of the NO_2 surface with the SiO_2 tip surface. Interestingly, from the force mapping, there appears to be a 12 μm region between the NH_2 and NO_2 regions, exhibiting an intermediate adhesive force, which is an average between the force seen in the neighbouring regions, possibly indicating a 50:50 ratio of NH_2 to NO_2 groups in this region. This intermediate region of the sample, can be attributed to a region of low surface density electron scattering at the edge of the exposed area only partially converting the SAM.

2.3.4 Effect of electron dose on the patterning of linear features (step 3)

To investigate the effect of electron dose upon feature quality and resolution of linear features, fabrication of linear features on NPHT SAMs on gold was carried

out. Grids of lines of width 500 nm with a 400 nm gap (type A) and 250 nm wide lines with a 550 nm gap (type B) were exposed over 30 000, 35 000, 40 000 and 45 000 μC/cm^2) informed by the large-scale exposures as affording the largest values of Au-NP attachment (figure 2.10).

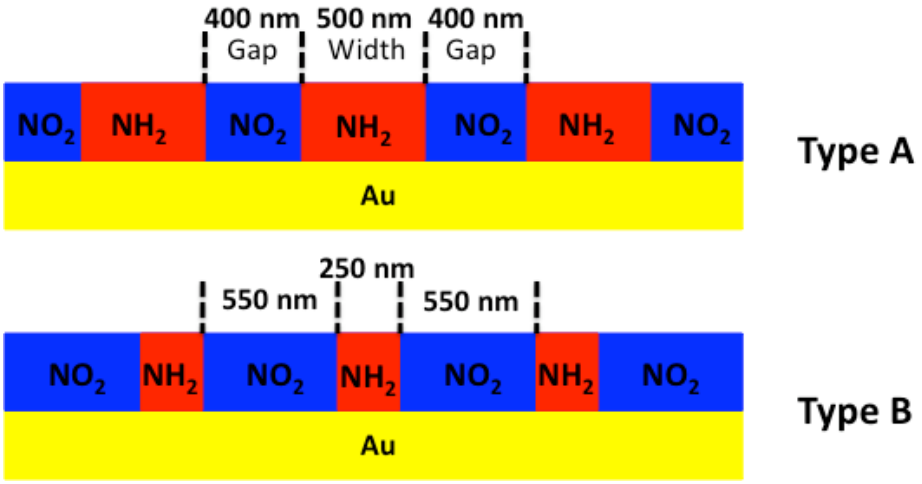

Figure 2.10. Diagram showing the areas exposed to the primary incident electron beam (red areas), **type A** (*500 nm wide, 400 nm gap*) and **type B** (*250 nm wide, 550 nm gap*) (**step 3**).

The sample was then immersed in Au-NPs (figure 2.11a). Upon decreasing feature size and spacing from the 120 μm squares used to examine the optimal electron dose, there was a slight shift in the required optimal electron dose so as to overcome possible over or under exposure relating to secondary electron contributions from neighbouring features (so-called proximity effects).[73]

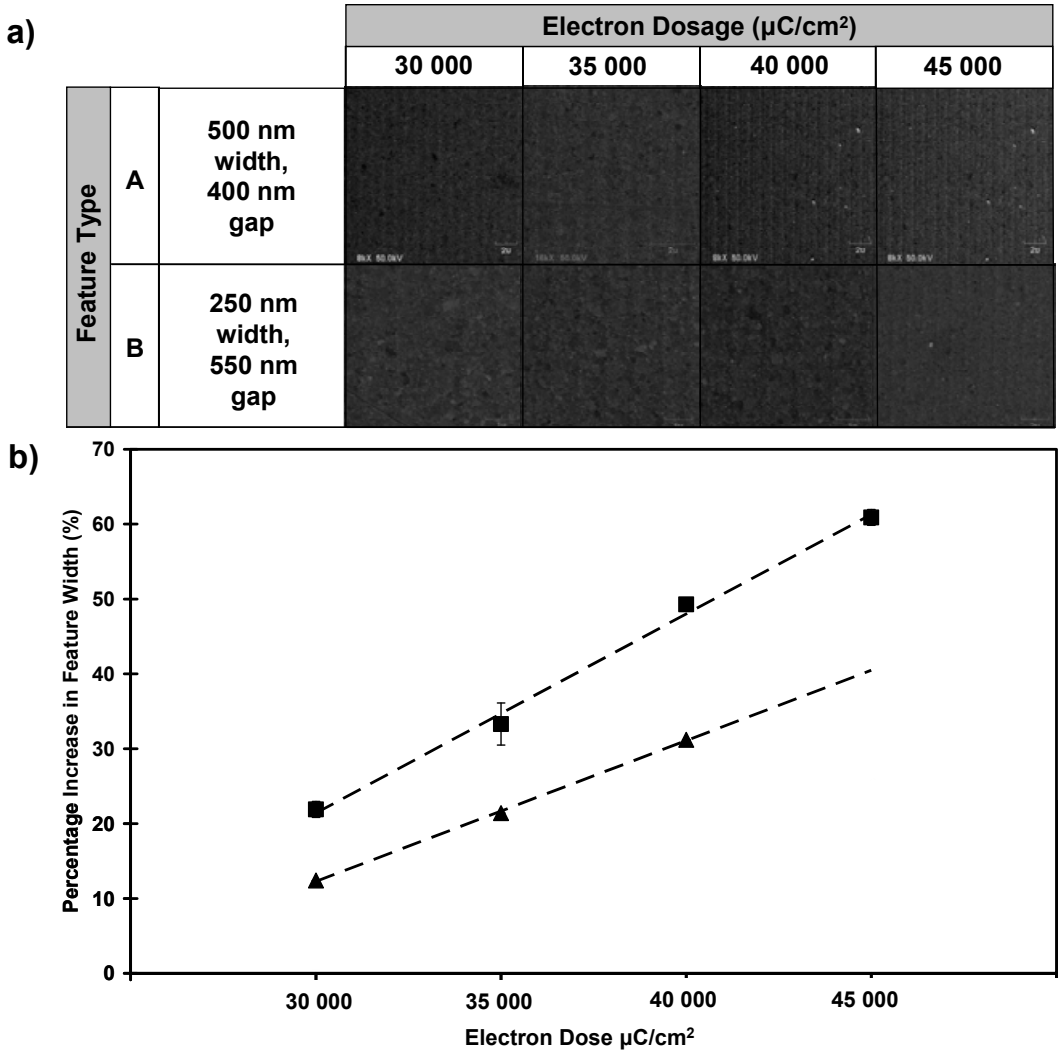

Figure 2.11. a) SEM images of **type A** & **B** features fabricated at increasing electron dose and after immersion in Au-NPs; **b)** Graph depicting the percentage increase (broadening) in line-widths of features after deposition of Au-NPs, ■ **type A** and ▲ **type B** (**step 3**).

Analysis of the fabricated features after immersion in Au-NPs showed that the width of the fabricated lines were broader than the defined writing process (figure 2.11b). This broadening of features is due to the secondary and backscattered electrons propagating beyond the incident primary electron beam. The feature broadening was seen to increase with increasing electron dose, with type A features broadening by up to 60% at a dose of 45 000 μC/cm^2. Features exposed at 30 000

μC/cm^2 showed smaller percentage increase (22%). Type B features followed the same dose-related feature broadening pattern, but a smaller amount of nanoparticle attachment which made judgement of feature width extremely difficult. Upon closer inspection of the features from EBL exposure at 40 000 μC/cm^2, the 500 nm wide, 400 nm gap (type B) lines appear well resolved with a good degree of attachment of the nanoparticles. The 250 nm wide, 550 nm gap (type B) lines fabricated at an electron dose of 40 000 μC/cm^2, were not well resolved, with only minimal attachment of nanoparticles at the feature edges and at 45 000 μC/cm^2 no attachment of Au-NPs (figure 2.12).

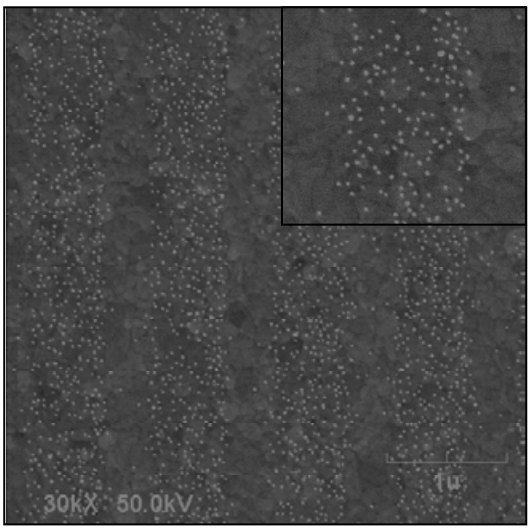

Figure 2.12. SEM image of **type A** feature, *inset*, magnified region of a single 500 nm wide feature **(step 3)**.

As the 500 nm features had broadened by up to 60% over the small dose range used, to examine the feature broadening at higher doses beyond 45 000 μC/cm^2, the 500 nm were spaced further apart (1000 nm, **type C**) to avoid merging of features if significant broadening occurred (figure 2.13). Interestingly, this increase in gap resulted in no nanoparticle attachment on the EBL patterned features.

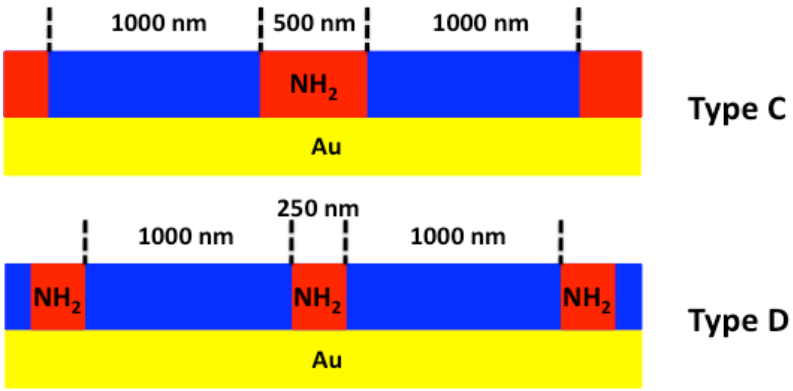

Figure 2.13. Diagram showing the areas exposed to the primary incident electron beam (red areas), **type C** (*500 nm wide, 1000 nm gap*) and **type D** (*250 nm wide, 1000 nm gap*) (**step 3**).

The lack of nanoparticle attachment on features with a 1000 nm gap is believed to be an indicator that the proximity of neighbouring features is also a controlling factor in feature quality, with the features simply not being exposed. Secondary electrons are generated as a function of the backscattered electrons from the primary electron dose. These backscattered electrons can scatter over large distances (up to tens of microns) within the sample and the subsequent secondary electron collisions result in further scattering and exposure effects in neighbouring features at the surface. The inter-feature gap controlled attachment of Au-NPs further agrees with the theory that scattered electrons play a key part in the SAM reduction process.[74] The reason for the lack of nanoparticle attachment on the features with increased gap is that most of the secondary electrons are spread within the inter-feature gap and not within the features themselves, leading to only partial conversion of the NO_2 groups below a certain key level per unit area required for the attachment of Au-NPs.

Furthermore, 250 nm lines were exposed with a 1000 nm gap (type D) (figure 2.12). As with the 500 nm features, not even the minimal nanoparticle attachment seen before was evident on the features due to the increase in inter-feature distance reducing the secondary electron contribution from neighbouring features as the amount of secondary electrons present reduces with increasing distance from the primary exposure point.[39] This inter-feature gap controlled attachment of nanoparticles, demonstrates that EBL feature quality on SAM surfaces is not purely controlled by the electron dose. In order to effectively use EBL to pattern SAMs, careful consideration of the feature size and gap to be used is thus required due to the backscattering dependence of electrons due to the ultrathin nature of the films used.

2.3.4.1 Immersion of 1000 nm spaced features in concentrated citrate-stabilised gold nanoparticles (C-Au-NPs) (step 3..cont)

It was believed that the lack of nanoparticle attachment was a function of slower kinetics of adsorption due to the less efficient reduction of NO_2 to NH_2 in the feature regions. Therefore, a concentrated (~4x) solution of Au-NPs (C-Au-NPs) was used to immerse the type C and D features. After immersion in the C-Au-NP solution, attachment of nanoparticles had occurred within both the type C and D exposed features. In order to analyse the different adsorption kinetics of the two nanoparticle solutions, two SAMs of 4-aminothiophenol (4-ATP) was formed on planar Au surfaces and the deposition of each nanoparticle solution over 2 hrs was examined by AFM (figure 2.14).

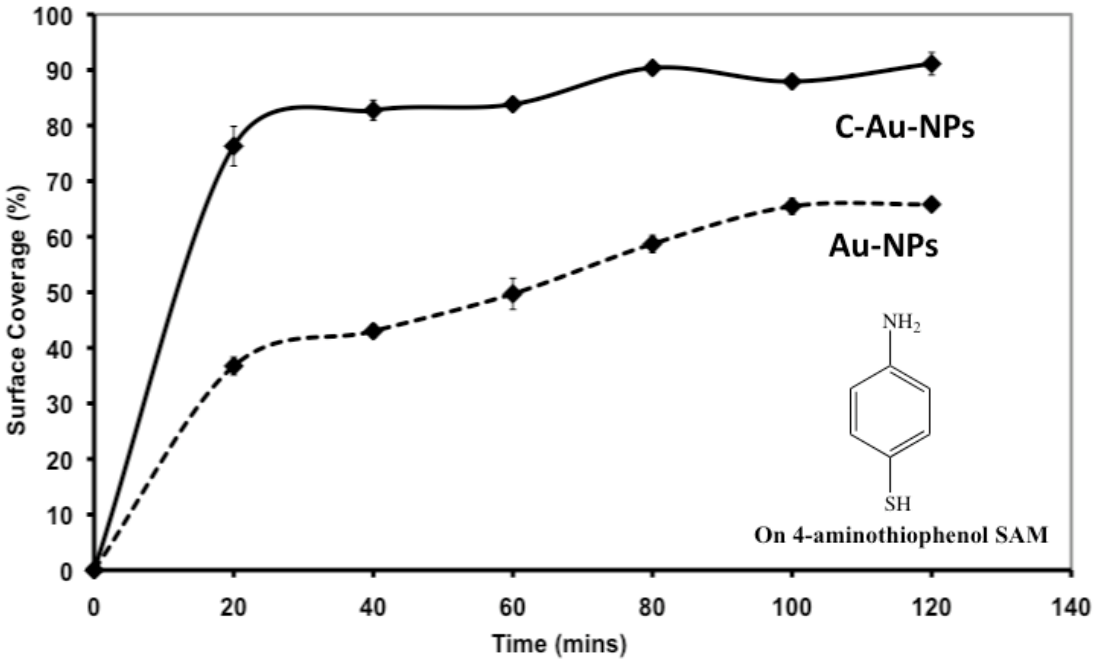

Figure 2.14. Surface coverage analysis from AFM images of Au-NPs and C-Au-NPs deposited on a 4-ATP SAM.

The resultant nanoparticle deposition graph showed that there was indeed a difference between the deposition behaviour of the two nanoparticle solutions with the C-Au-NP solution appearing to move towards its maximum surface coverage more rapidly and eventually giving a higher surface coverage than the Au-NP solution. The linewidths of the type C and D linear features after immersion in C-Au-NPs were then examined with AFM and the results presented in (figure 2.15).

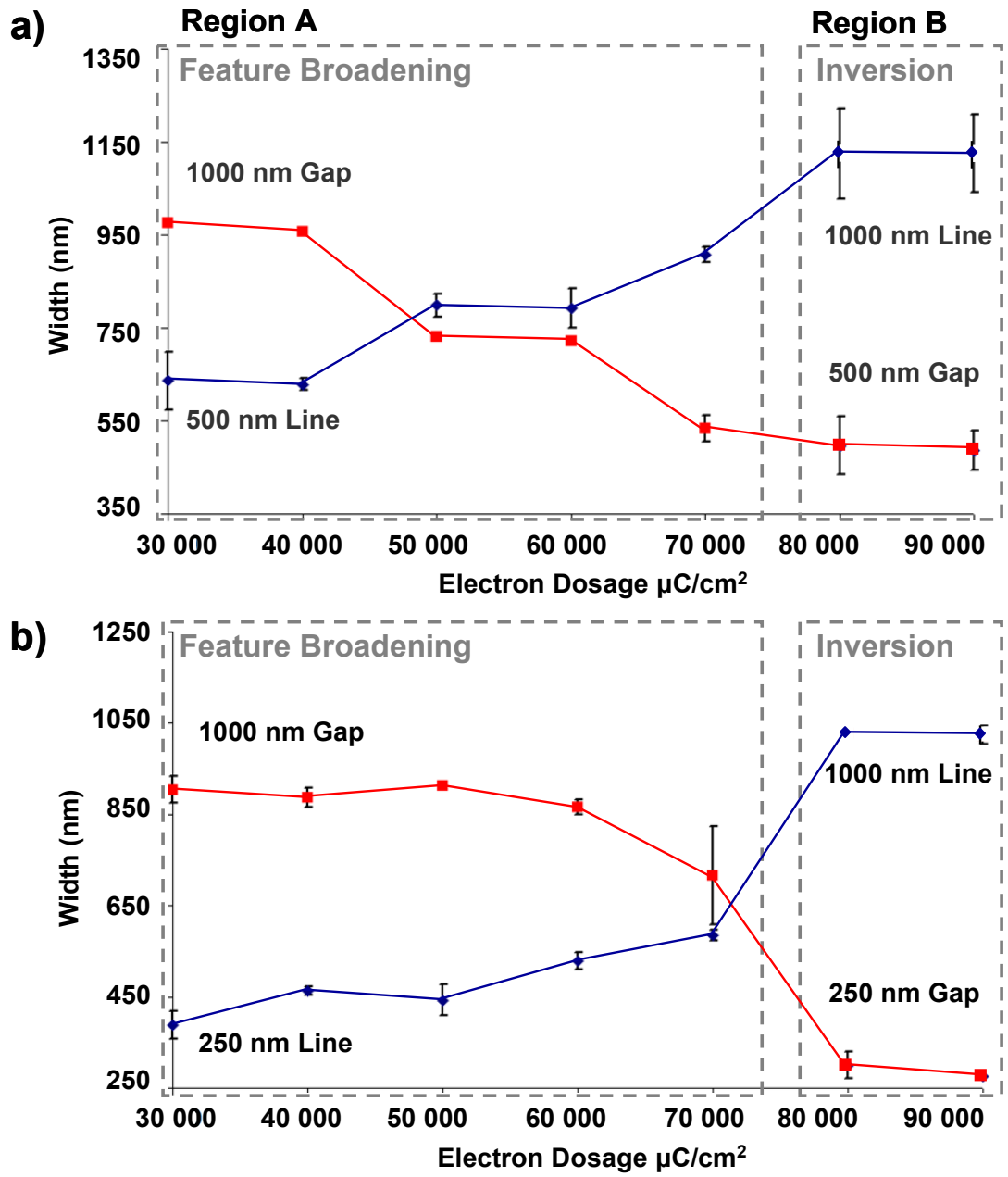

Figure 2.15. Graphs showing the 'actual' width of; **a)** 500 nm lines (**type C**); and **b)** 250 nm lines (**type D**) of C-Au-NPs with 1000 nm gap, measured by AFM, plotted against electron dosage of underlying SAM. Region A shows feature broadening with electron dose, while region B shows pattern inversion.

The tapping mode AFM images, showed that, as before, the features sizes varied from the intended feature sizes, with increasing feature broadening as a function of increasing electron dosage (figure 2.15, Region A). The 500 nm features (type C), were seen to broaden with increased electron dose, to a point where at 50 000 μC/cm^2 and above the features become wider than the inter-feature gaps. The 250 nm features were also seen to broaden with increasing electron dose, however, as they are initially smaller than the 500 nm features, they do not broaden significantly enough to become larger than the inter-feature gap. For both feature types, there was also increased non-specific absorption of the nanoparticles in the gaps between features, which also increased with electron dose (figure 2.16 and *inset*).

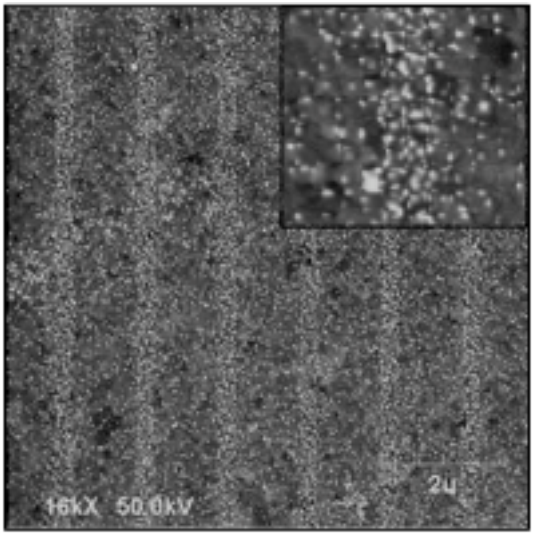

Figure 2.16. SEM image of 250 nm wide C-Au-NP lines exposed at 45 000 μC/cm^2 (**type D**), *inset*, magnified region of 250 nm wide feature showing non-specific adsorption either side of the feature.

It is hypothesised that this non-specific absorption may be due to physisorption effects and previously unseen proximity effects from the EBL exposure, exaggerated by the increase in nanoparticle concentration.

2.3.5 Pattern inversion at high electron doses (step 4)

For the type C and D features at doses of 80 000 μC/cm^2 and above it was seen that pattern inversion behaviour occurred after substrate immersion in the C-Au-NP solution. No attachment of C-Au-NPs was seen in the planned EBL exposed areas, but a high degree of attachment was seen in the intervening gaps (figure 2.17).

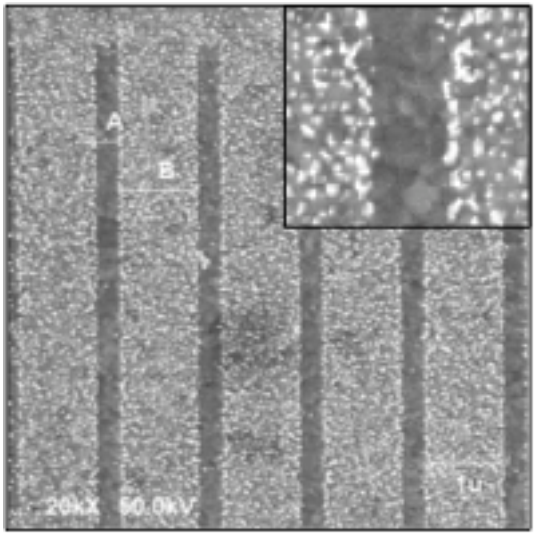

Figure 2.17. SEM image of inverted type D features exposed at 90 000 μC/cm^2, with no attachment of C-Au-NPs in regions of the primary electron dose of the SAM but attachment in the inter-feature gaps, *inset*, magnified region showing 250 nm wide feature free of C-Au-NPs (**step 4**).

This inversion behaviour is believed to be attributable to the larger overall dose of electrons causing damage to the SAM structure, with NO_2 to NH_2 conversion occuring in the gaps between features (figure 2.16 *inset*).[73] This behaviour agrees with the hypothesis that at increasing electron doses, there is an interplay between, causing the chemical conversion to afford nanoparticle attachment, feature broadening and degradation of the SAM structure.

AFM adhesion force mapping was carried out on the inverted pattern regions after immersion in C-Au-NPs and revealed contrast between the areas with and without the presence of C-Au-NPs (figure 2.18). The areas where C-Au-NPs were present, showed average adhesive forces of 38 nN.

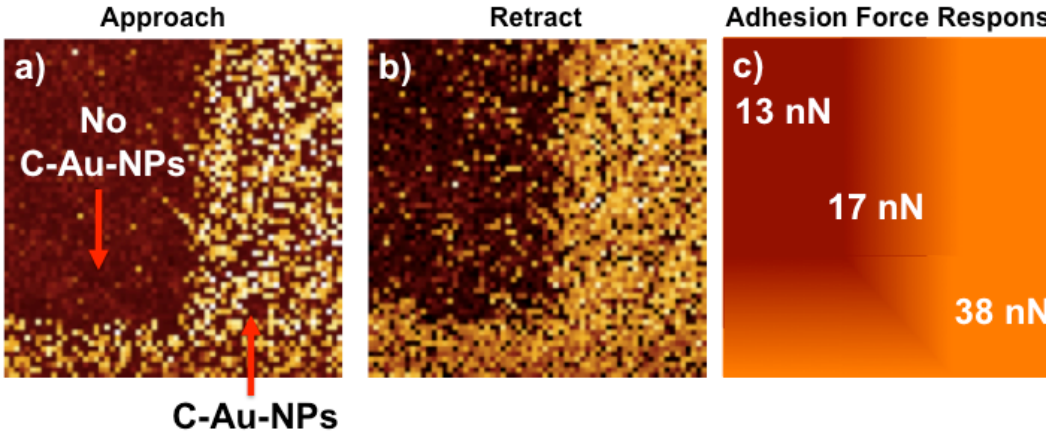

Figure 2.18. a,b & c) AFM adhesion force maps of inverted pattern regions after immersion in C-Au-NPs (**step 4**).

This adhesive force value was slightly higher than seen previously for COO- – terminated SAMs (~30 nN),[75] however, as the COO- layer here was present on the surface of nanoparticles with inter-particle gaps revealing the underlying SAM, this achieved value can be assumed to be realistic. In the areas where no C-Au-NPs are present, the adhesive force was seen to be of an average value of 13 nN (compared to 340 nN in the exposed region in figure 2.9). This low value indicates a low adhesive interaction between the AFM and surface and fits the hypothesis that the SAM on the Au surface in this region has been either damaged or removed.

AFM tapping mode imaging also confirmed the pattern inversion behaviour seen with SEM, with feature sizes becoming less broadened by scattering effects (figure 2.15, Region B), yet inverted in attachment of nanoparticles. This increase in feature resolution for inverted patterns could be a key step in overcoming the loss in resolution that is inherent in EBL due to scattering effects, allowing for more well-

defined nanostructures to be created by deposition of a secondary species within the gaps between nanoparticle tracks or on top of the nanoparticle tracks. However, such a fabrication method is reliant upon forming nested features and hence may not be practical for single, isolated features.

Overall, the feature broadening and feature inversion behaviour seen is believed to be a function of the electron dose used for patterning and believed to fit the model in figure 2.19).

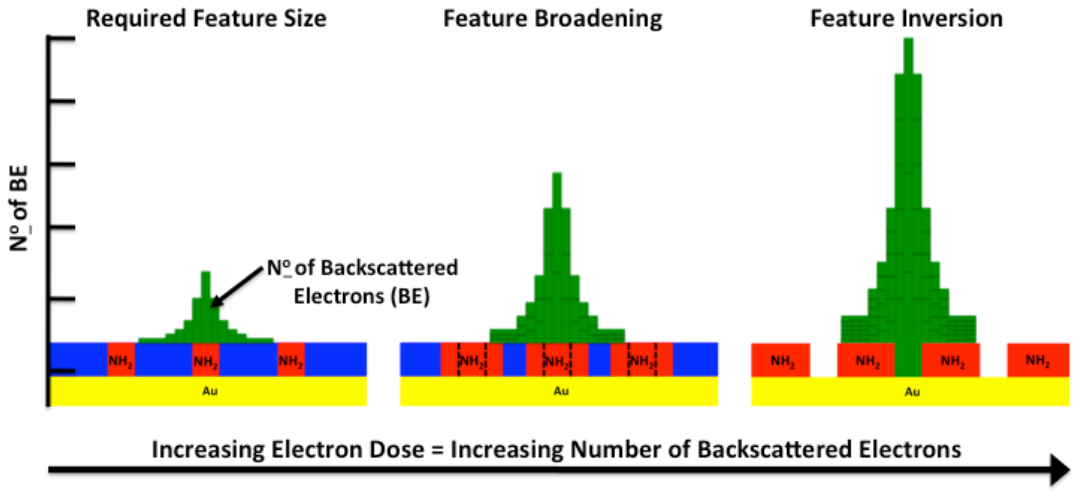

Figure 2.19. Diagram depicting the electron dose related behaviour of NPHT SAMs.

At lower electron doses, the actual features achieved have dimensions closest to the planned feature size. Only SAM regions with a number of backscattered electrons high enough to initiate the conversion process become converted to NH_2 groups. As the electron dose is increased, the number of backscattered electrons increases, meaning that regions further away from the primary dose site have enough backscattered electrons to cause the conversion process. As the electron dose is increased further still, the number of electrons at the primary dose site becomes great

enough to cause damage to the SAM and the gaps between the feature site then have the required amount of backscattered electrons for the conversion process.

2.4 Conclusions

This chapter has presented a fully repeatable characterisation of the electron dosages required to carry out spatially selective modification of NO_2 terminated thiol SAMs on gold surfaces. The optimum dosage of electrons was seen to vary for different feature sizes and gaps. If inter-feature distances are too large, then deposition of nanoparticles may not occur, due to incomplete conversion of SAM surface chemistry as the number of backscattered and secondary electron contributions from neighbouring features are reduced. It has also been demonstrated that deposition of colloids on EBL fabricated patterns on SAMs is a highly complicated system with many factors such as electron dose, feature size and gap (proximity effect) and colloid solution itself playing a key roll in the resolution and type of features achievable. The quality and type of fabricated features can be varied by careful choice of electron dose during the EBL stage of the fabrication process, allowing for both positive and negative pattern formation, which can then be related to electron behaviour theory by use of simulation software. Consideration of the type of features required is needed, as the doses required for nested features, will differ to the dose required for isolated features. The use of an EBL modified SAM and attachment of gold colloids can overcome the limitations of pattern transfer processes associated with current resist based systems, by precisely controlling the deposition of nanometer-scale species, which can serve as a template for further nanostructure fabrication.

2.5 Future work

For future developments of this work, it would be ideal to carry out a more rigorous appraisal of the effect of feature size and spacing on the quality of features obtained from this process. Furthermore, exploration of the interaction of the patterned substrates with other nanoscale species would provide greater insight into the architectures that can be achieved with this process.

2.6 Experimental

2.6.1 Materials

The commercially available starting materials and chemicals were purchased from Aldrich chemicals and used as received. Solvents were purchased from Aldrich (anhydrous EtOH).

2.6.2 Preparation of the gold substrates

Gold substrates were prepared using an Auto 306 vacuum evaporation chamber (Edwards) in a two pump system, the pressure was reduced to ~10^{-4} bar followed by a subsequent reduction to ~10^{-7} bar on the glass microscope slides. Prior to the evaporation of gold onto the glass slides, a Cr layer (6 nm) was evaporated onto the glass slides by heating Cr pieces (Agar Scientific, 99.99 % purity) of ~ 5 mm^3 volume by electrical resistance using a voltage of 30 V and a current of 3 A, to promote adhesion of the gold to the base material. Au was deposited in a similar manner. An Au wire (Advent Research Materials, 99.99+ % purity) of 0.5 mm diameter, which was placed into a Mo boat (Agar Scientific) was heated. The Au wire was heated by electrical resistance using a voltage of 10 V and a current of 3 A until ~ 100 nm of Au had been deposited onto the desired surface within the auto 306 vacuum evaporation chamber. Deposition rate were monitored using a quartz crystal

microbalance (QCM) thickness monitor. A deposition rate between 0.05- 0.1nm s^{-1} was used for both Cr and Au layers. The Au substrates were cut to 1 x 1 cm^2 using a diamond tipped scriber.

2.6.3 Preparation of the SAMs

Prior to the preparation of the SAMs, the glassware and the Au substrates were cleaned thoroughly to remove contaminants. Initially, the glassware was immersed in piranha solution (conc. H_2SO_4:30 % H_2O_2 = 7:3) for 60 mins followed by extensive rinsing with Ultra High Pure (UHP) H_2O (Resistivity = 18 MΩ.cm). The subsequent steps were followed: 30 min sonication in UHP H_2O, dried in oven at 120 °C for 30 min, allowed to cool to room temperature, 30 min sonication in EtOH, dried in oven at 120 °C for 30 min and wrapped in aluminium foil before use to prevent exposure to airborne contaminates and used within 24 h. The gold substrates were immersed in piranha solution at room temperature for 10 min with occasional stirring. Followed by thorough rinsing with UHP H_2O, then with EtOH (HPLC grade) and immediately immersed in a 1 mM solution of NPHT in EtOH (HPLC) for 24 hours. Finally, the SAMs were rinsed thoroughly with EtOH (HPLC grade) and dried with a stream of N_2.

2.6.4 SAM characterisation

2.6.4.1 Ellipsometry

The thicknesses of the deposited monolayers were determined by spectroscopic ellipsometry. A Jobin-Yvon UVISEL ellipsometer with a Xenon light source was used for the measurements. The angle of incidence was fixed at 70^o. A wavelength range of 280-820 nm was used. The DeltaPsi software was employed to determine the thickness values and the calculations were based on a three-phase

ambient/SAM/Au model, in which the SAM was assumed to be isotropic and assigned a refractive index of 1.50. The thicknesses reported are the average of six measurements taken on each SAM.

2.6.4.2 Water contact angle

Contact angles were determined by the sessile drop method using a home built contact angle apparatus, equipped with a charged coupled device (CCD) camera that is attached to a personal computer for video capture. The advancing (θ_a) and receding (θ_r) contact angles were measured as liquid was added quasi-statically or removed from the drop by a micro syringe. The drop is shown as a live video image on the PC screen and digitally recorded. The acquisition rate was 4 frames per second. Stored images of the droplets were analysed with software from FTÅ. Contact angles were determined from an average of five different measurements on each sample.

2.6.4.3 X-ray photoelectron spectroscopy (XPS)

Elemental composition of the SAMs were analysed using an Escalab 250 system (Thermo VG Scientific) operating with Avantage v1.85 software under pressure of ~ 5 x 10^{-9} mbar. An Al K_α X-ray source was used, which provided a monochromatic X-ray beam with incident energy of 1486.68 eV and a circular spot size of ~0.2 mm^2 was employed. The samples were attached onto a stainless steel holder using double-sided carbon adhesive tape (Shintron tape). In order to minimise charge retention on the sample, the samples were clipped onto the holder using stainless steel or Cu clips. The clips provided a link between the sample and the sample holder for electrons to flow, which the glass substrate inhibits.

Low resolution survey spectra were obtained using a pass energy of 150 eV over a binding energy range of -10 eV to 1200 eV obtained using 1 eV increments. The spectra recorded were an average of 3 scans. The high resolution spectra were obtained using a pass energy of 20 eV and 0.1 eV increments over a binding energy range of 20-30 eV, centred on the binding energy of the electron environment being studied. A dwell time of 20 ms was employed between each binding energy increment.

2.6.4.4 Atomic force microscopy (AFM)

AFM topography imaging was carried out using a Dimension D3100 AFM (Digital Instruments, Santa Barbara, CA) in tapping mode using etched silicon probes. Force mapping measurements were carried out in contact mode (NanoWizard II, JPK Instruments, Berlin, Germany). Spring constants for force measurements were estimated by determination of the deflection sensitivity of the cantilever used.

2.6.5 Synthesis of citrate stabilised gold nanoparticles (Au-NPs)

Citrate-stabilised gold nanoparticles (Au-NPs) were synthesised *via* the Frens method.[76] Briefly, an aqueous solution of $HAuCl_4.3H_2O$ (9.9 mg, 100 mL) was heated under reflux for 5-10 mins. An aqueous solution of sodium citrate (22.8 mg, 2 mL) was added. Heating under reflux was continued for a further 10 mins to ensure complete reduction of the gold salt. The red colloidal solution was centrifuged three times for 10 min (3500 rpm) and the supernatant collected. Adjustment of the colloid pH to 4.5 was carried out using HCL (0.06 M) HCl.

2.6.6 Synthesis of concentrated citrate stabilised gold nanoparticles (C-Au-NPs)

A concentrated solution of citrate-stabilised gold nanoparticles (C-Au-NPs) was also synthesised *via* the Frens method.[76] An aqueous solution of $HAuCl_4.3H_2O$ (40 mg, 49mL) was heated under reflux for 5-10 mins. An aqueous solution of sodium citrate (80 mg, 1 mL) was added. Heating under reflux was continued for a further 5 mins to ensure complete reduction of the gold salt. The colloidal solution was left to cool while stirring for 1 hour. Finally, the dark red solution was centrifuged three times for 10 min (3500 rpm) and the supernatant collected. Adjustment of the colloid pH to 4.5 was carried out using HCL (0.06 M).

2.6.7 Pattern fabrication

2.6.7.1 Electron beam lithography (EBL)

EBL was carried out using a dedicated Electron Beam Lithography Instrument (Crestec CABL-9500C High Resolution Electron Beam Lithography System – ISOM, Madrid). The beam voltage was kept constant at 50 keV with a current of 5 nA. The beam current was checked before and after lithographic processing using a Faraday cup. Beam diameter was kept constant at 10 nm and samples were secured to the sample stage with conductive tape to ground the samples.

2.6.8 Attachment of Au-NPs and C-Au-NPs

After electron beam exposure, substrates were immersed in an aqueous solution of citrate stabilised gold nanoparticles (5 ml) for 2 hours at pH 4.5. After immersion, substrates were rinsed with UHP H_2O, and dried under a stream of nitrogen. Samples were subsequently examined using SEM and AFM.

2.7 References

1) **Microsystem Technology**, *Volume 20*, Menz, W., Mohr, J. and Paul, O., **2001**, Wiley-VCH.

2) Smith, H. I. and Flanders, D. C., **X-ray Lithography - A Review and Assessment of Future Applications**, *J. Vac. Sci. Technol.* **1998**, *17*, 533-535.

3) S. Wegscheider, S., Kirsch, A., Mlynek, J. and Krausch, G., **Scanning Near-field Optical Lithography**, *Thin Solid Films*, **1995**, *264*, 264-67.

4) ***Nanochemistry, A Chemical Approach to Nanotechnology***, Ozin, G. A. and Arsenault, A. C., **2005**, RSC Publishing.

5) Iqbal, P., Sun, S., Hanwell, M. D., Attwood, D., Leggett, G. J., Preece, J. A., Richardson, T. H. and Tunnicliffe, D., **Photochemical Fabrication of Three-Dimensional Micro- and Nano-structured Surfaces from a C60 Monoadduct**, *J. Mater. Chem.*, **2008**, *18,* 2016-2021.

6) Sun, S., Mendes, P., Critchley, K., Diegoli, S., Hanwell, M., Evans, S. D., Leggett, G. J., Preece, J. A. and Richardson, T. H., **Fabrication of Gold Micro- and Nanostructures by Photolithographic Exposure of Thiol-Stabilized Gold Nanoparticles**, *Nanolett.*, **2006**, *6*, 345-350.

7) La, Y.-H., Jung, Y.J., Kim, H.J., Kang, T.-H., Ihm, K., Kim, K.-J., Kim, B. and Park, J.W., **Sub-100-nm Pattern Formation through Selective Chemical Transformation of Self-Assembled Monolayers by Soft X-ray Irradiation**, *Langmuir*, **2003**, *19*, 4390-4395.

8) Schmelmer, U., Jordan, R., Geyer, W., Eck, W., Gölzhäuser, A., Grunze, M. and Ulman, A., **Surface-Initiated Polymerization on Self-Assembled Monolayers: Amplification of Patterns on the Micrometer and Nanometer Scale**, *Angew. Chem. Int. Ed.*, **2003**, *42*, 559-563.

9) Mendes, P. M. and Preece, J. A., **Precision Chemical Engineering: Integrating Nanolithography and Nanoassembly**, *Curr. Op. Coll. Surf. Sci.*, **2004**, *9*, 236-248.

10) Love, J. C., Estroff, L. A., Kriebel, J. K., Nuzzo, R. G. and Whitesides, G. M., **Thiolates on Metals as a Form of Nanotechnology**, *Chem. Rev.*, 2005, **105**, 1103-1170.

11) deSmet, L. C. P. M., Zuilhof, H., Sudholter, E. J. R., Lie, L. H., Houlton, A. and Horrocks, B. R., **Mechanism of the Hydrosilylation Reaction of Alkenes at Porous Silicon: Experimental and Computational Deuterium Labeling Studies**, *J. Phys. Chem. B*, **2005**, 109, 12020-12031.

12) Laibinis, P. E. and Whitesides, G. M., **Self-assembled Monolayers of n-Alkanethiolates on Copper are Barrier Films that Protect the Metal Against Oxidation by Air**, *J. Am. Chem. Soc.*, 1992, **114**, 9022-9028.

13) La, Y. H., Kim, H. J., Maeng, I. S., Jung, Y. J., Park, J. W., Kang, T. H., Kim, K. J. Ihm, K. and Kim, B., **Differential Reactivity of Nitro-substituted Monolayers to Electron Beam and X-ray Irradiation**, *Langmuir*, **2002**, *18*, 301-303.

14) Brandow, S. L., Chen, M. S., Aggarwal, R., Dulcey, C. S., Calvert, J. M. and Dressick, W. J., **Fabrication of Patterned Amine Reactivity Templates Using 4-chloromethylphenylsiloxane Self-assembled Monolayer Films**, *Langmuir*, **1999**, *15*, 5429-5432.

15) Dressick, W. J., Dulcey, C. S., Brandow, S. L., Witschi, H. and Neeley, P. F., **Proximity X-Ray Lithography of Siloxane and Polymer Films Containing Benzyl Chloride Functional Groups**, *J. Vac. Sci. Technol. A.*, **1999**, *4*, 1432-1440.

16) Dyer. D. J., **Patterning of Gold Substrates by Surface-Initiated Polymerization**, *Adv. Funct. Mater.,* **2003**, ***13***, 667.

17) Diegoli, S., Hamlett, C. A. E., Leigh, S. J., Mendes, P. M. and Preece, J. A., **Engineering Nanostructures at Surfaces**, *Proc. Inst. Mech. Eng. Part G J. Aerosp. Eng.,* **2007**, *221*, 589-629.

18) Gibbons, F. P., Robinson, A. P. G., Palmer, R. E., Diegoli, S., Manickam, M. and Preece, J. A., **Fullerene Resist Materials for the 32nm Node and Beyond,** *Adv. Funct. Mater.*, **2008**, *18*, 1977-1982.

19) Gibbons, F. P., Robinson, A. P. G., Palmer, R. E., Manickam, M. and Preece, J. A., **Ultrathin Fullerene films as High-resolution Molecular Resists for Low-voltage Electron-beam Lithography**, *Small*, **2006**, *2*, 1003-1006.

20) Zailer, I., Frost, J. E. F., Chabasseur-Molyneuz, V., Ford, C. J. B. and Pepper, M., **Crosslinked PMMA as a High-resolution Negative Resist for Electron Beam Lithography and Applications for Physics of Low-dimensional Structures,** *Semicond. Sci. Technol.*, **1996**, 11, 1235-1238.

21) **Handbook of Microlithography, Micromachining and Microlithography**, Rai-Choudhury, P., **1997**, SPIE Press.

22) Groves, T. R., Pickard, D. Rafferty, B. Crosland, N. Adam D. and Schubert, G., **Maskless Electron Beam Lithography: Prospects, Progress, and Challenges**, *Microelectronic Engineering*, **2002**, *61-62*, 285-293.

23) Crommie, M. F., Lutz, C. P. and Eiger, M., **Confinement of Electrons to Quantum Corrals on a Metal Surface**, *Science*, **1993**, *262*, 218-220.

24) Sato, M., Ocala, L. E., Novembre, A. E., Ohmori, K., Ishikawa, K., Katsumata, K. and Nakayama, T., **Characteristics for Negative and Positive Tone Resists with Direct Write Electron Beam and SCALPEL Exposure Systems**, *J. Vac. Sci. Technol. B.*, **1999**, *17*, 2873-2877.

25) Novembre, A. E., Ocola, L. E., Houlihan, F., Knurek, C. and Blakey, M., **New Developments in Resist Materials for the SCALPEL Technology**, *J. Photopolym. Sci. Technol.*, **1998**, *11*, 541-545.

26) Lercel, M. J, Whelan, C. S., Craighead, H. G., Seshadri, K. and Allara, D. L., **High-resolution Silicon Patterning with Self-assembled Monolayer Resists**, *J. Vac. Sci. Tech. B.*, **1996**, *14*, 4085-4090.

27) Gentili, M., Lucchesini, A., Scopa, L., Lugli, P., Paoletti, A., Messina, G., Santangelo, S. and Tucciarone., A., **Modeling of Electron Beam Scattering in High Resolution Lithography for the Fabrication of X-Ray Masks**, European Transactions on Telecommunications, **1990**, *1*, 143-147.

28) Chang, T. H. P., **Proximity Effect in Electron-Beam Lithography**, *J. Vac. Sci. Technol.*, **1975**, *12*, 1271-1275.

29) Sternglass, E. J., **Backscattering of Kilovolt Electrons from Solids**, *Phys. Rev.*, **1954**, *95*, 345-358.

30) Dapor, M., **Monte Carlo Computations of the Electron Backscattering Coefficient for Bulk Targets and Surface Thin Films**, *Surf. Inter. Anal.,* **2008**, *40*, 714-717.

31) Fitting, H-J., Glaefeke, H., Wild, W. and Neumann., **Multiple Scattering of Fast Electrons and their Secondary Electron Generation Within Semi-Infinite Targets**, *J. Phys. D: Apply. Phys.,* **1976**, *9*, 2499-2510.

32) Sidorkin, V., van Run, A., van Langen-Suurling, A., Grigorescu, A. and van der Drift, E., **Towards 2–10 nm Electron-beam Lithography: A Quantitative Approach,** *Microelec. Eng.,* **2008**, *85*, 805-809.

33) Lee, S –Y. and Anbumony, K., **Analysis of Three-dimensional Proximity Effect in Electron-beam Lithography**, *Microelec. Eng.,* **2006**, *83*, 336-344.

34) **Introduction to Microfabrication**, Franssila, S., **2004**, Wiley.

35) Feldheim, D. L. and Keating, C. D., **Self-assembly of Single Electron Transistors and Related Devices**, *Chem. Soc. Rev.*, **1998**, *27*, 1-12.

36) Sato, T., Hasko, D. G. and Ahmed, H., **Nanoscale Colloidal Particles: Monolayer Organization and Patterning**, *J. Vac. Sci. Tech. B.*, **1997**, *15*, 45-48.

37) McConnell, W. P., Novak, J. P. Brousseau, L. C., Fuierer, R. R., Tenent, R. C. and Feldheim, D. L., **Electronic and Optical Properties of Chemically Modified Metal Nanoparticles and Molecular Bridged Nanoparticle Arrays**, *J. Phys. Chem. B*, **2000**, *104*, 8925-8930.

38) Liu, T., Tang, J., Zhao, H., Deng, Y. and Jiang, L., **Particle Size Effect of the DNA Sensor Amplified with Gold Nanoparticles**, *Langmuir*, **2002**, *18*, 5624-5626.

39) Li, H., Luk, Y. Y. and Mrksich, M., **Catalytic Asymmetric Dihydroxylation by Gold Colloids Functionalized with Self-Assembled Monolayers**, *Langmuir*, **1999**, *15*, 4957-4959.

40) Harriot, L. H., **Limits of Lithography**, *Proc. IEE.*, **2001**, *89*, 366-374

41) Ulman, A., **Formation and Structure of Self-Assembled Monolayers**, *Chem. Rev.*, **1996**, *96*, 1533-1554

42) Gölzhäuser, A., Eck, W., Geyer, W., Stadler, V., Weimann, T., Hinze, P. and Grunze, M., **Chemical Nanolithography with Electron Beams**, *Adv. Mater.*, **2001**, *13*, 806-809.

43) Mendes, P. M., Jacke, S., Critchley, K., Plaza, J., Chen, Y., Nikitin, K., Palmer, R. E., Preece, J. A., Evans, S. D. and Fitzmaurice, D., **Gold Nanoparticle Patterning of Silicon Wafers using Chemical E-beam Lithography**, *Langmuir*, **2004**, *20*, 3766-3768.

44) Mendes, P., Belloni, M., Ashworth, M., Hardy, C., Nikitin, K., Fitzmaurice, D., Critchley, K., Evans, S. and Preece, J., **A Novel Example of X-ray-Radiation-induced Chemical Reduction of an Aromatic Nitro-group-Containing Thin Film on SiO_2 to an Aromatic Amine Film**, *ChemPhysChem*, **2003**, *4*, 884-889.

45) Eck, W., Stadler, V., Geyer, W., Zharnikov, M., Gölzhäuser, A. and Grunze, M., **Generation of Surface Amino Groups on Aromatic Self-Assembled Monolayers by Low Energy Electron Beams - A First Step Towards Chemical Lithography,** *Adv. Mater.*, **2000**, *12*, 805-808.

46) **Physics and Chemistry of Interfaces**, Butt, H. J., Graf, K. and Kappi, M., **2003**, Wiley.

47) Rowntree, P., Dugal, P. C., Hunting, D. and Sanche, L., **Electron Stimulated Desorption of H-4 from Chemisorbed Molecular Monolayers**, *J. Phys. Chem.*, **1996**, *100*, 4546-4550.

48) Harnett, C. K., Satyalakshmi, K. M., and Craighead, H. G., **Bioactive Templates Fabricated by Low-energy Electron Beam Lithography of Self-assembled Monolayers**, *Langmuir*, **2001**, *17*, 178-182.

49) Lercel, M. J., Craighead, H. G., Parikh, A. N., Seshadri, K. and Allara, D. L., **Sub-10nm Lithography with Self-assembled Monolayers**, *Appl. Phys. Lett.*, **1996**, *68*, 1504-1506.

50) Zharnikov, M., Geyer, W., Golzhauser, A., Frey, S., and Grunze, M. **Modification of Alkanethiolate Monolayers on Au-substrate by Low Energy Electron Irradiation: Alkyl Chains and the S/Au Interface**, *PCCP*, **1999**, *1*, 3163–3171.

51) Zharnikov, M., Frey, S., Rong, H., Yang, Y. J., Heister, K., Buck, M., and Grunze, M. **The Effect of Sulfur-metal Bonding on the Structure of Self-assembled Monolayers**, *PCCP*, **2000**, *2*, 3359-3362.

52) Harnett, C. K., Satyalakshmi, K. M., and Craighead, H. G., **Bioactive Templates Fabricated by Low-energy Electron Beam Lithography of Self-assembled Monolayers**, *Langmuir*, **2001**, *17*, 178-182.

53) Rieke, P. C., Baer, D. R., Fryxell, G. E., Engelhard, M. H., and Porter, M. S., **Beam Damage of Self-assembled Monolayers**, *J. Vac. Sci. Technol. A, Vac. Surf. Films*, **1993**, *11*, 2292-2297.

54) Frey, S., Heister, K., Zharnikov, M., and Grunze, M, **Modification of Semifluorinated Alkanethiolate Monolayers by Low Energy Electron Irradiation**, *PCCP*, **2000**, *2*, 1979-1987.

55) Hutt, D. A. and Leggett, G. J., **Static Secondary Ion Mass Spectrometry Studies of Self-assembled Monolayers: Electron Beam Degradation of Alkanethiols on gold**, *J. Mater. Chem.*, **1999**, *9*, 923-928.

56) Muller, H. U., Zharnikov, M., Volkel, B., Schertel, A., Harder, P., and Grunze, M., **Low-energy Electroninduced Damage in Hexadecanethiolate Monolayers,** *J. Phys. Chem. B*, **1998**, 102, 7949-7959.

57) **Micromanufacturing and Nanotechnology: Fundamentals, Techniques, Platforms, and Experiments**, Mahalik, N. P., **2006**, Springer.

58) Biebricher, A., Paul, A., Tinnefeld, P., Gölzhäuser, A. and Sauer, M., **Controlled Three-dimensional Immobilization of Biomolecules on Chemically Patterned Surfaces**, *J. Biotech*., **2004**, *112*, 97-107.

59) Geyer, W., Stadler, V., Eck, W., Zharnikov, M., Gölzhäuser, A. and Grunze, M., **Electron Induced Crosslinking of Aromatic Self-assembled monolayers: Negative Resists for Nanolithography**, *Appl. Phys. Lett.*, **1999**, *75*, 2401-2403.

60) Iqbal, P., Critchley, K., Attwood, D., Tunnicliffe, D., Evans, S. D. and Preece, J. A., **Chemical Manipulation by X-rays of Functionalized Thiolate Self-Assembled Monolayers on Au**, *Langmuir*, **2008**, *24*, 13969-13976.

61) Seah, M. P., **Slow Electron Scattering from Metals: I. The Emission of True Secondary Electrons**, *Surf. Sci.,* **1969**, *17*, 132-160.

62) Lercel, M. J., Craighead, H. G., Parikh, A. N., Seshadri, K. and Allara, D. L., **Sub-10nm Lithography with Self-assembled Monolayers**, *Appl. Phys. Lett*., **1996**, *68*, 1504-1506.

63) Küller, A., Eck, W., Stadler, V., Geyer, W and Golzhauser, A, **Nanostructuring of silicon by electron beam lithography of self-assembled hydroxybiphenyl monolayers**, *Appl. Phys. Lett,* **2003**, *82*, 3776-3778.

64) Diegoli, S., Mendes, P. M., Baguley, E. R., Leigh, S. J., Iqbal, P., Garcia Diaz, Y. R., Begum, S., Critchley, K., Hammond, G. D., Evans, S. D., Attwood, D., Jones, I. P. and Preece, J. A., **pH-Dependent Gold Nanoparticle Self-Organization on Functionalized Si/SiO_2 Surfaces**, *J. Exp. Nano. Sci.*, **2006**, *1*, 333-353.

65) Kang, J. F., Ulman, A., Liao, S., Jordan, R., Yang, G. and Liu, G. Y., **Self-Assembled Rigid Monolayers of 4 '-Substituted-4- mercaptobiphenyls on Gold and Silver Surfaces**, *Langmuir*, **2001**, *17*, 95-106.

66) **Handbook of X-ray Photoelectron Spectroscopy**, Moulder, J. F., Stickle, W. F., Sobol, P. E. and Bomben, K., **1992**, Perkin-Elmer Corporation.

67) **An Introduction to Surface Analysis by XPS and AES**, Watts, J. F. and Wolstenholme, J., **2003**, Wiley.

68) Robinson, A. P. G., Zaid, H. M., Gibbons, F. P., Palmer, R. E., Manickam, M., Preece, J. A., Brainard, R., Zampini, T. and O'Connell, K., **Chemically Amplified Molecular Resists for Electron Beam Lithography**, *Microelectron. Eng.*, **2006**, *83*, 1115-1118.

69) Murata, K. and Kyser, D. F., **Monte Carlo Methods and Microlithography Simulation for Electron and X-ray Beams**, *Adv. Electron. Electron Phys.*, **1987**, *69*, 175-259.

70) Aizaki, N., **Proximity Effect Dependence on Substrate Material**, *J. Vac. Sci. Tech.*, **1979**, ***16***, 1726-1733.

71) **Handbook of Molecular Force Spectroscopy**, A. Noy, **2008**, Springer.

72) Hafizovic, S., Barrettino, D., Volden, T., Sedivy, J., Kirstein, K., Brand, O. and Hierlemann, A., **Single-chip mechatronic microsystem for surface imaging and force response studies,** *PNAS*, **2004**, 101, 17011-17015.

73) Chang, T. H. P., **Proximity Effect in Electron-beam Lithography**, *J. Vac. Sci. Tech.*, **1975**, *12*, 1271-1275.

74) Ivin, V. V., Silakov, M. V., Kozlov, D. S., Nordquist, K. J., Lu, B. and Resnick, D. J., **The Inclusion of Secondary Electrons and Bremsstrahlung X-rays in an Electron Beam Resist Model**, *Microelectron. Eng.*, **2002**, *61-62*, 343-349.

75) **Scanning Probe and Other Novel Microscopies of Local Phenomena in Nanostructured Materials**, Kalinin, S.V. Goldberg, B. Eng, L. M. and Huey, B. D., MRS Proceedings 838E, **2005**, p.O15.5.

76) Frens, G., **Controlled Nucleation for the Regulation of the Particle size in Monodisperse Gold Solution**, *Nat. Phys. Sci.*, **1973**, *241*, 20-22.

Chapter 3

From the Foundations Upwards:

Layer-by-layer Deposition of Bicomposite Polyelectrolyte/Nanoparticle Films

Abstract

With ever more effective methods for 2D surface patterning being developed, the development of techniques to build upon these patterned foundations in a bottom-up fashion to form truly 3D nanostructures is becoming increasingly more important. This chapter details the deposition of bicomposite polyelectrolyte/nanoparticle films in a layer-by-layer (sequential) fashion, leading to films of controllable composition. Film build-up is followed by multiple characterisation techniques and the results achieved from each technique are compared. The formation of layer-by-layer films is then interfaced with surface patterning techniques in order to explore the combination of top-down and bottom-up processes for structuring surfaces.

3.1 Introduction

In nature, function arises from the close spatial arrangement of molecular and supramolecular components, an arrangement of enzymes and co-enzymes, for instance, can be responsible for a series of consecutive transformations.[1] One of the most interesting properties evolving from the intricate interplay of thousands of subcellular components on the length scale of about one micron is life itself.[2] Life is such a complex process requiring so many components that they cannot be fitted into a compartment much smaller than a cell. In materials science most of today's "workhorses" are single- or two-component systems.[3] However, scientists are already

working on the design of smart materials that require much higher complexity.[4] It is of interest to bring together as many different materials as needed in order to create materials with new properties. This approach is similar to attempting to synthesize molecules possessing multiple functional groups, which may eventually become impractical if the number of functions required gets too high or the molecule gets too large. Layer-by-layer (LBL) self-assembly may be an alternative way to create multimaterial composites *(multicomposites)* in a simple fashion.

3.1.2 Layer-by-layer (LBL) deposition

LBL deposition describes the formation of multi-material assemblies on surfaces which are created by several consecutive adsorption steps. To do this assembly, one needs components that interact with each other, for example, electrostatically. If you have one molecule immobilised on the surface, this will attract a complementary partner molecule from the solution to the surface which can be repeated in a consecutive fashion, such that a multiple material film forms, (e.g ABABABAB) (scheme 3.1). Successful LBL assembly using electrostatic attraction relies upon each successive layer completely compensating for the charge of the previous layer and having an exposed surface charge to attract a further complementary layer.[2]

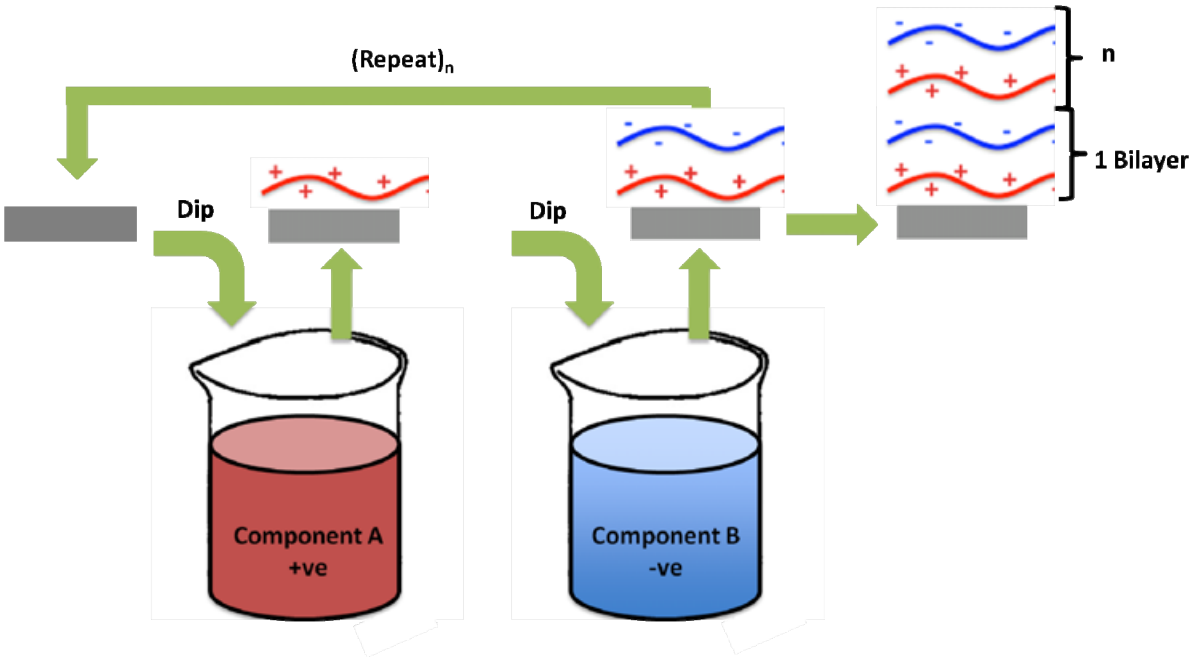

Scheme 3.1. Scheme showing the way in which LBL films are sequentially built-up.

At first, LBL deposition development began with exploiting electrostatic interactions, with materials such as charged polymers *(polyelectrolytes, chapter 1)*,[5] but there are other intermolecular interactions that can be used. *Decher et al.*[6] was one of the first groups to understand the possibilities of LBL fabrication and the *Science* paper entitled "***Fuzzy nanoassemblies: toward layered polymeric multicomposites"*** *(cited over 3,700 times as of September 2009)* demonstrated the use of polyelectrolytes to form multicomposite films. Since this *Science* paper, many more researchers have investigated the possibilities that this simple and versatile fabrication method holds. Researchers have also begun to exploit chemical reactions to form LBL films on surfaces rather than limiting fabrication to electrostatic interactions.[7] Typical materials that have been used by various researchers for making multilayer composites include polyelectrolytes,[8] DNA,[9] proteins,[10] and colloids.[11] Different materials can be utilised in this fashion to tailor the material and architecture to the required functionality.[12]

Another technique for depositing the materials on to a surface as an alternative to dipping, is spraying with an atomiser/airbrush gun.[13] The literature contains many examples of characterization of LBL polyelectrolyte film build-up using techniques such as ellipsometry[14] and contact angle.[15] The incorporation of nanoparticles into LBL films allows the build-up process to be followed more easily due to the larger size and optical properties of nanoparticles.[16] The resultant LBL films have shown many potential functionalities.[17-19]

3.1.3 Surface patterning of LBL films

The ability to pattern LBL films on surfaces, allows for further architectures derived from LBL films to be created. Surface patterning with LBL deposition can be approached in many ways. Mirkin *et al.*[20] utilised DPN to transfer polyelectrolytes to surfaces in patterns (figure 3.1).

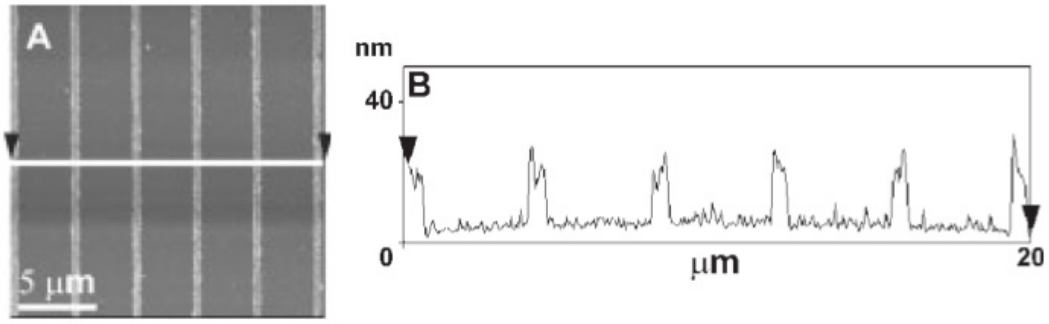

Figure 3.1. a) Topographical AFM image of PEM line arrays with (PDDA/ PSS)$_3$PAH layers and **b)** its corresponding height profile.[20]

Jiang *et al*.[21] presented the technique of polymer-on-polymer stamping, where patterning of polyelectrolyte multilayers was carried out using flexible PDMS stamps, similar to the technique of microcontact printing. Two further approaches to this patterning are either **(i)** forming the LBL films on photolithographically patterned

substrates, then removing the underlying resist, or **(ii)** building the LBL films on chemically patterned surfaces. The literature has many examples of both techniques.[22-25]

3.1.4 Gold nanoparticles

Gold nanoparticles possess interesting optical properties.[26] They exhibit a characteristic plasmon adsorption at approximately 500-550 nm (figure 3.2).

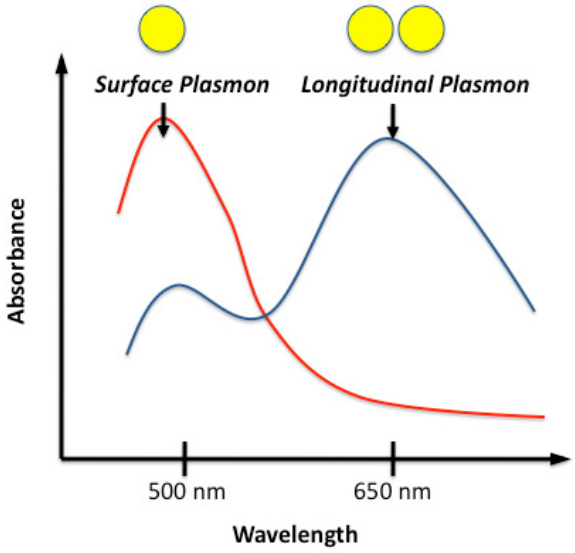

Figure 3.2. Figure demonstrating the optical properties of gold nanoparticles.

The position and size of this plasmon resonance is highly dependent on the size and shape of the gold nanoparticles,[27] and the local medium they are dispersed in. When two nanoparticles are brought into close proximity a second plasmon band (known as the longitudinal plasmon band) becomes apparent at 600-700 nm, arising from the coupling of two neighbouring plasmon resonances.[28] The same effect can also be seen when non-spherical nanoparticles are synthesised.[29]

3.1.5 Microfluidics

Microfluidics research deals with the behaviour, precise control and manipulation of fluids that are typically geometrically constrained to small-scale (typically sub-millimeter) vessels and transport networks on surfaces.[30] Advances in microfluidics technology have been of great benefit to areas such as molecular biology for enzymatic analysis (*e.g.* glucose and lactate assays),[31] DNA analysis (*e.g.* polymerase chain reaction and high-throughput sequencing),[32] and proteomics.[33] The basic idea of microfluidic biochips is to integrate assay operations such as detection, sample pre-treatment and sample preparation on a single chip. The ability to accurately manipulate such small volumes of liquid on surfaces allows for the accurate delivery of material to specific locations while minimising the material needed during the process. Microfluidic devices have been fabricated in many ways; a picture of a simple micro-mixer microfluidic device is presented in figure 3.3. Commonly, the required pattern of microfluidic channels, reservoirs and analysis chambers are first fabricated in a glass substrate with a combination of lithography and precision powder blasting.[34] The glass substrate is then bonded at either high temperature or pressure to a substrate of choice (commonly silicon or glass wafers). The final stage is fitting the required ports to the microfluidic channels to interface the device with the required system of pumps or syringes. Other microfluidic devices have been fabricated using stereolithography[35] and pre-tensioned polystyrene sheets.[36]

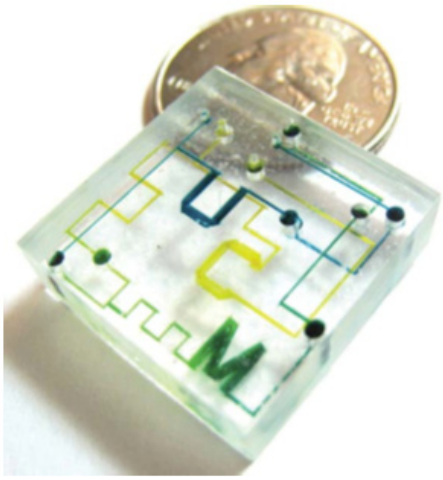

Figure 3.3. Photo of a simple microfluidic mixer device made from polystyrene.[36]

3.2 Aims & objectives

Patterned/structured templates such as those formed with electron beam lithography in chapter 2 are inherently pseudo 2D structures. In order to convert these templates into true 3D structures in a bottom-up fashion, methods are required to add further materials to these templates, building upwards from the surface. Thus, the aims of this work are two-fold.

Firstly to investigate the sequential deposition of a cationic polyelectrolyte (PDAC) (**scheme 3.2, step 1**) and anionic citrate stabilised gold nanoparticles (Au-NPs) (**step 2**) to glass and silicon surfaces as a method for carrying out the bottom-up assembly of materials on surfaces. Further layers will be deposited in the same way (**steps 3 & 4**) and the whole process followed with several methods and the results from each method compared and contrasted.

Secondly, the application of this sequential PDAC/Au-NP deposition system with patterned surfaces will be investigated using two methodologies:

i) Resist photolithography to block portions of the surface during deposition (**scheme 3.3, steps 5-9**) followed by removal of the remaining photoresist to leave a PDAC/Au-NP pattern (**step 10**)

ii) Thiol-stabilised gold nanoparticle (T-Au-NP) patterning photolithography to form patterned gold templates (**scheme 3.4, steps 11-14**) which are then sealed in a microfluific device (**step 15**) and derivatised with a NH_2 terminated SAM (step 15) for PDAC/Au-NP deposition (**steps 16 & 17**) via microfluidics.

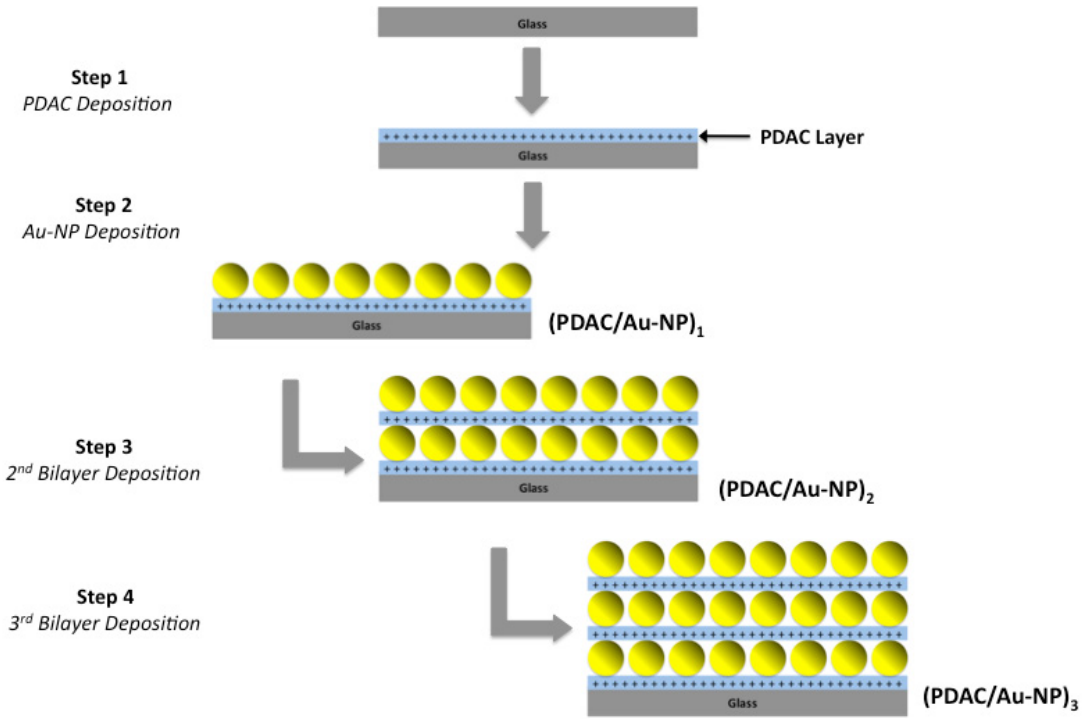

Scheme 3.2. Experimental scheme for sequential PDAC/Au-NP deposition process.

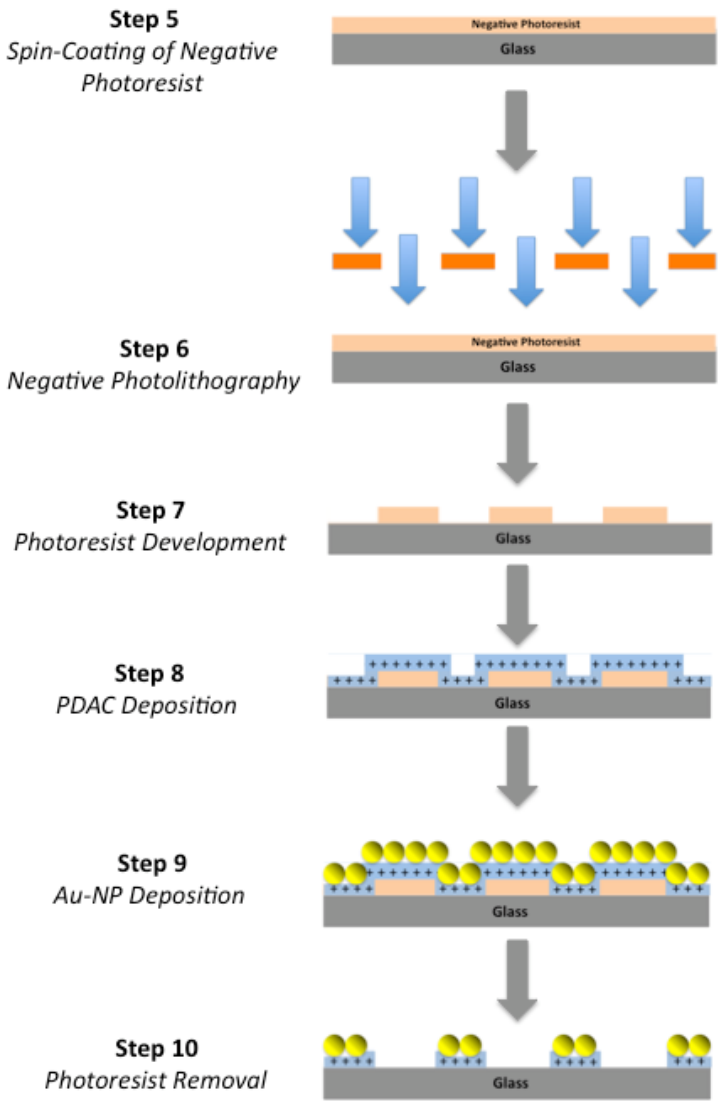

Scheme 3.3. Experimental scheme for sequential PDAC/Au-NP deposition process after photolithographic pre-patterning of underlying substrate.

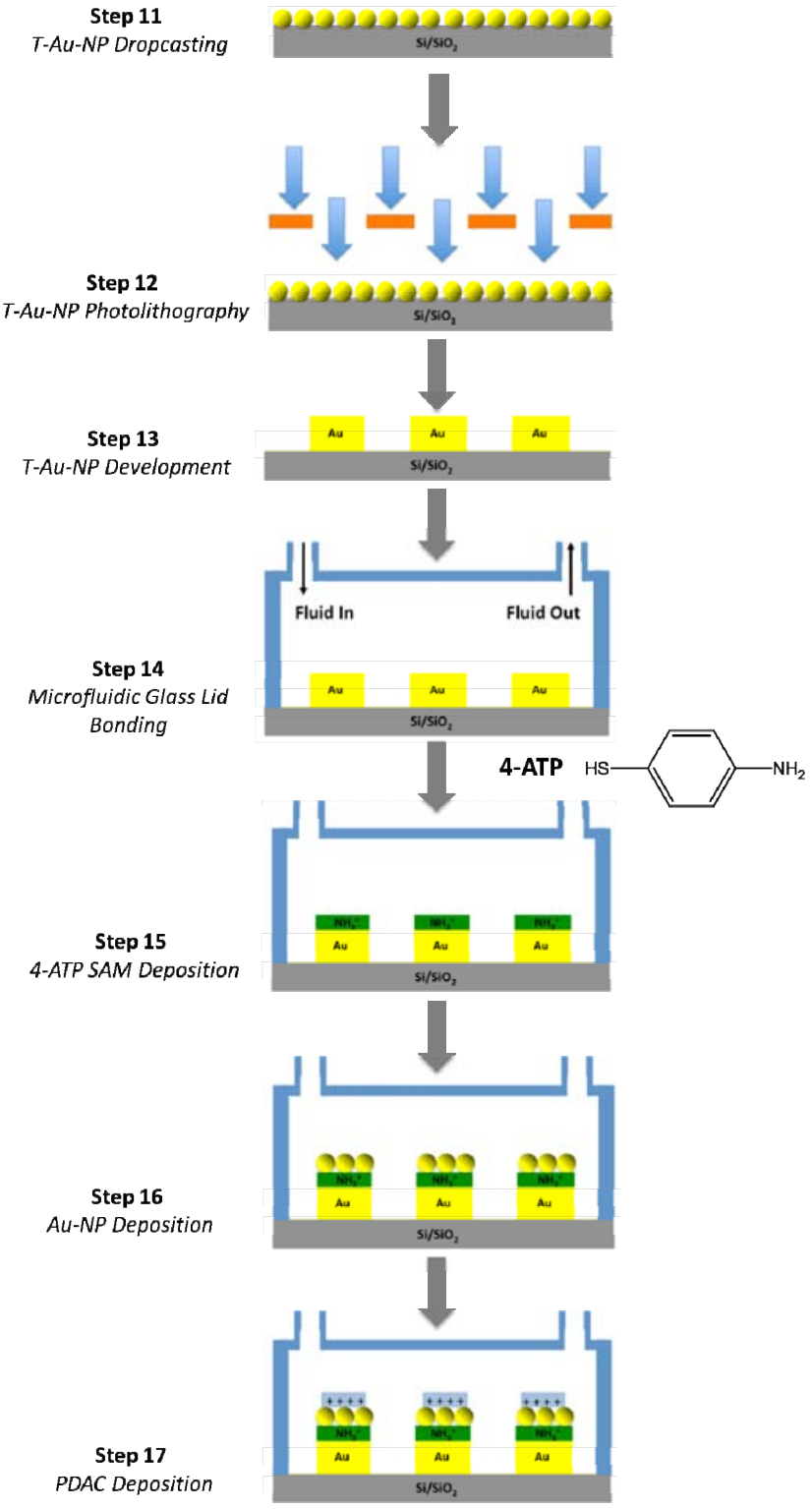

Scheme 3.4. Experimental scheme for sequential PDAC/Au-NP deposition process via microfluidics after T-Au-NP surface patterning & derivatisation with NH_2 terminated thiol SAM.

3.3 Results and Discussion

3.3.1 Formation kinetics of PDAC films on silicon surfaces (step 1)

The surface chemistry of silicon and glass surfaces (SiO_2) means that the positively charged polyelectrolyte, PDAC (scheme 3.5) will adsorb to these surfaces, forming a positively charged polymeric layer.[37]

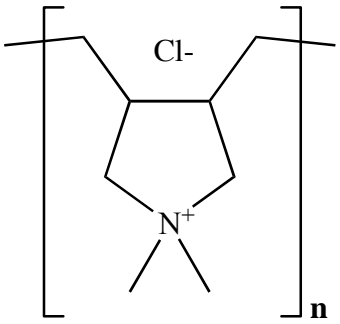

Scheme 3.5. Chemical structure of PDAC, n=100-200 kDa.

In order to evaluate the adsorption kinetics (**step 1**) of PDAC to these surfaces, the process of *in-situ*, liquid ellipsometry[38] was employed in combination with a silicon surface. This ellipsometric technique relies upon changing the ambient phase of the measurement to a liquid of known refractive index and measuring the thickness of any film formed at the surface of the substrate in the presence of this liquid phase. This type of ellipsometry measurement was chosen for two reasons:

i) firstly to get an *in-situ* value for the PDAC deposition process rather than a value after removal of substrates from solution and drying, and

ii) secondly, so as to allow for programming of the ellipsometer within the software options to automate the data acquisition over the experiment timeframe.

To carry out the measurement, a solution cell for the ellipsometer was fabricated (figure 3.4). The cell was made from standard glass microscope slides with quartz glass end-windows for the ellipsometer beam to pass through. Through the experiment, the cell was covered with another glass slide to avoid evaporation.

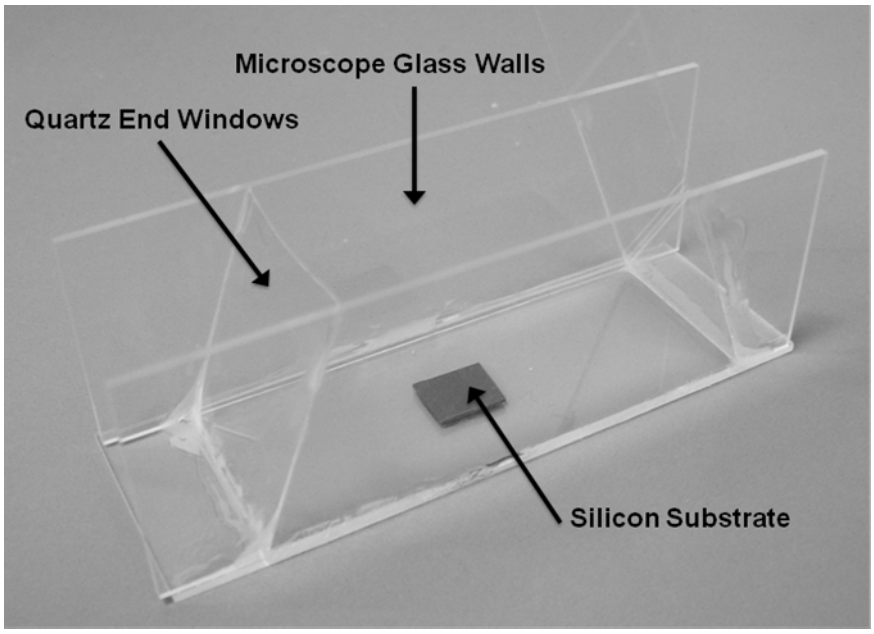

Figure 3.4. Photograph of the solution cell fabricated for the measurement.

The resultant graph of the PDAC layer thickness versus time is presented in figure 3.5. The refractive index of the PDAC is 1.375[39] in comparison to the water refractive index of 1.3. The data set obtained from the ellipsometry measurements was fitted against a constant refractive index of 1.375 as the PDAC was in a high concentration in the deposition solution (20 mM wrt to the polymer repeat unit, n), meaning that small changes concentration would not significantly alter the refractive index. From the adsorption graph, it can be seen that an optimum layer thickness (approximately 0.43 nm) can be achieved from a substrate immersion time of 20 minutes. This thickness value agrees with the literature observation that PDAC adsorbs to silicon wafer surfaces.[40] Below 10 minutes (figure 3.5, region A), the initial stages of PDAC deposition can be seen. Between 10 and 25 minutes (figure 3.5, region B), there appears to be period of layer stabilisation. After 25 minutes, the apparent thicknesses appears to vary quite considerably (figure 3.5 region C) which may be an effect of surface rearrangement of the PDAC,[41] or a charge screening

process.[42] Several repeats of the experiment gave similar data and the immersion time of 20 minutes was therefore used for all subsequent experiments.

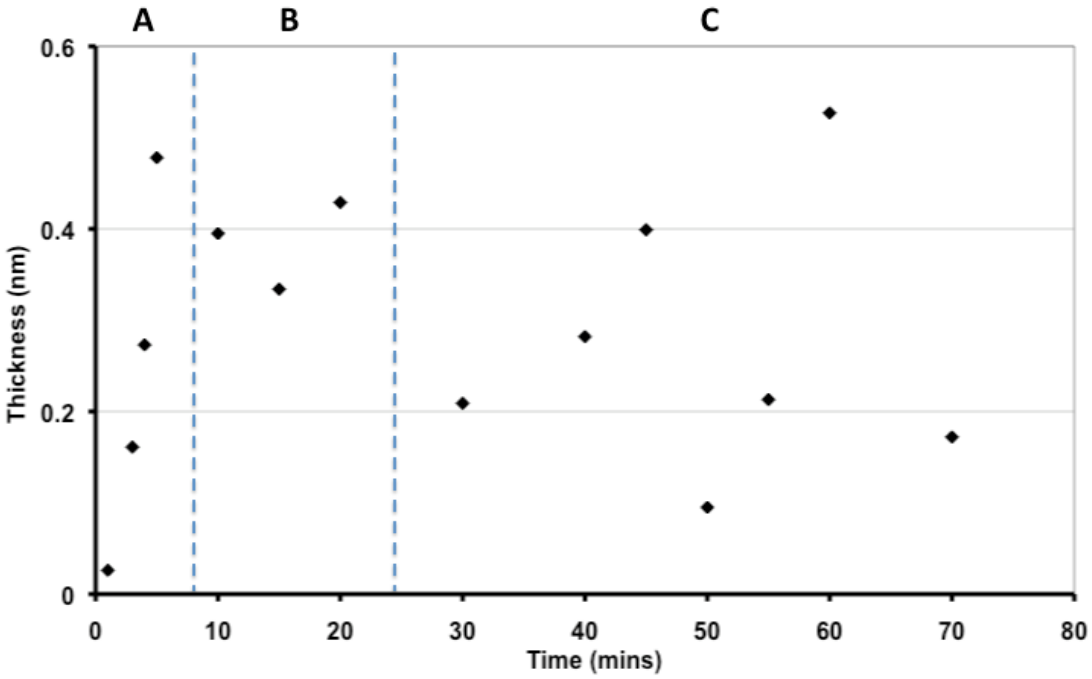

Figure 3.5. Time vs thickness data for deposition of PDAC on silicon surface examined with *in-situ* spectroscopic ellipsometry (**step 1**).

3.3.2 Formation of LBL films of PDAC and Au-NPs (steps 2, 3 & 4)

In-order to further derivatise the PDAC films deposited to glass and silicon surfaces, the cationic charge of the PDAC was used as an attractive element for anionically charged gold colloids (Au-NPs, approx 16 nm diameter). Using a literature reported method for the synthesis of this colloidal solution[43] and a reported immersion time of 2 hrs,[44] PDAC coated substrates were placed in the colloidal solution. After 2 hrs, the substrates were removed and rinsed with water. The deposition of one layer of PDAC and one layer of Au-NPs was termed a bilayer (or $(PDAC/Au\text{-}NP)_1$). The process was repeated for 2 and 3 bilayers, $(PDAC/Au\text{-}NP)_2$ and $(PDAC/Au\text{-}NP)_3$, respectively.

3.3.2.1 Atomic force microscopy imaging

Tapping mode AFM imaging allowed for examination of the number of nanoparticles present after each bilayer depostion (figure 3.6). Samples were imaged at each stage of the LBL build-up process after deposition in PDAC and Au-NPs.

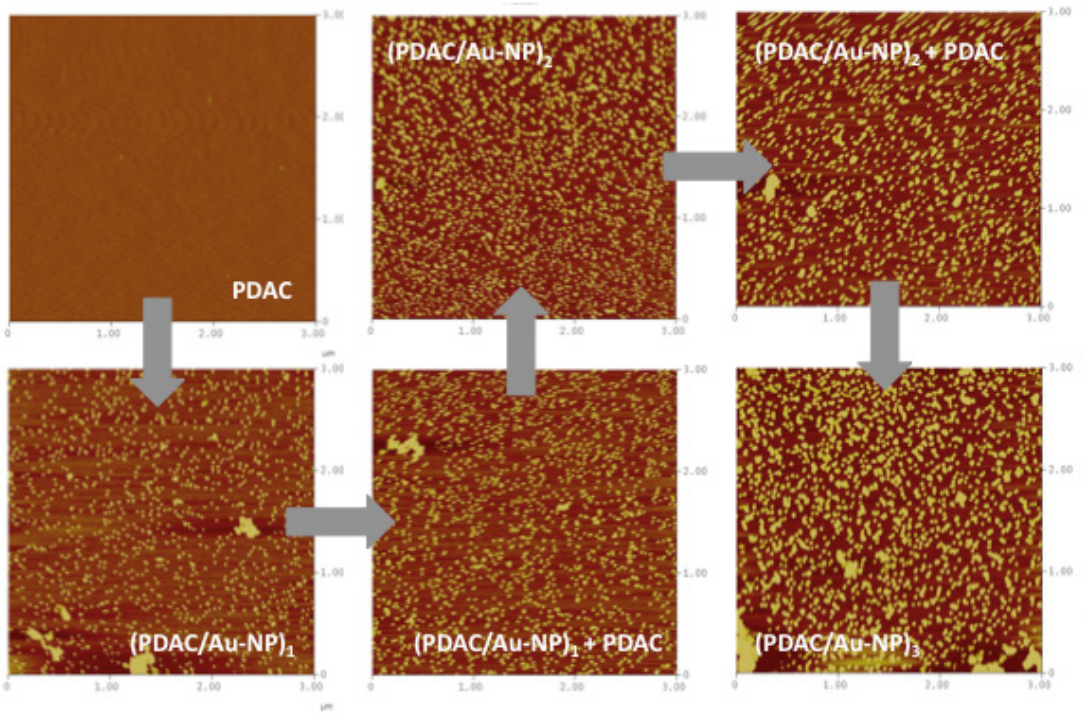

Figure 3.6. AFM tapping mode height images of PDAC/Au-NP sequential deposition on glass.

The tapping mode AFM height images showed an increase in the overall number of nanoparticles present on the substrate surface after each immersion in Au-NPs (figure 3.6). This observation fits with a hypothesis that after each Au-NP deposition step, the nanoparticles are deposited in closer proximity to surrounding nanoparticles (figure 3.7).

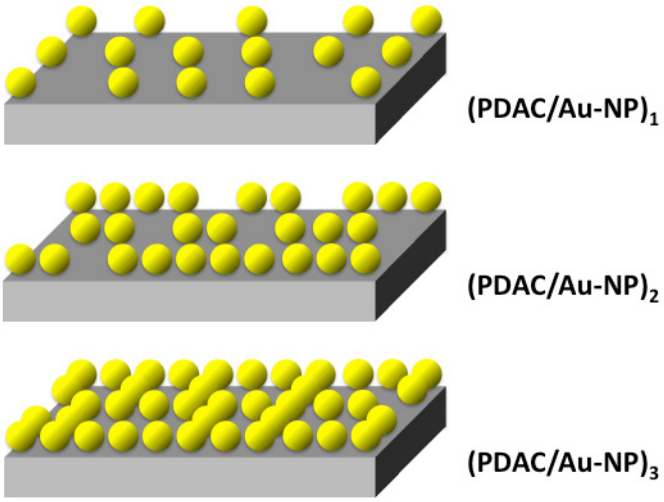

Figure 3.7. Model showing the sequential build-up of Au-NPs on the substrate surface.

After each immersion of a complete bilayer in a further solution of PDAC, the nanoparticles appear to become more aggregated. It was also noted, that rather than forming discrete individual layers of PDAC and Au-NPs, the process apparently led to the formation of a more and more dense layer of Au-NPs with each immersion step. The number of nanoparticles deposited on the surfaces can be counted from the AFM images obtained (figure 3.8).

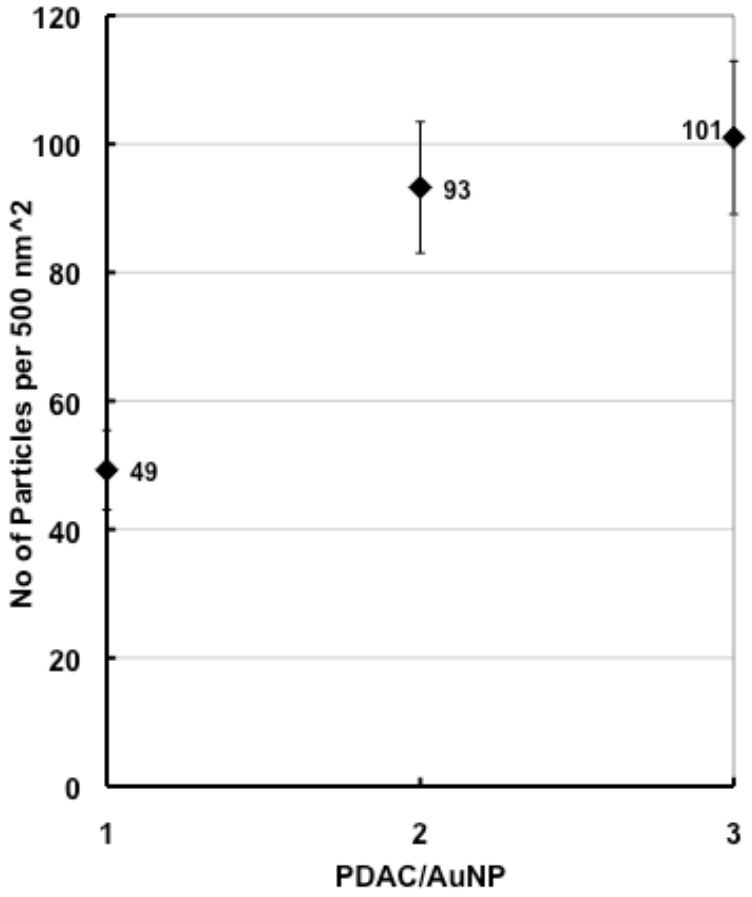

Figure 3.8. Results of a visual count of the number of Au-NPs per 500 nm^2 for each bilayer from AFM images.

3.3.2.2 UV-vis spectrophotometry

The $(PDAC/Au\text{-}NP)_{1\text{-}3}$ bilayer glass substrates were placed in a UV-vis spectrophotometer and their absorbance examined over the range of 200-800 nm (figure 3.9). For the $(PDAC/Au\text{-}NP)_1$ sample, at approximately 520 nm, the characteristic *plasmon resonance* of the Au-NPs could be observed, indicating the attachment of the Au-NPs to the cationically modified glass substrates. Visually, the substrates also exhibited the characteristic red colouration of Au-NPs of 16-20 nm. For the $(PDAC/Au\text{-}NP)_2$ sample, an increase in the magnitude of the peak at 520 nm was observed, as well as the presence of a second peak at 650-750 nm. This second peak is often referred to as the '*longitudinal plasmon resonance*'[45] and is thought to

arise from the coupling of two individual plasmon resonances when two nanoparticles are brought to within a distance three times that of the particle diameter.[46]

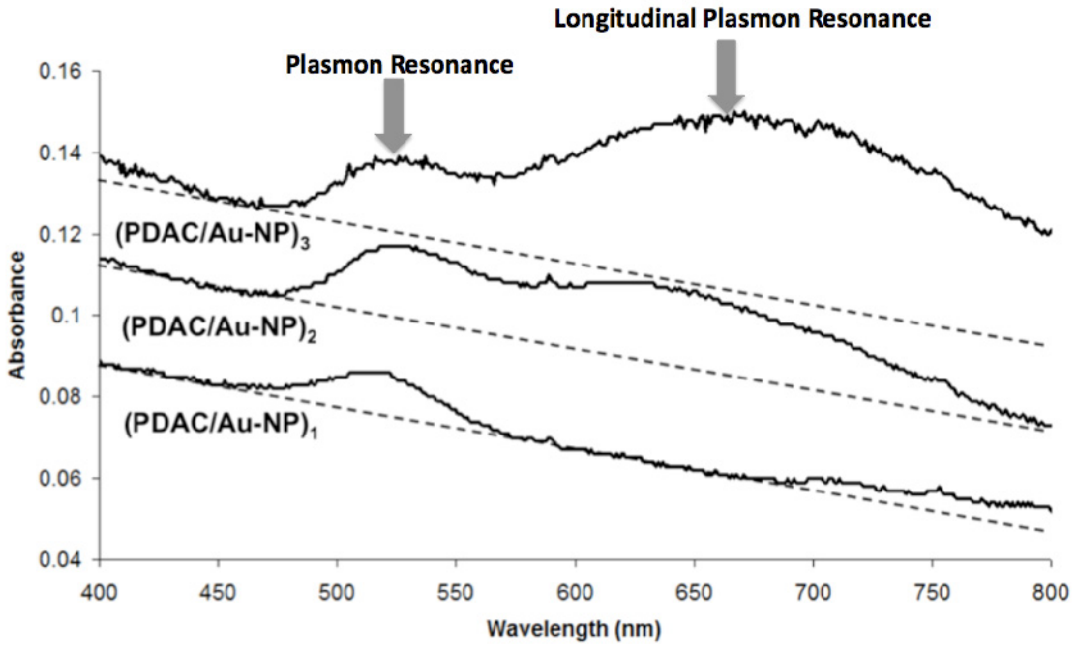

Figure 3.9. UV-vis spectrophotometry graphs for the $(PDAC/Au\text{-}NP)_{1\text{-}3}$ films on glass substrates (**steps 2, 3 & 4 respectively**).

The presence of this longitudinal plasmon peak, therefore, infers that the distance between the particles from the first and second layers is of the order of nm. For $(PDAC/Au\text{-}NP)_3$ a plasmon resonance of roughly equal magnitude to the previous cycle was observed along with a much broader longitudinal plasmon resonance, indicating that more Au-NPs have been deposited to the surface in close proximity to other Au-NPs. UV-vis spectrophotometry can offer qualitative detail on the structure of the deposited films through examination of the adsorption peaks of the Au-NPs present. This data, however, can be examined one-stage further and used to estimate the surface coverage of the substrate with Au-NPs after each bilayer deposition using the Beer-Lambert Law (**equation 3.1**).

$$A = \varepsilon bc \qquad \textbf{equation 3.1}$$

The literature value of the molar absorptivity (**ε**) of the nanoparticles is 2.01 x 10^8 M^{-1} cm^{-1}.[47] If the absorbance (**A**) of the plasmon peak is known and the path length (**b**) is defined as ($2d_n$) (scheme 3.6a) then the concentration (mol dm^{-3}) of the nanoparticles at the surface can be calculated. If we then define a volume of dimensions ($2d_n$) x *w* x *h* (scheme 3.6b) then we can then calculate the number of nanoparticles present in this volume. The glass slide does not contribute anything towards the absorbance of the system so its thickness contribution (t) can be ignored.

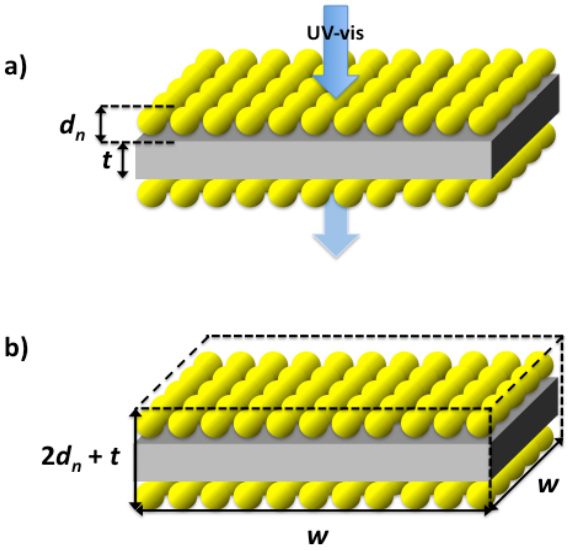

Scheme 3.6. Schematic representation of UV-vis experiment.

The complete calculation to work out the nanoparticle surface coverage can be derived and represented as **equation 3.2**.

$$\frac{\left(\frac{A_{1,2,3}}{\varepsilon(2d_n)}\right)\left(\frac{(2d_n)w}{1000}\right).N_A}{2} = C\_Au-NP_{1,2,3} \qquad \textbf{equation 3.2}$$

Where:

A	Absorbance from UV Graph
N_A	Avagadros Number (6.0221415×10^{23})
ε	Molar Absorptivity ($M^{-1}\,cm^{-1}$) (2.01×10^{8})
d_n	Diameter of Nanoparticle
w	3D Surface Width
C_Au-NP	Nanoparticle Surface Coverage

Using equation 3.2 and the absorbance values from 4 runs of the UV-vis spectrophotometry it is possible to calculate the average Au-NP coverage of the surface over a 500 x 500 nm region on one side of the substrate (figure 3.10). Utilising purely the absorbance at 520 nm for the $(PDAC/Au\text{-}NP)_3$ film gives the surface coverage with nanoparticles to be equal to the $(PDAC/Au\text{-}NP)_2$ substrate (79 Au-NPs per 500 x 500 nm). When the contribution of the longitudinal plasmon is added into the $(PDAC/Au\text{-}NP)_3$ value, then the number of nanoparticles is 172 per 500 nm^2 which shows that the addition of the third bilayer adds only to the longitudinal plasmon.

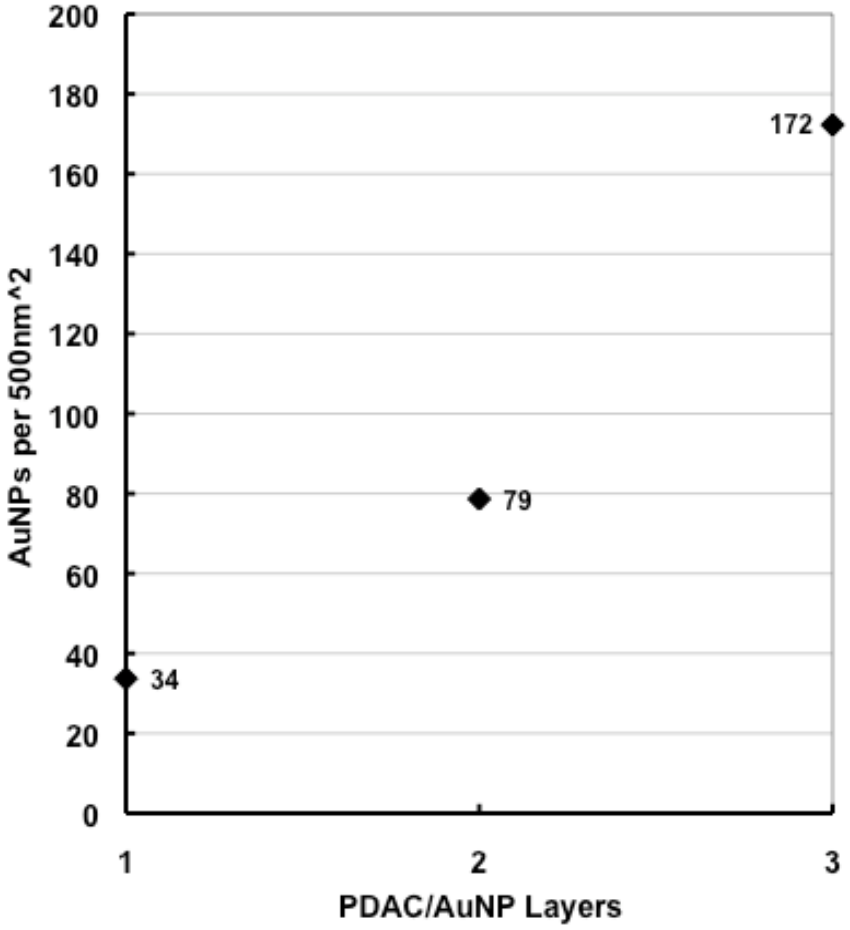

Figure 3.10. Graph showing the average number of nanoparticles per 500 nm^2 calculated from UV-vis results.

The results of the UV-vis spectrophotometry estimation analysis are of a similar magnitude to the values obtained from the visual nanoparticle count from AFM images, and show that estimation of the surface coverage of a surface with UV-vis spectrophotometry can be a useful tool for first point analysis before progressing to a more in-depth analysis technique such as AFM. Moreover, the AFM visual count for the $(PDAC/Au\text{-}NP)_3$ does not show a large difference (greater than error in values) compared to the $(PDAC/Au\text{-}NP)_2$ sample as shown by the UV-vis analysis. The reason for this lack of difference in the values is the difficulty in judging what 'is' and 'is not' a complete nanoparticle when the particles have come together and

aggregated, meaning that some particles would not be counted when visually counting the nanoparticles.

3.3.2.3 AFM cantilever mass adsorption measurements

Direct mass adsorption experiments provide a different paradigm in the measurement of the amount of material deposited on surfaces. By measuring the inherent resonant frequency of a surface before and after material deposition, the amount of material deposited to that surface can be estimated, as a result of the inverse relationship between frequency and mass adsorbed. This technique is the basis for quartz crystal microbalances (QCMs)[48] and many microelectromechanical (MEMs) sensors.[49] When the technique is employed with AFM, rather than using AFM tips to image nanoparticles deposited on glass or silicon surfaces, the tipless silicon nitride cantilevers themselves can be used as substrates on which to deposit both PDAC and Au-NPs, due to their native oxide layer. An AFM is an easy way to determine the resonant frequency of a cantilever as this is the process by which a tapping-mode AFM cantilever is initially tuned before imaging. By measuring the resonant frequency of the cantilever with the *auto-tune* routine of the AFM, both before and after the consecutive immersion in PDAC and Au-NPs, any differences in the resonant frequency can be attributed to deposition of material on the cantilever. This same principle has been utilised in MEMs technology for the formation of gas and mass sensors.[50] The cantilevers used for the experiment were tipless cantilevers supplied by Mikro Masch. At the end of the main chip body, there are 3 cantilevers (figure 3.11), named **A** (width (w) 35 μm, length (l) 110 μm and thickness (t) 1 μm), **B** ((w) 35 μm, (l) 90 μm and (t) 1 μm) and **C** ((w) 35 μm, (l) 130 μm and (t) 1 μm).

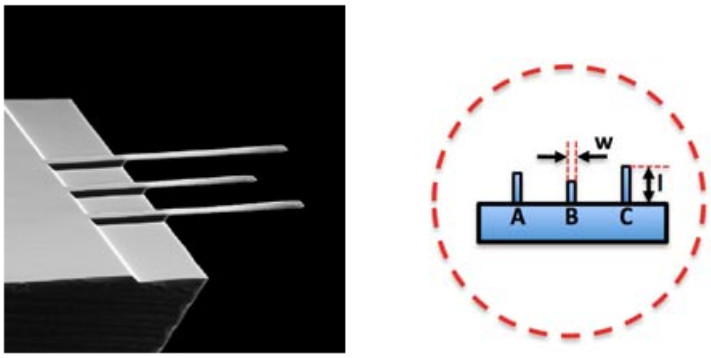

Figure 3.11. SEM image and schematic of the cantilevers used as supplied by the manufacturer.

AFM imaging of the cantilever chips themselves (figure 3.12) revealed that after each stage, more material had been added to the chips confirming that the cantilevers were suitable substrates for mass adsorption experiments.

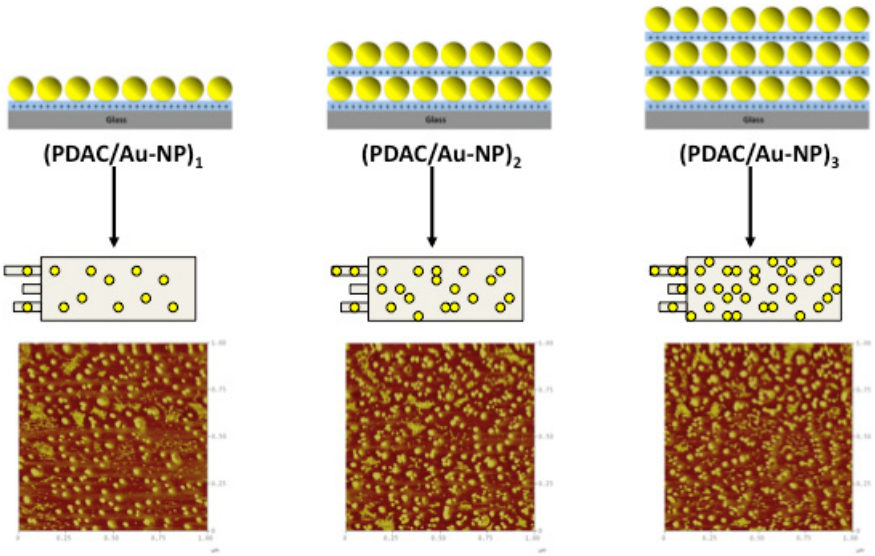

Figure 3.12. Tapping mode images of cantilevers after addition of each PDAC/Au-NP bilayer.

Table 3.1. Data obtained from PDAC/Au-NP mass adsorption experiments.

Cantilever A	**$(PDAC/Au\text{-}NP)_1$**	**$(PDAC/Au\text{-}NP)_2$**	**$(PDAC/Au\text{-}NP)_3$**
AFM tip resonant frequency before material deposition (kHz)	*144*	*128*	*88*
AFM tip resonant frequency after material deposition (kHz)	*134*	*-*[a]	*-*[a]
Resonant frequency difference	***-10***	*-*[a]	*-*[a]
Cantilever B	**$(PDAC/Au\text{-}NP)_1$**	**$(PDAC/Au\text{-}NP)_2$**	**$(PDAC/Au\text{-}NP)_3$**
AFM tip resonant frequency before material deposition (kHz)	*211*	*215*	*200*
AFM tip resonant frequency after material deposition (kHz)	*206*	*205*	*184*
Resonant frequency difference	***-5***	***-10***	***-16***
Cantilever C	**$(PDAC/Au\text{-}NP)_1$**	**$(PDAC/Au\text{-}NP)_2$**	**$(PDAC/Au\text{-}NP)_3$**
AFM tip resonant frequency before material deposition (kHz)	*92*	*92*	*93*
AFM tip resonant frequency after material deposition (kHz)	*89*	*87*	*86*
Resonant frequency difference	***-3***	***-5***	***-7***

[a]*cantilever broke*

Both cantilevers B and C showed a decrease in resonant frequency as expected with addition of material to the cantilever surface. No results were obtained from cantilever A as it broke during the PDAC/Au-NP deposition process and for this reason, only the results from cantilever B and C will be further discussed.

In order to obtain a sensible estimate for the surface coverage of the cantilevers with material from the resonant frequency values obtained, we need to consider deriving an equation for the process carried out. This estimation was carried

out in collaboration with Dr James Bowen (School of Chemical Engineering, University of Birmingham). Equation 3 was derived in an attempt to estimate the surface coverage.[51]

$$C_{Au} = \frac{3}{\pi\ d_{Au}^{3}} \left(\frac{3.84 L^{4} \rho_{Si} \pi^{2} \nu_{before}^{2}}{E_{Si}} \right)^{0.5} \left[\left(\frac{\nu_{after}}{\nu_{before}} \right)^{2} - 1 \right] \left(\frac{\rho_{Si}}{\rho_{Au}} \right)$$

equation 3.3

Where:

$\mathbf{C_{Au}}$	Nanoparticle Surface Coverage
$\mathbf{d_{Au}}$	Nanoparticle Diameter (nm)
L	Cantilever Length (m)
$\mathbf{V_{before}}$	Cantilever Resonant Frequncy Before Deposition (kHz)
$\mathbf{V_{before}}$	Cantilever Resonant Frequncy Before Deposition (kHz)
$\mathbf{E_{Si}}$	Youngs Modulus of Silicon
$\boldsymbol{\rho_{Si}}$	Density of Silicon
$\boldsymbol{\rho_{Au}}$	Density of Gold

The above equation makes the assumption that the particles used are all of a uniform diameter and the surface coverage is uniform across the sample. The values obtained from this estimation process for cantilevers B and C are presented in figure 3.13. There was good agreement between both cantilevers.

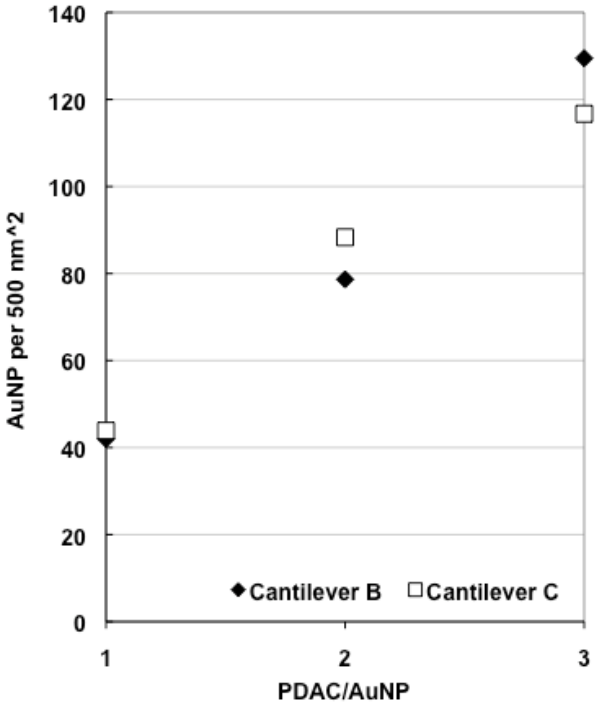

Figure 3.13. Graph showing the number of Au-NPs per 500 nm^2 estimated from mass adsorption experiments.

3.3.3 Comparison of the various methods for following LBL formation

The average values for the number of nanoparticles deposited per 500 nm^2 obtained from UV-vis estimation, direct counting with AFM and AFM cantilever mass adsorption experiments are presented in table 3.2.

Table 3.2. Average values for the number of nanoparticles deposited per 500 nm^2 obtained from UV-vis estimation, direct counting with AFM and AFM cantilever mass adsorption experiments.

Estimation Method	**$(PDAC/Au\text{-}NP)_1$**	**$(PDAC/Au\text{-}NP)_2$**	**$(PDAC/Au\text{-}NP)_3$**
AFM direct count	49	93	101
UV-vis	34	79	172
Mass adsorption	43	83	123

The first thing to note with the values obtained, is how remarkably similar the values obtained appear to be. If we consider the nanoparticle number obtained from the direct count of AFM images be the most accurate number, then the values obtained from the UV-vis estimation and mass adsorption experiments appear to slightly under-estimate the surface coverage value for the 1 and 2 bilayer samples. For the 3 bilayer sample, both methods appear to over-estimate the surface coverage and in the case of the UV-vis estimation, the difference is quite substantial. The reason for this substantial difference is that the estimated value is a summation of the contributions of both the plasmon resonance peak and the longitudinal plasmon resonance peak. By considering just the contribution of the longitudinal plasmon resonance peak for the 3 bilayer sample, this value would be reduced to 93 Au-NPs per 500 nm^2, a number much more similar to the 'real' value from the AFM direct count. Conceptually, this observation should lead to the conclusion that almost all of the nanoparticles added during the third bilayer formation stage are in close enough proximity to other nanoparticles so as to generate a longitudinal plasmon resonance. Overall, two methods (other than direct counting) for estimating the surface coverage of a surface with Au-NPs have been examined and shown to give results very similar to those obtained from a direct count with AFM imaging. Such techniques could prove useful as 'first point of call' techniques where a quick result is required and an imaging technique such as SEM may not be available.

3.3.4 Patterning of PDAC/Au-NP films

The ability to form structured/patterned LBL films is a key step in their exploitation for use in structured surfaces and devices. The two main approaches to this patterning are, **a)** pre-patterning of a surface before LBL deposition with a resist material then deposition over the complete sample, followed by removal of the

remaining resist material (**steps 5-10***)* or **b)** pre-patterning of the sample before LBL deposition then selective deposition to the patterned regions (**steps 10-15**). An example of each of these types was attempted and detailed below.

3.3.4.1 Photolithographic pre-patterning (steps 5-10)

Simple photolithographic patterning can be carried out using a standard photoresist material that can be patterned through a mask with a UV-lamp.[52] In this case a commercially available negative photoresist (negative photoresist kit, Sigma-Aldrich) was spin-coated onto silicon and glass substrates using a home-made spin coater built for this experiment (**step 5**). Spectroscopic ellipsometry showed the resist layer thickness to be approximately 620 nm. Once a layer of photoresist was coated on the substrates, a copper coated TEM grid was placed suspended on a thin layer of aluminium foil over the spin-coated film and the substrate exposed to UV light (365 nm) for 3 minutes (**step 6**). After 3 minutes the TEM grid mask was removed and the substrate rinsed in developing solution. The unexposed regions after development were found to be free of resist material with an ellipsometric thickness of approx 0 nm. After the development process, there then remained a negative pattern of the TEM grid mask in photoresist on the substrate and areas free of photoresist (**step 7**) (figure 3.14).

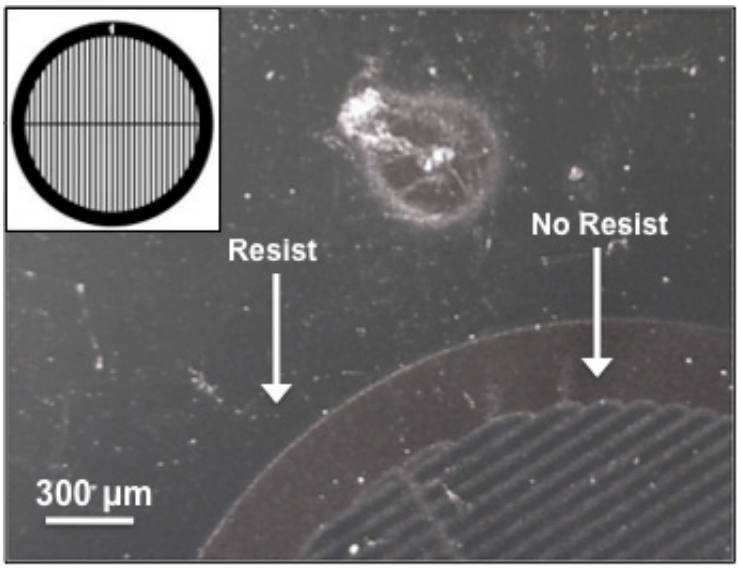

Figure 3.14. Optical microscopy of remaining negative pattern from a TEM grid after resist exposure and removal (**step 7**).

The substrates were then sequentially immersed in PDAC (**step 8**) and Au-NPs (**step 9**) using the standard protocol, coating the whole of the substrate in one bilayer of PDAC and Au-NPs. After this coating, the whole substrate was immersed in hot photoresist remover followed by H_2SO_4 to remove the remaining photoresist (as per photoresist standard procedure) and any PDAC and Au-NPs deposited on the resist (**step 10**). Figure 3.15 shows representative optical images of the PDAC/Au-NP film remaining after the final photoresist removal stage.

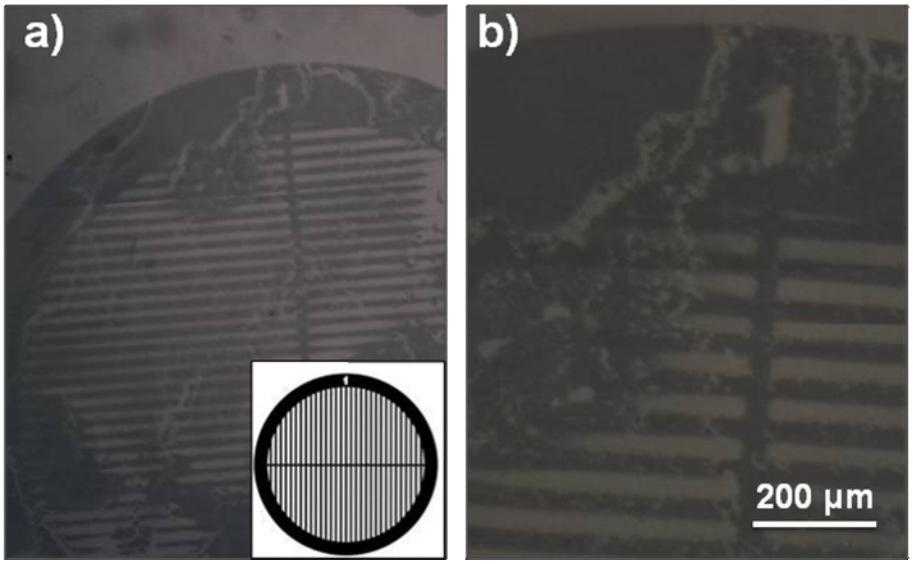

Figure 3.15. a) Optical microscopy image of $(PDAC/Au\text{-}NP)_1$ features (darker regions) after removal of the underlying photoresist with inset schematic of TEM grid mask; **b)** zoomed in image of patterned region (**step 10**).

The remaining features should be composed of PDAC and Au-NPs and exactly replicate the features seen on the TEM grid mask (figure 3.15a, inset). The films appear to have a much darker purple colouration than normally seen after film deposition indicating a more closely aggregated structure of gold nanoparticles.

To quantify this observation, UV-vis spectrophotometry of an unpatterned $(PDAC/Au\text{-}NP)_1$ sample on glass before and after immersion in resist remover solution showed that upon coming into contact with the remover solution, the nanoparticles on the surface appear to become much more aggregated as a longitudinal plasmon peak appears between 600 and 700 nm (figure 3.16).

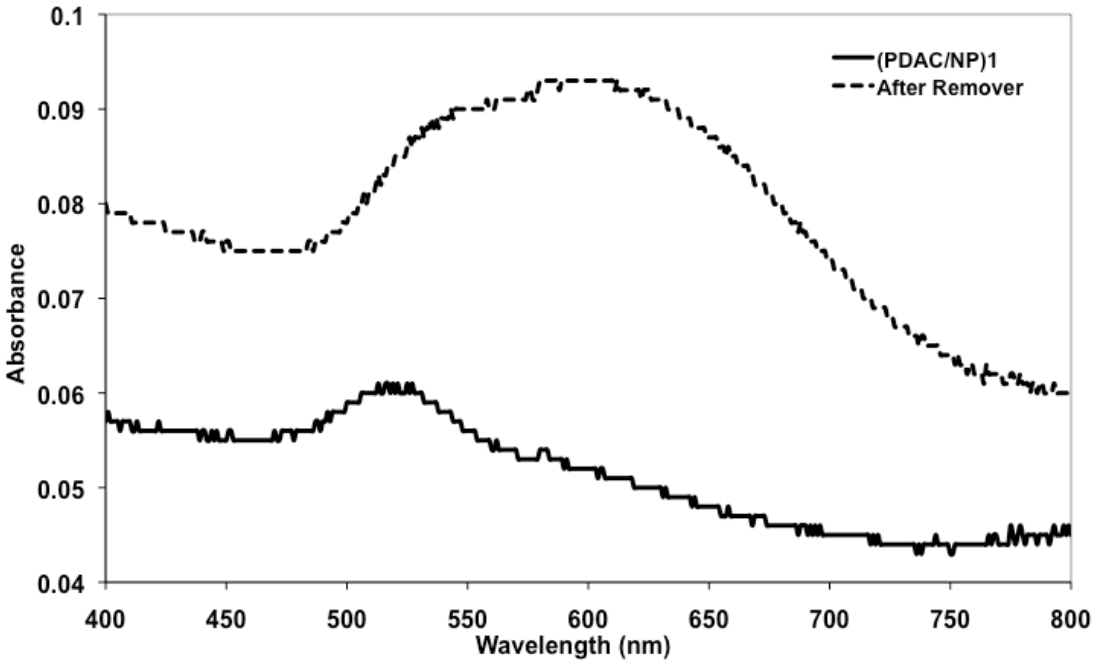

Figure 3.16. UV-vis spectra of $(PDAC/Au\text{-}NP)_1$ sample on glass before and after immersion in photoresist remover (**step 9**).

XPS of a sample of PDAC/C-Au-NPs after immersion in the hot resist remover and H_2SO_4 showed that the Au peaks were still present on the substrate. AFM tapping mode imaging also revealed a highly aggregated nanoparticle structure after exposure to photoresist remover (figure 3.17).

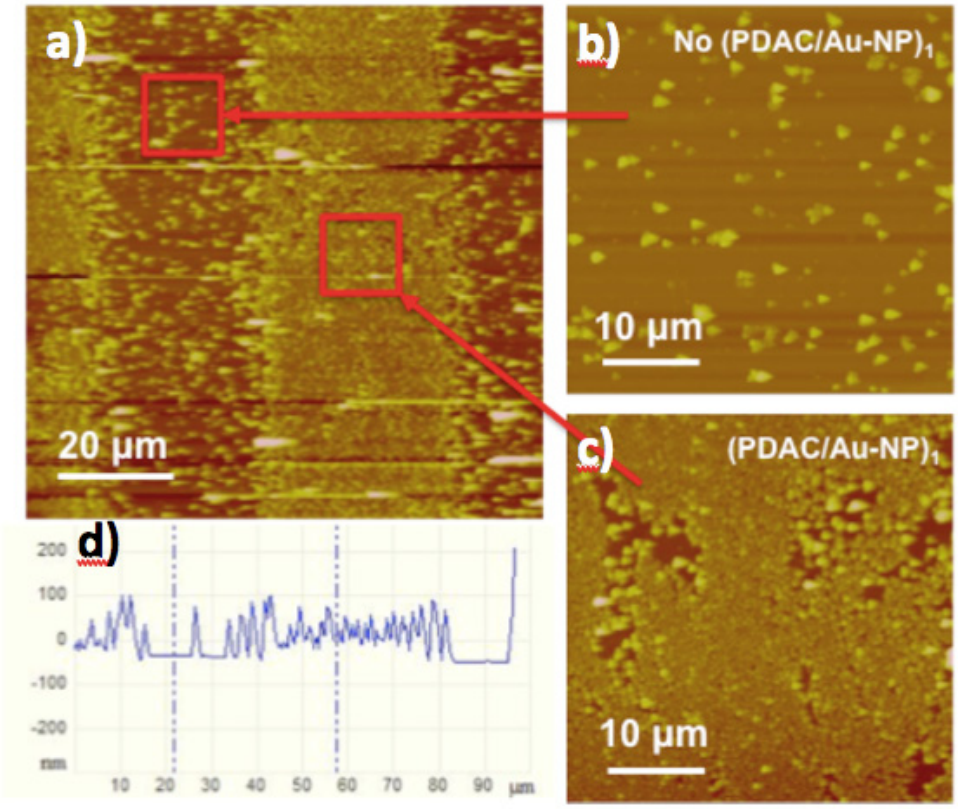

Figure 3.17. a) AFM tapping mode images of $(PDAC/Au\text{-}NP)_1$ features after photoresist removal, magnified regions; **b)** with and **c)** without aggregated nanoparticle structures; and **d)** line section across image a).

3.3.4.2 Microfluidic delivery of LBL films to pre-patterned gold Features (steps 11-17)

In order to examine the delivery of LBL films to pre-patterned gold features, the work carried out by Sun *et al.*[53] was initially replicated, for forming gold features on silicon substrates *via* irradiation of a film of decanethiol gold nanoparticles (T-Au-NPs) with 244 nm laser. A solution of octadecane thiol nanoparticles (T-Au-NPs) was drop-cast onto silicon substrates and allowed to air dry at room temperature (**step 11**). The films of T-Au-NPs were then masked with a TEM grid and exposed to 244 nm light for 20 minutes (**step 12**).

The final microfluidic device would consist of a silicon wafer base with these Au patterned features then a glass lid containing the microfluidic channels would be bonded to the silicon wafer.

The schematic of the microfluidic device design is presented in figure 3.18. Four flow ports (2 materials input and output) addressed two optical analysis sites.

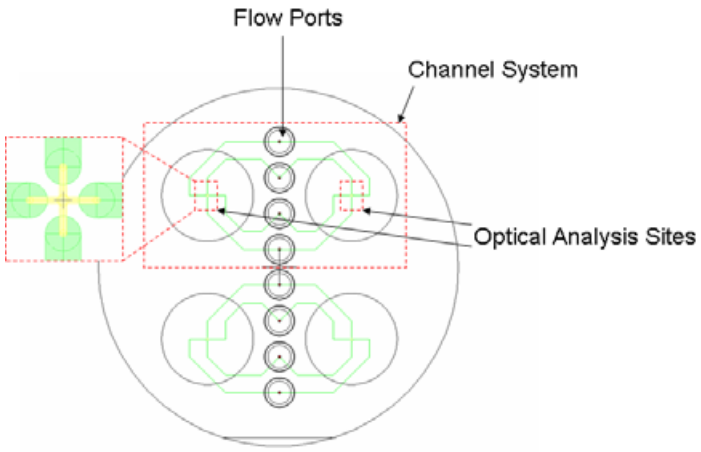

Figure 3.18. Diagram of microfluidic wafer layout.

The Au features were placed at locations that would be optically viewable when the bonded glass lid was in place on top of the wafer. With an optically transparent window, the deposition of further nanoparticles on the features could be followed with an optical microscope (figure 3.19).

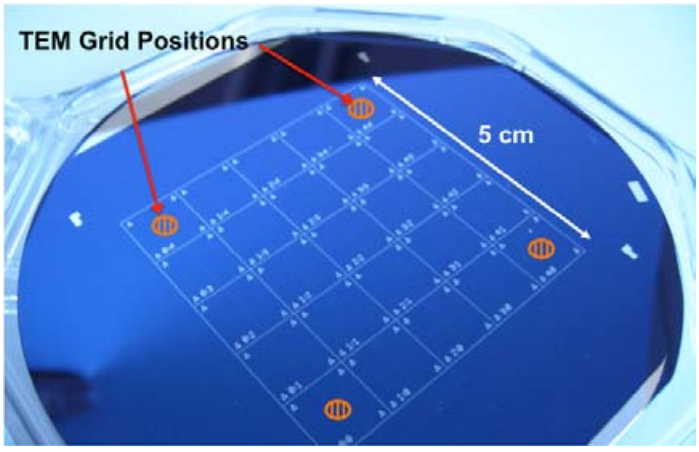

Figure 3.19. Photograph and markings for positions of TEM grids on silicon wafer (**step 12**).

After exposure, the substrates were rinsed with chloroform to reveal the physisorbed, aggregated Au nanoparticle pattern (**step 13**). These Au patterns were subsequently imaged with optical microscopy (figure 3.20).

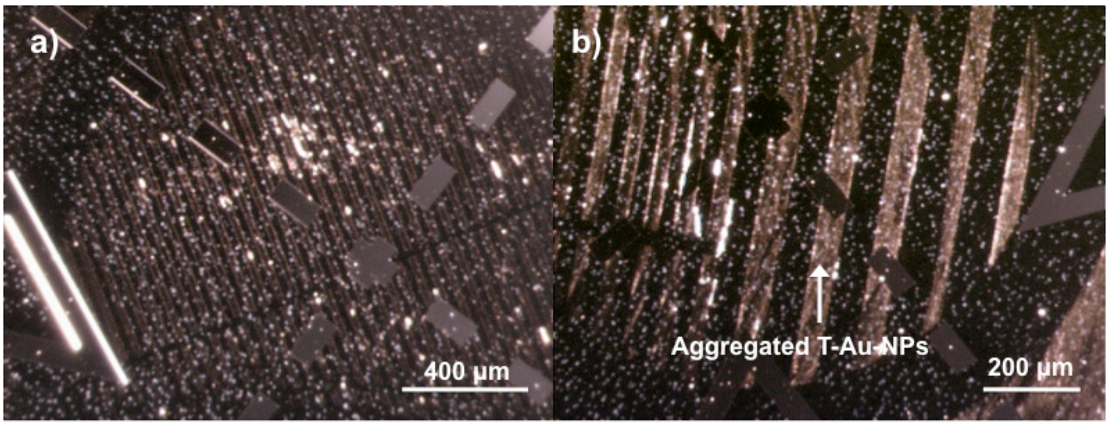

Figure 3.20. Optical microscopy images of **a)** Surface of silicon wafer after patterning through TEM grid mask with 244 nm laser and rinsing with chloroform, **b)** magnified region (**step 13**).

Once formed, the Au patterns were passed to a collaborator (BAE systems) to undergo a microfluidic wafer bonding process, to bond a lid to the silicon wafer. It was hoped that the Au features might survive the wafer bonding process if the cleaning conditions and wafer bonding conditions used were not too aggressive. To clean the wafers before bonding, a simple immersion and sonication in isopropyl alcohol was used. The glass lid was joined to the silicon wafer using anodic bonding methodology (**step 14**).[54] Pictures of the device after lid bonding and port attachment are presented in figure 3.21.

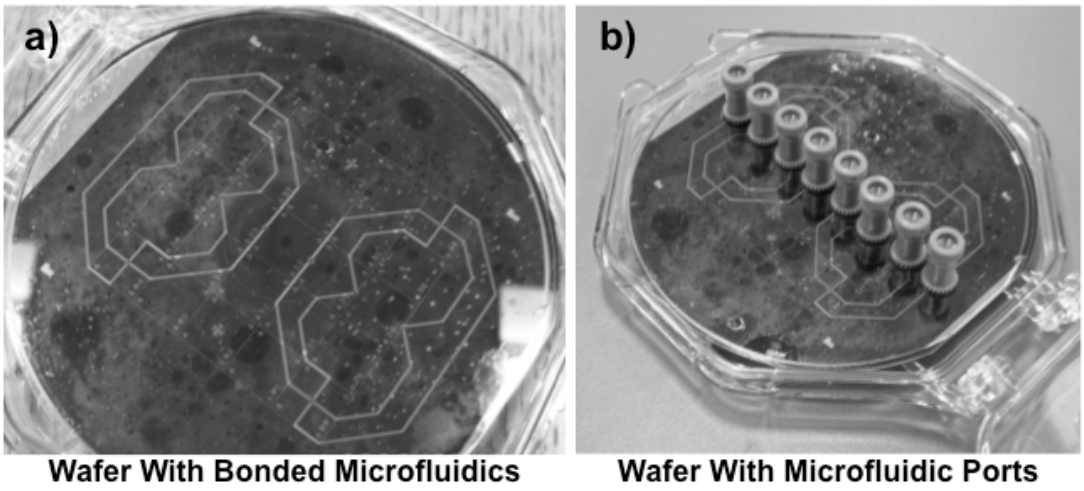

Figure 3.21. a) Silicon wafer after microfluidic lid bonding and **b)** the complete wafer after fitting of microfluidic ports (**step 14**).

Optical microscopy of the bonded microfluidic device after the bonding process, however, revealed that some of the Au features appeared to have blurred (figure 3.22). The main reason for this blurring is believed to be the high temperature (~600^{o}C) used during the bonding process inducing the aggregated nanoparticles to become mobile and come together combined with the sonication step.

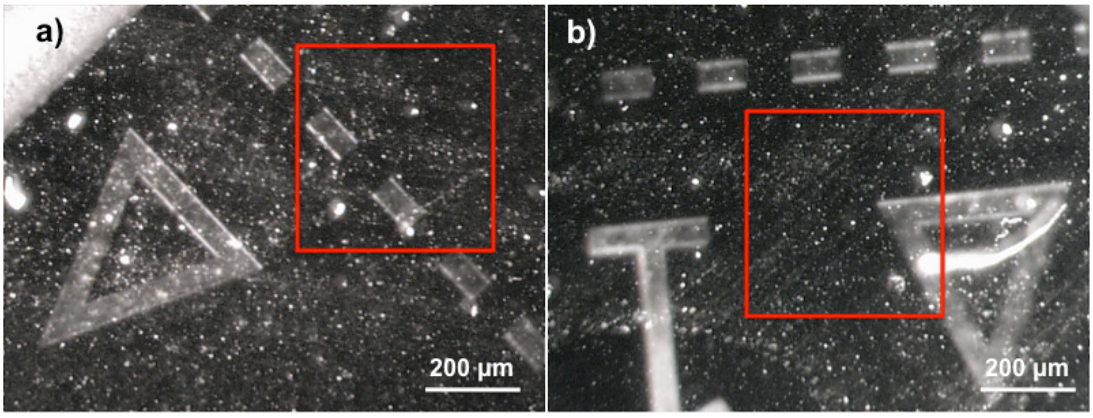

Figure 3.22. Optical microscopy images of two regions of the surface of silicon wafer after microfluidic lid bonding (**step 14**).

This temperature-induced aggregation behaviour could have been exaggerated by the pre-treatment and cleaning procedures that the wafer underwent before bonding. It was decided to proceed with the deposition procedure to demonstrate the ability of microfluidics to efficiently deliver a solution of 4-aminothiophenol (4-ATP), PDAC and Au-NPs to the required location on the microfluidic device. The microfluidic device was designed with two separate channel loops (figure 3.18). Each separate channel system had two optical analysis sites, connected through the same fluidic loop. Different chemical species were delivered to the analysis sites via different entrance and exit ports *(e.g PDAC thorough horizontal channels and C-Au-NPs through vertical channels)* to avoid aggregation in the fluidic ports.

Although the T-Au-NP features had not fully survived the bonding process, it was decided to proceed with the microfluidic deposition experiments to see if any features could be visible. The empty microfuidic device (figure 3.23a) was first flushed and filled with a 1 mM solution of 4-ATP for 2 hours in order to form an amino-terminated SAM on the remnant T-Au-NPs on the substrate surface (**step 15**).[55] After 2 hours, the 4-ATP solution was removed and the relevant channels rinsed thoroughly with HPLC EtOH. This deposition of 4-ATP caused no change in the appearance of the optically visible area of the underlying surface (figure 3.23b). The first solution of negatively charged citrate Au-NPs was then passed into the microfluidic device and held in place for a period of one hour (**step 16**). After 1 hour, the Au-NP were rinsed through thoroughly with UHP H_2O. The two optically visible areas were once again examined and revealed a change in appearance from the deposition of the citrate Au-NPs to the underlying Au-NP film, with a gold sheen (figure 3.23c). This deposition of Au-NPs was also indication of the deposition of the 4-ATP SAM during the previous step. PDAC was then deposited on top of the deposited Au-NPs (**step 17**). Assembly was then commenced as carried out

previously for sequential deposition of citrate Au-NPs. Each deposition step was followed with thorough rinsing with UHP H_2O. The resultant optical microscopy images from a single run are presented in figure 3.23.

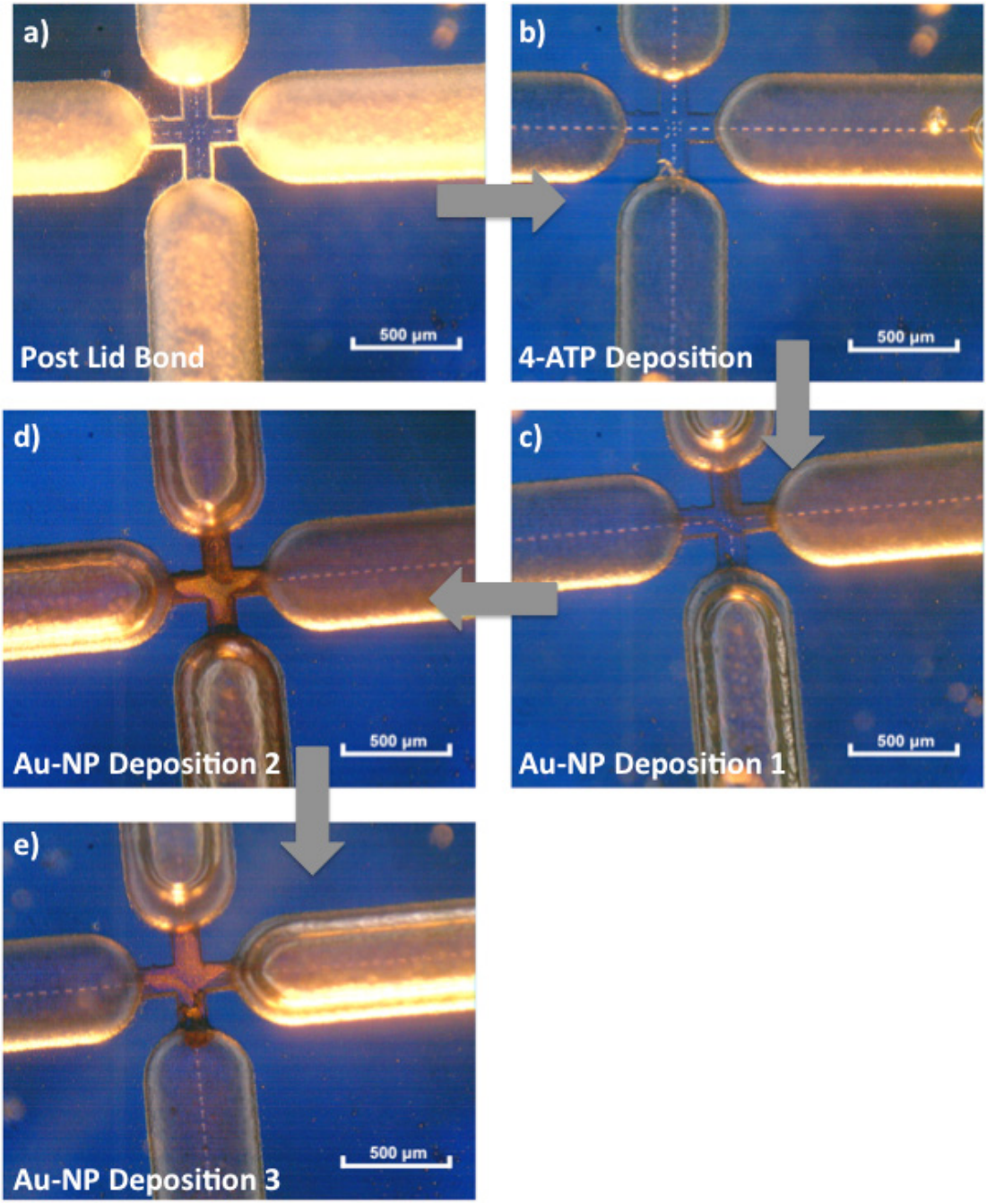

Figure 3.23. Optical microscopy images of inspection windows of microfluidics wafer; **a)** before addition of any liquids; **b)** after deposition of 4-ATP; **c)** after deposition of 1 layer Au-NPs; **d)** after further deposition of a $(PDAC/Au\text{-}NP)_1$ layer; and **e)** after deposition of $(PDAC/Au\text{-}NP)_2$ layers.

During the deposition process, the build-up of the gold sheen from the deposition of increasing amounts of gold nanoparticles at the optical windows can be seen at the cross junction in the centre of the images (figure 3.23c, d and e) Also, increasing amounts of Au-NPs can be seen depositing to the inside of the main fluidic channels, indicating that the affinity of the PDAC for the inside of the glass lid can induce the nanoparticles to deposit within the channels. From examination of the optical images, this deposition of the nanoparticles to the glass lid only becomes a major factor after the third Au-NP stage, as after the second stage, some of the channel surface is free of the gold sheen. The successful delivery and sequential assembly of nanoscale species to required sites on substrate surfaces demonstrates that microfluidics would be a versatile method for carrying out 3-dimensional assembly of nanostructures.

3.4 Conclusions

The sequential, LBL deposition presented here has proved a useful method for controlling the amount of nanoparticles deposited to a surface with subsequent immersions in PDAC and Au-NPs. The use of complementary chemistries to carry out the electrostatic assembly allows for the use of many different charged species to be used. With the system explored here, the initial deposition stages examined were shown to effect the controlled deposition of increasing numbers of Au-NPs on the surface as opposed to forming discrete PDAC and Au-NP layers. The three methods presented for following the deposition process are shown to give results of the same order of magnitude for the surface coverage with Au-NPs. Differences between the values obtained by the three methods can be accounted for by differences in the way in which they handle aggregated Au-NPs as opposed to discrete Au-NPs. The use of standard photolithographic techniques to introduce patterns into the LBL films proved

a successful methodology for patterning of LBL deposited structures, where patterns could be initially defined on the surface, then material added to these patterns then developed. The use of microfluidics to deposit the two components to chemically patterned surfaces proved to be an interesting technique, showing that small volumes of material could be used to structures surfaces (see chapter 4). With the microfluidics the stability of the chemically pre-patterned regions to the microfluidic bonding process was an issue, meaning that the initial patterns were lost (see section 3.5 for a possible development). Overall, the LBL technique is seen to be a robust and useful technique for the surface scientist to form multicomponent films on large scale or patterned surfaces.

3.5 Future Work

Future work based on this chapter, would be to examine more subsequent layers of PDAC and Au-NPs by the techniques used and to incorporate the LBL deposition methodology with the EBL patterned surfaces from chapter 2. After the initial microfluidics study, the next iteration of this research would be to first bond the glass lid to the clean silicon surface. After the bonding process, the fluidic system would be flooded with Au-NP solution then allowed to dry as much as possible. The 244 nm light source could then be passed through a TEM grid based mask and through the glass lid onto the Au-NP layer, providing the correct glass was chosen for the lid so as to allow un-interfered passage of the required wavelength of light through the lid. After the irradiation, the fluidic system would be rinsed through with chloroform to reveal the patterned Au-NP features and allow further assembly of nanoscale species.

3.6 Experimental

3.6.1 PDAC solution preparation

An aqueous poly-diallyldimethyl ammonium chloride (PDAC) solution (20 wt%, average M_w 200,000-350,000, 0.7 ml) was dissolved in an aqueous NaCl solution (75 ml, 0.5g). The solution was stored at room temperature.

3.6.2 Synthesis of citrate-stabilised gold nanoparticles

Nanoparticles were synthesised by the Frens method. An aqueous solution of $HAuCl_4.3H_2O$ (0.25 mM, 100 mL) was heated under reflux for 5-10 mins. An aqueous solution of sodium citrate (38.8 mM, 2 mL) was added. Heating under reflux was continued for a further 10 mins to ensure complete reduction of the gold salt. The colloidal solution was centrifuged for 10 min at 3500 rpm and the supernatant collected.

3.6.3 Glass substrate preparation

Glass microscope slides or silicon wafers (average thickness 1 to 1.2 mm) were cut to a size of 1cm x 5.5 cm. Substrates were cleaned with EtOH under ultrasonication and stored in fresh EtOH.

3.6.4 PDAC/Au-NP LBL assembly

Multilayer films were formed on glass substrates by sequential dipping of the substrates into PDAC solution, UHP H_2O to rinse away excess PDAC, a Au-NP solution, then UHP H_2O. Samples were dried with N_2 and stored in a dessicator.

3.6.5 LBL characterisation

3.6.5.1 UV-vis spectrometry

Glass substrates with LBL structures on the surface were placed into the sample holder of a UV-vis spectrometer and a scan made between 400 and 800 nm to check for the presence of the characteristic plasmon resonance band and for the presence of a shifted resonance band indicating collective resonance of nanoparticles.

3.6.5.2 AFM imaging

AFM imaging was carried out using a Dimension D3100 Nanoscope AFM from Veeco, USA. Images were acquired in tapping mode, using RTESP Silicon tips.

3.6.5.3 AFM added mass analysis

Added mass analysis was carried out using tipless cantilevers (MikroMasch, CSC12). Cantilevers were initially tuned to the first resonant frequency in the Nanoscope software, averaging readings from 5 individual readings. Cantilevers were then sequentially dipped into the PDAC/Au-NP solutions and the tuning process repeated to obtain a value after material deposition.

3.6.6 Photolithographic patterning of LBL films

Glass slides were spin coated (2300 RPM) with negative photoresist (Sigma-aldrich negative photoresist kit I, Thinner: Resist, 2:1) using a homemade spin coater. Samples were given a prebake at 82°C for 20 min, then exposed to UV light through a copper coated TEM grid (Agar Scientific) for 3 seconds. After exposure, samples were developed by immersion in developer for 30 secs and rinsing with isopropyl alcohol. A final postbake for 10 min at 120°C was then carried out. For resist removal Negative resist remover I was used to swell the photoresist in conjunction with hot

H_2SO_4 to effectively remove the resist film. Both solutions were used at 50-60 °C. Initially, the removal process was checked for completion with spectroscopic ellipsometry.

3.6.7 T-Au-NP synthesis

Decanethiol-stabilized gold nanoparticles were synthesized and characterized by the Brust method.[56] $HAuCl_4$ was transferred from water to toluene by stirring an aqueous solution of $HAuCl_4.3H_2O$ (30 mL, 30 mM) with tetraoctylammonium bromide solution in toluene (80 mL, 50 mM) for 30 min. The toluene phase was separated, and a solution of decanethiol in toluene (10 mL, 90 mM) was added. After 5 min, an aqueous $NaBH_4$ solution (25 mL, 0.4 M) was slowly added to the mixture. After 3 h, the organic phase containing the gold nanoparticles was separated and concentrated to 10 mL under reduced pressure. The nanoparticles were purified by precipitation from the toluene solution with ethanol followed by centrifugation of the suspension. The supernatant was discarded. This precipitation/centrifugation process was repeated two more times after which the dark-brown solid was dried under vacuum.

3.6.8 Silicon wafer patterning with T-Au-NPs

A toluene solution of T-Au-NP was dropcast onto the silicon wafer. Photopatterning was carried out using light from a frequency doubled argon ion laser (Coherent FreD 300C, Coherent U.K., Ely), which emits at 244 nm through a copper coated TEM grid. After exposure, samples were rinsed with $CHCl_3$.

3.6.9 Microfluidics

The microfluidic device was designed & fabricated by BAE systems (Bristol, UK). Prior to lid bonding, the T-Au-NP patterned wafer was sonicated in isopropyl alcohol. The glass lid was bonded to the wafer using elevated temperature anodic bonding. Prior to use, microfluidic ports were attached into the holes in the glass lid. Fluids were delivered to and removed from the device using 5 ml syringes.

3.7 References

1) **Human Physiology: The Mechanisms of Body Function**, Vander, A. J., Sherman, J. H. and Luciano, D. S., **1985**, McGraw-Hill.
2) **Henderson's Dictionary of Biology**, Lawrence, E., **2008**, Pearson Education.
3) **Mechanised Nanoparticles for Drug Delivery,** Cotí, K. K., Belowich, M. E., Ambrogio, M. W., Lau, Y. A., Khatib, H. A., Zink, J. I., Khashab, N. M. and Stoddart, J. F., *Nanoscale*, **2009**, *1*, 16-39.
4) Schlenoff, J. B. and Dubas, S. T., **Mechanism of Polyelectrolyte Multilayer Growth: Charge Overcompensation and Distribution**, M*acromolecules*, **2001**, *34*, 592-598.
5) Schoeler, B., Kumaraswamy, G. and Caruso, F., **Investigation of the Influence of Polyelectrolyte Charge Density on the Growth of Multilayer Thin Films Prepared by the Layer-by-Layer Technique**, *Macromolecules*, **2002**, *35*, 889-897.
6) Decher. G., **Fuzzy Nanoassemblies: Toward Layered Polymeric Multicomposites**, *Science*, **1997**, *277*, 1232-1237.
7) Seo, J., Schattling, P., Lang, T., Jochum, F., Nilles, K., Theato, P. and Char, K., **Covalently Bonded Layer-by-Layer Assembly of Multifunctional Thin Films Based on Activated Esters**, *Langmuir*, Article ASAP, **DOI: 10.1021/la902574z.**
8) Decher, G., Hong, J. D., Schmitt, J., **Build-up of Ultrathin Multilayer Films by a Self-assembly Process: III. Consecutively Alternating Adsorption of Anionic and Cationic Polyelectrolytes on Charged Surfaces**, *Thin Solid Films*, **1992**, *210/211*, 831-835.

9) Johnston, A. P. R., Read, E. S. and Caruso, F., **DNA Multilayer Films on Planar and Colloidal Supports: Sequential Assembly of Like-Charged Polyelectrolytes**, *Nano. Lett.*, **2005**, *5*, 953-956.

10) Caruso, F. and Mohwald, H., **Protein Multilayer Formation on Colloids through a Stepwise Self-Assembly Technique**, *J. Am. Chem. Soc.* **1999**, *121,* 6039-6046.

11) Musick, M. D., Keating, C. D., Keefe, M. H. and Natan, M. J., **Stepwise Construction of Conductive Au Colloid Multilayers from Solution**, *Chem. Mater.*, **1997**, *9*, 1499-1501.

12) Jiang, B., Barnett, J. B. and Li, B., **Advances in Polyelectrolyte Multilayer Nanofilms as Tunable Drug Delivery Systems**, *Nanotech. Sci. App.*, **2009**, *2*, 21-27.

13) Schlenoff, J. B., Dubas, S. T. and Farhat, T., **Sprayed Polyelectrolyte Multilayers**, *Langmuir*, **2000**, *16*, 9968-9969.

14) Elzbieciak, M., Kolasińska, M., Zapotoczny, S., Krastev, R., Nowakowska, M. and Warszyński, P., **Nonlinear Growth of Multilayer Films Formed from Weak polyelectrolytes**, *Coll. Surf. A.*, **2009**, *343*, 89-95.

15) Chen, J. Y., Luo, G. B. and Cao, W. X., **The Study of Layer-by-layer Ultrathin Films by the Dynamic Contact Angle Method**, *J. Coll. Int. Sci.,* **2001**, *238*, 62-69.

16) Bogdanovic, G., Sennerfors, T, Zhmud, B. and Tiberg, F., **Formation and Structure of Polyelectrolyte and Nanoparticle Multilayers: Effect of Particle Characteristics**, *J. Coll. Int. Sci.*, **2002**, *255*, 44-51.

17) Antipov, A. A., Sukhorukov, G. B., Leporatti, S., Radtchenko, I. L. Donath, E. and Mohwald, H., **Polyelectrolyte Multilayer Capsule Permeability Control**, *Coll. Surf. A.*, **2002**, 198 – 200, 535-541.

18) Jessel, N., Oulad-Abdelghani, M., Meyer, F., Haıkel, P. L. Y., Schaaf, P. and Voegel, J.-C., **Multiple and Time-scheduled *In-situ* DNA Delivery Mediated by β-cyclodextrin Embedded in a Polyelectrolyte Multilayer**, *PNAS*, **2006**, *103*, 8618-8621.

19) Chua, P-H., Neoh, K-G., Kang, E-T. and Wang, W., **Surface Functionalization of Titanium with Hyaluronic Acid/Chitosan Polyelectrolyte Multilayers and RGD for Promoting Osteoblast Functions and Inhibiting Bacterial Adhesion**, *Biomaterials*, **2008**, *29*, 1412-1421.

20) Lee, S. W., Sanedrin, R. G., Oh, B.-K. and Mirkin, C. A., **Nanostructured Polyelectrolyte Multilayer Organic Thin Films Generated via Parallel Dip-Pen Nanolithography,** *Adv. Mater.*, **2005**, *17*, 2749-2753.

21) Jiang, X., Zheng, H., Gourdin, S. and Hammond, P. T., **Polymer-on-Polymer Stamping: Universal Approaches to Chemically Patterned Surfaces**, *Langmuir*, **2002**, *18*, 2607-2615.

22) Yang, S. Y. and Rubner, M. F., **Micropatterning of Polymer Thin Films with pH-Sensitive and Cross-linkable Hydrogen-Bonded Polyelectrolyte Multilayers**, *J. Am. Chem. Soc.*, **2002**, *124*, 2100-2101.

23) F. Hua, J. Shi, Y. Lvov, and T. Cui, **Patterning of Layer-by-Layer Self-Assembled Multiple Types of Nanoparticle Thin Films by Lithographic Technique**, *Nano. Letts.*, **2002**, *2*, 1219-1222.

24) Chen, K. M., Jiang, X., Kimerling, L. C. and Hammond, P. T, **Selective Self-Organization of Colloids on Patterned Polyelectrolyte Templates**, *Langmuir*, **2000**, *16*, 7825-7834.

25) Zheng, H., Lee, I., Rubner, M. F. and Hammond, P. T., **Two Component Particle Arrays on Patterned Polyelectrolyte Multilayer Templates**, *Adv. Mater.*, **2002**, *14*, 569-572.

26) **Nanoparticle Assemblies and Superstructures**, Kotov, N. A., **2006**, CRC Press.

27) Kelly, K. L., Coronado, E., Zhao, L. L. and Schatz, G. C., **The Optical Properties of Metal Nanoparticles: The Influence of Size, Shape, and Dielectric Environment**, *J. Phys. Chem. B.,* **2003**, *107,* 668-677.

28) Lin, S., Li, M., Dujardin, E., Girard, C. and Mann, S., **One-Dimensional Plasmon Coupling by Facile Self-Assembly of Gold Nanoparticles into Branched Chain Networks**, *Adv. Mater.*, **2005**, *17*, 2553-2559.

29) Perez-Juste, J., Rodríguez-Gonzμlez, B., Mulvaney, P. and Liz-Marzμn, L. M., **Optical Control and Patterning of Gold Nanorod-Poly(vinyl alcohol) Nanocomposite Films**, *Adv. Funct. Mater.*, **2005**, *15*, 1065-1071.

30) Gravesen, P., Branebjerg, J. and Jensen, O. S., **Microfluidics-A Review**, *J. Mioromech. Microeng.*, **1993**, *3*, 168-182.

31) Krenková, J. and Foret, F., **Immobilized Microfluidic Enzymatic Reactors**, *Electrophoresis,* **2004**, *25*, 3550-3563.

32) Lagally, E. T., Medintz, I. and Mathies, R. A., **Single-Molecule DNA Amplification and Analysis in an Integrated Microfluidic Device**, *Anal. Chem.*, **2001,** *73*, 565-570.

33) Lion, N., Rohner, T. C., Dayon, L., Arnaud, I. L., Damoc, E., Youhnovski, N., Wu, Z-Y., Roussel, C., Josserand, J., Jensen, H., Rossier, J. S., Przybylski, M. and Girault, H. H., **Microfluidic Systems in Proteomics**, *Electrophoresis,* **2003**, *24,* 3533-3562.

34) Schlautmann, S., Wensink, H., Schasfoort, R., Elwenspoek, M. and van den Berg, A., **Powder-blasting Technology as an Alternative Tool for Microfabrication of Capillary Electrophoresis Chips with Integrated Conductivity Sensors**, *J. Micromech. Microeng.*, **2001**, *11*, 386-389.

35) **Introduction to Microfluidics**, Tabeling, P., **2005**, Oxford University Press

36) Grimes, A, Breslauer, D. N., Long, M., Pegan, J., Lee, L. P. and Khine, M., **Shrinky-Dink Microfluidics: Rapid Generation of Deep and Rounded Patterns**, *Lab Chip*, 2008, 8, 170-172.

37) Trotter, H., Zaman, A. A. and Partch, R., **Preparation and Characterization of Polymer Composite Multilayers on SiO_2,** *J. Coll. Int. Sci.*, **2005**, *286*, 233-238.

38) Stchakovsky, M., **Spectroscopic Ellipsometric Measurements on Biochip Structures in a Liquid Flow Cell Environment**, **Horiba Jobin Yvon Application Note,**

http://www.horiba.com/fileadmin/uploads/Scientific/Documents/TFilm/se-10.pdf.

39) http://www.sigmaaldrich.com/catalog/ProductDetail.do?N4=409014%7CALDRICH&N5=SEARCH_CONCAT_PNO%7CBRAND_KEY&F=SPEC&lang=en_US - Accessed 20/09/09.

40) Stemme, S. and Ödberg, L., **Layer Thickness for High Molecular Weight Cationic Polyacrylamides Adsorbed on a Surface with a Preadsorbed Poly-diallyldimethylammonium Chloride,** Coll. Surf. A., **1999**, *157*, 307-313.

41) Farhat, T., Yassin, G., Dubas, S. T. and Schlenoff, J. B., **Water and Ion Pairing in Polyelectrolyte Multilayers,** *Langmuir*, **1999**, *15*, 6621-6623.

42) Neff, P. A., Wunderlich, B. K., Klitzing, R. V. and Bausch, A. R., **Formation and Dielectric Properties of Polyelectrolyte Multilayers Studied by a Silicon-on-Insulator Based Thin Film Resistor,** *Langmuir*, **2007**, *23*, 4048-4052.

43) G. Frens., **Controlled nucleation for the regulation of the particles size in monodisperse gold suspensions**, *Nature. Phys. Sci.*, **1973**, *241*, 20.

44) Diegoli, S., Mendes, P. M., Baguley, E. R., Leigh, S. J., Iqbal, P., García Díaz, Y. R., Begum, S., Critchley, K., Hammond, G. D., Evans, S. D., Attwood, D., Jones, I. P. and Preece, J. A., **pH-Dependent Gold Nanoparticle Self-Organization on Functionalized Si/SiO_2 Surfaces**, *J. Exp. Nano. Sci.*, **2006**, *1*, 333-353.

45) Eustis, S and El-Sayed, M. A., **Why Gold Nanoparticles are More Precious Than Pretty Gold: Noble Metal Surface Plasmon Resonance and its Enhancement of the Radiative and Nonradiative Properties of Nanocrystals of Different Shapes**, *Chem. Soc. Rev.*, **2006**, *35*, 209-217.

46) Su, K.-H., Wei, Q.-H. and Zhang, X., **Interparticle Coupling Effects on Plasmon Resonances of Nanogold Particles**, *Nano. Letts.*, **2003**, *3*, 1087-1090.

47) Maye, M. M., Han, L., Kariuki, N. N., Ly, N. K., Chan, W-B., Luo, J. and Zhong, C. J., **Gold and Alloy Nanoparticles in Solution and Thin Film Assembly: Spectrophotometric Determination of Molar Absorptivity,** *Analytica. Chimica. Acta.*, **2003**, *496*, 17-27.

48) Mayya, K. S., Patil, V. and Sastry, M., **Lamellar Multilayer Gold Cluster Films Deposited by the Langmuir-Blodgett Technique**, *Langmuir*, **1997**, *13*, 2575-2577.

49) Boonliang, B., Prewett, P. D., Hedley, J., Preece, J. and Hamlett, C. A., **A Focused-Ion-Beam-Fabricated Micro-paddle Resonator for Mass Detection**, *J. Micromech. Microeng.*, **2008**, *18*, 015021, 4pp.

50) Hagleitner, C., Hierlemann, A., Lange, D., Kummer, A., Kerness, N., Brand, O. and Baltes, H., **Smart Single-chip Gas Sensor Microsystem**, *Nature,* **2001**, *414*, 293-296.

51) Sader, J. E., Larson, I., Mulvaney, P. and White, L. R., **Method for the Calibration of Atomic Force Microscope Cantilevers,** *Rev. Sci. Instrum.,* **1995**, *66* , 3789-3798.

52) Vijayendran, R. A., Motsegood, K. M., Beebe, D. J. and Leckband, D. E., **Evaluation of a Three-Dimensional Micromixer in a Surface-Based Biosensor**, *Langmuir*, **2003**, *19*, 1824-1828.

53) Sun, S., Mendes, P., Critchley, K., Diegoli, S., Hanwell, M., Evans, S. D., Leggett, G. J., Preece, J. A. and Richardson, T. H., **Fabrication of Gold Micro- and Nanostructures by Photolithographic Exposure of Thiol-Stabilized Gold Nanoparticles**, *Nano. Letts.*, **2006**, *6*, 345-350.

54) Knowles, K. M. and vanHelvoort, A. T. J., **Anodic Bonding**, International Materials Reviews, **2006**, *5*, 273-311.

55) Ma, Y., Jiao, K., Yang, T. and Sun, D., **Sensitive PAT Gene Sequence Detection by Nano-SiO_2/*p*-aminothiophenol Self-assembled Films DNA Electrochemical Biosensor Based on Impedance Measurement**, *Sens. Act. B.*, **2008**, *131*, 565-571.

56) Brust, M., Walker, M., Bethell, D., Schiffrin, D. J., Whyman, R., **Synthesis of Thiol Derivatised Gold Nanoparticles in a Two Phase Liquid/Liquid System**, *J. Chem. Soc. Chem. Commun.,* **1994**, 801-802.

Chapter 4

Printing & Scratching:

Fabrication of Composite Polyelectrolyte/Nanoparticle Films with Inkjet Printing (IJP) and AFM Nano/Microscratching.

Abstract

The work described in this chapter represents insights into the use of consumer grade IJP hardware for depositing cationically charged polyelectrolytes and polyanionic gold nanoparticles. IJP is powerful and low-cost technique that allows for repeatable volumes of liquids to be deposited to a multitude of surfaces at varying material densitites in user-defined patterns. Here, the technique of IJP of soft materials is combined with mechanical 'machining' of the printed structures with an AFM, to gain a versatile, yet simple, technique for defining surface micro-architectures.

4.1 Introduction

4.1.1 Inkjet printing (IJP)

IJP refers to any system in which droplets of ink are ejected onto a printing surface to form characters, codes or graphic patterns. Inkjet printers are found atop desks throughout the world. IJP technology is by far the most common form of printing technology for use by consumers wishing to transfer digital information into a paper copy. Inkjet technology is also one of the most versatile, where printing surfaces can range from paper and photographic paper, through to textiles and CD/DVD storage media. The basic principle of IJP is that the coloured inks are held in reservoirs (*cartridges*) within a carriage which moves over the surface of the paper

or surface being printed on. When required, the print head pulls the liquid ink from these reservoirs and transfers the ink to the paper. Large areas of printed colour are composed of lots of individual droplets of the coloured inks. This droplet effect can be seen by magnifying (approx 300X) any inkjet printed image to view the dried droplets (scheme 4.1a and b). Two major types of inkjet technology exist;

i) Drop on demand technology, where the ink is formed into droplets by the printer and deposited to the printing surface in the required location, or

ii) Synchronous inkjet where the ink is constantly flowing through the print-nozzle in a jet which then breaks up into droplets due to instabilities.

The range of different inkjet printers available work in different ways, but they can roughly be grouped into three different technologies, *thermal inkjet* (section 4.1.1.1), *piezoelectric inkjet* (section 4.1.1.2) and *continuous inkjet* (section 4.1.1.3).

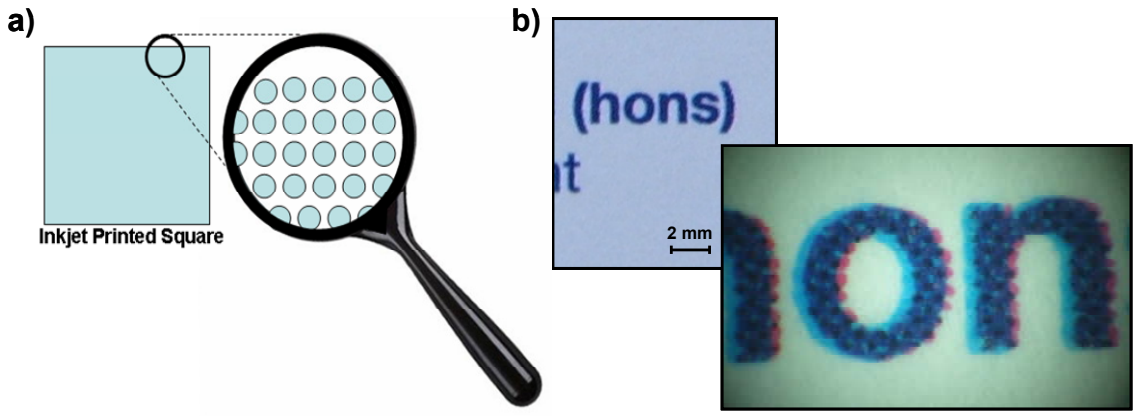

Scheme 4.1. a) Schematic diagram of magnification of an inkjet printed image; and **b)** photograph of a section of business card and magnified image showing dried inkjet printed droplets.

4.1.1.1 Thermal inkjet *(drop-on-demand)*

Most consumer inkjet printers are based upon thermal inkjet technology. Thermal inkjet printers use print cartridges with a series of microscale electrically

heated chambers constructed by photolithography (figure 4.1). To produce an image, the printer runs a pulse of current through the heating elements causing a steam explosion in the chamber to form a bubble, which propels a droplet of ink onto the paper.[1]

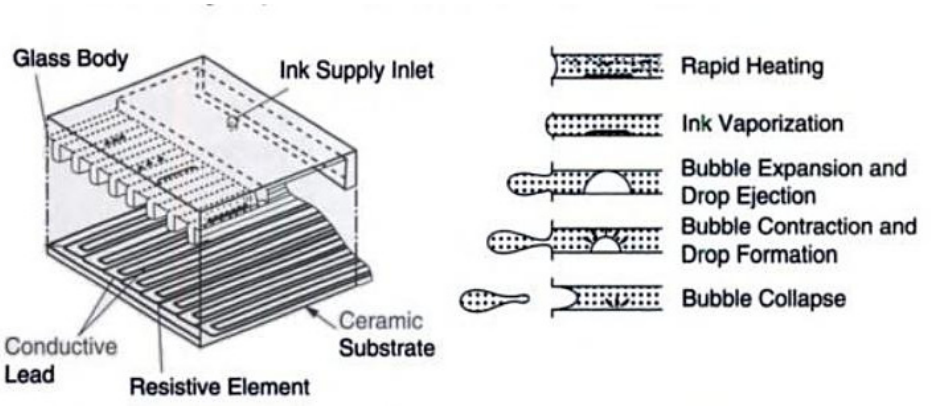

Figure 4.1. Schematic of a thermally activated Canon impulse jet printhead.[1]

The ink's surface tension as well as the condensation, and thus contraction of the vapour bubble, pulls a further charge of ink into the chamber through a narrow channel attached to an ink reservoir. For thermal inkjet printers, the ink used is generally *aqueous* (i.e. water-based inks using pigments or dyes). The print head is generally cheaper to produce than other inkjet technologies. The principle was discovered by Canon engineer, Ichiro Endo, in August 1977.[2]

4.1.1.2 Piezoelectric inkjet printers *(drop-on-demand)*

Most commercial and industrial ink jet printers use a piezoelectric material in an ink-filled chamber behind each nozzle instead of a heating element. When a voltage is applied, the piezoelectric material changes shape or size, which generates a pressure pulse in the fluid forcing a droplet of ink from the nozzle. This is essentially the same mechanism as the thermal inkjet, but generates the pressure pulse using a

different physical principle. Piezoelectric (also called Piezo) ink jet allows for a wider variety of inks than thermal or continuous ink jet, due to volatile solvents not being required, however the print heads are more expensive. Piezo inkjet technology uses stationary heads, which are built with robust construction and are designed for high volume production, faster print speeds, and lower costs. Piezoelectric IJP is a drop-on-demand process, with software that directs the heads to apply between zero to eight droplets of ink per dot and only where needed.

4.1.1.3 Continuous inkjet printers *(synchronous)*

The continuous ink jet method is used commercially for marking and coding of products and packages. The idea was first patented in 1867, by Lord Kelvin[3] and the first commercial devices (medical strip chart recorders) were introduced in 1951 by Siemens. In continuous ink jet technology, a high-pressure pump directs liquid ink from a reservoir through a gunbody and a microscopic nozzle, creating a continuous stream of ink droplets *via* Plateau-Rayleigh instability. A piezoelectric crystal creates an acoustic wave as it vibrates within the gunbody and causes the stream of liquid to break into droplets at regular intervals – 64,000 to 165,000 drops per second. The ink droplets are subjected to an electrostatic field created by a charging electrode as they form; the field varies according to the degree of drop deflection desired. This electrostatic field results in a controlled, variable electrostatic charge on each droplet. Charged droplets are separated by one or more uncharged "guard droplets" to minimize electrostatic repulsion between neighbouring droplets. The charged droplets pass through an electrostatic field and are directed (deflected) by electrostatic deflection plates to print on the printing surface, or allowed to continue on undeflected to a collection gutter for re-use. The more highly charged droplets are

deflected to a greater degree. Only a small fraction of the droplets are used to print, with the majority being recycled.

4.1.2 Inkjet printing of *'chemical inks'*

Because IJP has the ability to deposit well-defined volumes of liquid, reproducibly across both absorbing and non-absorbing surfaces, IJP has found many uses in the area of surface science and surface patterning.[4] The distinct advantage in using inkjet printers for this task is the ease with which patterns and structures can be defined in standard consumer interface software, without the need for special and often costly lithographic design software, operator training or costly mask fabrication. IJP used in this way falls into a rapidly developing class of fabrication technologies which includes such techniques as rapid prototyping technology,[5] micro-stereolithography[6] and electrospinning,[7] where developments in nanoscale and polymeric materials by chemists are being interfaced with engineering methodologies, directly impacting on current material and device fabrication technologies. Formulation of standard imaging inks is highly reliant on developing the correct ink chemistry, which then determines attributes such as viscosity, drop flight, corrosive properties, surface tension, drying time, dot shape, optical density, edge acuity, fade resistance and compatibility with printing surfaces. For the best results, inks should be matched to the printing technology and equipment used. Traditional imaging inks are liquid with an aqueous or non-aqueous base, with thermal printers requiring high boiling point inks which are usually water based.

The field of IJP for forming functional surface structures is not a new one and many bespoke systems have been made that deliver small volumes of liquid material to precise locations on surfaces.[8,9] Kazuhiro Murata presented a custom-made ultra-fine inkjet system as a tool for nanotechnology research which allowed arrangements

of islands of material with a minimum size of less than one micron. Diverse materials such as conductive polymers, fine ceramics, metal particles can be used as ink materials. Using an ultra-fine silver paste, Murata achieved the direct print of an ultra-fine metallic wire of only a few micrometers in width without any pre-patterning treatment of the substrate. Furthermore, using the transition-metal nano-particles as catalyst-ink, patterned array of carbon nano-tubes were successfully obtained (figure 4.2). A field emission from the patterned carbon nano-tubes was also confirmed.[10]

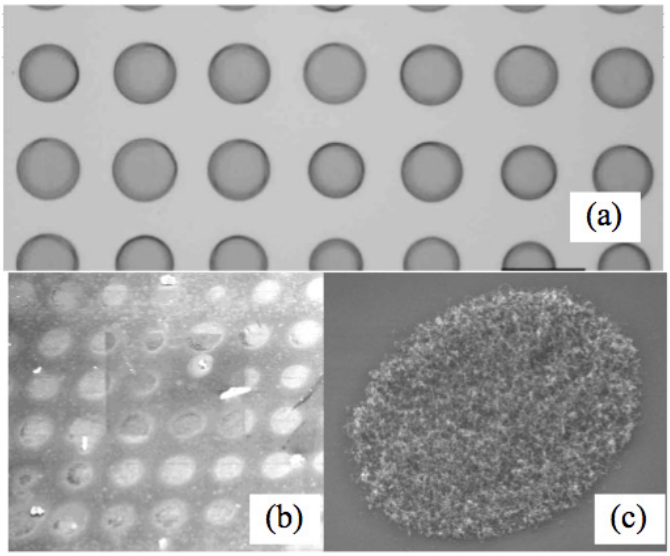

Figure 4.2. a) Optical microscope image of patterned carbon nanotube catalyst dot pitch 20 μm; **b)** and **c)** SEM image of multi wall carbon nanotubes grown at the patterned area.[10]

IJP has also been useful in the field of microelectronics, being used to fabricate conductive surfaces,[11,12] printed transistors[13,14] and display technologies.[16] The major functions in operation during IJP are:

i) creation of an ink stream or droplets under pressure,

ii) ejection of ink from a nozzle or orifice,

iii) control of drop size and uniformity,

iv) placement of drops on the printing surface.

Control of these functions depends on several design variables of the inkjet system, such as nozzle size, firing rate, drop deflection methods and ink viscosity. Changing these variables in a custom-made system can often prove costly and slow. Therefore, the ability to adapt a cheap, commercially available, consumer grade inkjet system to achieve useable features and patterns is an attractive option to researchers beginning to explore the possibilities of inkjet technology.[8]

When utilising a commercial inkjet system, careful consideration should be paid to the formulation of the 'chemical inks' used and where possible, the inks should have their viscosities matched to the standard inkjet ink. This matching of ink properties enables the printer to easily handle the solutions used as they mimic the solutions it was designed to optimally utilise. Mismatches in inks and printing technology can lead to complications and a need to understand processes such as Rayleigh instability.[17]

4.1.2.1 Inkjet printing of polymers

IJP has proved to be a useful method for controlled and reproducible delivery of small, defined volumes of polymers to solid surfaces. Calvert *et al.*[18] utlised both a custom made and adapted inkjet printer to print biopolymer and polymer materials in a layer-by-layer fashion to form insoluble complexes. Roth *et al.*[19] modified a consumer grade inkjet printer to print collagen as a lithographic basis for high throughput cell patterning (figure 4.3).

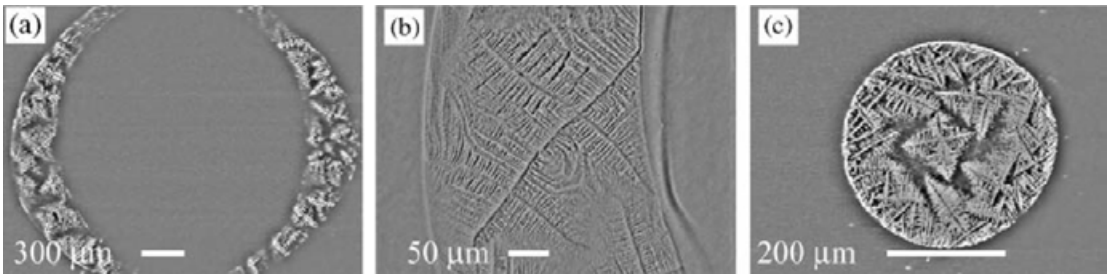

Figure 4.3. Light microscopy images of printed collagen patterns, including a ring and a circle, prior to cell seeding at **a)** x40 **b)** x100 and **c)** a circular pattern at x40 magnifications.[19]

IJP was used to create 200 µm diameter dots of polyvinylcarbazol using a Canon PJ-1080A color inkjet printer.[20] The polymer was doped with various emitting dyes to obtain different colors in a polymer light emitting display (PLED) display. An all-polymer capacitor and an RC filter were printed using an Epson Stylus Color 480 SXU inkjet printer[21] using Baytron-P and polyaniline as conducting polymers and poly(4-vinylphenol) (PVPh) as resistor. Polytetrafluoroethylene could not be used as the resistor, as it easily clogged the printer nozzle, and ethanol and acetone were poor inkjet solvents due to rapid evaporation leaving PVPh particles blocking the printer nozzles. Moon *et al.*[22] used IJP for depositing ceramic suspensions in a structured fashion on surfaces. As part of this work, they carried out an extensive investigation of various polymeric binder solution types, using a Hewlett Packard DeskJet 400 inkjet printer. Aqueous solutions of poly(acrylic acid) (PAA, Mw 5000) were tested, as well as poly[styrene-co-(acrylic acid)] (Joncryl, Mw 1,700, 4,900, 6,500, 12,500), and an acrylic copolymer (Neocryl, Mw 20,000, 38,000). Solutions contained 10 to 20 vol% of polymer. IJP is also starting to play a role in the preparation of DNA microarrays. Oligonucleotide arrays have been printed with both bubble-jet[23] and piezo technology.[24] IJP of an ink containing 1 g L^{-1} of a 600 base-pair DNA fragment

has also been reported.[25] The use of inkjet printing of DNA fragments would be another methodology to consider when wishing to carry out patterning with such biomolecules in comparison to the method presented in chapter 5.

4.1.2.2 Inkjet printing of nanoparticles

Inkjet printable materials are not just confined to polymeric materials, IJP has proved to be a viable method for printing of colloids. Lee *et al*.[26] presented the printing of nanosized silver colloids using an adapted consumer grade Espon printer, demonstrating that colloidal materials can be deposited on surfaces with a consumer grade inkjet system. Bespoke drop-on-demand systems have found much use for printing nanoparticle based materials. Magdassi *et al.*[27] presented research into using stabilized concentrated citrate-reduced silver nanocolloids for use as pigments in ink-jet inks. Kolbe *et al.*[28] formulated and printed a silver colloid filled adhesive using a bespoke microdosing system coupled with a fine glass capillary. Chung *et al.*[29] printed gold nanoparticle ink structures and post processed them by laser curing in order to form conductor microstructures. IJP has been utilised to print microemulsion-based inks for forming organic nanoparticles by printing droplets of material and post-processing to form nanoparticles.[30] IJP and its variations are promising techniques for controlled volume deposition and lithographic patterning with nanoparticulate materials.[31]

4.1.3 AFM mechanical fabrication

Nanoindentation is a method that was first employed to probe the deformation characteristics of a surface or material using the tip of an AFM. More recently, this technique has been used for fabrication of nanosize ‘wells’ or indentations on the surface of a material (figure 4.4a). The basic principle of nanoindentation fabrication

involves: bringing the tip of an AFM in close proximity with a substrate; using the controls of the AFM to lower the tip into contact with the substrate surface; controlling the force of the lowering operation and hence the depth up to which the tip penetrates into the material surface. The AFM tip is subsequently lifted from the surface and then the substrate or tip is moved to a new position for the repetition of the process.

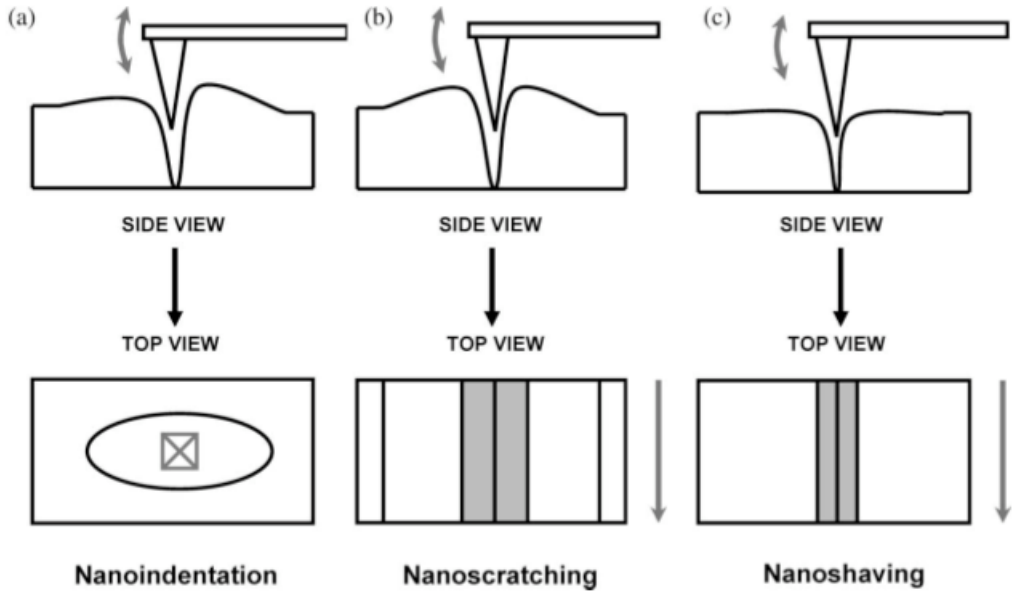

Figure 4.4. Diagrammatic representation of nanoindentation, nanoscratching, and nanoshaving fabrication processes from side views and top views: **a)** nanoindentation is the local deformation of a material formed by indenting the surface; **b)** nanoscratching is the extended formation of an abrasion on the surface of a material; and **c)** nanoshaving is the removal of material from the surface of a material.

Nanoscratching is a further development of the nanoindentation process (figure 4.4b). The nanoscratching process involves bringing the AFM tip in contact with a surface and then moving either the substrate or tip ensuring the tip is still in contact with the surface, allowing formation of trench like structures on the substrate surface.

Two types of nanoscratching operation can be performed, namely, *static* and *dynamic* scratching. The dynamic process involves the operation of AFM tip in an oscillating mode, conversely no oscillation is applied during a static process. Substrates such as silicon wafers coated with 'soft materials' such as polyimide layers several micrometers thick have been patterned using AFM scratching (figure 4.5).[32]

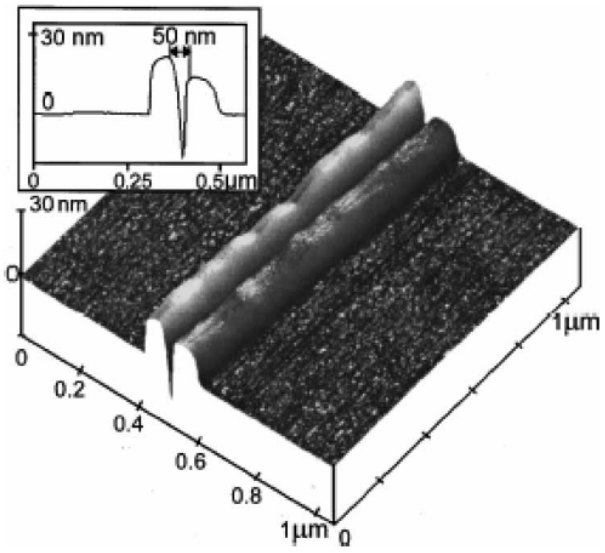

Figure 4.5. AFM image of a furrow scratched into polyimide; *inset,* cross-section of feature.[32]

Grooves were made by single passes across the surface at loads of up to 490 nN on polyimide. The narrowest achievable grooves using this method and polymer are 20 nm wide and 2 nm deep, fabricated at a force of 100 nN using Kapton-H as the commercial polyimide. Nanoscratched patterns in soft polyimide layers can be transferred through an underlying germanium layer by dry etching. The dry etching removes any remaining polyimide and etches through a small portion of germanium, followed by the removal of underlying PMMA-MAA to form a suspended germanium mask above a lower gold substrate.[32] These mask structures can then be further employed to pattern evaporated metallic layers. The AFM scratching operations are carried out using sharp silicon tips at speeds in a range of 0.2-2 μm s^{-1} and at applied

vertical forces in the range 1.5-3 μN. These conditions produce furrows diameter of approximately 50 nm. With scratching of PMMA resist films, trenches of up to 50 μm in length and widths of approximately 40 nm have also been formed.[33] It has been observed that material can accumulate on either or both sides of the scratch depending on the fabrication direction relative to the AFM tip. Also, feature depth is dependent on the setpoint amplitude of the tip. Nanoscratching can further be employed to pattern much more robust materials than just organic molecules and polymers. Nanoscratching allows alteration of the conduction behaviour of AlGaAs layered heterostructures.[34] Features roughly 4 nm in depth with widths of approximately 120 nm can be fabricated in such materials using standard AFM tips at a force of approximately 50 μN. Advances in tip design, such as being able to modify tips with electron beam deposition, allow the user to 'plough' scratches into superconducting materials.[35] Scratches in superconducting materials are used to define a 'weak link' (also known as a Josephson junction) in the superconducting material. More conventional microelectronic materials (*e.g.* silicon) have also been modified using AFM nanoscratching.[36] It is possible to scratch through the native oxide layer (approximately 2.0 nm in thickness) of silicon (100) wafers using a diamond coated tip at loads in excess of 13 μN. Grooves show a uniform V-shape and sizes range from 8 nm in depth at a force of 14 μN to 25 nm in depth at a force of 23 μN. Widths range from 90 to 240 nm for forces of 14 and 23 μN, respectively. As expected, feature size increases linearly with applied force. To further modify the substrate surface, features can be coated in Cu *via* electrochemical deposition.[36] Nanoscratching fabrication has also been exploited to create nanostructures on aluminium surfaces.[37] Pyramidal diamond tips with a radius of approximately 15 nm have been employed to create square features of approximately 600 nm × 600 nm with depth ranges of 1-10 nm.

The Oxford English dictionary definition of shaving is: “to scrape away the surface of, to cut down or pare away with a sharp tool, thereby removing very thin portions of the surface”. If we transfer this definition into the context of nanostructure formation, we can define nanoshaving as the process of dragging a sharp object, usually an AFM tip over a material to remove selected resist nanomaterial for creating nanometre scale patterns on surfaces (figure 4.4c). From this definition, the major difference between the processes of scratching and shaving is the fate of the displaced material during and after the fabrication process. Shaving is a process, which involves the removal of material, whereas scratching purely involves marking the surface or displacing material from one location to another on the surface. Overall, nanoscratching is a highly useful technique for defining structures in ‘bulk’ materials, especially soft materials where material can be easily displaced.

4.2 Aims and objectives

For smaller research institutions and businesses, the capital investment required to purchase or build fabrication equipment for applications such as surface patterning or microfluidics can often be too great. Therefore, the ability to use cheap, readily available and mass produced equipment (where the research and design costs have already been outlaid by the equipment supplier) to microstructure surfaces could be the key to success for these small research institutions and businesses. The aims of this chapter are two-fold:

i) The first aim is to demonstrate that a commercially available IJP system can be used to sequentially print polyelectrolytes and nanoparticles to glass surfaces to form microstructured polyelectrolyte/nanoparticle structures (scheme 4.2). From forming complete films of material, the limits of the minimum achievable feature size will be examined. Once

the minimum accessible feature size has been determined, attempts will be made to further reduce this minimum feature size through modification of the surface chemistry of the glass printing surface from hydrophobic to hydrophilic. A layer of gold nanoparticles (AuNPs) will then be printed on-top of the PDAC features, with the nanoparticles being attracted to the PDAC through electrostatic attraction.

ii) The second aim of this chapter is to examine the composite structures formed from the first section and examine the use of mechanical scratching away of the material in specific regions to further pattern the inkjet printed features to further improve the minimum feature resolution achievable. The tool used for this process will be the sharp tip of an AFM to define features within the composite structures but it is a technique that if successful could forseeably be replicated with a much cheaper rapid prototyping type fabrication device such as a RepRap.[38]

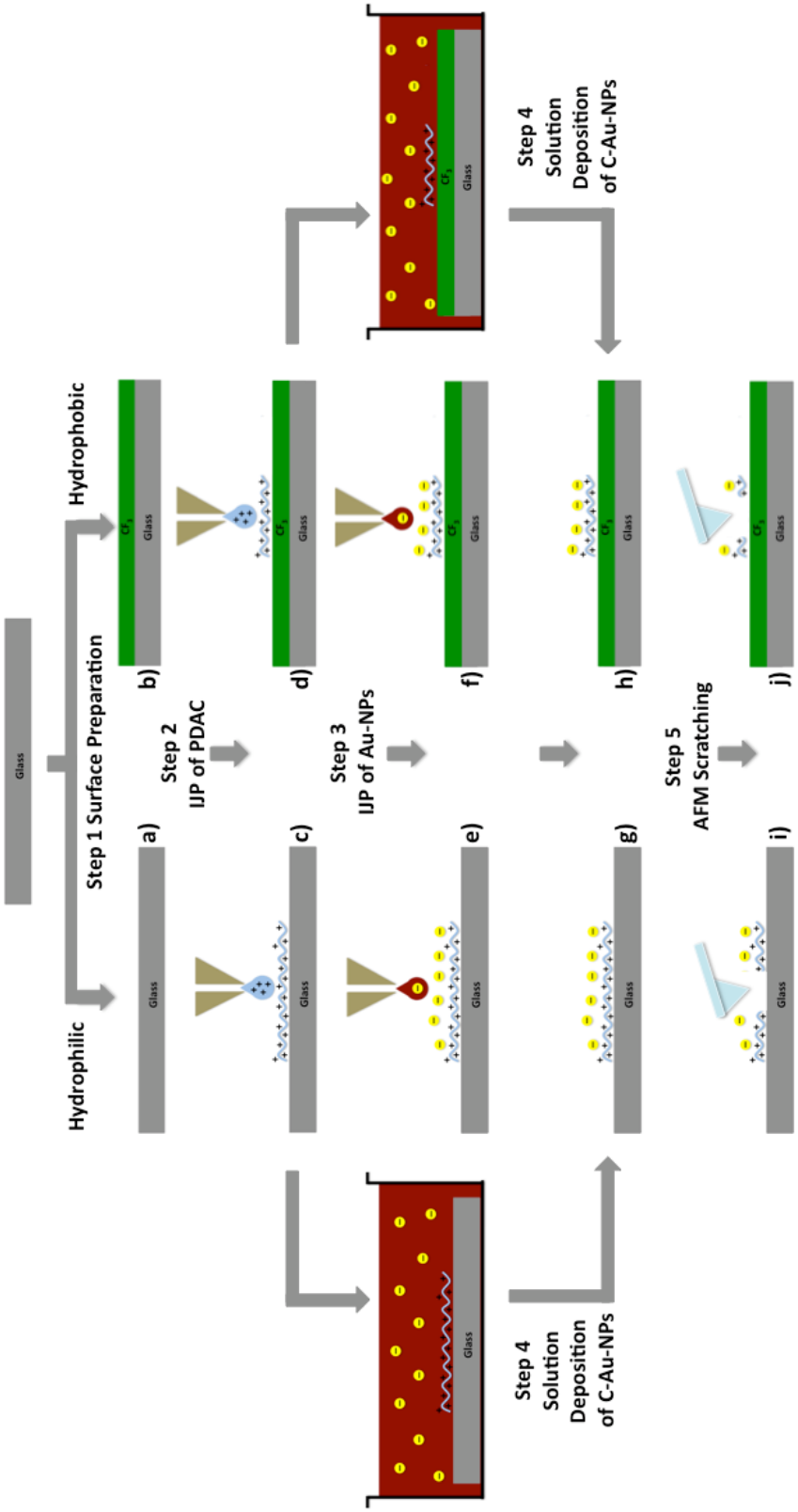

Scheme 4.2. Schematic representation of work carried out.

4.3 Results and discussion

The experimental work in this chapter can be broken down into several steps. **Step 1** will be carrying out surface preparation, so that hydrophilic (substrate a) and hydrophobic (substrate b) surfaces can be formed. **Step 2** will be to load the

polyelectrolyte solution into the standard cartridges of the inkjet printer and print positively charged polyelectrolyte to the hydrophilic (substrate c) and hydrophobic surfaces (substrate d). **Step 3** will be to load a second printer cartridge with an AuNP solution and with the same printer, print negatively charged gold nanoparticles to the PDAC printed regions (substrates e & f). **Step 4** will be to carry out the solution deposition of gold nanoparticles instead of deposition *via* IJP (substrates g & h). Finally, **Step 5** will be to use the tip of an AFM to press into the inkjet printed surfaces in order to scratch away material, thus defining even smaller structures on the inkjet printed surfaces (substrates i & j). Step 4 is alternative way to deposit the gold nanoparticles from solution. The process was used to overcome problems with IJP of gold nanoparticles.

4.3.1 Printer choice

The printer chosen for the experiments presented here uses thermal technology for drop formation and is produced by Canon (Canon Pixma ip5300). This particular inkjet printer was chosen for several reasons. The thermal inkjet technology used in this printer means that the initial cost of the printer is kept low (approx £50). This printer model also uses small droplet sizes down to 1 picolitre (table 4.1) and aqueous inks which are desirable characteristics when trying to achieve high resolution structures with aqeuous polyelectrolyte and colloidal materials. The specifications for the printer are located in table 4.1.

Table 4.1. Operating Specifications for Canon Pixma ip5300 Inkjet Printer.

Print Speed	***Black:*** *31 ppm (pages per min)* ***Colour:*** *24 ppm*
Number of Nozzles	***Black:*** *512* ***Color:*** *512 x 3 (C/M), 512 x 1 (Y/BK)* ***Total:*** *4,608*
Print Resolution	***Black:*** *600 x 600 dpi (dots per inch)* ***Colour:*** *9600 x 2400 dpi*
Ink Droplet Size	*1, 2 & 5 Picolitres*

Another main advantage of the model of printer used is that the ink delivery system is based upon 'single ink technology'. The term 'single ink technology' refers to the fact that each base colour ink has its own individual ink cartridge. More complex colours are then created with a combination of the base colour inks. With the ink delivered in this manner, it would be possible to use several 'chemical inks' per printer, delivering a different species from each ink cartridge and more importantly, choose to deliver a single 'chemical ink' to the substrate surface by printing structures with one of the base colours. This model of printer also comes with the capability to print directly to the surface of printable CD-R disks (writable CDs), *via* loading the CD-R into a cassette designed to carry the CD-R into the printer and to the print head. This cassette was easily modified to accept a standard size microscope slide (76 x 26 x 1.2 mm) (figure 4.6).

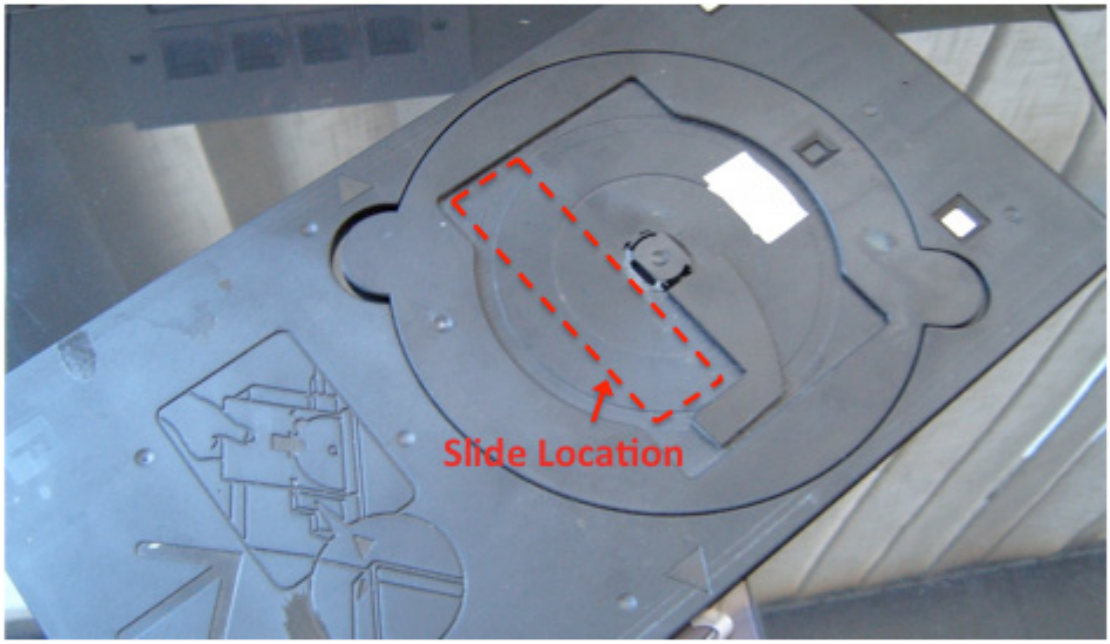

Figure 4.6. Photograph of the adapted CD carriage for printing directly to standard microscope slides with highlighted area for microscope slide placement.

The amount of material printed per unit area on the glass substrates was controlled by using the computer program MS PowerPoint. The materials used were loaded into the ink cartridge of the printer and 4 printing densities chosen in PowerPoint *(arbitrarily named 1Y, 2Y, 3Y, 4Y)* representing the increasing drop sizes (*1Y*, *2Y* and *3Y*) and a multiple pass over the same area at the biggest drop size (*4Y*).

4.3.2 Hydrophobisation of glass substrates (substrate b, step 1)

No chemical pre-treatment was required for type a substrates. To achieve smaller features without carrying out modifications to the printer itself or building a custom made system, tailoring of the material/surface interaction was perceived to be a route worth investigation. For this reason, glass surfaces derivatised with a hydrophobic silane layer *(Trifluoropropylsilane, TFPS,* scheme 4.4) were formed. CF_3 terminated surfaces such as those formed with TFPS have been shown to induce high contact angles for aqueous solutions deposited on them.[39] Glass substrates were

immersed in an ethanolic solution of the TFPS for 2 hours then removed and rinsed with fresh ethanol.

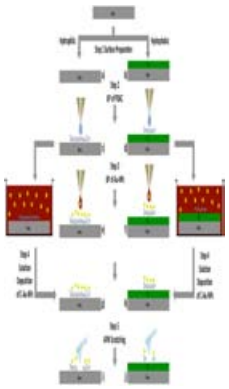

Scheme 4.4. Chemical structure of trifluoropropylsilane, TFPS.

Spectroscopic ellipsometry analysis confirmed the presence of a film 7.4 nm thick on the surface of a section of silicon wafer derivatised at the same time as the glass substrates. The thickness obtained indicates the presence of a TFPS multilayer structure as opposed to a single monomolecular layer (molecular length approx 0.7 nm, terminal Cl to terminal F). By comparing the contact angle of a 2 µl droplet of the PDAC solution on a hydrophilic glass microscope slide (figure 4.7a) and on an CF_3 terminated, hydrophobic glass slide (figure 4.7b), it was found, as expected, that PDAC exhibited a higher contact angle (~80^o) on the hydrophobised surfaces as compared to an untreated glass surface (<5^o).

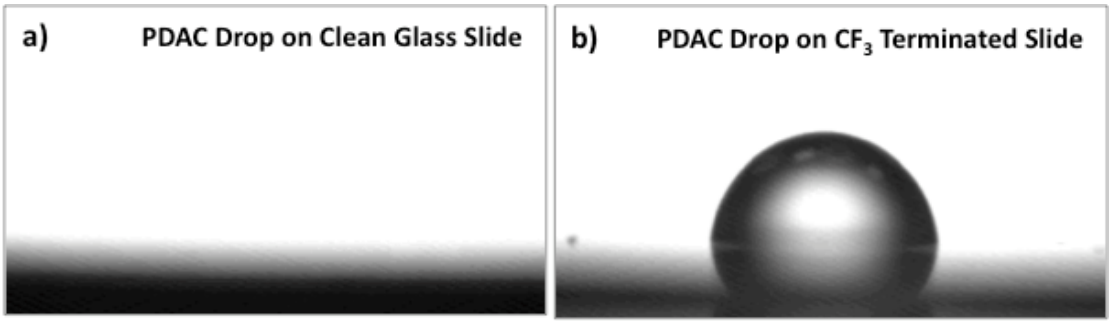

Figure 4.7. Digital photographs showing the contact angle of a 2µl droplet of aqueous PDAC solution on **a)** clean glass surface (<5^o); and **b)** hydrophobised glass surface (~80^o).

4.3.3 IJP of charged PDAC polyelectrolytes to hydrophilic surfaces (substrate c, step 2)

The cationic polyelectrolyte, polydiallyldimethylammonium chloride (PDAC, scheme 4.3) was used to print films of varying morphologies on glass surfaces.

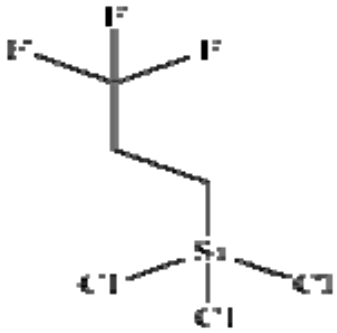

Scheme 4.3. Chemical structure of PDAC, n=100,000 – 200,000 MW.

By varying the printing densities (1Y to 4Y) it was possible to form discrete PDAC features or complete PDAC films on the glass surface. The aqueous PDAC solution was loaded into standard inkjet cartridges by drilling a hole in the top of the cartridge reservoir and first rinsing the standard imaging ink from the cartridge with H_2O and ethanol. Any remaining ink was removed by continuously printing an image

on the printer until no ink colouration was evident. An aqueous NaCL solution of PDAC (4 ml) was mixed and added to the cleaned cartridges through the drilled hole in the top of the cartridge. A glass slide was placed into the adapted CD printing tray of the printer and printing was commenced. Table 4.2 shows optical microscopy images of the complete range of film morphologies observed after printing PDAC to glass surfaces at 1Y, 2Y, 3Y and 4Y densities. The approximate amount of material deposited from the inkjet printer at each density is also presented in table 4.2 (calculated from weighing of a substrate before and after printing).

Table 4.2. Optical microscopy images of the varying film morphologies of PDAC inkjet printed at various densities per unit area (all images same scale) and mass of material deposited at each density (*calculated through weighing of substrate before and after printing*) on hydrophilic surfaces.

1Y	**2Y**	**3Y**	**4Y**
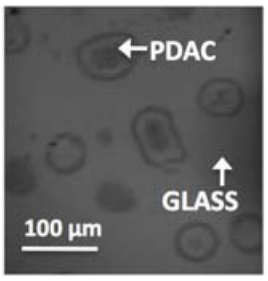	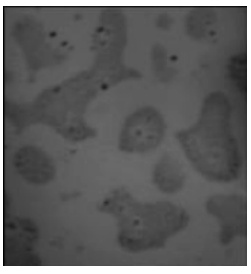		
PDAC = 31 µg/cm^2	**PDAC = 74 µg/cm^2**	**PDAC = 140 µg/cm^2**	**PDAC = 640 µg/cm^2**

It can be seen from table 4.2 at the lowest printing density (1Y, smallest drop size), individual circular 'island-like' structures are formed by the dried PDAC on the surface of the glass slides. The PDAC islands formed were approximately 50-60 microns in diameter. Attempts to carry out AFM on the islands did not yield good

quality images, possibly due to the PDAC chains interacting with the AFM tip and causing distortion of the image. As the printing density was increased, the drop sizes increased in size causing the droplets to merge and dry, creating larger structures. At the greatest printing density (4Y) the droplets have merged into a complete dried PDAC film.

Figure 4.8 shows transmitted light optical microscopy images of these printed PDAC regions. The clear PDAC solution was seen to take on a white colouration upon printing and drying on the glass surface. Figure 4.8a shows a PDAC film, inkjet printed (at 4Y density) in the form of text on a glass surface. This text printed at 4Y density showed that the individual droplets had merged together to form a complete PDAC film on the surface. Image 4.8b shows a magnified version of the highlighted PDAC area. The crystallisation of the PDAC solution that has occurred upon drying can be seen clearly in this image. Image 4.8c shows the edge of the highlighted 4Y printed feature. It can be seen that upon drying of the PDAC feature, the edge of the PDAC film has retracted from its original position, leaving a thinner film of PDAC at the edge. Image 4.8d shows a formation of text composed of individual droplets of PDAC printed at 1Y density, measuring roughly 50-60 microns in diameter, corresponding to the picolitre volumes of deposited material quoted in the printer specifications.

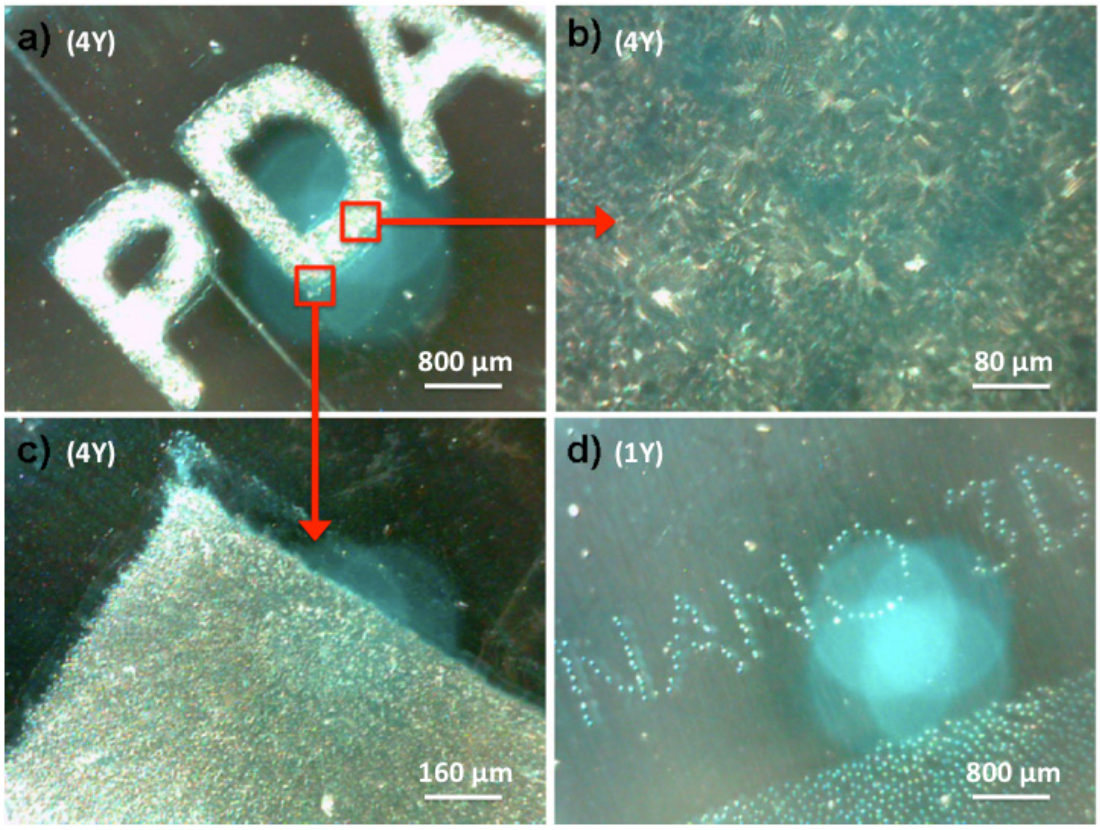

Figure 4.8. Optical microscopy images of inkjet printed PDAC regions on hydrophilic glass surfaces.

4.3.4 IJP of PDAC to hydrophobised surfaces (substrate d, step 2)

Utilising PDAC on a hydrophilic glass surface it appears that circular features in the range of 36-55 µm are inherently the smallest features that can be obtained utilising this printer, due to the interaction between the polyelectrolyte and glass surface and the volume of liquid dispensed (figure 4.9a). IJP of PDAC to hydrophobic glass microscope slides, was then carried out (figure 4.9b).

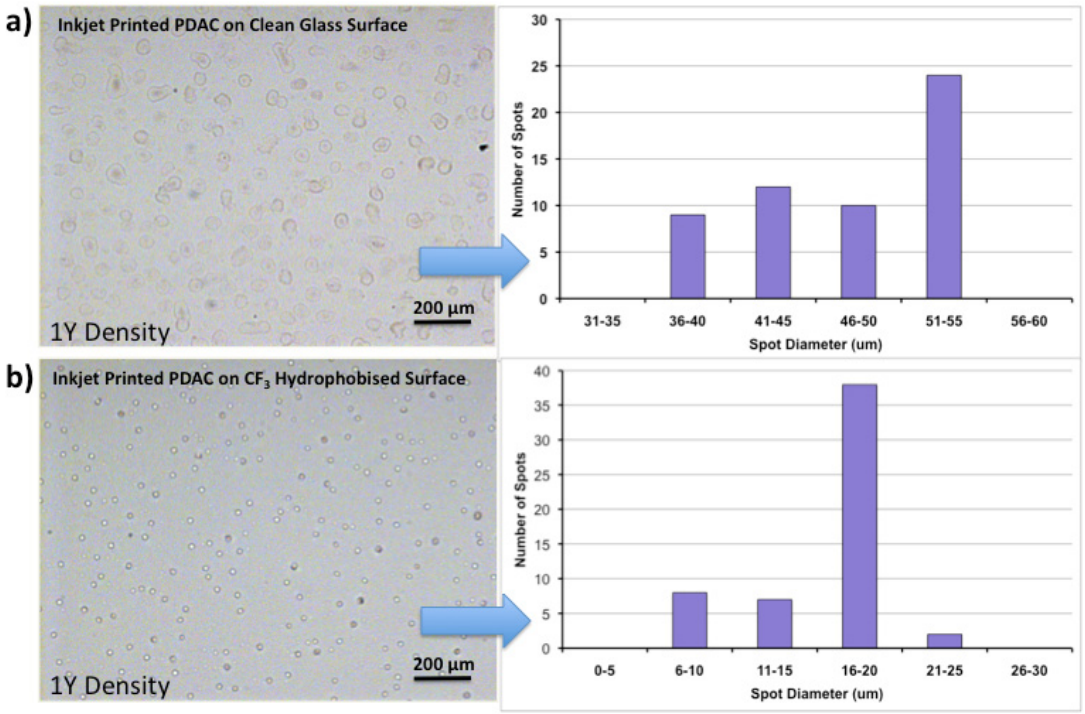

Figure 4.9. Optical microscopy images and size analysis of PDAC islands printed at 1Y density on both hydrophilic and hydrophobised surfaces.

The contrast between the feature sizes on hydrophilic and hydrophobic glass tsurface types is shown visually and quantified in figure 4.9. The size analysis carried out across 4 individual samples revealed much smaller PDAC features (approx 6 to 25 µm), on the hydrophobised surface as the PDAC droplets were unable to fully spread before drying. Figure 4.10 explains the reason for this difference in size of the dried PDAC droplets with the two types of surface used.

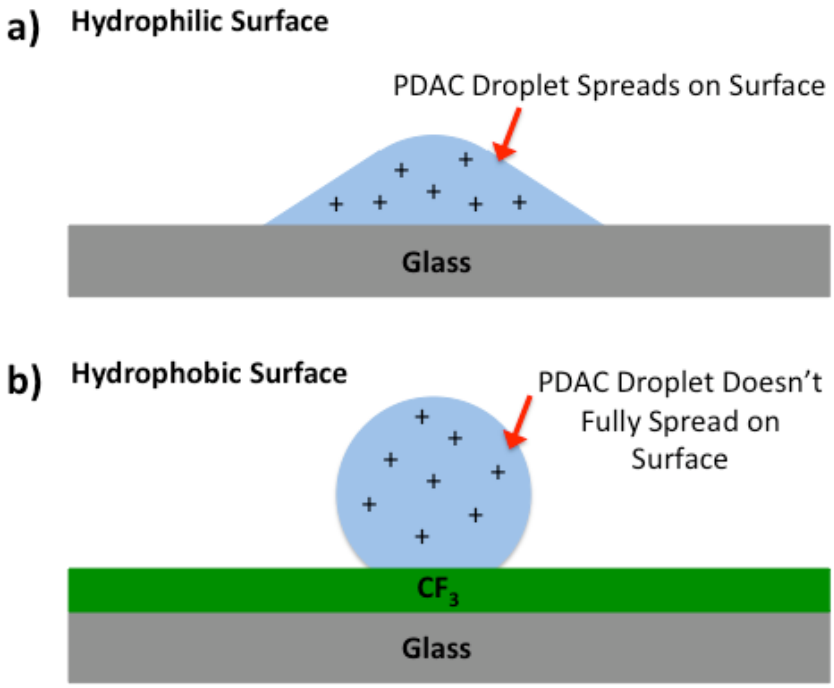

Figure 4.10. Diagrammatic representation of aqueous PDAC droplet on a **a)** hydrophilic surface; and **b)** hydrophobic surface.

4.3.5 Inkjet printing of gold nanoparticles onto PDAC features (substrates e & f, step 3)

Similar to the work presented in chapter 3, it was attempted to use IJP to deposit (through electrostatic attraction) alternating layers of PDAC and poly-anionic citrate stabilised gold nanoparticles (Au-NPs) to the same region on the hydrophilic and hydrophobised surfaces *via* IJP. However, after printing of a PDAC base pattern, the evolution on the glass surface of the red colour (from the Au-NP plasmon band absorbance) associated with LBL structures of this type was only weak and not observable with the naked eye, which was in contrast to the LBL deposition in chapter 3. It was believed at this stage that the lack of red colouration was due to the Au-NP solution being too dilute, with only a small amount of colloid being delivered to the surface. Therefore, a more concentrated (4x) solution of nanoparticles (C-Au-NP) was prepared (as detailed in chapter 2). The degree of red colour evident after printing of

both solutions was visualised by printing the neat nanoparticle solution to photographic paper. (figure 4.11)

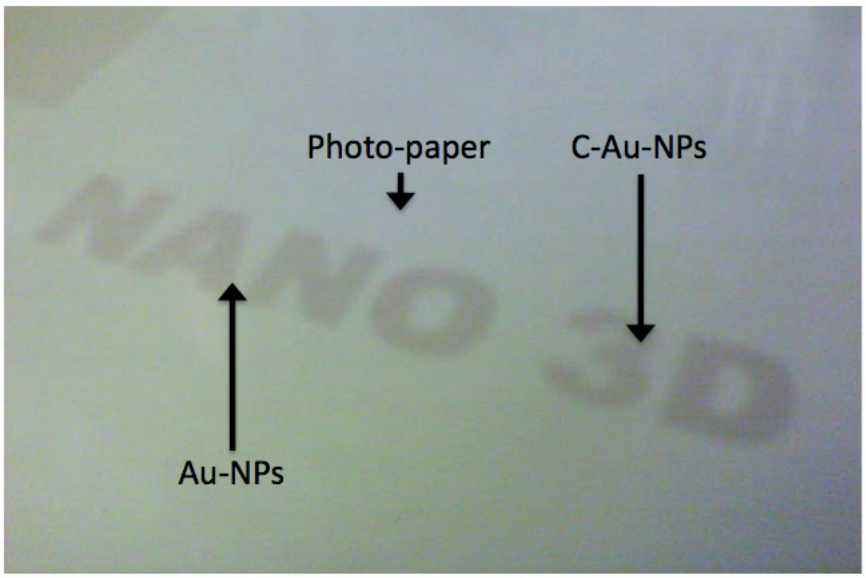

Figure 4.11. Digital photograph of Au-NPs printed to absorbant photographic paper in order to visualise their characteristic red colouration after 20 printing runs.

This method of visualisation with photographic paper revealed that for both solutions, an almost identical weak red colouration was present after a single printing run. A much deeper red colour for both solutions was only evident after 10-20 printing runs over the same region. After printing, examination of the print cartridge loaded with the Au-NP and C-Au-NP solutions revealed aggregation of the particles within the delivery nozzle of the cartridge and into the ink well (figure 4.12). After rinsing through of the printer print head with UHP H_2O and repeating the printing with fresh nanoparticle loaded cartridges, the same aggregation process still occurred in the print nozzle. As the literature has previously shown that colloids could be successfully printed using inkjet technology and observations had shown the colloids used here to be stable to high temperature, it was believed that the aggregation process of the particles within the cartridge was due to persistent PDAC

contamination within the print head of the printer causing aggregation within the nanoparticle solutions even after copious rinsing with H_2O.

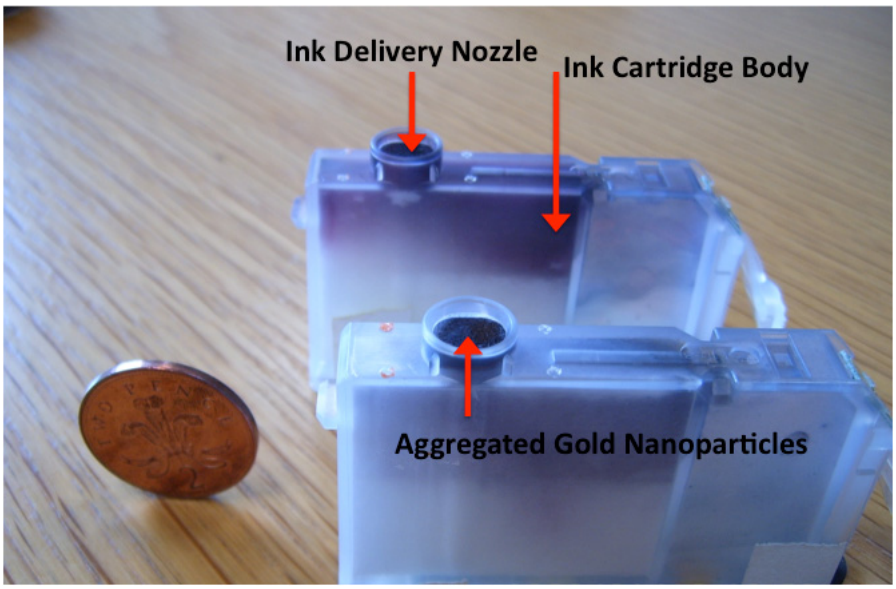

Figure 4.12. Photograph showing Au-NP aggregation (dark purple colouration) in the nozzle of an ink cartridge.

In order to overcome this aggregation problem it was decided to continue experiments by depositing PDAC *via* IJP and then, rather than printing a nanoparticle solution to the surface, the surfaces would be immersed in a C-Au-NP solution (scheme 4.2, step 4). This new immersion route can be likened to the concept of utilising a combination of top-down fabrication methodology (IJP) and bottom-up self-assembly of the nanoparticles introduced in chapter 2.

4.3.6 Inkjet printing of PDAC and solution deposition of C-Au-NPs (substrates g & h, step 4)

Before immersion in the C-Au-NPs dispersion, the printed PDAC features were rinsed for 1 minute with UHP H_2O. The H_2O rinse removed the white colouration of the PDAC that forms upon drying (presumably from the NaCl) to re-wet the PDAC layer. Figure 4.13a shows a typical area of PDAC droplet features

(printed at 1Y on a hydrophilic glass surface) during exposure to a C-Au-NP solution in order to examine the kinetics of the C-Au-NP deposition to the printed PDAC features. As time is increased, the evolution of the characteristic dark red colour on the PDAC features is seen (from the nanoparticle *plasmon band*, chapter 3), which turns to a dark purple colour over time (from the nanoparticle *longitudinal plasmon band*, chapter 3). The colouration of the PDAC/C-Au-NP features was not seen to increase past a deposition time of 1 hour. Figure 4.13b shows the resultant graph of the blue pixel intensity of the highlighted region throughout the kinetic study, showing the evolution of the blue colouration. The same behaviour was seen over 4 repeat runs.

a)

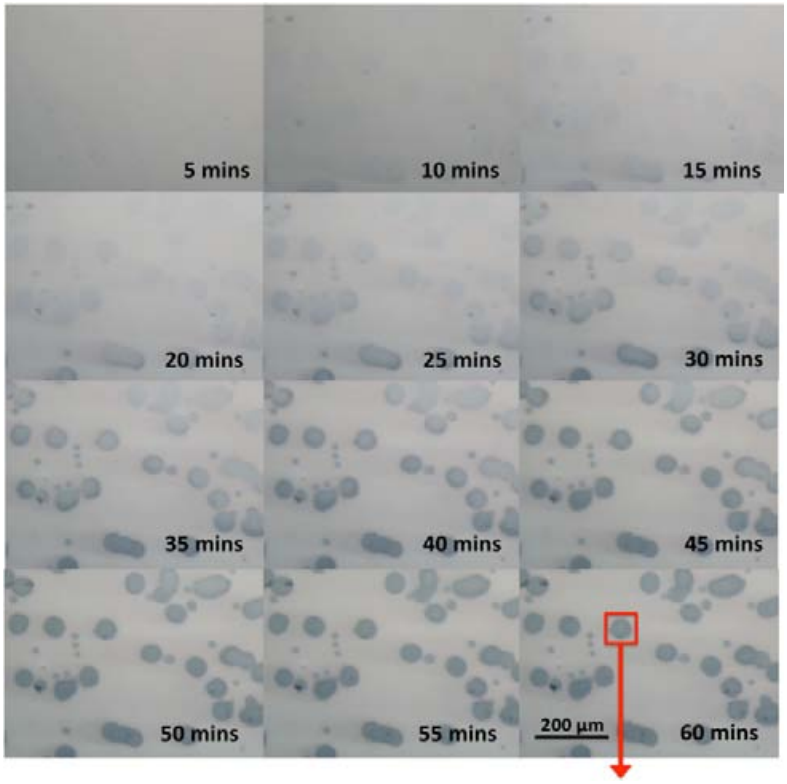

b)

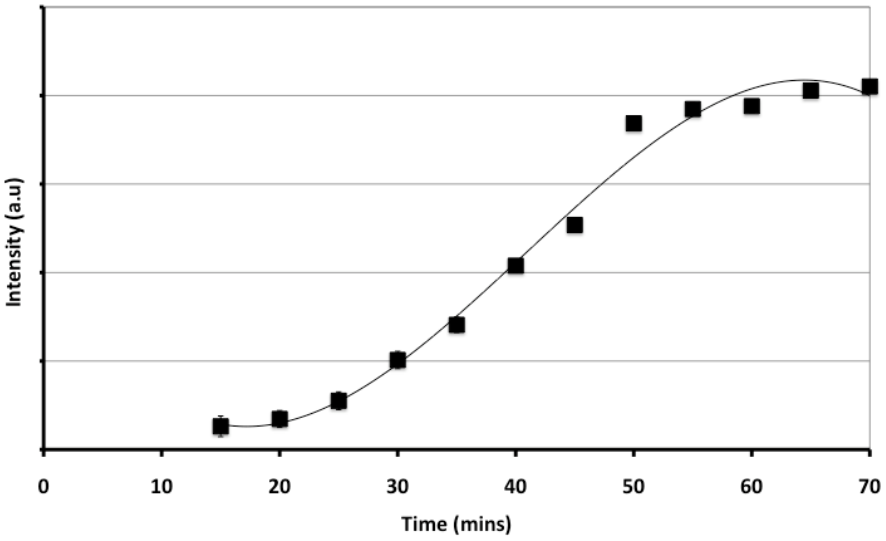

Figure 4.13. a) Optical microscopy images of inkjet printed PDAC features during immersion in a solution of C-Au-NPs; and **b)** graph showing the blue pixel count of the resultant PDAC/C-Au-NP features as a function of time.

Once an appropriate solution deposition time of 1 hour had been determined, printed PDAC features (*1Y*, *2Y*, *3Y* and *4Y*) on both the hydrophilic and

hydrophobised surfaces were immersed in the C-Au-NP solution for 1 hour then examined with optical microscopy. The resultant features are shown in figure 4.14. The deposition of the C-Au-NPs on the PDAC features visualised the regions of high PDAC concentration by depositing and aggregating on the PDAC features, giving rise to a dark blue/purple colouration (see chapter 3, explanation). In both cases (hydrophilic and hydrophobic surfaces), while not only depositing on the PDAC features, some lighter pink was observed between features. This pink colouration is believed to be where C-Au-NPs have deposited on residual PDAC left from the UHP H_2O rinsing step carried out before immersion. When printing to the hydrophobised surfaces, a complete homogeneous film was not achieved (unlike the glass surfaces) at highest 4Y density as the droplets did not spread to join up with each other.

The deposition of the C-Au-NPs allowed for better visualisation of the PDAC features and lead to the formation of bi-component films. The site specific deposition of gold nanoparticles to micron-scale features was carried out with cheap, readily available equipment that is currently within the consumer marketplace. Such technology opens up possibilities for printing of devices to substrates of choice, such as glass, silicon, gold and even flexible substrates such as polycarbonate.

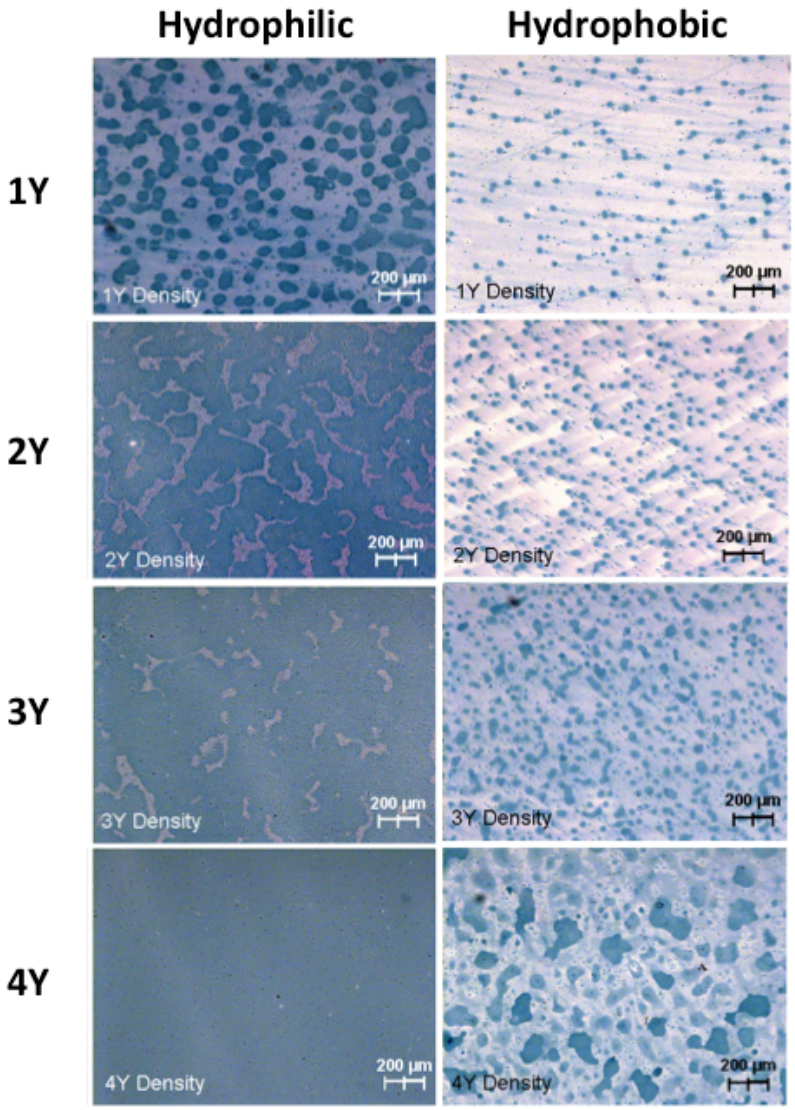

Figure 4.14. Optical microscopy of PDAC templated features on clean glass and hydrophobised glass surfaces after deposition of C-Au-NPs.

4.3.7 1Y density printing-feature size analysis (substrates g & h)

A size comparison of the circular features formed after deposition of C-Au-NPs on 1Y printed features on hydrophilic and hydrophobic surfaces revealed the true extent in the shift in feature size upon printing to hydrophobised surfaces (figure 4.15). On hydrophilic glass surfaces, the PDAC/C-Au-NP features exhibited a bi-modal distribution with a large population of feature sizes between 50 and 60 µm. The second smaller feature population was centred around 21-25 µm. For the

hydrophobised glass surfaces, a bi-modal distribution was observed, with high populations between 31 to 35 µm and 16 to 20 µm. This comparison reveals that as hypothesised, reduction in feature diameter is easily possible by simply modifying the substrate surface chemistry.

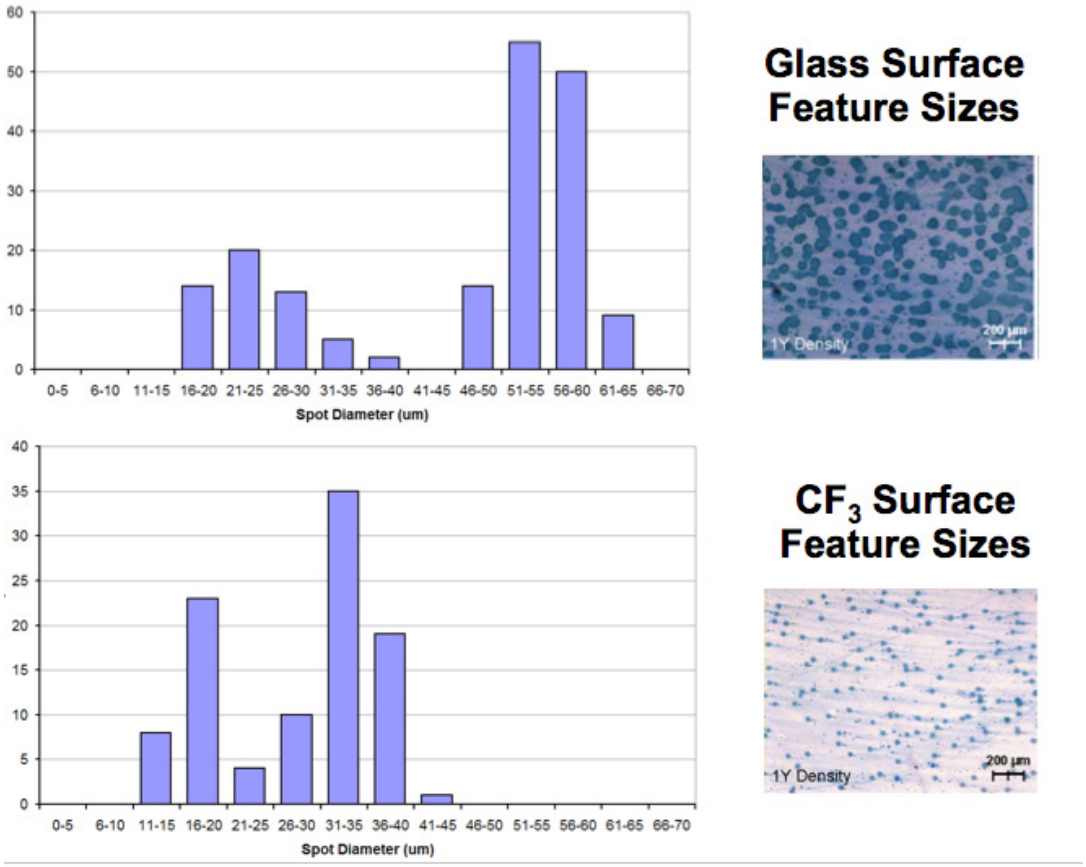

Figure 4.15. Comparison of 1Y PDAC feature sizes on clean glass and hydrophobised glass surfaces after immersion in C-Au-NPs.

The reason for the difference between the size analysis values achieved before (figure 4.9) and after deposition of nanoparticles (figure 4.15) for both the hydrophilic and hydrophobic surfaces is due to the inability to fully judge the size and extent of the bare PDAC droplets due to their refractive index being similar to that of the glass. The presence of the C-Au-NPs allowed full visualisation of all the PDAC drops.

4.3.8 AFM scratching fabrication (substrates i & j, step 5)

Once the IJP of composite PDAC/C-Au-NP features had been achieved and characterised and the minimum size features obtained through chemical modification of the glass surface chemistry, the technique of AFM scratching was examined as a route for defining structures within the IJP templated features. Initially, a 4Y PDAC/C-Au-NP film was scratched at an AFM vertical deflection value of -0.5 V (figure 4.16).

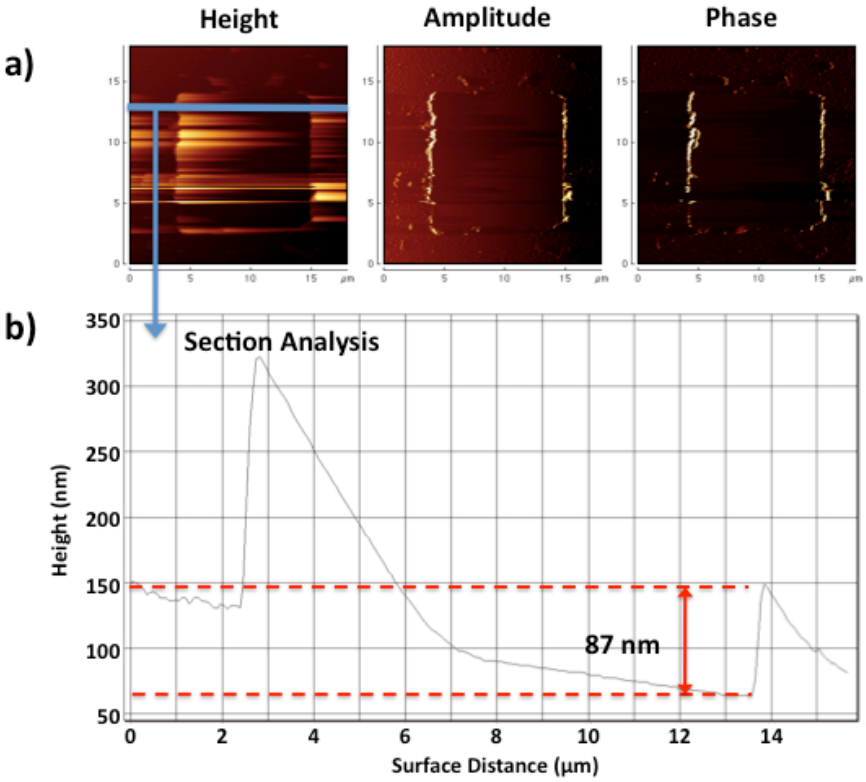

Figure 4.16. AFM **a)** *height, amplitude* and *phase* images of area after nanoscratching process; and **b)** section analysis showing apparent height from top of (PDAC/C-Au-NP) to bottom of scratched feature.

Figure 4.16a shows the presence of material at the edges of the scratched features, where it has been displaced to the sides. Figure 4.16b shows a line section from the AFM images showing this presence of material at the feature edges. The AFM section also shows that not all material has been removed across the width of

the feature, which is hypothesised to be due to the material build-up at the feature edge causing the AFM tip to not fully 'press down' into the material beneath the debris at the feature edge. The depth of the feature itself at its lowest point was 87 nm. As it was thought that the tip was not exerting enough force to displace the PDAC and C-Au-NPs, another complete PDAC/C-Au-NP film (4Y) was examined under increasing AFM tip loads. Optical microscopy of a range of square features scratched at increasing AFM vertical deflection values (figure 4.17a) revealed an optical contrast between the scratched and non-scratched regions, indicating material had been displaced. Figure 4.17b shows a close-up image of the highlighted region from figure 4.17a. This close-up image reveals that a vertical deflection on the photodiode of the AFM of -0.75 to -1 V gave rise to the most complete material displacement. This vertical deflection value can be calculated to roughly equate to an applied force of 1.95 μN, based upon a quoted cantilever spring constant of ~40 N/m and an approximate deflection sensitivity of 65 nm/V. Therefore, the applied force (μN) is 40 x 65 x volts x 0.75. This value for the required force is similar to that seen for scratching away soft materials from hard substrates.[32]

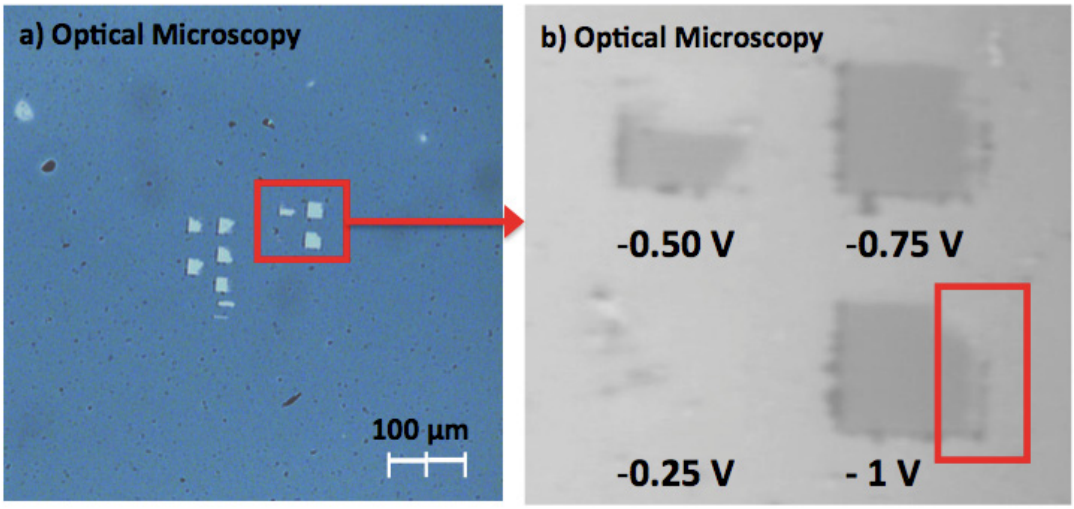

Figure 4.17. a) Large-scale optical microscopy image of AFM scratched regions of inkjet printed PDAC and solution deposited C-Au-NP film under increasing load *(or decreasing vertical deflection settings)*; **b)** close-up image of highlighted region (image a) of AFM scratched squares with highlighted region of material build-up.

The region highlighted in figure 4.16b shows the build-up of material in the top right hand corner and down the right hand side of the square features which is believed to also be some of the material removed under the motion of the tip and deposited at the feature edge of the feature as the AFM tip moves from right to left and from top to bottom. Attempts to re-image the scratched regions with the same AFM tip after the scratching were largely unsuccessful, with only poor quality images obtained. The reason for the poor quality imaging potential of the tip after scratching is thought to be due to both potential blunting of the tip and material build-up on the tip causing increased interactions between the tip and remaining material on the surface.[40] The same behaviour was seen over two runs of the experiment.

After determination of the required force, to carry out the removal of material, the circular droplet features printed at 1Y density (on both hydrophilic and hydrophobic surfaces) and immersed in C-Au-NPs, were subjected to AFM imaging under the same increased load (figure 4.18). After the scratching process, the droplets

were imaged with the camera system of the AFM. As expected, the removal of material with the AFM tip had been replicated in the centre of the droplets, showing that it was possible to further modify fabricated features after IJP.

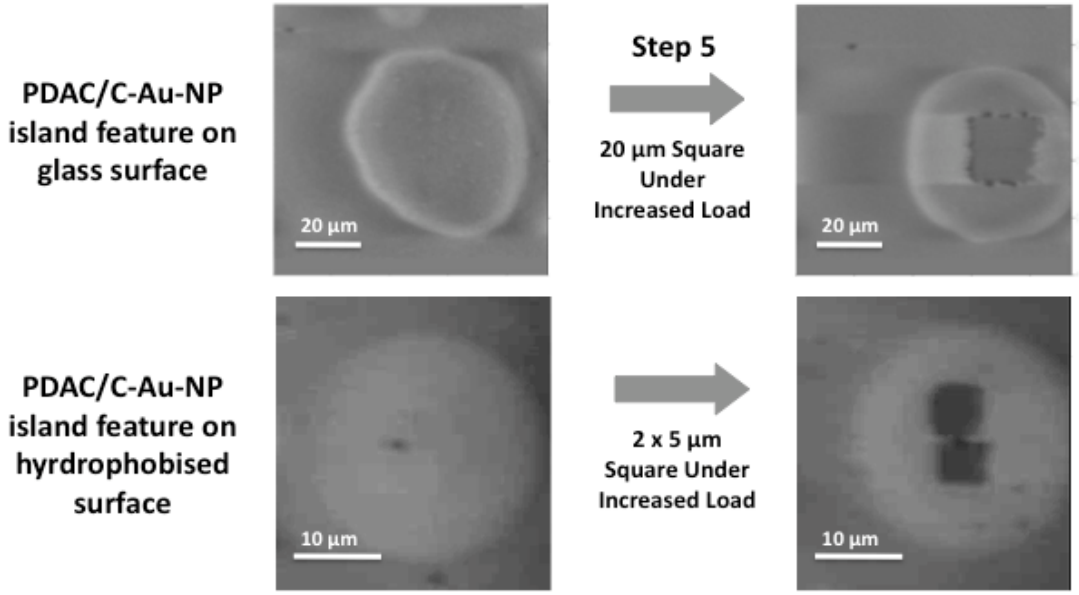

Figure 4.18. Representative optical microscopy images of the circular island PDAC/C-Au-NP features both before and after AFM scratching procedures.

In order to confirm the removal of material from the centre of the features, the features were examined with a transmitted light optical microscope. The centre of the features appeared free of the purple colour of the deposited nanoparticles (fig 4.19). The ability to define an optically transparent feature in the centre of the circular feature, opens up possibilities for forming microscale wells and recesses that may be used to optically follow reactions or biological assays occurring at their centre.

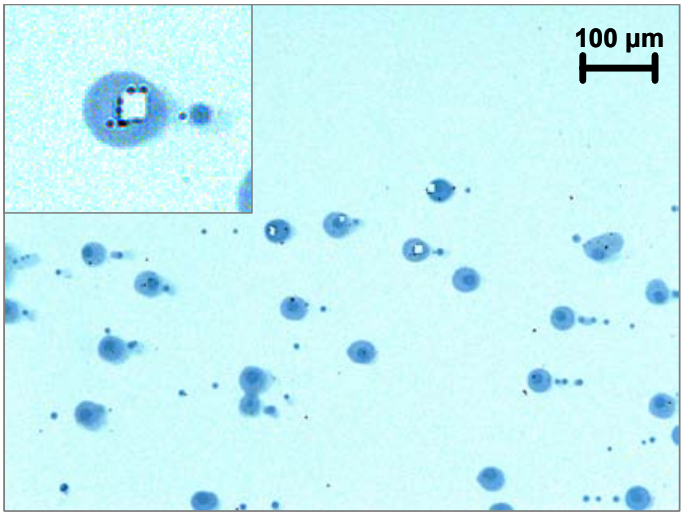

Figure 4.19. Colour transmitted-light optical microscopy image confirming the removal of the C-Au-NPs from the centre of the IJP templated features, *inset,* magnified region.

The AFM used for the scratching process did not come pre-packaged with a lithographic interface, but through careful control of the image size, image aspect ratio and tip motion of the AFM in a normal imaging mode, features other than squares were formed within the printed features. Figure 4.20 shows a 3D-rendered optical microscopy image of a group of channels scratched into a 1Y PDAC/C-Au-NP circular feature on a glass surface. The channel features were easily repeatable and had a 'V' shape cross-section resulting from the shape of the AFM tip and are approximately 2 µm wide at their widest point. The analysis of the depth of channels scratched along their length, allowed for better judgment of the thickness of the PDAC/C-Au-NP features, as no large raised edges at the tops of the channels were apparent, indicating that material has not been simply displaced to the side of the channel, but pulled completely away, possibly to the end of the channel. The depth of the channels was approximately 30 µm. This observed depth would also seem to indicate that the circular features are not composed of a single PDAC layer and a single layer of C-Au-NPs (approximately 16-20 nm) but rather an assembly of both

materials. Also interesting to note is that the bottom of the channel appears to be lower than the height of the area surrounding the circular feature. This observation could also agree with the earlier theory that residual PDAC (and hence C-Au-NPs) are located around the circular feature, or be where the AFM tip has begun to scratch the underlying glass surface. Subsequent tests however, using the same applied tip force on plain glass surfaces revealed that no scratching of the glass surface occurred under the increased tip load. The ability to define such features in the inkjet printed structures offers attractive possibilities in the fields of lab-on-chip[41] or microfluidics devices.[42]

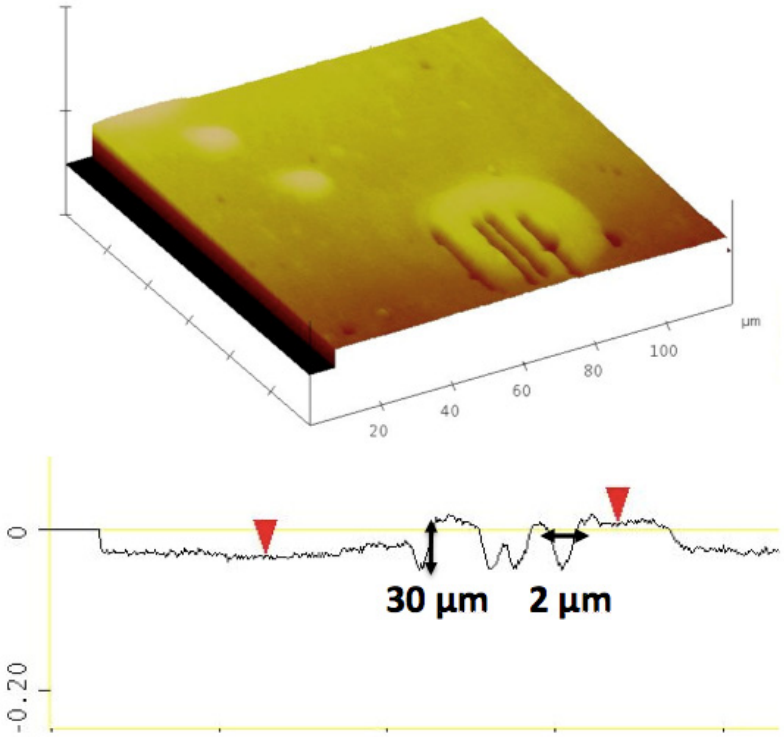

Figure 4.20. a) 3D rendered optical microscopy image of a series of linear channels scratched into the PDAC/C-Au-NP features and **b)** the resultant image cross-section.

4.4 Conclusions

In conclusion, IJP provides a viable route for surface patterning with polymers and gold nanoparticles. IJP of two interacting materials through the same printer proved difficult due to persistent contamination from the PDAC even after rinsing. To

print such materials in future, two completely separate printers or printer heads (one for each material) would be required. The combination of the top-down process of IJP of polyelectrolyte and the bottom-up process of nanoparticle assembly, therefore provided a robust and simple route to form chemically distinct patterns on surfaces. By combining IJP with surface chemical pre-treatment, smaller minimum feature sizes were achieved. The 'soft' nature of the species deposited to the surface means that features can be modified through a further top-down process (AFM scratching) to increase the range of structures that can be achieved. Further work to be carried out would be to further explore the range of materials that can be printed in this manner and improve the contrast in attachment of the C-Au-NPs on the PDAC features and any material in-between the features. The work carried out here begins to provides insights into how cheap, commercially available inkjet technology can be used to reproducibly produce structured surfaces, with applications in many different disciplines such as electronics,[43] engineering[44] and biology.[45]

4.5 Future work

While the work presented in this chapter provides firm basis for utilising inkjet technology for surface patterning tasks, further work would be required to expand the range of features achievable and materials that can be used. It is predicted that the minimum feature size achievable could eventually be further reduced by choosing a different hydrophobising agent for the glass surface, or altering the salt concentration of the PDAC solution to tailor the interaction between the PDAC solution and the surface. Furthermore, if both PDAC and the colloid or any interacting species were to be printed it would be recommended to utilise two separate printers, each containing one of the materials to minimise contamination or aggregation issues.

4.6 Experimental

4.6.1 Hydrophobisation of glass surface (step 1)

Glass surfaces were hydrophobised by immersion of a fresh glass microscope slide in piranha solution for 30 minutes, followed by rinsing with UHP H_2O. The glass slides were then immersed in RCA solution for 1 hour followed by rinsing and storage in UHP H_2O. For the hydrophobisation step. The glass slides were immersed in a solution of Trifluoropropylsilane (TFPS, 25 mM, EtOH) under ultrasonication for 2 hours. After removal from the TFPS solution, the glass slides were twice rinsed with EtOH and $CHCl_3$ and sonicated in fresh EtOH. To aid in crosslinking of the silane layer, the slides were placed in an oven at 120^{o}C for 2 hours.

4.6.2 Formulation of poly-diallyldimethylammonium chloride (PDAC) solution and loading of ink cartridges

PDAC (20 mM) was added to an aqueous NaCl (0.1M) solution. CLI-8Y (Yellow, Canon Inc) ink cartridges had a hole drilled into the top of the reservoir and the majority of the yellow ink was removed with a needle and syringe. The cartridges were then rinsed extensively with UHP H_2O (Resistivity = 18 MΩ.cm) to remove all the remaining yellow ink. To fill the cartridges with PDAC solution, the remaining H_2O was removed with a syringe and then the cartridge was filled by syringe until with the PDAC solution dripped out of the cartridge nozzle.

4.6.3 IJP of PDAC (step 2)

A commercially available inkjet printer (Canon Pixma ip5300) was used without modification. The CD printing tray for the printer was modified to accept standard size glass microscope slides. Prior to printing, fresh glass microscope slides were rinsed with ethanol and dried under a stream of nitrogen. Prior to printing the PDAC solution, the standard CLI-8Y print cartridge was removed and replaced with

an H_2O filled cartridge and several pages of plain yellow printing were printed to remove final traces of the standard ink from the printhead. When the H_2O filled cartridge was removed, it was replaced with the PDAC filled cartridge and printing was commenced. PDAC was printed at 4 different surface densities, corresponding to the four available shades of pure yellow within the software (1Y, 2Y, 3Y and 4Y). PDAC was printed onto clean glass microscope slides then allowed to air dry at room temperature then stored in a desiccator.

4.6.4 IJP of gold nanoparticles (step 3)

Solutions of Au-NPs and C-Au-NPs were loaded into empty CLI-8Y print cartridges through the same procedure used for filling with PDAC. After each use, the cartridges were removed from the print-head and the print-head rinsed thoroughly with UHP H_2O.

4.6.5 Solution deposition of concentrated nanoparticle (C-Au-NP) solution (step 4)

Prior to deposition of the C-Au-NP solution, the PDAC printed slides were rinsed with UHP H_2O for 1 minute, then immersed into a concentrated citrate gold nanoparticle (C-Au-NP) solution.

4.6.6 AFM scratching & analysis (step 5)

AFM scratching and analysis was carried out using a Veeco Dimension 3100 AFM operating in contact mode. Veeco tapping mode cantilevers (model RTESP, Veeco Instruments, Inc) were used for all experiments. For scratching experiments, scratching was carried out in contact mode and then AFM was switched to tapping mode and the same cantilever used to acquire an image of the area after scratching.

4.6.7 Optical microscopy of features

Optical microscopy of the inkjet printed and scratched features was carried out using a combination of various different optical microscopy systems. For first-point analysis, a USB microscope (DynoLite) was used. For higher magnification analysis a Zeiss Axioscope fitted with 5X and 10X objectives was utilised. For analysis of scratched features and for sizing analysis, the calibrated optical system of the Dimension 3100 AFM was used.

4.7 References

1) Jaffe, A. B. and Mills, R. N., **Color Hardcopy for Computer Systems**, *SID Proceedings*, **1983**, *24*, 219-234.
2) **Corporate Creativity: How Innovation and Improvement Actually Happens**, Robinson, A. G. and Stern, S., **1998**, Berrett-Koehler Publishers.
3) **Coatings Technology Handbook**, Satas, D. and Tracton, A. A., **2001**, Marcel Dekker.
4) Perelaer, J., Smith, P. J., Hendriks, C. E., van den Berg, A. M. J. and Schubert, U. S., **The Preferential Deposition Of Silica Micro-Particles At The Boundary Of Inkjet Printed Droplets**, *Soft Matter*, **2008**, *4*, 1072-1078.
5) **Rapid Prototyping & Manufacturing: Fundamentals Of Stereolithography,** Jacobs, P. F. and Reid, D. T., **1992**, SME Press.
6) Zhang, X., Jiang, X.N. and Sun, C., **Micro-stereolithography of Polymeric and Ceramic Microstructures**, *Sensors and Actuators*, **1999**, *77*, 149-156.
7) Hamlett, C. A. E. Jayasinghe, S. N. and Preece, J. A., **Electrospinning Nanosuspensions Loaded with Passivated Au Nanoparticles**, *Tetrahedron*, **2008**, *64*, 8476-8483.
8) Jan de Gans, B., Duineveld, P. and Schubert, U. S, **Ink-jet Printing of Polymers: State of the Art and Future Developments**, *Adv. Mat*., **2004**, *16*, 203-213.
9) Yuki, K., Takako, N., Tatsuro, N. Nobuko, S., Masaki, S. and Katsumi, U., **Development of a Surface-reaction System in a Nanoliter Droplet Made by an Ink-jet Microchip**, *Anal. Sci.*, **2007**, *23*, 91-95.
10) Murata, K., Matsumoto, J., Tezuka, A., Matsuba, Y. and Yokoyama, H., **Super-fine Ink-jet Printing: Toward the Minimal Manufacturing System**, *Microsys. Technol.*, **2005**, *12*, 2-7.

11) Xu, F., Wang, T., Li, W. and Jiang, Z, **Preparing Ultra-thin Nano-MnO_2 Electrodes Using Computer Jet-printing Method**, *Chemical Physics Letters*, **2003**, *375*, 247-251.

12) Zhao, Y., Zhou, Q., Liu, L., Xu, J., Yan, M. and Jiang, Z., **A Novel and Facile Route of Ink-jet Printing to Thin Film SnO_2 Anode for Rechargeable Lithium Ion Batteries**, *Electrochimica Acta*, **2006**, *51*, 2639-2645.

13) Shimoda, T., Morii, K., Seki, S. and Kiguch, H., **Inkjet Printing of Light-Emitting Polymer Displays,** *MRS Bulletin*, **2003** p829.

14) Sirringhaus, H., Kawase, T., Friend, R. H., Shimoda, T., Inbasekaran, M., Wu, W. and Woo, E. P., **High-Resolution Inkjet Printing of All-Polymer Transistor Circuits**, *Science,* **2000**, *290*, 2123-2126.

15) Koo, H. S., Chen, M., Pan, P. C., Chou, L. T., Wu, F. M., Chang, S. J. and Kawai, T., **Fabrication and Chromatic Characteristics of the Greenish LCD Colour-filter Layer with Nano-particle Ink Using Inkjet Printing Technique,** *Displays*, **2006**, 27, 124-129.

16) Dijksman, J. F., Duineveld, P. C., Hack, M. J. J., Pierik, A., Rensen, J., Rubingh, J.-E., Schram, I. and Vernhout, M. M., **Precision Ink Jet Printing of Polymer Light Emitting Displays**, *J. Mater. Chem.*, **2007**, **17**, 511-522.

17) **Direct-write Technologies for Rapid Prototyping Applications: Sensors, Electronics, and Integrated Power Sources**, Piqué, A. and Chrisey, D. B., **2002***,* Academic Press.

18) Calvert, P., Limem, S., Iyengar, S., and Patra, P., **Inkjet Printing of Insoluble Biopolymer and Polymer Complexes**, PMSE preprints, **2007**, *48*, 1023-1024.

19) Roth, E. A., Xu, T., Das, M., Gregory, C., Hickman, J. J. and Boland, T., **Inkjet Printing for High-throughput Cell Patterning**, *Biomaterials*, **2004**, *25*, 3707-3715.

20) Hebner, T. R., Wu, C. C., Marcy, D., Lu, M. H. and Sturm, J. C., **Ink-jet Printing of Doped Polymers for Organic Light Emitting Devices**, *Appl. Phys. Lett.* **1998**, *72*, 519-521.

21) Chen, B., Cui, T., Liu, Y. and Varahramyan, K., **All-polymer *RC* Filter Circuits Fabricated with Inkjet Printing Technology,** *Solid-State Electron.*, **2003**, *47*, 841-847.

22) Moon, J., Grau, J. E., Knezevic, V., Cima, M. J. and Sachs, E. M., **Ink-jet Printing of Binders for Ceramic Components**, *J. Am. Ceram. Soc.*, **2002**, *85*, 755-762.

23) Okamoto, T., Suzuki, T. and Yamamoto, N., **Microarray Fabrication with Covalent Attachment of DNA using Bubble Jet Technology**, *Nat. Biotechnol.*, **2000**, *18*, 438-441.

24) Sloane, A. J., Duff, J. L., Wilson, N. L., Gandhi, P. S., Hill, C. J., Hopwood, F. G., Smith, P. E., Thomas, M. L., Cole, R. A., Packer, N. H., Breen, E. J., Cooley, P. W., Wallace, D. B., Williams, K. L., and Gooley, A. A., **High Throughput Peptide Mass Fingerprinting and Protein Macroarray Analysis Using Chemical Printing Strategies,** *Mol. Cell. Proteomics.*, **2002**, *1*, 490-499.

25) T. Goldmann, T. and Gonzalez, J. S., **DNA-printing: Utilization of a Standard Inkjet Printer for the Transfer of Nucleic Acids to Solid Supports,** *J. Biochem. Biophys. Methods.*, **2000**, *42*, 105-110.

26) Lee, H-H., Chouand, K-S. and Huang, K. C., **Inkjet Printing of Nanosized Silver Colloids,** Nanotechnology, **2005**, 16 2436-2441.

27) Magdassi, S., Bassa, A., Vinetsky, Y. and Kamyshny, A., **Silver Nanoparticles as Pigments for Water-Based Ink-Jet Inks**, *Chem. Mater.* **2003,** *15,* 2208-2217.

28) Kolbe, J., Arp, A., Calderone, F., Meyer, E. M., Meyer, W., Schaefer, H. and Stuve, M., **Inkjettable Conductive Adhesive for use in Microelectronics and Microsystems Technology**, *Microelectronics Reliability,* **2007**, *47*, 331-334.

29) Jaewon Chung, J., Ko, S., Bieri, N. R., Grigoropoulos, C. P. and Poulikakos, D., **Conductor Microstructures by Laser Curing of Printed Gold Nanoparticle Ink,** *Appl. Phys. Lett.*, **2004**, *84*, 801-803.

30) Kamyshny, A., Ben-Moshe, M., Aviezer, S. and Magdassi, S., **Ink-Jet Printing of Metallic Nanoparticles and Microemulsions**, *Macromol. Rapid Commun.*, **2005**, *26*, 281-288.

31) Fuller, S. B., Wilhelm, E. J. and Jacobson, J. M., **Ink-jet Printed Nanoparticle Microelectromechanical,** *J. Mems. Sys.*, **2002**, *11*, 54-60.

32) Bouchiat, V. and Esteve, D., **Lift-off Lithography Using an Atomic Force Microscope**, *Appl. Phys. Lett.*, **1996**, *69*, 3098-3100.

33) Heyde, M., Rademann, K., Cappella, B., Geuss, M., Sturm, H., Spangenberg, T., and Niehus, H., **Dynamic Plowing Nanolithography on Polymethylmethacrylate Using an Atomic Force Microscope**, *Rev. Sci. Instrum.*, **2001**, *72*, 136-141.

34) Schumacher, H. W., Keyser, U. F., Zeitler, U., Haug, R. J., and Eberl, K., **Nanomachining of Mesoscopic Electronic Devices Using an Atomic Force Microscope**, *Appl. Phys. Lett.*, **1999**, *75*, 1107-1109.

35) Irmer, B., Simmel, F., Blick, R. H., Lorenz, H., Kotthaus, J. P., Bichler, M., and Wegscheider, W., **Nano-ploughed Josephson Junctions as On-chip Radiation Sources**, *Superlattices. Microstruct.*, **1999**, 25, 785-795.

36) Santinacci, L., Djenizian, T., and Schmuki, P., **Nanoscale Patterning of Si(100) Surfaces by Scratching Through the Native Oxide Layer Using Atomic Force Microscope**, *Appl. Phys. Lett.*, **2001**, *79*, 1882-1884.

37) Fang, T.-H. and Chang, W.-J., **Effects of AFM-based Nanomachining Process on Aluminum Surface**, *J. Phys. Chem. Solids.*, **2003**, *64*, 913-918.

38) http://reprap.org/bin/view/Main/WebHome - Accessed 16th September 2009

39) Coelho, M. A. N., Vieira, E. P., Motschmann, H., Mohwald, H. and Thunemann, A. F., **Human Serum Albumin on Fluorinated Surfaces,** *Langmuir*, **2003**, *19*, 7544-7550.

40) Carpick, R. W. and Salmeron, M., **Scratching the Surface: Fundamental Investigations of Tribology with Atomic Force Microscopy,** *Chem. Rev.* **1997,** *97*, 1163-1194.

41) Abgrall, P. and Gué, A-M., **Lab-on-chip Technologies: Making a Microfluidic Network and Coupling it into a Complete Microsystem - A Review,** *J. Micromech. Microeng.,* **2007**, *17*, R15-R49.

42) Koji Abe, Koji Suzuki, Daniel Citterio, **Inkjet-Printed Microfluidic Multianalyte Chemical Sensing Paper,** *Anal. Chem.*, **2008**, *80*, 6928-6934

43) Windle, J. and Derby, B., **Ink Jet Printing of PZT Aqueous Ceramic Suspensions**, *J. Mat. Sci. Lett.*, **1999**, *18*, 87-90.

44) Calvert, P., **Inkjet Printing for Materials and Devices**, *Chem. Mater.*, **2001**, *13*, 3299-3305.

45) Derby, B., **Bioprinting: Inkjet Printing Proteins and Hybrid Cell-containing Materials and Structures,** *J. Mater. Chem.***, 2008**, *18*, 5717-5721.

Chapter 5

Corrugations & Collagen:

The Recovery of Corrugated Au Surfaces from Au Coated CD-R Disks and the Controlled, Directional Deposition of Collagen on the Resultant Corrugated Au Surfaces, Enabling Investigation of the Mechanical Properties of Collagen Fibrils.

Abstract

The work presented in this chapter describes the use of the technique of template stripping to recover micro/nanoscale topographically structured Au surfaces from cheap, readily available Au coated CD-R disks and their transfer to silicon substrates, without the need for costly pre-fabrication costs. The corrugated Au surface is then used in conjunction with a novel technique based on the phenomenon of circular couette flow, to effect the deposition of collagen fibres and fibres with controlled orientation on the Au surface. Finally the use of these surfaces is exploited to examine the mechanical properties of the collagen through examining its suspension over the surface corrugations with AFM.

5.1 Introduction

The ability to influence control over the deposition of species to surfaces is becoming increasingly important for carrying out repeatable processing and fabrication of micro/nanostructured surfaces,[1, 2] while the ability to define the placement[3] and directionality[4] of such surface deposited species is a highly desirable tool for the experimental scientist. Topographically structured surfaces can be fabricated *via* many methods such as photolithographic processes,[5,6] DPN,[7] μCP[8] or

mechanical methods.[9] Such surfaces find uses in applications such as microfluidics.[10] As reported by Hua Zhong,[11] a cheap, commercially available topographically structured surface can be found on CD-R (Writable CDs) disks for data storage. CD-R disks containing an Au reflective layer have been utilized as a cheap substrate on which SAMs can be formed. There has also been recent interest in the use of so-called *'on-plastic'* or *'flexible'* electronic technology.[12, 13] Such technology has also found use in many systems for sensors and display technology.[14] The ability to form micro/nanostructured surfaces based on such substrates opens up the possibility for forming more robust devices or sensors as opposed to the standard *'un-flexible'* substrates currently employed, such as glass, quartz and silicon wafers[15] and Au on glass.[16]

5.1.1 Structure of Au-coated CD-R disks

In pre-recorded CD-ROM disks, the data is stamped as low reflectivity pits or valleys on a high reflectivity background. A standard disk has a reflectivity of 70% (achieved by using an aluminium layer), whereas the valleys have a reflectivity of 30%. A CD drive uses this difference in reflectivity to read the information stamped on the disk. To be compatible with this CD drive technology a CD-R disk must also use a difference in reflectivity when recording data. To accomplish this reflectivity difference, the CD-R disk is coated with a photosensitive organic dye, such as phthalocyanine or poly-methane-cyanine that changes its reflectance permanently upon heating by a focused laser spot.[17]

Commercially available gold coated CD-R disks are composed of a multilayer structure of a

a) 5-20 μm protective polymer coating

b) 50-100 nm gold reflective layer

c) 50-100 nm photosensitive dye layer

d) polycarbonate base (figure 5.1).

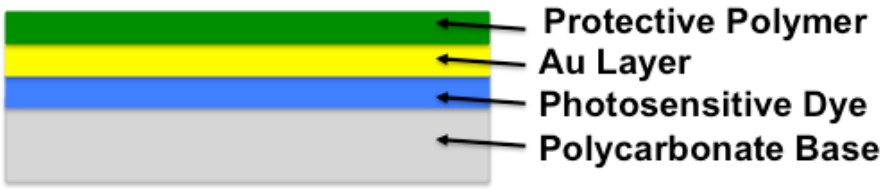

Figure 5.1. Structure of gold coated CD-R disks.

For long-term data archiving, an Au reflective layer within the CD-R is favoured due to the long-term unreactivity of the Au, meaning that data can be stored for long periods. The Au surfaces can be accessed by a simple immersion in concentrated (70%) HNO_3 to remove the protective polymer coating.[11] The advantage of such substrates over more conventional glass based Au surfaces is firstly, the polycarbonate base, making them robust, but also allowing for ease of dicing with just a standard pair of scissors and secondly, the pre-formed surface corrugations that allow movement of the read-write head of the CD drive. The structure of the surface is a regular repeating pattern of approximately 120 nm deep 'valleys' and 1 μm wide 'peaks', similar to diffraction gratings.[18] Such substrates are ideal for carrying out analysis of advanced materials and prototyping microfluidic systems as the size of the surface corrugations is highly uniform and directional. These topographically structured surfaces are also ideal donor surfaces for transfer to more common surfaces such as silicon through a process such as template stripping.[19]

5.1.2 Template stripping

The technique of template stripping was first published by Hegner *et al*. [19] for preparing ultraflat Au surfaces. For high resolution imaging techniques, a highly flat surface is required in order to image absorbates on surfaces. Surfaces prepared by techniques such as thermal evaporation and sputtering suffer from regions of high defect density with small grain sizes and high roughness.[20,21] The template stripping technique involves coating a flat substrate such as mica with a gold layer (by evaporation and condensation) of the required thickness. The gold surface is then coated with an epoxy resin and a second substrate, usually a silicon wafer is bonded via epoxy to the gold layer and allowed to set. The two substrates are then separated at the Au/mica interface affording an ultraflat gold surface that was templated on the atomically smooth mica surface.

5.1.3 Collagen

Collagen, is a biologically important protein and the primary structural component in extracellular matrices, has been the subject of much interest for developing micro/nanostructured surfaces due to its high tensile strength,[22] inherent biocompatibility and hierarchical nature. Extracellular matrices normally contain collagen molecules (tropocollagen) packed into fibrils 20 to several hundred nanometers in diameter and fibril bundles (fibres) as large as several hundred microns (figure 5.2) .[23]

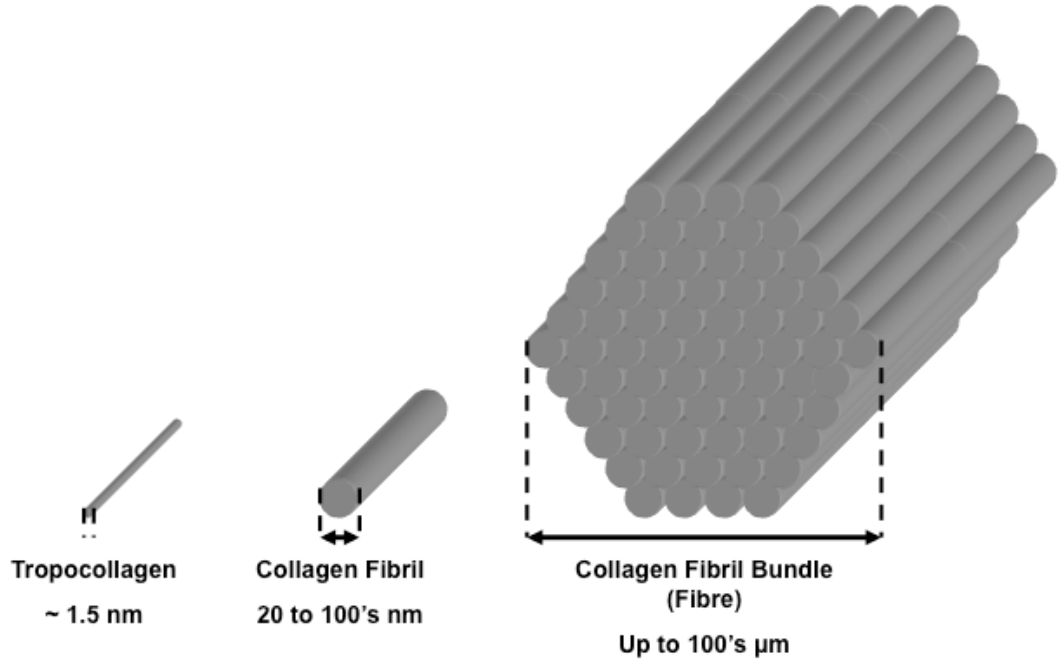

Figure 5.2. Diagram showing the hierarchical nature of collagen.

A body of work has been carried out to relate the diameter of collagen fibrils to its tensile strength,[24] as well as analysing the origins of this mechanical strength experimentally and through simulation.[25] Such tests, however, are reliant upon obtaining control over the collagen fibres and fibrils themselves to isolate them and test their deformation along a given direction.[26] Much work has been done on analysing the deposition properties of collagen [27, 28, 29] and forming surface adsorbed collagen structures [30, 31] and networks.[32] To accurately test collagen structures or form bespoke collagen networks, a technique is required that can direct the orientation of collagen effectively and controllably. For alignment of collagen on surfaces, research presented previously has relied upon pre-fabrication of microfludic channels through which collagen can flow to influence its orientation,[33] utilizing electrostatically influenced organization of fibrils at high concentrations[34] or pattern formation upon solvent evaporation.[35, 36] Pre-experiment fabrication for microfluidic systems can often be costly and time consuming and other techniques might not yield the required directional control over collagen fibres and fibrils. The development of a simple

technique to direct the orientation of not only collagen but other species of interest such as microfibres[37] or nanotubes[38] would afford the experimentalist a cheap yet powerful tool for controlling the deposition of such species. Such a technique would require readily available equipment and the ability to deposit the species (especially collagen) from solution or a suspension. The movement of fluids under force or pressure is well known to create instabilities[39, 40] or regular repeating patterns.[41] One such phenomenon is known a Couette-Flow.

5.1.4 Circular-couette flow

In fluid dynamics, couette flow refers to the laminar flow of a viscous fluid in the space between two parallel plates, one of which is moving relative to the other. The flow is driven by virtue of viscous drag force acting on the fluid and the applied pressure gradient parallel to the plates. This type of flow is named after Maurice Marie Alfred Couette, a Professor of Physics at the French university of Angers in the late 19th century.[42] Circular-couette flow is an extension of this phenomenon, where the two parallel plates are in-fact two surfaces of concentric cylinders (figure 5.3). Circular-couette flow is the basis for apparatus to measure the viscosity of liquids.[43] The regions of laminar flow can often be seen as horizontal patterns forming in the solution.

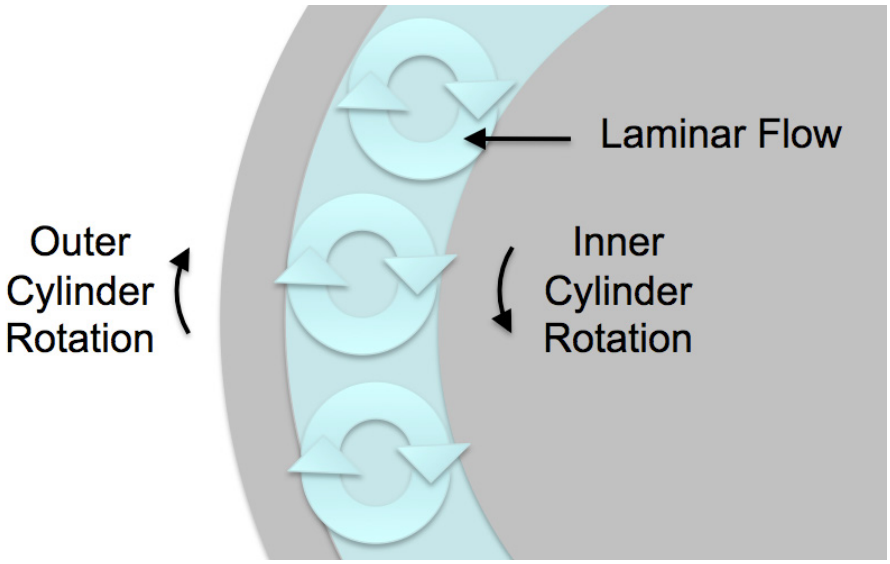

Figure 5.3. Diagrammatic representation of two rotating cylinders acting upon a viscous liquid to induce circular couette flow viewed from above.

5.2 Aims & objectives*:*

The aims of this chapter are three-fold (scheme 5.1).

i) The first aim is the use of commercially available gold coated CD-R disks (usually used for archiving purposes) as donor substrates for surface science applications is to be investigated (**scheme 5.1, Surface Preparation**). The structured gold surfaces offered by these substrates presents a regular repeating pattern of 'peaks' and 'valleys' with both micro and nanoscale dimensions that could have many applications in surface science. In their native form, the gold surfaces exist attached to the flexible polycarbonate backing of the CD-R disk. In order to be used in some applications, the structured surfaces would require transfer to a more conventional substrate such as glass or silicon. Therefore, the removal of the gold structured surfaces from the polycarbonate backing and transfer to silicon wafers to form a pseudo surface of the same structure (CD-Au) will be carried out. This transfer will be achieved through the process of template stripping and the quality of the surface after the procedure will be assessed with AFM, XPS and SEM.

ii) The second aim of this chapter is to utilize the acquired CD-Au surfaces in conjunction with a new technique conceived for this work (**scheme 5.1, Collagen Deposition**). By using the phenomenon of circular couette flow with a small CD-Au substrate attached to the inner cylinder while rotated in a suspension of collagen it is hoped that the directed, directional deposition of collagen fibres and fibrils on CD-Au topographically structured surfaces can be achieved. The technique to be used exploits the phenomenon of circular couette flow to impart directionality on collagen fibres and fibrils when depositing to surfaces. The use of such structured surfaces and the ability to control the orientation of the collagen fibres/fibrils would allow the

experimentalist to orientate the collagen in any required direction.

iii) The final aim of this chapter is to take the CD-Au topographically structured surfaces and collagen deposited over the valleys of the surface and demonstrate that the mechanical properties of the collagen can be examined using AFM (**scheme 5.1, AFM Analysis**).

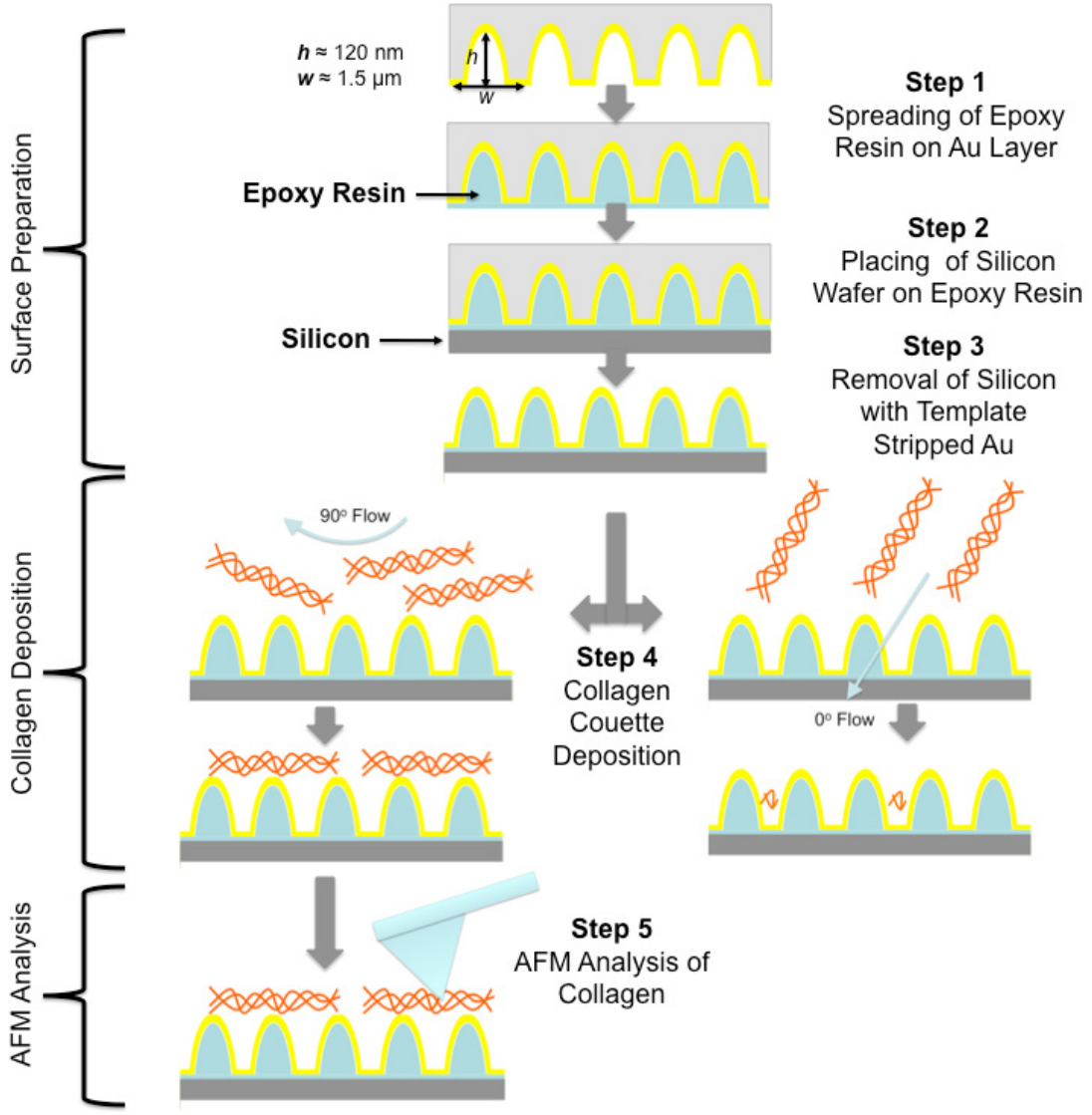

Scheme 5.1. Schematic diagram of the experimental process carried out.

5.3 Results & discussion

The research methodology for the work carried out is as follows (scheme 5.1): **Step 1** involves the spreading of epoxy resin onto the surface of the gold-coated polycarbonate CD-R-Au disk. **Step 2** places a silicon substrate on top of the epoxy resin layer before the epoxy hardens. **Step 3** Removes the silicon substrate from the polycarbonate carrying the attached gold surface with it. **Step 4** then uses the prepared silicon CD-Au surfaces as substrates for the directed, directional deposition of collagen at either 90^0 to the corrugations or 0^0 to the corrugations. **Step 5** uses AFM after the collagen deposition to examine the deformation of the 90^0 deposited collagen into the corrugations of the Au surface.

Overall, the complete experimental process examines a new method for achieving low-cost pre-patterned Au surfaces with nanoscale dimensions, a technique for influencing the deposition direction of micro/nanoscale species and the combination of the two processes for probing mechanical properties of the micro/nanoscale species.

5.3.1 Preparation of CD-Au surfaces

5.3.1.1 Pre-preparation & structure of CD-R-Au disks

The Au layers of the Au coated CD-R-Au disks were exposed by immersion in concentrated HNO_3 for approximately 3 mins.[11] After removal of the protective polymer coating, the sections of CD-R disk were imaged with AFM (figure 5.4). AFM imaging showed the CD-R disks to have a regular repeating pattern of ‘peaks’ and ‘valleys’ (corrugations).

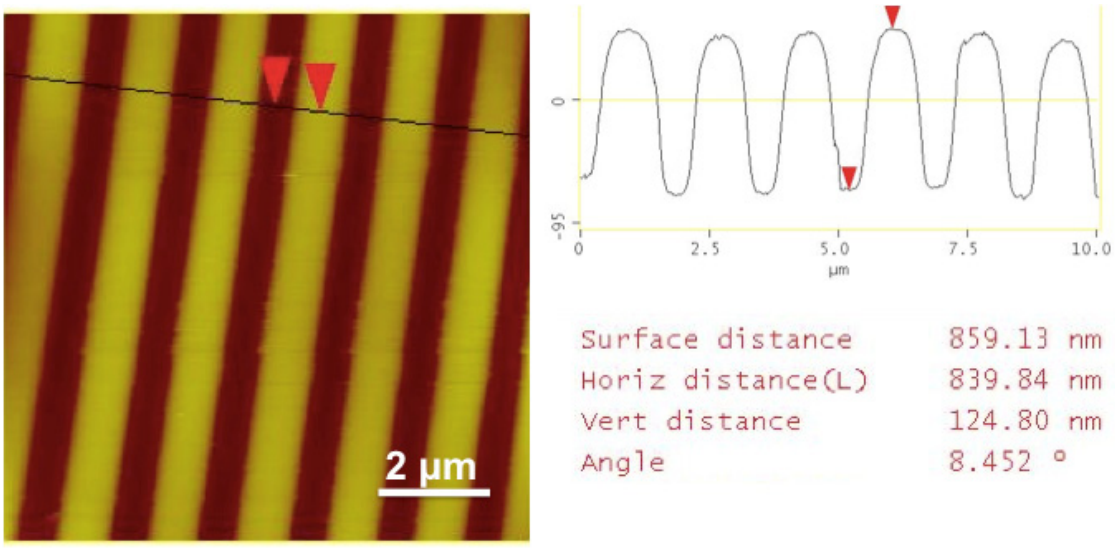

Figure 5.4. Contact mode AFM image of Au coated CD-R disk and line section showing depth of the 'valleys' after immersion in HNO_3.

The peak to peak distance of the surface structure were 1.5 µm and the depth of the corresponding valleys were 120 nm. This pattern was repeated across the entire surface area of the CD-R disks.

5.3.1.2 Template stripping (steps 1-3)

Template stripping was carried out using the procedure detailed by Hegner *et al.*[44] for preparing flat Au surfaces by template stripping from Au coated mica surfaces. The main concern with template stripping the corrugated Au surface was that the CD-Au substrates retained the corrugated structure of the original surface. A thin layer of epoxy resin (Epotech 301/2) was applied to the freshly prepared Au coated CD-R disks and allowed to spread to fill all the surface corrugations (scheme 5.1, step 1). A section of silicon wafer was pressed down onto the resin layer and the resin allowed to harden overnight (scheme 5.1, step 2). To separate the polycarbonate base and the silicon section a thin, sharp scalpel blade was passed between the two and pressure applied to separate the layers. The Au layer was transferred to the silicon

substrate (scheme 5.1, step 3). After the transfer process, the CD-Au surface was re-examined with optical microscopy and AFM (figure 5.5).

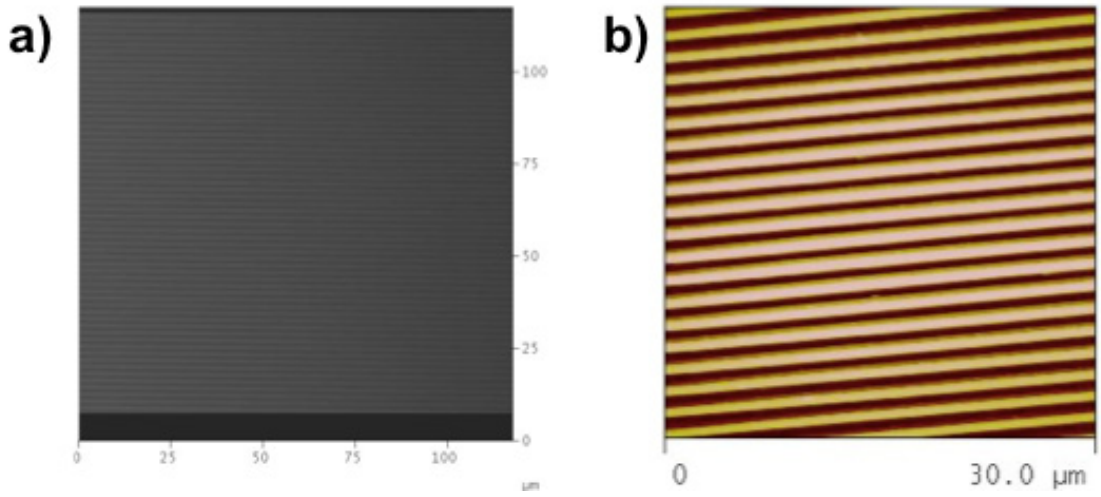

Figure 5.5. a) optical microscopy image; and **b)** contact AFM height image of CD-Au substrate.

The CD-Au substrates retained the corrugated structure of the original Au coated CD-R template, showing that the Au layer could be successfully transferred with large areas free from defects. A sole defect on a 1cm^2 sample was imaged with SEM (figure 5.6). The SEM image showed the outermost Au layer with its corrugated structure and the underlying hardened epoxy resin layer with the imprint of the corrugations from the gold surface. The process was carried out over ten times with reproducible results.

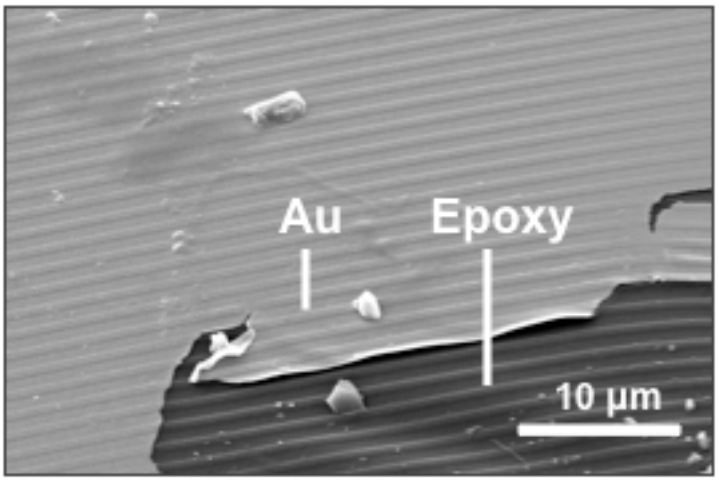

Figure 5.6. SEM image of a defect area showing the outermost Au layer and the underlying epoxy resin layer.

In order to confirm that the Au layer was exposed, XPS analysis was carried out to look for the characteristic Au $4f_{5/2}$ peaks at 88 eV and Au $4f_{7/2}$ peak at 84 eV, confirming the presence of the Au layer.

5.3.2 Circular-couette deposition of collagen (step 4)

5.3.2.1 Couette cell design

The couette cell used for the procedure was fabricated from two concentric glass cylinders (figure 5.7). The central cylinder had a flat recess to locate a small 1 cm^2 Au substrate.

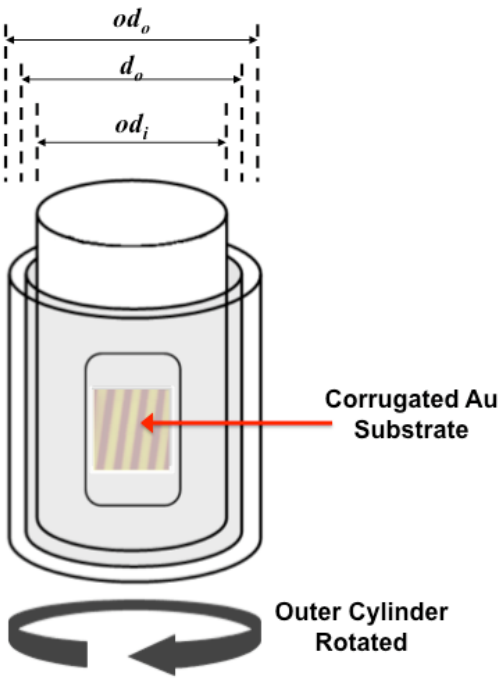

Figure 5.7. Diagram showing the design and dimensions of the couette cell designed for and utilised in this study, with the substrate attached to the inner cylinder.

The outside diameter of the inner cylinder (od_i) was 22.8 mm. The inside diameter of the outer cylinder (id_o) was 23.8 mm, which corresponded to a gap between the two cylinders of 0.5 mm. For completeness, the outside diameter of the outer cell (od_o) was 25.2 mm. For the experiment, only the outer cylinder was rotated, which served two purposes, to keep the experimental setup as simple as possible and to not impose a greater angular momentum on the solution. Higher angular momentums have been seen to induce turbulent flow at 90^o to the direction of imposed flow, with the phenomenon known as *taylor-couette flow*.

The rotation of the outer cylinder was carried out with a 12 V motor connected to a DC power supply. The rotation speeds of the outer cylinder were determined *in-situ* using a high speed camera by counting the passes of a known point over a set time and with a laser tachometer using a reflective target on the outer cylinder (figure 5.8). The values obtained for the speeds of rotation are presented in figure 5.9.

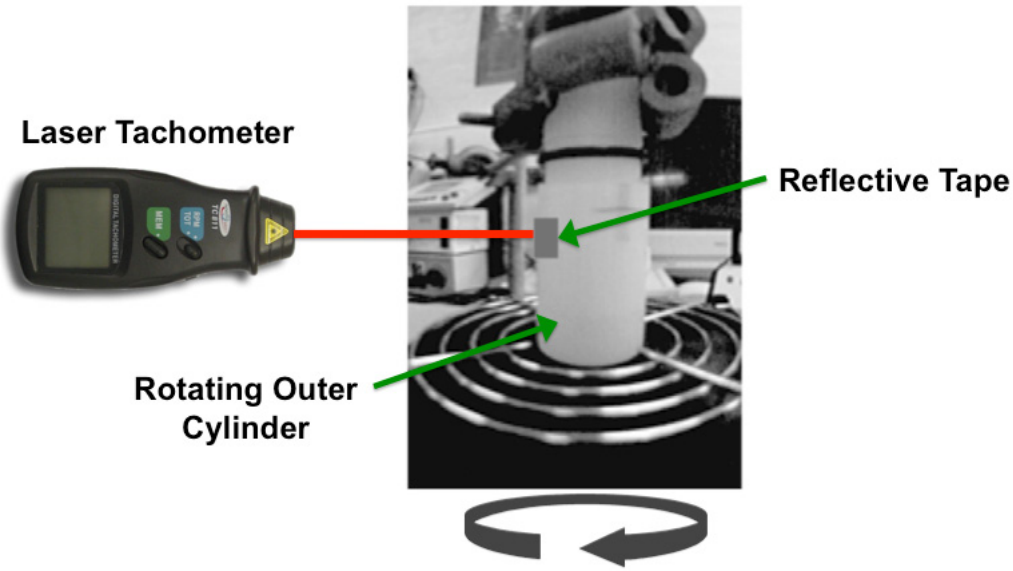

Figure 5.8. Diagram showing setup for measuring the speed of rotation.

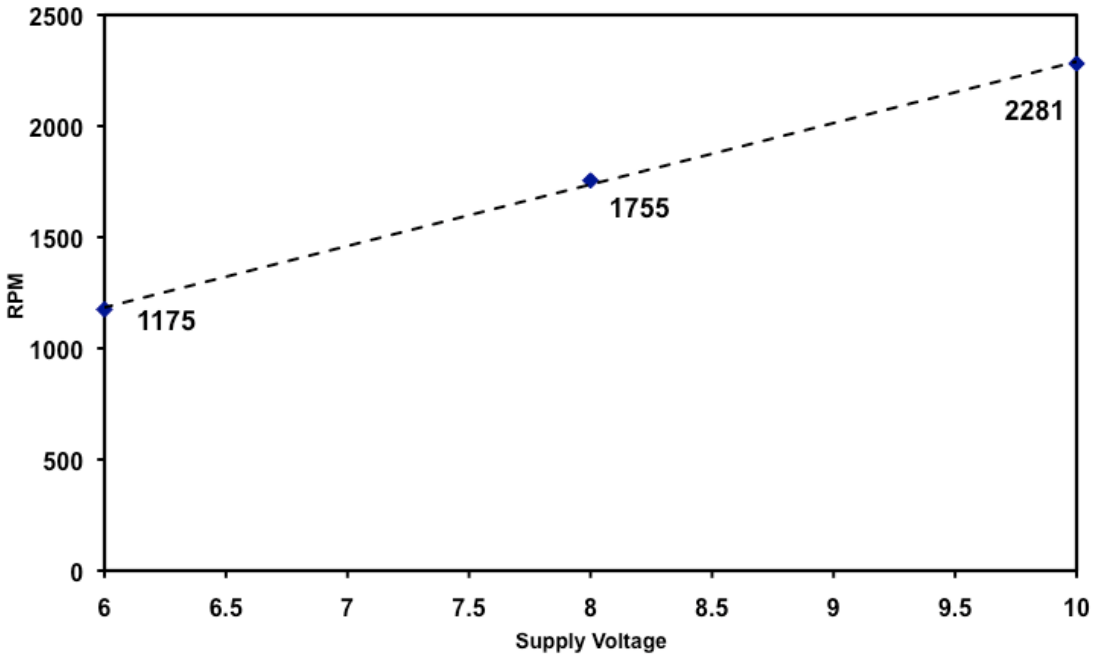

Figure 5.9. Graph showing the measured rotation speeds achieved at the motor supply voltages.

5.3.2.2 Collagen fibre and fibril deposition at 0^0 to corrugations.

Samples were freshly prepared by removing the template stripped CD-Au from the polycarbonate backing and placing into the recess on the inner cylinder of the couette cell with the direction of flow in-line with the surface corrugations (0^0). A freshly prepared collagen solution was placed into the outer cylinder and the two cylinders assembled on the motor assembly. The collagen used was Azocoll, an insoluble ground collagen impregnated with an azo-dye, normally used as a protease substrate. To deposit the collagen, the speed was at first ramped to 2280 rpm and maintained for 10 secs, then lowered to 1755 rpm and maintained for a further 10 secs and finally lowered to 1175 rpm for 5 secs. After the deposition process the samples were examined by optical microscopy (figure 5.10).

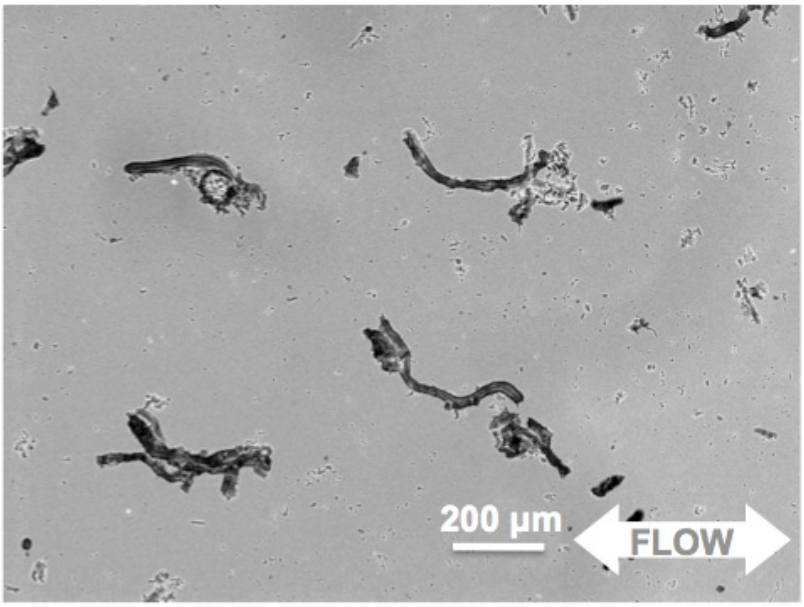

Figure 5.10. Optical microscopy image of collagen fibres aligned in the direction of the flow of the suspension over the surface.

Figure 5.10 shows collagen fibres aligned in the direction of the couette imposed flow over the substrate showing that this technique for aligning fibres had succeeded. Under the optical microscope, the collagen fibres appeared red from the presence of the impregnated azo-dye, where the azocoll collagen stock is normally utlilised as a protease substrate. For the experiments here, the azo-dye served the purpose of a contrast agent, allowing the collagen fibres to be easily found and resolved against the substrate background. Collagen fibres show some self-assembling properties in their native environment, but this process leads to closely packed fibres in contact with each other.[45] The fibres examined here on the CD-Au surface, however were spaced well apart showing the effect to not be due to any self-assembling and aggregation induced alignment.

To better understand the interactions of collagen fibres with the underlying CD-Au surface, it was decided to analyse samples of collagen deposited on template stripped Au (0^0) with SEM (figure 5.11). Figure 5.11a shows a 170 μm length of collagen fibre deposited in the direction of the CD-Au corrugations. Along the length of the fibre, there are bulges caused by the helical twist of the collagen fibre (figure 5.11a). The end of the fibre shows spreading behaviour where the individual fibrils of the fibre have spread onto the CD-Au surface forming a 'carpet' of collagen (figure 5.11b). Figure 5.11b shows another collagen fibre with a larger area of spreading at the fibre end with the fibril 'carpet' mimicking the structure of the underlying CD-Au. This spreading behaviour acts as evidence for a hypothesis that during the deposition process, the loose fibrils (which the fibres are composed of)[46] at the ends of the fibres attach first to the surface, therefore causing the rest of the fibre to be pulled to the surface and deposited (figure 5.12).

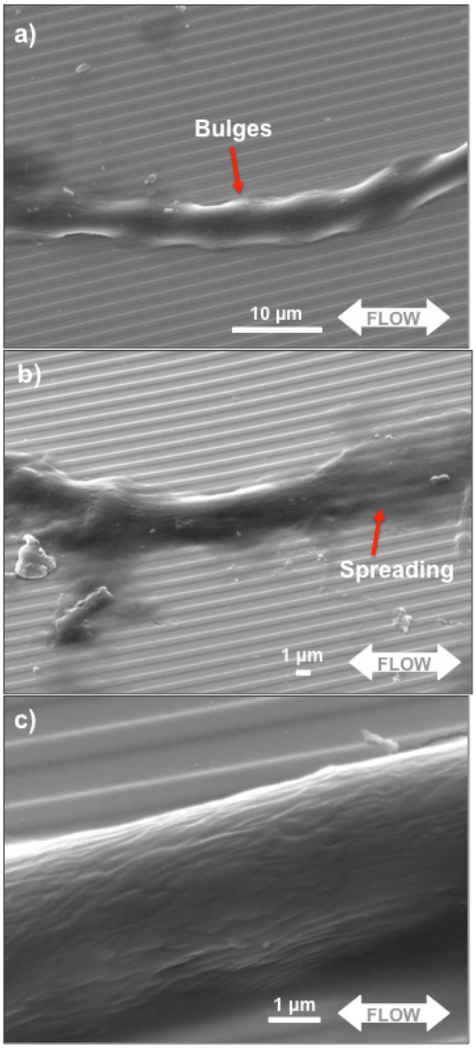

Figure 5.11. SEM images of **a)** a collagen fibre on a corrugated Au surface; **b)** the end of a collagen fibre where the smaller composite fibres and fibrils have spread on the surface; **c)** a close-up of a collagen fibre showing the composite fibres and fibrils.

This observed behaviour is in agreement with the literature behaviour of proteins on surfaces.[47] Figure 5.11c shows a close-up image of a collagen fibre, confirming the alignment and presence of the collagen with its component collagen fibrils visible on the fibre surface.

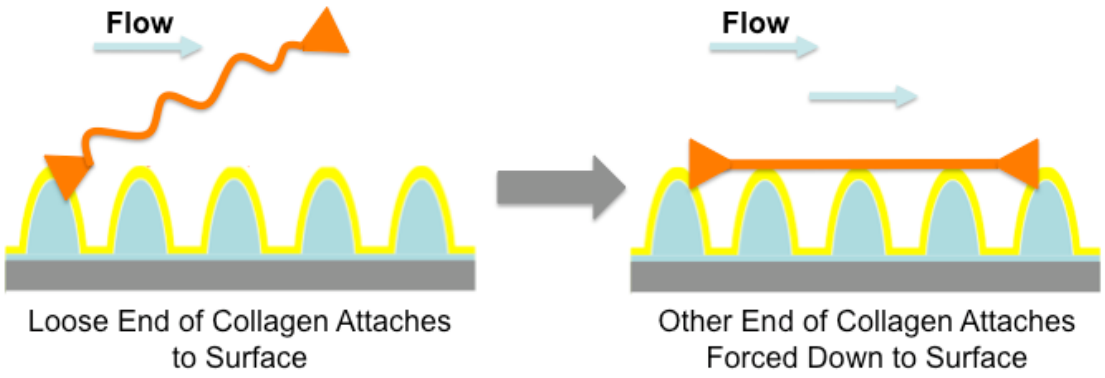

Figure 5.12. Diagram showing the way in which collagen is proposed to attach to surface

AFM is a valuable technique for achieving high resolution of images of biological fibres and polymers on surfaces.[48] Previously, AFM and techniques based on Scanning Probe Microscopy (SPM) such as Scanning Force Microscopy (SFM) have been used to image collagen, with monomer (tropocollagen) scale resolution.[49] Here, AFM analysis was used to further probe the deposition process and to achieve higher resolution images of the surface and individual collagen fibrils. AFM analysis of a length of collagen fibril deposited at 0^0 was acquired in order to assess the ability of the couette technique to align the small fibrils in the direction of the surface corrugations, oriented parallel with the surface corrugations (figure 5.13). The fibril exhibits regions where it follows the track direction and crossing over to the side of the neighbouring 'peak' (figure 5.13, i*nset*). From comparing the section analysis of the AFM image of the fibril over the 'valley' and on the 'peak', it appears that the fibril is suspended approximately 15 nm above the 'valley' floor.

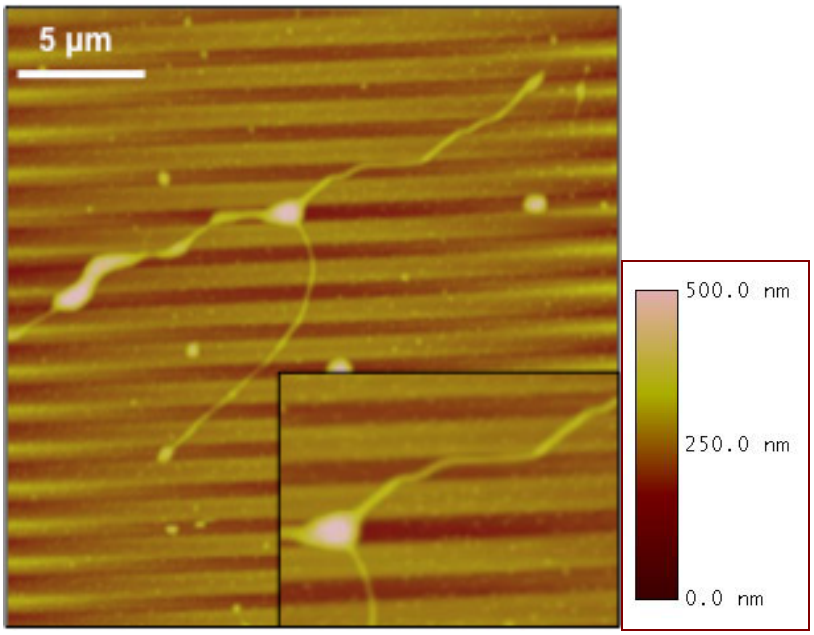

Figure 5.13. AFM contact mode image of collagen fibril aligned in the direction of the Au corrugations, *inset,* magnified region of fibril crossing surface valley.

5.3.2.3 Collagen fibre and fibril deposition at 90^0 to corrugations.

Figure 5.14a shows large-scale contact AFM height (*left*) and deflection (*right*) images of the substrate after processing in the couette cell. It can be seen that most of the collagen fibres are completely aligned with each other at 90^o to the surface corrugations (scheme 5.1, step 4), an effect that was readily reproducible. The deflection image presents more detail than is seen by the height image, allowing the full extent of the fibre alignment to be seen more clearly. The highlighted area is then magnified in figure 5.14b revealling the alignment of individual collagen fibrils with more clarity where all the present collagen fibres are aligned parallel to each other in the direction of the flow across the sample. It is hypothesised that the collagen fibrils are deposited by the ends of the fibrils initially making contact with the surface and the remainder of fibrils being laid down over the surface corrugations as the sample is further rotated. This again is evidenced by the bulbous ends of the fibrils being set

down into the ‘valleys’ and the fibrils stretched out over the corrugations of the CD-Au. Figure 5.14c, again, is an enlarged image of a section of the collagen fibril across the surface corrugations. From the height image, the collagen fibril is seen to trace the peaks and valleys of CD-Au indicating the fibril is to an extent ‘sagging’ down into the valleys. The AFM images were obtained in contact mode as attempts to image the individual fibrils in tapping mode proved to yield poorly resolved images, possibly due to the mobility of the collagen under the AFM tip.[50] The collagen fibrils were especially difficult to resolve in tapping mode over the surface ‘valleys’, indicating the fibrils were to some degree suspended above the ‘valleys’ and able to move under the motion of the AFM tip. This ability of collagen to suspend over macroscale surface channels has been observed previously and been used as a means of testing its mechanical properties.[51]

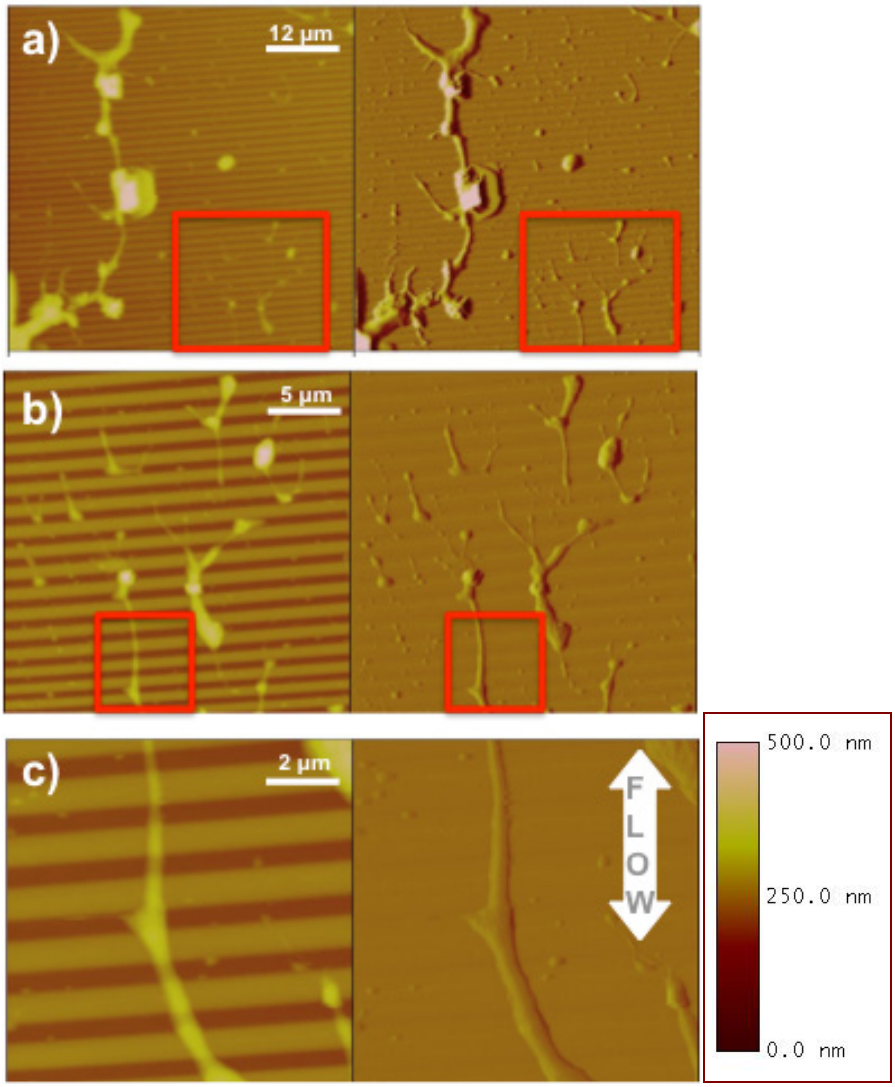

Figure 5.14. AFM contact **(a, b, c, *left*)** and deflection **(a, b, c, *right*)** images of collagen fibrils aligned at 90^0 on corrugated Au surfaces.

5.3.3 Probing the mechanical properties of collagen fibrils with AFM (step 5)

In order to demonstrate that a combination of the use of corrugated surfaces and circular couette deposition could be utilised to probe the mechanical properties of micro and nanoscale species, it was decided to analyse the degree of deformation of the collagen fibrils into the 'valleys' of the underlying corrugated surface. Although collagen fibrils exhibit little strength in either torsion or flexion (especially at smaller diameters) they exhibit high tensile strengths, thought to arise from intermolecular

cross-links.[22] Due to the nature of the deformation of collagen into the surface corrugations, the tensile strength and the flexion strength of the fibrils will be a factor in the overall mechanics of its deformation. Initial qualitative AFM force/distance spectroscopy measurements showed the degree of indentation possible in the collagen both on the Au surface and above the surface corrugation was almost identical. This identical response indicated that just the local material properties of collagen were being probed, showing that AFM force/distance measurements of fibres over corrugations of this size were not practical. Over much larger surface channels however, force/distance techniques have proved to be a useful tool in analyzing the deformation of collagen.[52]

As force/distance spectroscopy had proved unfruitful it was decided to examine the individual AFM scan section analyses from the obtained AFM images. Measurements were carried out on the fibril both laying on the 'peaks' and suspended above the 'valleys'. The distance from the top of the fibril to the underlying surface was compared to estimate a value for the fibril deformation (figure 5.15 and equation 5.1), Where Z_{valley} is the depth of the corrugation 'valley', d_{fibril} is the fibril diameter and Z_{height} is the distance from the bottom of the 'valley' to the top of the fibril suspended above it.

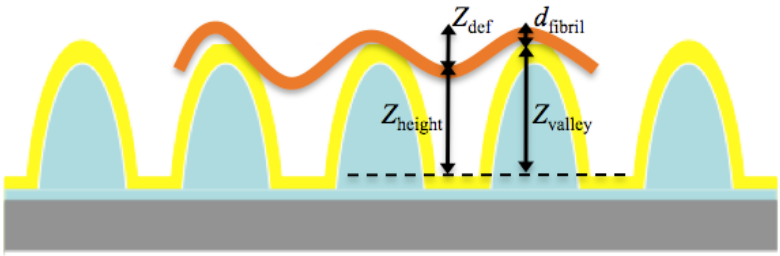

Figure 5.15. Diagram depicting the measurements taken with AFM to determine the deformations exhibited by the collagen fibres over the corrugated surface.

$$Z_{def} = Z_{valley} + d_{fibril} - Z_{height}$$ **equation 5.1**

The results of the AFM section analyses for one deposition run are presented in figure 5.16. From figure 5.16a it can be seen that as the aligned fibril section length increases, the diameter of the collagen fibrils decreases. The limited typical length of tropocollagen,[53] indicates that longer fibrils should be composed of more individual strands of tropocollagen, meaning an increased ability for shearing interactions of the component tropocollagen. However, the size distribution of the collagen fibres and fibrils observed for this set of experiments does not follow this proportional increase in diameter with increase in fibre/fibril length. This unexpected bevaviour with the collagen length and diameter by is believed to be a product of the grinding process used to form the azocoll stock.

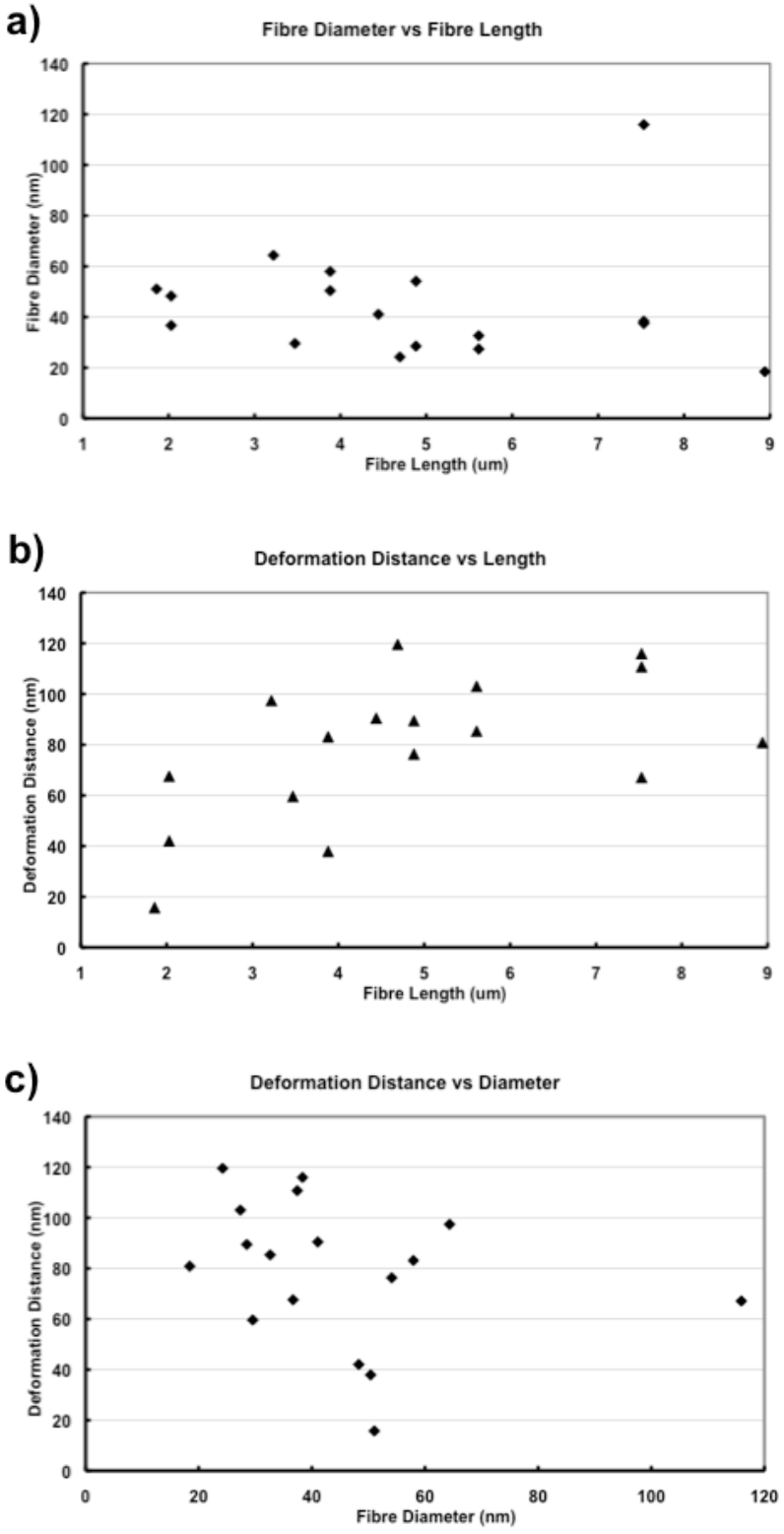

Figure 5.16. Graphs depicting the relationship between **a)** the fibril lengths to fibril diameter; **b)** fibril diameter to deformation distance; and **c)** fibril length to deformation distance.

Previously, the tensile strength of collagen fibrils was related to the fibril diameter.[22] However, literature observations have also concluded that the viscoelastic mechanical properties of collagen are related more to the overall fibril length than diameter.[54] Figure 5.16b plots the length of the collagen fibrils against the deformation distance and it can be seen that as the fibril length increases, the deformation distance increases. Figure 5.16c shows that as the fibril diameter is increased the deformation of the collagen fibrils into the surface corrugations is decreased. This agrees with literature observations that the mechanical strength of the collagen fibrils is seen to increase with increased diameter. It has been established in the literature that multiple mechanisms are at play in the strength and deformation of collagen[55, 56] and the results seen here agree with such a view. The spread in results of the graphs overall could arise due to the inhomogenity of the collagen stock due to the grinding action imposed on the initial collagen fibres. The ability to probe the mechanical properties of collagen using only a corrugated Au surface, simple deposition procedure and AFM has implications for carrying out directional deposition and mechanical testing on other materials such as micro/nano-fibres[37] and carbon nanotubes.[38]

5.4 Conclusions

Overall, it has been demonstrated that corrugated Au surfaces can be recovered from Au coated CD-R disks *via* the process of template stripping. The alignment of collagen fibres and fibrils on surfaces can be controlled with simple apparatus composed of two concentric glass cylinder and a motor, without requiring fabrication of costly microfluidic systems. The ability to control the alignment of collagen fibrils on a surface with well-defined and repeatable topography allows the experimentalist to probe the mechanical properties of individual collagen fibrils with

AFM and gain insight into the deformation of collagen fibrils in surface corrugations as a function of the observed fibril diameter and length.

5.5 Future work

The future work generated by this chapter is to investigate how the application of the circular couette deposition technique can be applied to other materials such as fibres and nanotubes in order to induce alignment. Furthermore, further investigations into more uses of the corrugated Au surfaces achieved by the template stripping process may prove advantageous.

5.6 Experimental

5.6.1 Pre-preparation of CD-R-Au surfaces

Sections of CD-R-Au were diced into 1cm^2 portions using a standard pair of scissors. The substrates were then immersed in conc HNO_3 (70%) for 3 mins, removed and rinsed with UHP H_2O and HPLC EtOH and dried under a stream of N_2.

5.6.2 Template-stripping of corrugated CD-R-Au surfaces to form CD-Au surfaces *(steps 1-3)*

Template-stripped corrugated Au surfaces were formed by initially immersing polycarbonate backed CD-R-Au substrates in conc nitric acid for 10 mins to remove the protective polymer coating. After rinsing with UHP H_2O and EtOH, the substrates were dried then diced into 1 cm^2 pieces. The exposed Au surfaces of the CD-R-Au diced pieces were then covered with epoxy resin (Epotech 377/302) and either glass or silicon backing substrates laid on-top and pressed down. After overnight curing, the silicon or glass backing substrates were then separated from the original

polycarbonate base, facilitating the transfer of the corrugated Au surface to the glass or silicon backing.

5.6.3 Circular-couette deposition of collagen (step 4)

A custom made circular couette cell was fabricated with two recessed areas on the surface of the inner cylinder for 1 cm^2 Au coated samples to be placed. To carry out collagen deposition, the inner cylinder with attached freshly stripped CD-Au surfaces was lowered into the outer cylinder containing approximately 3 ml of collagen suspension (Azocoll (Merck, Calbiochem) 5000 μg/ml, Sodium Acetete Buffer, 0.037 M solution, pH 4.8). The outer cylinder was then rotated at 2280 rpm (10 secs), 1755 rpm (10 secs) and 1175 rpm (5 secs) (Calibrated with Laser Tachometer & High Speed Camera). After rotating the outer cylinder for the desired speed and time, the inner cylinder was removed , rinsed with UHP H_2O and the samples allowed to air dry.

5.6.4 X-ray photoelectron spectroscopy (XPS).

XPS spectra were obtained on a VG ESCALAB 250 controlled by a SPECTRA data system (PSP Vacuum Technology). Samples for analysis were immobilised on stainless steel sample holders with stainless steel retaining screws to form a conductive path between the Au surface and the sample holder. XPS experiments were carried out using a monochromatic Al Kα X-ray source (1486.6 eV) operated at 10 kV and 20 mA. Au (4f) spectra were recorded using a pass energy of 80-90 eV and a step size of 0.1 eV. Analysis of XPS peaks was performed using the spectra processing program (PRESENTS) in the XPS software.

5.6.5 Optical microscopy analysis

Optical microscopy analysis was carried out using a transmitted light microscope (Zeiss, Axio Scope) and the optical system of a D3100 (Dimension) AFM (Digital Instruments, Santa Barbara, CA).

5.6.6 SEM analysis

SEM analysis was carried out by coating the template stripped Au substrates with attached collagen with a thin carbon layer to improve contrast. The SEM imaging was carried out under vacuum using a Jeol 7000 FEGSEM instrument.

5.6.7 AFM analysis (step 5)

AFM analysis was carried out using a D3100 (Dimension) AFM (Digital Instruments, Santa Barbara, CA) operated in tapping mode using etched silicon probes with a nominal spring constant of 20–80N/m and a tip radius <10nm (model RTESP, Veeco Instruments, Inc). AFM images were acquired in air with a scan rate of 1.00 Hz. Surface section measurements were carried out using Nanoscope software (Version 6.13, Digital Instruments, Santa Barbara, CA).

5.7 References

1) Diegoli, S., Hamlett, C. A. E., Leigh, S. J., Mendes, P. M. and Preece, J. A., **Engineering Nanostructures at Surfaces**, *Proceedings of the Institution of Mechanical Engineers Part G-Journal of Aerospace Engineering*, **2007**, *221*, 589-629.

2) Diegoli, S., Mendes, P. M., Baguley, E. R., Leigh, S. J., Iqbal, P., García Díaz, Y. R., Begum, S., Critchley, K., Hammond, G. D., Evans, S. D., Attwood, D., Jones, I. P. and Preece, J. A., **pH-Dependent Gold Nanoparticle Self-Organization on Functionalized Si/SiO_2 Surfaces,** *J. Exp. Nano. Sci*, **2006**, *1*, 333-353.

3) Williams, P. A., Papadakis, S. J., Falvo, M. R., Patel, A. M., Sinclair, M., Seeger, A., Helser, A., Taylor II, R. M., Washburn, S. and Superfine, R., **Controlled Placement of an Individual Carbon Nanotube onto a Microelectromechanical Structure**, *Appl. Phys. Lett.,* **2002**, *80*, 2574-2576.

4) Dai, H., Kong, J., Zhou, C., Franklin, N., Tombler, T., Cassell, A., Fan, S. and Chapline, M., **Controlled Chemical Routes to Nanotube Architectures, Physics, and Devices,** *J. Phys. Chem. B* **1999,** *103,* 11246-11255.

5) Kostovski, G., Mitchell, A., Holland, A. and Austin, M., **Tuning the Tunnel Coupling of Quantum Dot Molecules with Longitudinal Magnetic Fields**, *Appl. Phys. Lett.*, **2008**, *92*, 223109.

6) Lee, H.Y. and Yao, T., **Wet-etching Selectivity of Ag-photodoped AsGeSeS Thin Films and the Fabrication of a Planar Corrugated One-dimensional Photonic Crystal by a Holographic Method**, *J. Vac. Sci. Technol. B.***, 2002**, *20*, 2017-2023.

7) Zhang, H., Li, Z. and Mirkin, C. A., **Dip-Pen Nanolithography-Based Methodology for Preparing Arrays of Nanostructures Functionalized with Oligonucleotides**, *Adv. Mater*., **2002**, *14*, 1472-1474.

8) Craighead, H. G., James, C. D. and Turner, A. M. P., **Chemical and Topographical Patterning for Directed Cell Attachment**, *Curr. Opin. Sol. Stat. Mat. Sci.*, **2001**, *5*, 177-184.

9) Youn, S. W., Kang, C. G., **Maskless Pattern Fabrication on Pyrex 7740 glass Surface by Using Nano-scratch with HF Wet Etching**, *Scripta Materialia,* **2005**, *52*, 117-122.

10) Mali, P., Sarkar, A. and Lal, R., **Facile Fabrication of Microfluidic Systems using Electron Beam Lithography**, *Lab. Chip.*, **2006**, *6*, 310-315.

11) Hua-Zhong, Y., **New Chemistry on Old CDs**, *Chem. Comm.*, **2004**, 2633-2636

12) Mohammadi Gheidari, A., Hadad Dabaghi, H., Kalhor, D., Iraj, M., Kazemzad, M., and Behafarid, F., **Post Annealing Effects on the Properties of Sputtered Nano-crystallite Indium Tin Oxide Thin Films on Flexible Polyimide Substrate**, *Phys. Stat. Sol. C*., **2008**, *5*, 3338-3343.

13) Chen, H. J. H., Chen, L. C., Lien, C., Chen, S. R., Ho, Y. L., **Nano-scale Metallization of Au on Flexible Polyimide Substrate by Reversal Imprint and Lift-off Process**, *Microelec. Eng.*, **2008**, 85, 1561-1567.

14) Briseno, A. L., Mannsfeld, S. C. B., Ling, M. M., Liu, S., Tseng, R. J., Reese, C., Roberts, M. E., Yang, Y., Wudl, F. and Bao, Z., **Patterning Organic Single-Crystal Transistor Arrays**, *Nature,* **2006**, *444*, 913-917.

15) Tan, J. and Saltzman, W. M., **Topographical Control of Human Neutrophil motility on Micropatterned Materials with Various Surface Chemistry**, *Biomaterials*, **2002**, *23*, 3215-3225.

16) Nuraje, N., Banerjee, I. A., MacCuspie, R. I., Yu, L. and Matsui, H., **Biological Bottom-up Assembly of Antibody Nanotubes on Patterned Antigen Arrays**, *J. Am. Chem. Soc.*, **2004**, *126*, 8088-8089.

17) **The Electronics Handbook – 2nd ed**, J. C. Whitaker, **2005**, Taylor and Francis.

18) Watts, R. A and Sambles, J. R., **Reflection Gratings as Polarization Converters**, *Optics Comms.,* **1997**, *140*, 179-183.

19) Hegner, M, Wagner, P, Semenza, G, **Ultralarge Atomically Flat Template-Stripped Au Surfaces for Scanning Probe Microscopy**, *Surf. Sci.*, **1993**, *291*, 39-46.

20) Tang, W, Xu, K, Wang, P and Li, X, **Surface Roughness and Resistivity of Au Film on Si-(111) Substrate**, *Microelec. Eng.*, **2003**, *66*, 445-450.

21) Steudel, S, De Vusser, S, De Jonge, S, Janssen, D, Verlaak, S, Genoe, J and Heremans, P, **Influence of the Dielectric Roughness on the Performance of Pentacene Transistors**, *Appl. Phys. Lett.*, **2004**, *85*, 4400-4402.

22) Parry, D. A. D, **The Molecular and Fibrillar Structure of Collagen and its Relationship to the Mechanical-properties of Connective-tissue**, *Biophysical Chemistry*, **1988**, *29*, 195-209.

23) **The Cell Biology of the Extra Cellular Matrix - 2nd ed**, Hay. E. D., **1983**, Academic Press.

24) Christiansen, D. L, Huang, E. K and Silver, F. H, **Assembly of Type I Collagen: Fusion of Fibril Subunits and the Influence of Fibril Diameter on mechanical properties**, *Matrix Biol.*, **2000**, *19*, 409-420.

25) in 't Veld, P. J and Stevens, M. J, **Simulation of the Mechanical Strength of a Single Collagen Molecule**, *Biophysical Journal*, **2008**, *95*, 33-39.

26) Miyazaki H and Kozaburo H., **Tensile Tests of Collagen Fibers Obtained from the Rabbit Patellar Tendon**, *Biomed. Microdevices*, **1999**, *2*, 151-157.

27) Penners, G, Priel, Z, Silberberg, A, **Irreversible Adsorption of Triplehelical Soluble Collagen Monomers from Solution to Glass and Other Surfaces**, *J. Coll. Int. Sci.*, **1981**, *80*, 437-444.

28) De Cupere, V. M, Van Wetter, J, Rouxhet, P. G, **Nanoscale Organization of Collagen and Mixed Collagen-pluronic Adsorbed Layers**, *Langmuir*, **2003**, *19*, 6957-6967.

29) Elzbieta, G, Christine, C, Booth J; Roberts, C. J and Rouxhet, P. G, **Resolution of the Vertical and Horizontal Heterogeneity of Adsorbed Collagen Layers by Combination of QCM-D and AFM**, *Langmuir*, **2005**, *21*, 10684-10692.

30) Wilson, D. L, Martin, R, Hong, S, Cronin-Golomb, M, Mirkin, C. A and Kaplan, D. L, **Surface Organization and Nanopatterning of Collagen by Dip-pen Nanolithography**, *PNAS*, **2001**, *24*, 13660-13664.

31) Roth, E. A, Xu, T, Das, M, Gregory, C, Hickman, J. J and Boland, T, **Ink-jet Printing for High Throughput Cell Patterning**, *Biomaterials*, **2004**, *25*, 3707-3715.

32) Chen, Q, Xu, S, Li, R, Liang, X and Liu, H, **Network Structure of Collagen Layers Absorbed on LB film**, *J. Coll. Int. Sci.*, **2007**, *316*, 1-9.

33) Lee, P, Lin, R, Moon, J & Lee, L. P, **Microfluidic Alignment of Collagen Fibers for *in-vitro* Cell Culture**, *Biomed. Microdev.*, **2006**, *8*, 35-41.

34) Bozec, L and Horton, M, **Topography and Mechanical Properties of Single Molecules of Type I Collagen Using Atomic Force Microscopy**, *Biophysical Journal*, **2005**, *88*, 4223-4231.

35) Maeda, H, **An Atomic Force Microscopy Study of Ordered Molecular Assemblies and Concentric Ring Patterns from Evaporating Droplets of Collagen Solutions**, *Langmuir*, **1999**, *15*, 8505-8513.

36) Maeda, H, **Observation of Spatially Rhythmic Patterns from Evaporating Collagen Solution Droplets**, *Langmuir*, **2000**, *16*, 9977-9982.

37) Hamlett, C. A. E, Jayasinghe, S and Preece, J. A, **Electrospinning Nanosuspensions Loaded with Passivated Au Nanoparticles**, *Tetrahedron*, **2008**, *64*, 8476-8483.

38) Palumbo, M, Lee, K. U, Ahn, B. T, Suri, A, Coleman, K. S, Zeze, D, Wood, D, Pearson, C, Petty, M. C, **Electrical Investigations of Layer-by-layer Films of Carbon Nanotubes**, *J. Phys. D: Appl. Phys.*, **2006**, *39*, 3077-3085.

39) Taylor, G. I, **Stability of a Viscous Liquid Contained between Two Rotating Cylinders**, *Phil. Trans. R. Soc. London. A.*, **1923**, *223*, 289-343.

40) **Pattern Formation in Viscous Flows- The Taylor Couette Problem and Rayleigh-Bernard Convection**, Rita Meyer-Spasche, **1999**, Birkhauser Verlag.

41) **The Couette-Taylor Problem**, Pascal Chossat, Gerard Looss, **1999**, Springer Verlag.

42) Piau J. M., Bremond, M, Couette, J. M and Piau, M, **Maurice Couette, One of the Founders of Rheology**, *Rheologica. Acta.*, **1994**, *33*, 357-368.

43) Merrill, E. W., Smith, K. A., Shin, H and Mickley, H. S., **Study of Turbulent Flows of Dilute Polymer Solutions in a Couette Viscometer**, *Trans. Soc. Rheology.,* **1996**, *10*, 335-351.

44) Wagner, P, Hegner, M, Güntherodt, H. J, Semenza, G, **Formation and *in-situ* Modification of Monolayers Chemisorbed on Ultraflat Template-stripped Gold Surfaces**, *Langmuir **1995,** 11,* 3867-3875.

45) Silver, F. H, Freeman J. W, Seehra, G, P, **Collagen Self-assembly and the Development of Tendon Mechanical Properties,** *J. Biomech.*, **2003**, *36*, 1529-1553.

46) Ushiki, T., **Collagen Fibers, Reticular Fibers and Elastic Fibers. A Comprehensive Understanding from a Morphological Viewpoint**, *Arch. Histol. Cytol.*, **2002**, *65*, 109-126.

47) Denis, F. A, Hanarp, P, Sutherland, D. S, Gold, J, Mustin, CH, Rouxhet, P. G and Dufrene, Y. F, **Protein Adsorption on Model Surfaces with Controlled Nanotopography and Chemistry**, *Langmuir*, **2002**, *18*, 819-828.

48) Nasanit, R, Iqbal, P, Soliman, M, Spencer, N, Allen, S, Davies, M. C, Briggs, S. S, Seymour, L. A, Preece, J. A and Alexander, C, **Combination Dual Responsive Polypeptide Vectors for Enhanced Gene Delivery**, *Mol. Biosyst.*, **2008**, *4*, 741-745.

49) Mertig, M, Thiele, U, Bradt, J, Leibiger, G, Pompe, W, Wendroc, H, **Scanning Force Microscopy and Geometric Analysis of Two-Dimensional Collagen Network Formation**, *Surf. Int. Anal.*, **1997**, *25*, 514-521.

50) Dupont-Gillain, C.C., Rouxhet, P.G, **AFM Study of the Interaction of Collagen with Polystyrene and Plasma-oxidized Polystyrene**, *Langmuir*, **2001**, *17*, 7261-7266.

51) Yang, L, Van der Werf, K. O, Fitie, C. F. C, Bennink, M. L, Dijkstra, P. J and Feijen, J, **Mechanical Properties of Native and Cross-linked Type I Collagen Fibrils**, *Biophysical Journal*, **2008**, *94*, 2204-2211.

52) Wenger, M. P. E, Bozec, L, Horton, M. A and Mesquida, P, **Mechanical Properties of Collagen Fibrils**, *Biophysical Journal*, **2007**, *93*, 1255-1263.

53) **Collagen: Primer in Structure, Processing and Assembly**, Brinckmann, J, Notbohm, H and Müller, P. K, **2005**, Springer.

54) Silver, F. H, Christiansen, D. L, Snowhill, P. B, Chen, Y, **Role of Storage on Changes in the Mechanical Properties of Tendon and Self-Assembled Collagen Fibers**, *Connect. Tissue. Res*, **2000**, *41*, 155-164.

55) Puxkandl, R, Zizak, I, Paris, O, Keckes, J, Tesch, W, Bernstorff, S, Purslow, P and Fratzl, P, **Viscoelastic Properties of Collagen: Synchrotron Radiation Investigations and Structural Model**, *Phil. Trans. R. Soc. Lon. B.*, **2002**, *357*, 191-197.

56) Fratzl, P, Misof, K, Zizak, I, Rapp, G, Amenitsch, H and Bernstorf, S, **Fibrillar Structure and Mechanical Properties of Collagen**, *J. Struct. Biology.*, **1997**, *122*, 119-122.

Chapter 6

DNA Based Foundations and Walls:

Fabrication of Patterned Silicon Surfaces by Photolithographic Exposure of DNA-Hairpins Carrying Photolabile Groups

Chapter 6 is based upon an article entitled:

'Fabrication of Patterned Silicon Surfaces by Photolithographic Exposure of DNA-Hairpins Carrying Photolabile Groups' by Brendan Manning, Simon J. Leigh, Roger Ramos, Jon A. Preece and Ramon Eritja. The Journal of Experimental Nanoscience, **2010**, 5, 26-39

Abstract

The work here demonstrates an overall method for the fabrication of patterned surfaces using hairpin oligonucleotides carrying one photolabile group at the central/apical loop position. Photolysis of surfaces carrying the photolabile hairpin oligonucleotides results in the dissociation of one of the oligonucleotide strands and formation of areas carrying single-stranded DNA sequences that direct the deposition of the complementary sequence at the photolyzed sites. The non-photolyzed areas carrying the intact hairpin do not bind so readily to complementary sequences due to the presence of the more stable intra-molecular hairpin duplex. The chapter follows the step-wise chemical derivatisation and grafting of functional molecules onto silicon surfaces with contact angle, spectroscopic ellipsometry and atomic force microscopy. The photolysis and photolithographic patterning is then carried out to demonstrate the photo-responsive behaviour of the surface grafted oligonucleotide. Finally, the

resultant single stranded oligonucleotide sequences are used to direct the self-assembly of molecular and nanoscale components carried on a second complementary sequence. The overall method described offers an attractive option for the fabrication of patterned surfaces with potential interest in electronics and biosensors through integration of the well-defined assembly of biomolecules with surface chemical modification

6.1 Introduction

There is a growing interest in the development of efficient methods to self-organize nanoscale components such as nanoparticles, nanotubes and biomolecules onto surfaces to fabricate nanostructured systems for electronic[1] or biological[2] or sensing applications.[3-6] Hybrid top-down/bottom-up processes, which combine the precision of lithographic techniques and the parallelism of self-assembly have been actively pursued in order to create patterns on silicon surfaces functionalised with self-assembled monolayers (SAMs).[7-9] SAMs have proved useful tools for surface structuring[10] or patterning[11] due to their ease of formation, stability and ability to facilitate further grafting of functional molecules onto a surface.[12] The ability to organize biomolecules such as DNA on surfaces such as glass[13,14] and gold[15-17] is also an area of increased interest. Recent advances in the development of techniques to integrate semiconductor technology with biomolecules has allowed for the possibility of utilizing the key specific recognition properties of biomolecules to assemble functional devices based on DNA to semiconductor surfaces.[18] The highly specific recognition of complementary strands of oligonucleotides is an ideal way of carrying out highly controlled, precise, species specific self-assembly, where only a specific component carrying the complementary sequence to the surface bound sequence will assemble at that location.[19-21] Methods used previously to pattern surfaces with

oligonucleotides have included pre-patterning of the underlying silicon layer by micron-scale UV light exposure of hydrogen-terminated silicon (100) coated with alkenes functionalised with *N*-hydroxysuccinimide ester groups.[22] The resultant *N*-hydroxysuccinimide ester surfaces act as a template for the subsequent covalent attachment of DNA oligonucleotides.[23] A similar affect can be achieved by pre-patterning self-assembled monolayers on silicon surfaces by electron beam lithography.[24] Kershner *et al*[25] recently presented a paper where they carried out placement of DNA shapes known as 'DNA origami' on surfaces patterned by electron beam lithography (figure 6.1, i). Other methodologies have utilised soft lithographic techniques such as contact printing to pattern DNA on surfaces (figure 6.1, ii).[26]

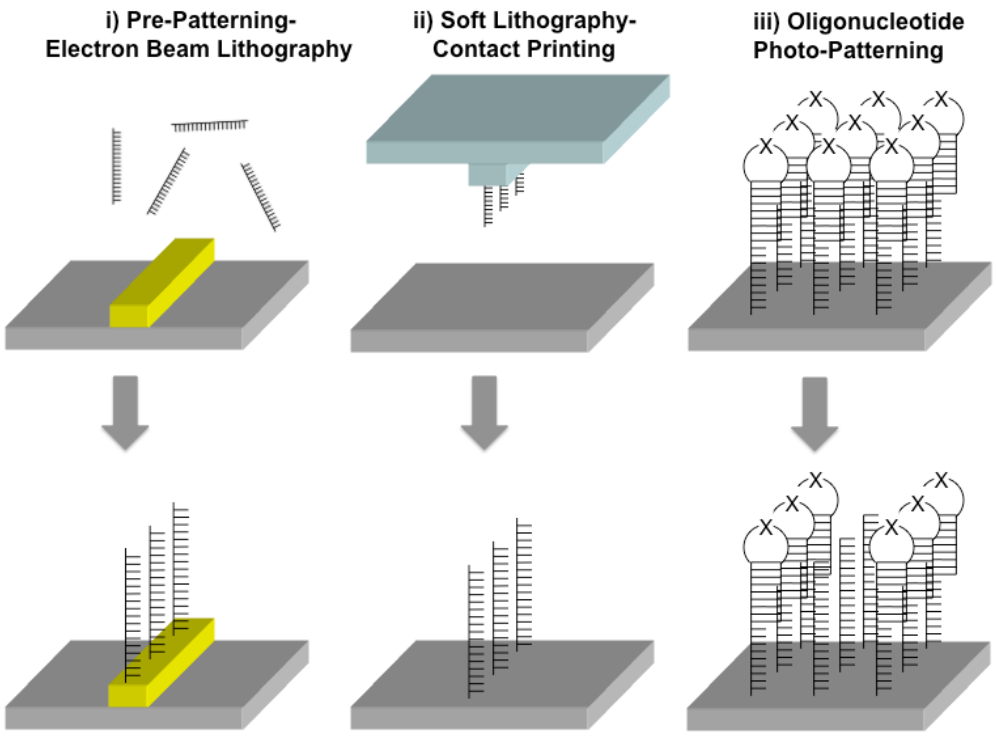

Figure 6.1. Comparison of some available methods for patterning DNA on surfaces, soft-lithography using PDMS stamps, surface lithographic pre-patterning and the method presented here of photo-patterning the DNA molecules themselves.

By introducing the method for patterning of the oligonucleotides surfaces into the DNA oligonucleotide themselves, by way of a photolabile group (figure 6.1, iii), a

more robust surface patterning technique can be achieved with the possibility for multiple exposure and hybridization steps once the oligonucleotides are *in-situ*, as opposed to a single patterning step before attachment of the oligonucleotides. Some conventional routes to biomolecule immobilisation rely on weak electrostatic attraction or physisorption.[27] However, to allow for the most robust system, a strong convalent bond between the surface and the biomolecule is prefered to increase the chance that the molecule will survive further fabrication steps.[28] If initial site-selective deposition of the oligonucleotides is first required due to a need for high-resolution structures, a chemical contrast between regions on a surface would make an ideal template. To make this chemical contrast on a surface, patterns have been created by exposure of thiol-stabilized gold NPs supported on silicon wafers to UV light leading to oxidation of the thiol and coagulation of the NPs,[29] or photo-crosslinking of C60 derivatives,[30] forming dense structures that are resistant to removal by organic solvents. Methods exist to further derivatize gold surfaces such as those formed, with oligonucleotide sequences.[16, 31, 32] Alternatively it is possible to modify a specific region of a surface introducing chemical functionality to direct the adsorption of particulate species *via* the method of EBL (as discussed in chapter 2).[33] The ability to deposit further particulate species to chemically patterned substrates is a robust method for three dimensional nanostructuring of surfaces, as the only change to the surface upon patterning is chemical and not physical.

6.2 Aims and objectives

The aim of this work is to carry out the chemical modification of silicon surfaces with synthetic hairpin oligonucleotide strands. These oligonucleotide strands will carry a photolabile group at the apex of hairpin and thus can be photocleaved and used to direct the site specific self-assembly of complementary oligonucleotide strands carrying fluorescent dye and gold nanoparticle (AuNP) labels. The combination of a top-down photolithographic technique with the inherent bottom-up specific self-assembling nature of complementary oligonucleotide strands exploits advances in surface chemical modification and oligonucleotide synthesis to introduce a new route to surface patterning and structuring for novel applications. By labelling the self-assembling complementary strands, the resultant system can be used to direct the self-assembly of both molecular and nanoscale components. The complete process is illustrated in scheme 6.1.

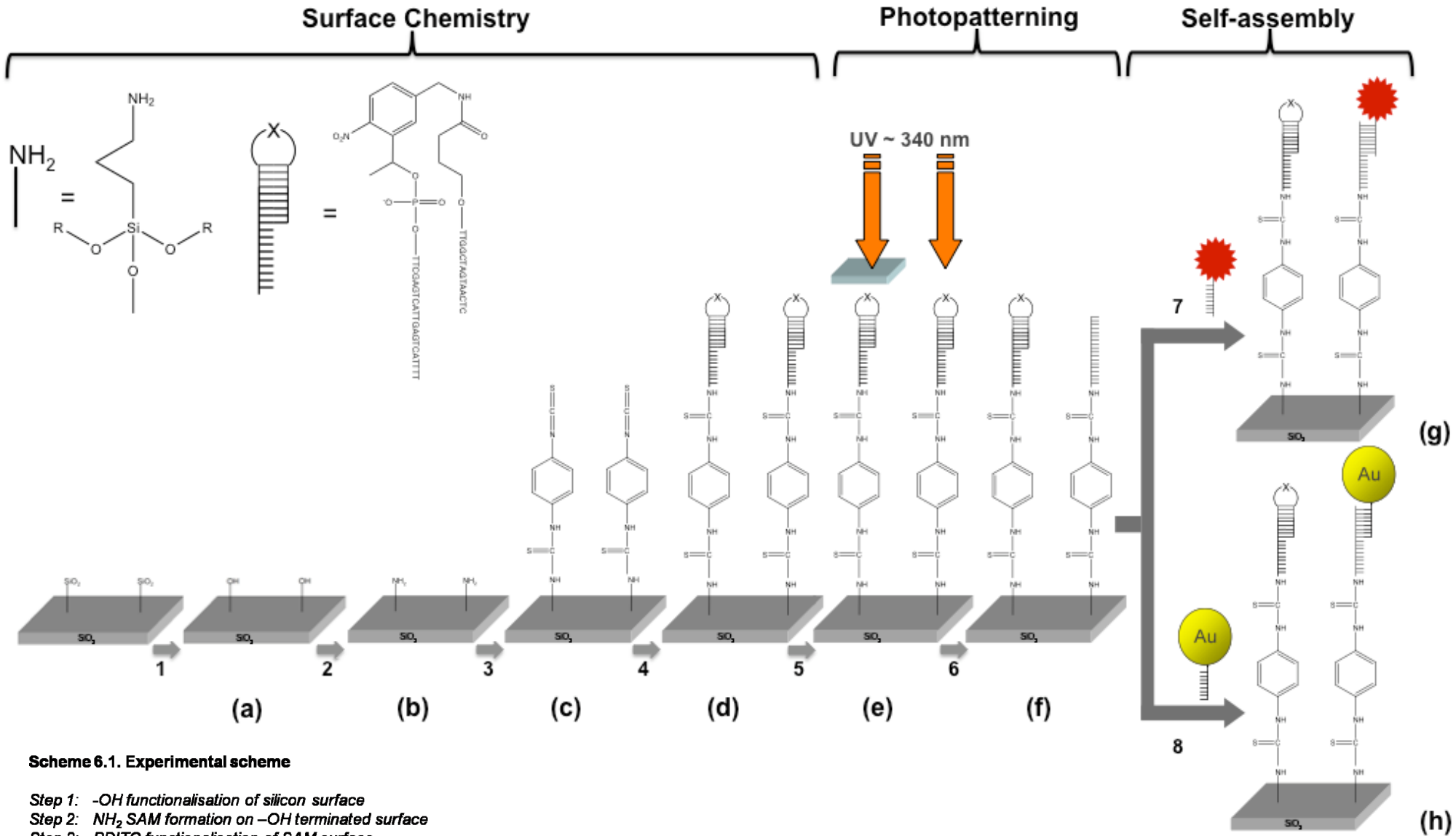

Scheme 6.1. Experimental scheme

Step 1: -OH functionalisation of silicon surface
Step 2: NH_2 SAM formation on –OH terminated surface
Step 3: PDITC functionalisation of SAM surface
Step 4: Chemical derivatisation with hairpin oligonucleotide
Step 5: Photopatterning
Step 6: Rinsing
Step 7: Self-assembly of rhodamine labelled complementary oligonucleotide
Step 8: Self-assembly of nanoparticle labelled complementary oligonucleotide

6.3 Results & discussion

The experimental work in this chapter can be broken down into three distinct areas, *surface chemistry*, *photopatterning* and *self-assembly* (scheme 6.1). The surface chemistry section will follow the step-wise derivatisation of SiO_2 to a clean hydroxylated surface (**step 1**) and then to an APTMS SAM (**step 2**). This will be followed by grafting of p-phenylene diisothiocyanate forming a -SCN terminated surface (**step 3**). The final chemical step is the grafting of the hairpin oligonucleotide to the surface (**step 4**). The photopatterning section will explore the photolysis behaviour of the grafted oligonucleotide sequences (**step 5**) to effect dissociation and removal of the hairpin loop (**step 6**) to leave a single stranded oligoucleotide. The self-assembly section will examine the self-assembly of complementary oligonucleotide sequences carrying dye (**step 7**) and nanoparticle labels (**step 8**) after photopatterning. Each sample had one repeat completed.

6.3.1 Surface chemistry

6.3.1.1 Silicon surface preparation & characterisation methodology, substrates a - d

Cleaned hydroxyl terminated silicon wafers (-OH, substrate a)[34] were functionalised with 3-aminopropyltrimethoxysilane as described in the literature,[35] affording amino-terminated surfaces (-NH_2, substrate b). The APTMS SAM surfaces were then treated with *p*-phenylene diisothiocyanate (PDITC) to form isothiocyanate terminated surfaces (-SCN, substrate c).[36-38] These surfaces were then coupled with the –NH_2 terminated photolabile hairpin oligonucleotide A to form the –OLIGO terminated surfaces ((-OLIGO, substrate d) (scheme 6.1, step 3).

6.3.1.1.1 –OH, substrate (a)

Dynamic contact angle measurements of the silicon wafers (Si/SiO_2) after cleaning to form the hydroxyl terminated surfaces (step 1) revealed contact angles of 34 ± 6^o (Av Adv) and 19 ± 5^o (Av Rec) agreeing with literature values for hydrophilic surfaces of this type.[39] AFM imaging of the clean hydroxylated SiO_2 surface showed that the surfaces were clean and free from contamination (figure 6.2) with an average RMS roughness of 0.2 nm.

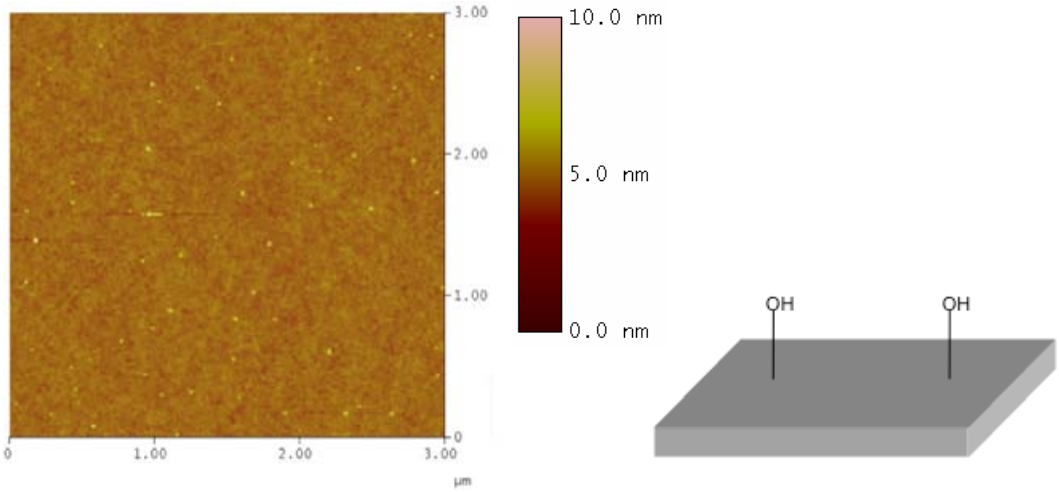

Figure 6.2. Tapping mode AFM image of SiO_2 surface after cleaning and –OH functionalisation (**-OH, substrate a**).

6.3.1.1.2 –NH_2, substrate (b)

After formation of NH_2 SAM surfaces (step 2), the average contact angles changed to $66^o \pm 7^o$ (Av Adv) and $42^o \pm 4^o$ (Av Rec), which were higher than literature values for SAMs fully terminated with NH_2 groups.[40] It has been demonstrated that a water film (one or several molecular layers thick) covering the substrate is necessary for the formation of a complete monolayer.[41, 42] On the other hand, a too high content of water in the organosilane solution promotes the formation of oligomeric siloxanes that results in the deposition of a multilayered structure and an increase in the film roughness (a reason for a higher contact angle).[43] Ellipsometry

measurements showed average APTMS thicknesses of 0.88 nm ± 0.1 nm, which was also comparable to the estimated molecule length (0.69 nm, Chem3D Software), (Table 1), therefore excluding the formation of multilayers as a reason for the slightly higher than expected contact angle values. One hypothesis is that the high contact angle values were therefore due to some disorder being present within the SAM structure. AFM imaging revealed that upon APTMS functionalisation of hydoxyl terminated silicon surfaces, a similar average RMS roughness to the SiO_2 surface was achieved (0.2 nm) and the surfaces were free from polymeric aggregates (figure 6.3).

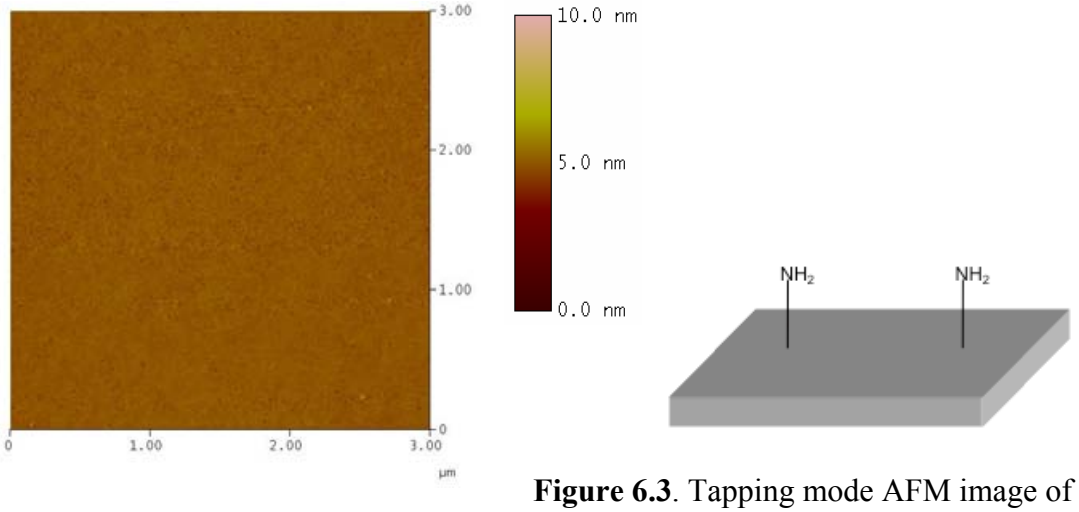

Figure 6.3. Tapping mode AFM image of SiO_2 after APTMS SAM functionalisation (**-NH_2, substrate b**).

The similarity of the roughness values of the –OH surface of the APTMS surface is evidence of disorder of the APTMS chains as the formation of organosilane SAMs usually give rises to smoother overall surfaces.

Table 6.1. Water contact angles, thickness and RMS roughness of functionalised silicon surfaces.

Surface	Contact Angle (^{0})		Thickness (nm)		Average RMS Roughness (nm)
	(Adv)	(Rec)	Measured	Expected	
-OH (a)	34 ± 6	19 ± 5	0	0	0.22 ± 0.02
-NH_2 (b)	66 ± 7	42 ± 4	0.88 ± 0.1	0.69	0.20 ± 0.01
-SCN (c)	78 ± 6	51 ± 4	1.20 ± 0.2	1.60	0.21 ± 0.02
-OLIGO (d)	66 ± 3	39 ± 2	10.8 ± 0.7	8.90	0.66 ± 0.03
-SINGLE (f)	-	-	1.30 ± 0.6	1.70	0.38 ± 0.02
-RHODAMINE (g)	-	-	-	-	1.06 ± 0.03
-AuNP (h)	-	-	-	-	1.45 ± 0.03

X-ray photoelectron spectroscopy of the silicon based substrates in the region for N (1s) showed the presence of 2 peaks for the APTMS functionalised surfaces (figure 6.4). The peak at approx 400 eV is thought to originate from the NH_2 species of the APTMS and the second peak at approx 401.5 eV is thought to originate from the protonated form of the APTMS SAM (NH_3^+).[34] The two peak areas are approximately in a 1:1 ratio, indicating a 50/50 split in amount of both at the surface. The protonated NH_3^+ may have arisen from incomplete washing of the silicon substrate after cleaning leading to an acidic environment at the surface of the silicon during SAM formation.

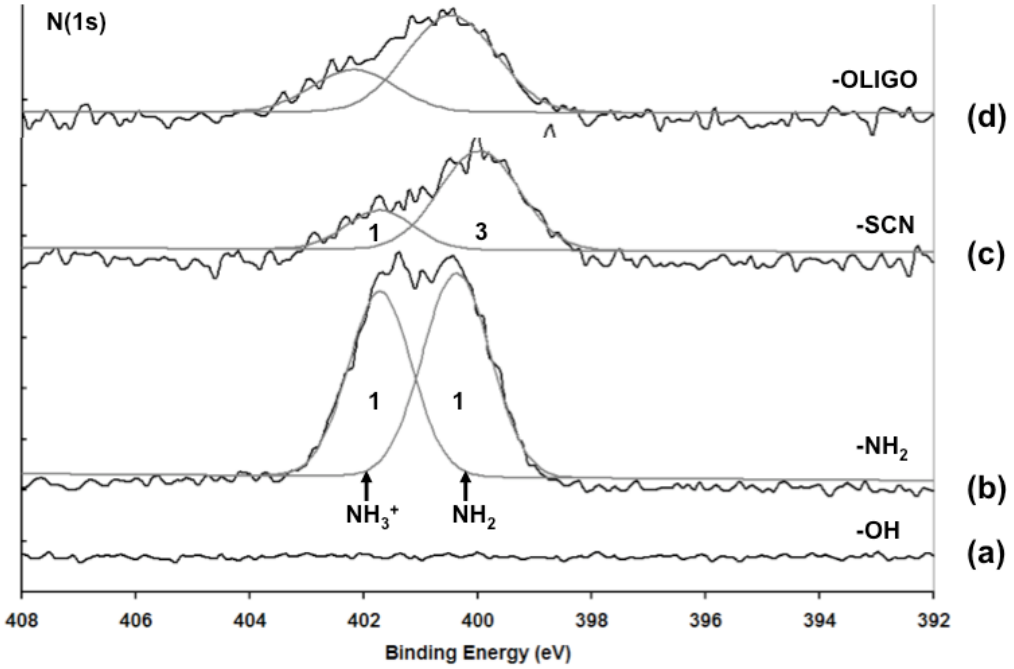

Figure 6.4. N (1s) X-ray photoelectron spectra of substrates a-d.

6.3.1.1.3 –SCN, substrate (c)

PDITC was grafted to the $–NH_2$ surfaces through formation of bond between the terminal N atom of the NH_2 surface and the outermost carbon of the PDITC molecule (scheme 6.1, step 3). Dynamic contact angle measurements of –SCN terminated surfaces revealed an increase in contact angle upon formation of –SCN terminated surfaces 78 ± 6 (Av Adv) and 51 ± 4, (Av Rec), which is in good agreement with previously seen behaviour (table 1).[34] Ellipsometry of the –SCN terminated surfaces revealed a thickness of 1.2 nm ± 0.2 nm, which is comparable with the estimated length of the molecule (1.6 nm, Chem3D Software). XPS of the –SCN surfaces (figure 6.4) revealed that the peak at approx 400 eV was seen to shift and slightly broaden, as might be expected with the addition of other N functionality ((R(NH)R & C=N-R). The two N1s peaks then are in a ratio of 3:1, indicating that addition of the PDITC species may only occur on 50% of the surface N atoms with three nitrogen environments from the APTMS-SCN conjugate to every NH_3^+ environment on the underlying APTMS SAM. This 50% grafting efficiency is

possibly due to disorder in the SAM and steric interactions of the PDITC molecule. These XPS observations also agree with the contact angle values for the NH_2 SAMs showing a disordered SAM. It was believed that such spacing of the PDITC moieties while maybe advantageous for providing a suitable spacing for the oligonucleotide grafting process could lead to non-specific adsorption at later stages of the experiment. (as observed in section 6.3.3.2) AFM imaging (figure 6.5) showed the average RMS roughness of the –SCN surface to be 0.214 nm, a roughness value similar to that obtained for the NH_2 SAMs.

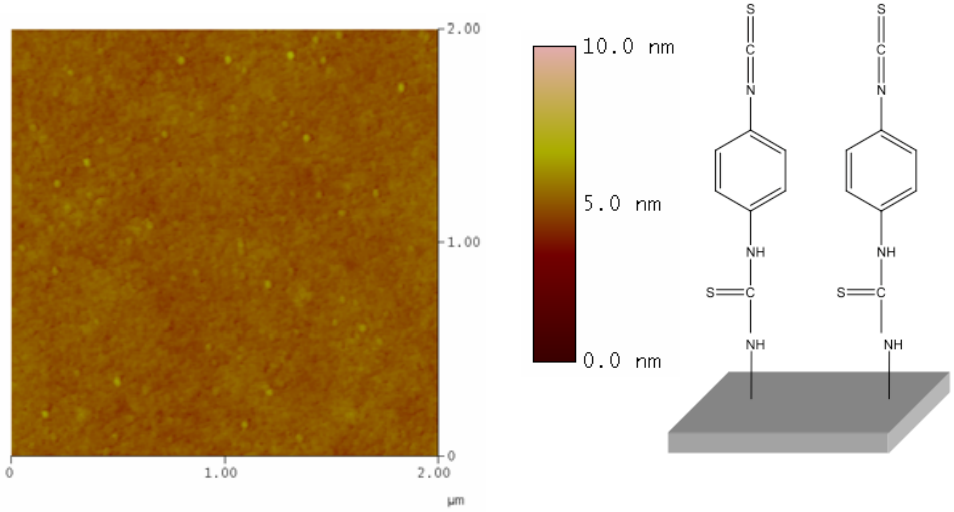

Figure 6.5. Tapping mode AFM image of SiO_2 surface functionalised with isothiocianate groups (**-SCN, substrate c**).

6.3.1.2 Oligonucleotide grafting

The photolabile hairpin oligonucleotide sequence A (5'-CTCAATGACTCGTT-X-TTCGAGTCATTGAGTCATTTTT-hexyl-NH_2-3', X = photolabile linker) was provided by the group of Dr Ramon Eritja, IRB, Barcelona, Spain.[44] Oligonucleotide A contained a terminal amino group at the 3' end[45] followed by 5 thymidines allowing for covalent attachment of the oligonucleotide to the –SCN terminated surfaces as a strong covalent interaction of the oligonucleotide with the surface was the preferred method for attachment of such biomolecules to surfaces to

ensure that the hairpin was not desorbed during further fabrication steps.[46] The oligonucleotide had a self-complementary sequence of 15 base pairs linked by a tetrathymidine loop. In the middle of the loop there is a photolabile 2-nitrobenzyl group (scheme 6.1).

6.3.1.2.1 –OLIGO, substrate (d)

Dynamic contact angle measurements of -OLIGO terminated surfaces (scheme 6.1, step 4) revealed a decrease in contact angle upon formation of –OLIGO terminated surfaces (table 1). The contact angle obtained closely resembles that of the APTMS SAM. We can attribute this similar contact angle to the polar nature of the oligonucleotide and hairpin link added to the surface. The thickness obtained from ellipsometry measurements (10.8 nm) was slightly longer than the estimated length of the oligonucleotide (8.9 nm) and was possibly due to some weak physisorption of further hairpin oligonucleotides. Quantitative XPS examination of the addition of the oligonucleotide to the silicon surfaces was inconclusive due to broadening of the nitrogen peak, especially in the region between the NH_2 and NH_3^+ regions, consistent with the addition of multiple nitrogen species and especially (N-(C=O)-N) from the high levels of thymine present in the oligonucleotide.[30] The AFM image of the -OLIGO functionalised surface is shown in figure 6.6. Upon attachment of the hairpin oligonucleotide to the surface, there is an increase in the average surface RMS roughness from 0.214 nm to 0.659 nm due to the presence and orientation of the hairpin oligonucleotide.

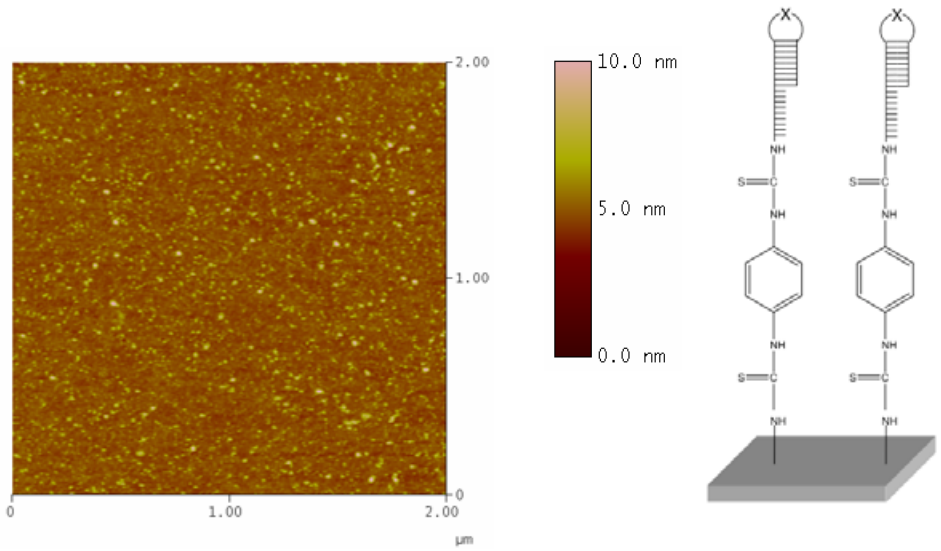

Figure 6.6. Tapping mode AFM image of surface functionalised with oligonucleotide A, (**-OLIGO, substrate d**).

6.3.2 Photopatterning

6.3.2.1 Photolysis control

The 2-nitrobenzyl group used in the hairpin oligonucleotide is widely used in organic synthesis as a protecting group and a cleavable linker because of its high photocleavage efficiency by near-UV light irradiation[47-50] (scheme 6.2). A cleavage quantum yield of 0.49–0.63 has been reported in the literature for 1-(2-nitrophenyl)ethyl phosphate esters.[51]

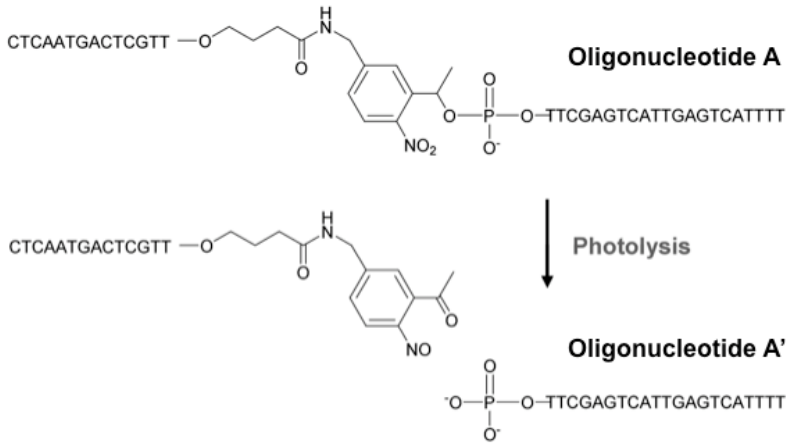

Scheme 6.2. Photocleavage of the hairpin oligonucleotide A carrying the 2-nitrobenzyl group (DMT, dimethoxytrityl group).

6.3.2.2 –SINGLE, substrate (f)

Investigations carried out in Dr Eritja's group examining the photolabile nature of oligonucleotide A showed that in solution, photolysis was completed after 30 minutes as judged by analytical HPLC.[42] The hairpin was photolyzed with a Black Eye lamp (340 nm) at room temperature. Upon carrying out the surface photolysis of oligonucleotide A functionalised surfaces (substrate d), AFM images (figure 6.7) showed a decrease in RMS roughness from 0.659 nm to 0.384 nm (scheme 6.1, step 6). The RMS decrease was attributed to the formation of a single stranded oligonucleotide A' on the surface, which has a shorter persistence length caused by self-coiling and/or collapse of the single stranded oligonucleotide.

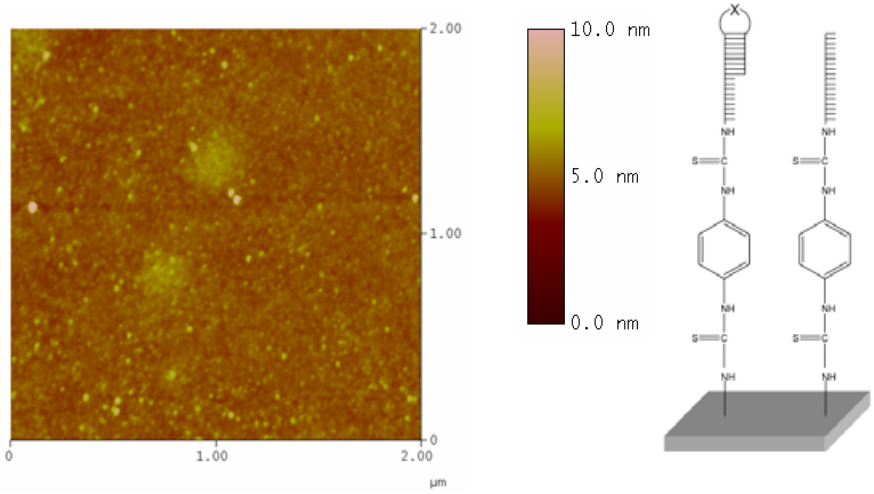

Figure 6.7. AFM tapping mode image of surface after photolysis and rinsing with single oligonucleotide strand (**-SINGLE, substrate f**).

This conclusion from the RMS roughness value is further supported by ellipsometry analysis which showed a drop in oligonucleotide layer thickness to 1.3 ± 0.6 nm after photolysis and rinsing, which is consistent with photolysis of the photolabile hairpin group and collapse of the single stranded oligonucleotide (figure 6.8).

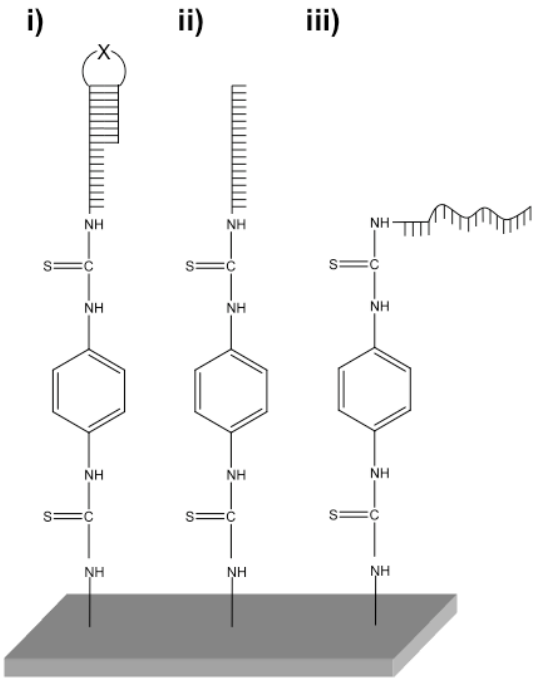

Figure 6.8. Figure showing **i)** the presence of the hairpin loop, **ii)** the removal of the hairpin loop, revealing the single stranded oligonucleotide and **iii)** self-coiling and/or collapse of the resultant single-stranded oligonucleotide.

Hybridization of completely photolyzed surfaces with complementary oligonucleotide labelled with rhodamine (step 7) was examined in Dr Eritja's group with epifluorescence microscopy of the surfaces and showed a strong fluorescent signal from the sample hybridised with the complementary rhodamine oligonucleotide (figure 6.9).

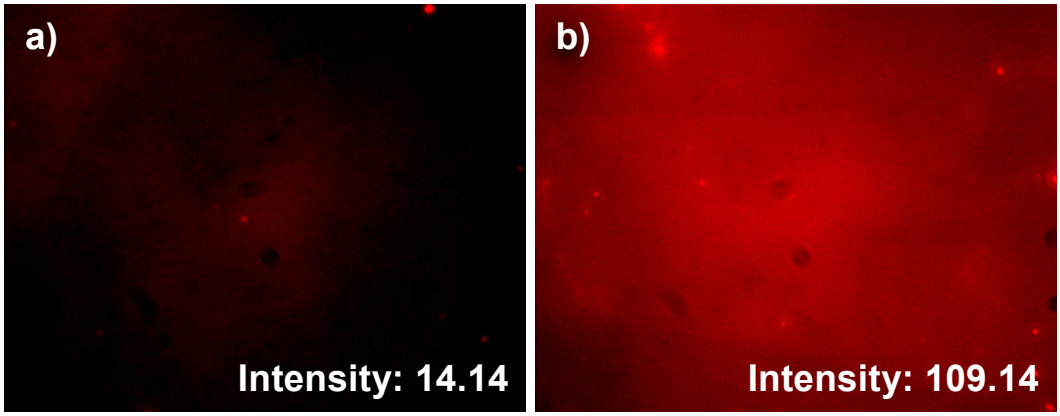

Figure 6.9. Assessment of intramolecular versus intermolecular duplex formation by photolysis and subsequent hybridization. Two silicon surfaces were functionalised with hairpin oligonucleotide A. One surface was not photolyzed with UV light **a)** while the other wasphotolyzed **b)**. Hybridization with the complementary oligonucleotide labelled with rhodamine showed a more intense fluorescence at the photolyzed surface **b)**. *Inset*, are the average fluorescence intensities of the unphotolyzed / photolyzed surfaces in arbitrary units (a.u.).

The non-photolyzed sample showed a weak background intensity after the hybridisation procedure which is believed to be due to the low grafting density of the underlying PDITC allowing physisorption of the labelled complementary strand.

6.3.3 Self-assembly

6.3.3.1 –RHODAMINE, substrate (g)

Examination of an oligonucleotide surface after photolysis and hydridisation with a rhodamine labelled oligonulceotide B showed an increase in average RMS roughness seen by AFM (1.062 nm) (figure 6.10)

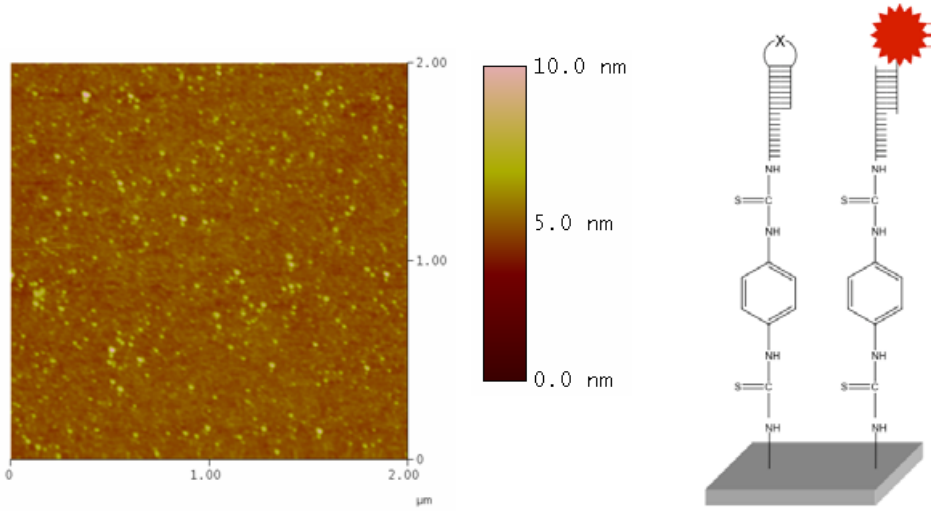

Figure 6.10. AFM tapping mode image of surface after hybridisation with complementary strand B carrying rhodamine label (**-RHODAMINE, substrate g**).

The rhodamine labelled surface roughness is now approaching that of the original non-photolyzed sample by AFM, due to the return of a double stranded oligonucleotide on the surface and its associated increase in persistence length. After denaturing using NaOH the fluorescence decreased dramatically, indicating nearly complete removal of the rhodamine labelled oligonucleotide from the surface and the ability to disassemble the hybridized structures after they have been formed. The surfaces treated with NaOH were hybridized a second time with the complementary rhodamine oligonucleotide and the surfaces showed again a strong fluorescent signal. Three cycles of hybridization and denaturation were performed without apparent loss of fluorescence indicating the robustness of the immobilization method and the reversibility of the denaturation process.

6.3.3.2 –AuNP, substrate (h)

Samples of oligonucleotide surfaces after photolysis and hybridisation with complementary strand B labelled with 5 nm gold nanoparticles when imaged with AFM gave an RMS roughness of 1.45 nm (scheme 6.1, step 8). The roughness of the nanoparticle surface appeared greater than the rhodamine labeled surface due to the size difference between the 5 nm gold NPs and the molecular rhodamine label (figure 6.11).

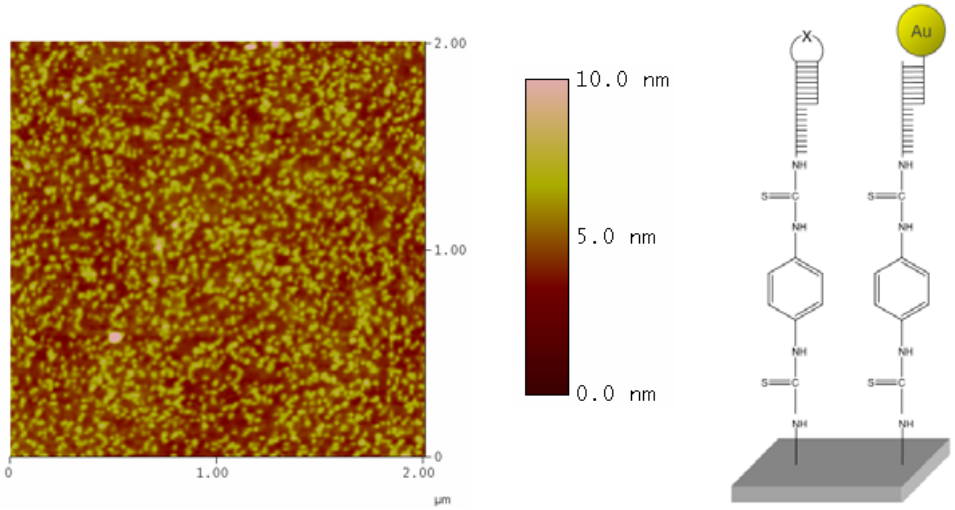

Figure 6.11. AFM tapping mode image of surface after hybridisation with complementary strand B carrying gold nanoparticle label (**-AuNP, substrate h**).

Patterning experiments of silicon oxide surfaces carrying hairpin-oligonucleotides by UV photolithography were performed. Samples of silicon oxide surfaces functionalised with the hairpin oligonucleotide A were irradiated for 1 min with a high intensity lamp through a calibration mask of vinyl acetate with lines ranging from 4 to 170 □m. After irradiation, substrates were washed and hybridized with complementary rhodamine labelled oligonucleotide B. (step 7) Figure 6.12a shows a fluorescent strip observed by epifluorescence. The pattern of 4 lines from the

mask was easily observed, although there was some fluorescence background due to non-specific adsorption. There are many reasons for the non-specific adsorption seen, however, the initial low grafting density of the underlying PDITC could be the major factor, with the labelled complementary strands able to penetrate the oligonucleotide layer and physisorb to the surface.

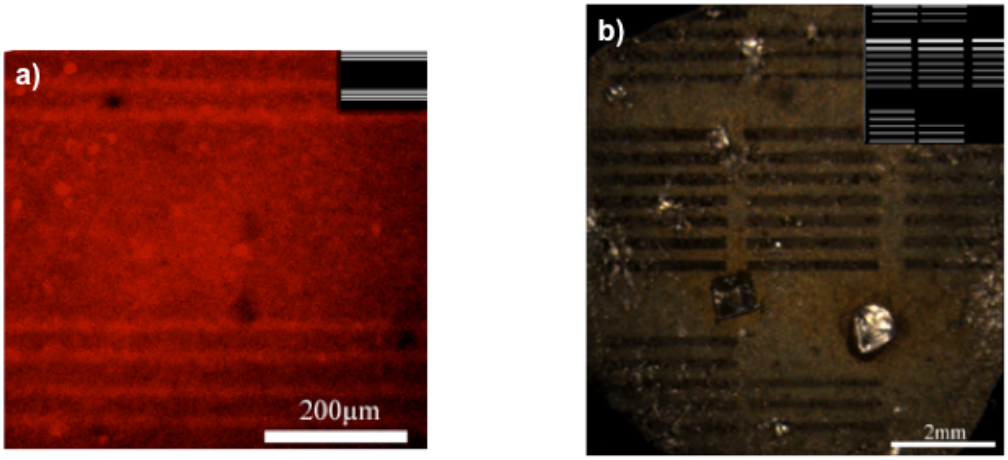

Substrate (g) **Substrate (h)**

Figure 6.12. **a)** Fluorescence image after photo-patterning and hybridization with complementary sequence B labelled with rhodamine (substrate g) (step 7), *inset:* Image of the calibration mask used in the photolysis. **b)** Optical microscopy image after photo-patterning and hybridization with complementary sequence B labelled with 10 nm gold nanoparticles (substrate h) (step 8). *Inset:* Image of the calibration mask used in the photolysis. The visible lines are areas that were masked during photolysis and hence have no nanoparticles attached. Photography obtained with a stereomicroscope with lateral illumination.

A similar experiment was performed using the complementary oligonucleotide B linked to 5 nm gold NPs (scheme 6.1, step 7). The pattern of the mask formed by gold NPs on the surface could be easily observed with lateral light (figure 6.12b).

Most of the NPs were in the photolyzed areas, again some colouration from the NPs was observed in the non-photolyzed areas due to non-specific adsorption.

6.4 Conclusions

In summary, it has been shown that a hairpin oligonucleotide carrying a photolabile group at the loop provides a simple basis for the formation of micrometer-scale patterns on silicon wafers. The process allows for patterning of DNA oligonucleotides *in-situ*, negating the need for any pre-patterning step on the surface before oligonucleotide attachment. The ability to attach photolabile oligonucleotides to amino-terminated semiconductor surfaces allows existing techniques for chemically patterning semiconductor surfaces to be further exploited in the formation of nanostructured surfaces comprised of SAMs and DNA oligonucleotides. Exposure of surfaces functionalised with the hairpin to UV light causes the formation of areas functionalised with single stranded oligonucleotides that direct specific deposition of fluorescent compounds or NPs using the complementary oligonucleotide sequence. Due to the specific self-assembling properties of DNA and the existing methods for the synthesis of oligonucleotides it is expected that the set of methods described here may find a wide use for the fabrication of functional nanostructured systems for electronic, biological and sensing applications.

6.5 Future work

While providing the basis for an interesting and useful approach to patterning surfaces with DNA oligonucleotides to direct site-specific self-assembly, further work is needed to reduce non-specific adsorption in non-photolyzed areas. It is predicted that this reduction in non-specific adsorption will be overcome by increasing initial grafting density, using blocking agents such as polyethyleneglycol or albumine and by increasing the length of the oligonucleotide.

6.6 Experimental section

6.6.1 Materials

Silicon wafers (Si/SiO_2) were purchased from Virginia Semiconductors Inc and were of the type: <111> orientation, resistance of 1-10 Ω cm, 100 nm (+ 5%) thick oxide layer on both sides and polished on one side. All commercially available chemicals and solvents were purchased from Fisher Scientific and Sigma Aldrich and used as supplied. Ultra high purity (UHP) H_2O was purified using a UHQ filtration system and used with resistivity > 18 MΩ,cm.

6.6.2 Equipment preparation

Glassware was immersed in piranha solution (70% H_2SO_4, 30% H_2O_2), rinsed and then sonicated in Ultra High Purity water (UHP H_2O, resistivity 18 Ω cm^{-1}) followed by drying in an oven at 127 ºC for 30 minutes. Finally the glassware was rinsed and sonicated in ethanol for 30 minutes before being dried in the oven at 127 ºC for 24 hours prior to use. Clean plastic equipment was rinsed with UHP H_2O for 30 minutes followed by rinsing with ethanol and a final sonication in ethanol for 30 minutes.

6.6.3 Silicon substrate cleaning (step 1)

A silicon wafer was cut into 1cm^2 squares using a diamond tipped scribber. They were rinsed with ethanol to clear the surface of any dust produced by the cutting process. The 1cm^2 squares were then immersed in piranha solution at 90-100 ºC for 60 minutes. Once cooled, the piranha solution was rinsed off the substrate with UHP water and each one was sonicated in RCA solution (UHP water; 30% H_2O_2; 28% NH_4OH , 5:1:1) for 60 minutes. Sonication in RCA at this stage functionalizes the surface with hydroxyl groups to allow monolayer formation. Repeated rinsing of the

substrate in UHP water finishes the cleaning procedure. The substrates were stored in UHP water and used within 2 days to minimise loss of surface hydroxyl groups.

6.6.4 Preparation of APTMS functionalised self-assembled monolayers (NH_2-SAM) (step 2)

The cleaned silica substrates were transferred from UHP H_2O into anhydrous ethanol by stepwise exchange from H_2O to ethanol with mixtures in the ratio 3:1, 2:2, 1:3, ethanol and finally anhydrous ethanol. The wafers were then immersed into a 0.5 mM solution of (3-aminopropyl)-trimethoxysilane (APTMS) in anhydrous ethanol (5 ml) under a N_2 atmosphere and sonicated at room temperature for 1 hour. The substrates were rinsed for 20 seconds each with ethanol and chloroform, followed by sonication of the wafers twice in fresh ethanol and a final rinsing with ethanol and chloroform. Each sample was then dried under a stream of nitrogen and cured at 120 ºC for 30 minutes under vacuum to promote cross-linking of the SAM's

6.6.5 p-phenylene diisothiocyanate coupling to APTMS SAM (step 3)

APTMS SAMs were treated with a 0.2% solution of PDITC in 10% pyridine / *N*,*N*-dimethylformamide (DMF). After incubation, samples were washed with methanol and acetone and stored in a vacuum dessicator.

6.6.6 Coupling of photolabile hairpin oligonucleotide (step 4)

A solution carrying 0.68 O.D. (optical density) units at 260 nm of the photolabile-hairpin-NH_2 (sequence A) in sodium borate buffer (pH 8.0) was prepared and drop cast onto substrates and incubated at 37°C for 2 hours. Samples were then washed with 1% NH_4OH, copious amounts of UHP H_2O and methanol. Samples were then dried under a thin stream of N_2 and stored in vacuum desiccator.

6.6.7 Photolysis of hairpin oligonucleotide (step 5 & 6)

Photolysis was carried out using a Mercury lamp (Black Eye lamp, 340 nm) for 30 min. Followed by washing with 200 mM sodium hydroxide and water.

6.6.8 UV photolithography (steps 5 & 6)

UV photolithography was carried out using a Suss Microtech MJB4 mask aligner, samples of APTMS SAMs functionalised with the hairpin oligonucleotide were irradiated from 5 sec to 1 min with a high intensity UV lamp (340 nm). A mask of vinyl acetate was used for the patterning. After irradiation substrates were washed with 0.2 M NaOH, followed by washing with water and drying under Ar. Before hybridization the substrate was washed with 1 x SSC and dried under argon. To deactivate remaining isothiocyanate groups the substrates were treated with 50 mM 6-amino-1-hexanol and 150 mM *N*,*N*-diisopropylethylamine in DMF for 2 h and subsequently rinsed with DMF, acetone and dried under argon.

6.6.9 Surface hybridisation of complementary oligonucleotide B (steps 7 & 8)

A sample of 10μM complementary rhodamine or nanoparticle labelled oligonucleotide in hybridization buffer (6x SSC, 0.1% SDS, water) was prepared. Hybridization was carried out for 2 h at room temperature, followed by washing with 6 x SSC, 2 x SSC and water.

6.6.10 Surface characterisation

Samples were analysed via dynamic contact angle measurements, ellipsometry, AFM and epi-fluorescence microscopy.

6.6.10.1 Contact angle

Water contact angle analysis was carried out using the sessile drop method on a home built contact angle apparatus equipped with a CCD camera attached to a PC for image capture. Contact angles are quoted as the average advancing (Adv) and receding (Rec) angles from images analysed with software from FTÅ for 5 locations on the same substrate.

6.6.10.2 Spectroscopic ellipsometry

Spectroscopic ellipsometry was carried out using a Jobin-Yvon UVISEL spectroscopic ellipsometer with a white light source. The angle of incidence was fixed at 70º and a wavelength range of 250-800 nm was used. Ellipsometric thicknesses were estimated from data taken from a fresh surface in 5 locations and modelled against a cauchy oscillator model.

6.6.10.3 Atomic force microscopy (AFM)

AFM topography analysis was carried out using a multimode Nanoscope IIIA (Digital Instruments, Santa Barbara, CA) in tapping mode using RTSEP etched silicon probes.

6.6.10.4 Epi-fluorescence microscopy

Epi-fluorescence images were acquired using a Nikon Eclipse e1000, with a G-2A filter equipped with a Roper coolSNAPfx CCD camera. Images were captured at 20X or 40X in air. Image analysis was carried out using imageJ software and average fluorescence intensities were calculated over the whole image.

6.7 References

1) Brust, M., Bethell, D., Kiely, C. J. and Schiffrin, D. J., **Self-Assembled Gold Nanoparticle Thin Films with Nonmetallic Optical and Electronic Properties,** *Langmuir*, **1998,** 14, 5425-5429.

2) Sotiropoulou, S. and Chaniotakis, N. A., **Carbon Nanotube Array-based Biosensor**, *Anal. Bioanal. Chem.*, **2003**, 375, 103-105.

3) Mendes, P. M. and Preece. J. A., **Precision Chemical Engineering: Integrating Nanolithography and Nanoassembly**, *Curr. Opinion Coll. Inter. Sci*. **2004**, 9, 236-248.

4) Ball, P., **Chemistry Meets Computing**, *Nature,* **2000**, 406, 118-120.

5) Demirel, G., Caglayan, M. O., Garipcan, B. and Piskin, E., **A Novel DNA Biosensor Eased on ellipsometry**, *Surf. Sci*. **2008**, 602, 952-959.

6) Kavanagh, P. and Leech, D., **A DNA Biosensor Based on the Detection of Doxorubicin-Conjugated Ag Nanoparticle Labels Using Solid-State Voltammetry,** *Anal. Chem*., **2006**, 78, 2710-2716.

7) Diegoli, S., Hamlett, C. A. E., Leigh, S. J., Mendes, P. M. and Preece, J. A., **Engineering Nanostructures at Surfaces Using Nanolithography,** *Proc. of the IMECH E Part G J. of Aerospace Engineering,* **2007**, 221, 589-629.

8) Del Campo, A., Boos, D., Spiess, H. W. and Jonas, U., **Surface Modification with Orthogonal Photosensitive Silanes for Sequential Chemical Lithography and Site-Selective Particle Deposition,** *Angew. Chem. Int. Ed*., **2005**, 44, 4707-4712.

9) Jonas, U., Del Campo, A., Krüger, C., Glasser, G. and Boos, D., **Colloidal Assemblies on Patterned Silane Layers,** *Proc. Natl. Acad. Sci. USA,* **2002**, 99, 5034-5039.

10) Böltau, M., Walheim, S., Mlynek, J., Krausch, G. and Steiner, S., **Surface-Induced Structure Formation of Polymer Blends on Patterned Substrates**, Nature, **1998**, *391*, 877-879.

11) Lahiri, J., Ostuni, E. and, Whitesides, G. M.**, Patterning Ligands on Reactive SAMs by Microcontact Printing**, *Langmuir*, **1999**, *15*, 2055-2060.

12) Ruckenstein, E. and Li, Z.F., **Surface Modification And Functionalization Through The Self-Assembled Monolayer And Graft Polymerization,** *Adv. Coll. Int. Sci.*, **2005**, 113, 43-63.

13) Joos, B., Kuster, H. and Cone, R., **Covalent Attachment of Hybridizable Oligonucleotides to Glass Supports,** *Anal. Biochem*., **1997**, 247, 96-101.

14) Fernandes, R., Yi, H., Wu, L. Q., Rubloff, G. W., Ghodssi, R., Bentley, W. E. and Payne, G. F., **Thermo-biolithography: A Technique for Patterning Nucleic Acids and Proteins**, *Langmuir*, **2004**, 20, 906-913.

15) Boozer, C., Chen, S. and Jiang, S., **Thermo-biolithography: A Technique for Patterning Nucleic Acids and Proteins,** *Langmuir,* **2006**, 22, 4694-4698.

16) Mukumoto, K., Ohtsuka, K., Nojima, T. and Takenaka, S., **Preparation of Carbodiimide-terminated Dithiolane Self-Assembly Monolayers as a New DNA-Immobilization Method,** *Anal. Sci*., **2006**, 22, 349-355.

17) Tombelli, S., Mascini, M. and Turner, A. P. F., **Improved Procedures For Immobilization Of Oligonucleotides On Gold-Coated Piezoelectric Quartz Crystals**, *Biosens. Bioelectron.,* **2002**, 17, 929-936.

18) Berganza, J., Olabaria, G., García, R., Verdoy, D., Rebollo, A. and Arana, S., **DNA Microdevice for Electrochemical Detection of Escherichia Coli 0157:H7 Molecular Markers**, *Biosens. Bioelectron*., **2007**, 22, 2132-2137.

19) Sakao, Y., Nakamura, F., Ueno, N. and Hara, M., **Hybridization of Oligonucleotide by Using DNA Self-Assembled Monolayer**, *Colloids Surf. B,* **2005**, 40, 149-152.

20) Ladd, J., Boozer, C., Yu, Q., Chen, S., Homola, J. and Jiang, S., **DNA-Directed Protein Immobilization on Mixed Self-Assembled Monolayers via a Streptavidin Bridge**, *Langmuir,* **2004**, 20, 8090-8095.

21) Kerman, K., Morita, Y., Takamura, Y., Ozsoz, M. and Tamiya, E., **Modification of Escherichia Coli Single-Stranded DNA Binding Protein with Gold Nanoparticles For Electrochemical Detection of DNA Hybridization**, *Anal. Chim. Acta.,* **2004**, 510, 169-174.

22) Yin, H. B., Brown, Y., Greef, R., Wilkinson, J. S. and Melvin, T., **Chemical Modification and Micropatterning of Si(100) with Oligonucleotides**, *Microelectronic Engineering*, **2004**, *73-74*, 830-836.

23) Yin, H. B., Briwn. T., Greef, R., Mailis, S., Eason, R., Wilkinson, J. S. and Melvin, T., **Photo-Patterning of DNA Oligonucleotides On Silicon Surfaces with Micron-Scale Dimensions,** *Proc. SPIE,* **2004**, 5461, 1-8.

24) Zhang, G. J., Tanii, T., Funatsuac, T. and Ohdomari, I., **Patterning of DNA Nanostructures on Silicon Surface by Electron Beam Lithography of Self-Assembled Monolayer**, *Chem. Commun*., **2004**, 786-787.

25) Kershner, R. J., Bozano, L. D., Micheel, C. M., Hung, A. M., Fornof, A. R., Cha, J. N., Rettner, C. T., Bersani, M., Frommer, J., Rothemund, P. W. K . and Wallraff, G. M., **Placement and Orientation of Individual DNA Shapes on Lithographically Patterned Surfaces**, *Nature Nanotechnology*, **2009**, *4*, 557-561.

26) Björk, P., Holmström, S. and Inganäs, O., **Soft Lithographic Printing of Patterns of Stretched DNA and DNA/Electronic Polymer Wires by Surface-Energy Modification and Transfer**, *Small,* **2006**, 2, 1068-1074.

27) Wang, X., Cooper K. L., and Wang, A., **Study on the Layer-by-layer Electrostatic Self Assembly Method for Biomolecule Immobilization onto Biosensor Surface**, *Proc. SPIE*, **2007**, Vol. 6647, 66470G.

28) M Beier, M. and Hoheisel, J. D., **Versatile Derivatisation of Solid Support Media for Covalent Bonding on DNA-microchips**, *Nucl. Acids Res.*, **1999**, *27*, 1970-1977.

29) Sun, S., Mendes, P. M., Critchley, K., Diegoli, S., Hanwell, M., Evans, S. D., Leggett, G. J., Preece, J. A. and Richardson, T. M., **Fabrication of Gold Micro- and Nanostructures by Photolithographic Exposure of Thiol-Stabilized Gold Nanoparticles,** *Nano Lett*., **2006**, 6, 345-350.

30) Iqbal, P., Sun, S., Hanwell, M. D., Attwood, D., Leggett, G. J., Preece, J. A., Richardson, T. H. and Tunnicliffe, D., **Photochemical Fabrication of Three-Dimensional Micro- and Nano-structured Surfaces from a C60 Monoadduct**, *J. Mat. Chem*., **2008**, 18, 2016-2021.

31) Huang, E., Satjapipat, M., Han, S. and Zhou, F., **Surface Structure and Coverage of Oligonucleotide Probe-Tethered Onto Gold Substrate and Its Hybridization Efficiency for Polynucleotide Target**, *Langmuir,* **2001**, 17, 1215-1224.

32) Satjapipat, M., Sanedrin, R. and Zhou, F., **Selective Desorption of Alkanethiols in Mixed Self-Assembled Monolayers for Subsequent Oligonucleotide Attachment and DNA Hybridization**, *Langmuir,* **2001**, 17, 7637-7644.

33) Harnett, C. K., Satyalakshmi, K. M., and Craighead, H. G., **Bioactive Templates Fabricated by Low-energy Electron Beam Lithography of Self-Assembled Monolayers**, *Langmuir*, **2001**, *17*, 178-182.

34) Diegoli, S., Mendes, P. M., Baguley, E. R., Leigh, S. J., Iqbal, P., García Díaz, Y. R., Begum, S., Critchley, K., Hammond, G. D., Evans, S. D., Attwood, D., Jones, I. P. and Preece, J. A., **pH Dependent Gold Nanoparticles Self-Organisation on Functionalized Si/SiO_2 Surfaces**, *J. Exp. Nanosci*., **2006**, 1, 333-353.

35) Vilar, M. R., Botelho do Rego, A. M., Ferraria, A. M., Jugnet, Y., Noguès, C., Peled, D. and Naaman, R., I**nteraction of Self-Assembled Monolayers of DNA with Electrons: HREELS and XPS studies**, *J. Phys Chem. B.,* **2008**, 112, 6957-6964.

36) Manning, M. and Redmond, G., **Formation and Characterization of DNA Microarrays at Silicon Nitride Substrates**, *Langmuir,* **2005**, 21, 395-402.

37) Manning, M., Galvin, P. and Redmond, G., **A Robust Procedure for DNA Microarray Fabrication and Screening in the Molecular Biology Laboratory. Application Note**, *Am. Biotech. Lab*., **2002**, 20, 16-17.

38) Cras, J. J., Rowe-Taitt, C. A., Nivens, D. A., Ligler, F. S., **Comparison of Chemical Cleaning Methods Of Glass in Preparation for Silanization**, *Biosensors & Bioelectronics,* **1999**, 14, 683-688.

39) Sieval, A. B., Linke, R., Heij, G., Meijer, G., Zuilhof, H. and Sudhölter, E. J. R., **Amino-Terminated Organic Monolayers on Hydrogen- Terminated Silicon Surfaces**, *Langmuir,* **2001**, 17, 7554-7559.

40) Silberzan, P., Leger, L., Ausserre, D. and Benattar, J. J., **Silanation of Silica Surface. A New Method of Constructing Pure or Mixed Monolayers**, *Langmuir,* **1991**, 7, 1647-1651.

41) Angst, D. L. and Simmons, G. W., **Moisture Absorption Characteristics of Organosiloxane Self-Assembled Monolayers**, *Langmuir,* **1991**, 7, 2236-2242.

42) Ulman, A., **Formation and Structure of Self-Assembled Monolayers**, *Chem. Rev.*, **1996**, 96, 1533-1554.

43) Ramos, R., Manning, B., Aviñó, A., Gargallo, R. and Eritja, R., **Photocleavage of Peptides and Oligodeoxynucleotides Carrying 2-Nitrobenzyl Groups**, *Helv. Chim. Acta.,* **2009**, 92, 613-794.

44) Nelson, P. S., Kent, M. and Muthini, S., **Oligonucleotide Labelling Methods. 3. Direct Labeling of Oligonucleotides Employing a Novel, Non-Nucleosidic, 2-Amino-1,3-propanediol Backbone**, *Nucleic Acids Res*., **1992**, 20, 6253-6259.

45) Lockett, M. R., Phillips, M. F., Jarecki, J. L., Peelen, D. and Smith, L. M., **A Tetrafluorophenyl Activated Ester Self-Assembled Monolayer for The Immobilization of Amine-Modified Oligonucleotides**, *Langmuir,* **2008**, 24, 69-75.

46) Pillai, V. N. R., **Photoremovable Protecting Groups In Organic Chemistry**, *Synthesis,* **1980**, 1-26.

47) Guillier, F., Orain, D., Bradley, M., **Linkers and Cleavage Strategies in Solid-Phase Organic Synthesis and Combinatorial Chemistry**, *Chem. Rev.,* **2000,** 100, 2091-2157.

48) Bochet, C. G., **Photolabile Protecting Groups and Linkers**, *J. Chem. Soc. Perkin. Trans.,* **2002**, 1, 125-142.

49) Kahl, J. D., Greenberg, M. M., **Introducing Structural Diversity in Oligonucleotides via Photolabile, Convertible C5-Substituted Nucleotides**, *J. Am. Chem. Soc.,* **1999**, 121, 597-604.

50) Walker, J. W., Reid, G. P., McCray, J. A. and Trentham, D. R., **Photolabile 1-(2-Nitrophenyl)ethyl Phosphate Esters of Adenine Nucleotide Analogues**, *J. Am. Chem. Soc.,* **1988**, 110, 7170-7177.

51) Mirkin, C. A., Letsinger, R. L., Mucic, R. C. and Storhoff, J. J., **A DNA-Based Method for Rationally Assembling Nanoparticles into Macroscopic Materials,** *Nature,* **1996**, 382, 607-609.

Chapter 7

Conclusions

The work carried out in this thesis has taken the concept of micro- and nanostructuring surfaces and presented a range of techniques based around this concept and developed the ideas introduced in each chapter. One of the highest resolution techniques available for surface patterning at present is the use of EBL with polymeric resists. As conventional polymeric resists usually have to go through a further etching step to topographically pattern an underlying material, being able to build 3D structures directly on top of a resist type material is of great interest. The aim of **Chapter 2** was to carry out a systematic study of the electron dose vs functional group conversion of an aromatic-NO_2 terminated SAM to an aromatic-NH_2 terminated SAM gold surface. The SAM acts like a molecular resist, and at a dose of 30 000 $\mu C\ cm^2$ achieved its maximum functional group conversion, as judged by the assembly of negatively charged gold nanoparticles on the patterned surfaces. A second aim of this chapter was to examine how feature size and quality were affected by varying electron doses. It was observed that increasing electron dose caused feature broadening and high electron doses caused feature inversion. The observed behaviour could be rationalized with an understanding of the physics of electron interactions with solid surfaces. Overall, the chapter showed that EBL could be used to pattern features on a surface with a molecular resist, which could then be directly used to build 3D structures upon.

Chapter 3 took its cues from the previous chapter and began to examine how the negatively charged gold nanoparticles assembled on the patterned features may be used as a building block for creating much larger 3D structures. The chapter also examined other methods of patterning for the 3D structures. The first aim of the

chapter was to investigate the sequential deposition of a cationic polyelectrolyte and anionic citrate stabilised gold nanoparticles (the same particles used in the previous chapter). The polyelectrolyte and nanoparticles were observed to assemble in a facile manner to surfaces via a dip-wash-dip-wash (layer-by-layer) deposition strategy. The deposition processes were characterized using AFM imaging, cantilever resonance measurements and spectrophotometry on transparent substrates. All the techniques gave values of the same order of magnitude, not only demonstrating the 3D building process, but also the viability of the techniques themselves. The second aim of the chapter was to examine routes other than EBL that could be used to pattern the layer-by-layer structures. The patterning of structures was achieved by first carrying out a conventional photolithography process with a polymeric resist, followed by assembly of the polyelectrolyte and nanoparticles. Secondly, lithography using thiol-stabilisd gold nanoparticles and a laser to pattern aggregated gold features was attempted. The features were intended as foundations on which the polyelectrolyte and anionic nanoparticles could be assembled via a microfluidic device. Although the lithography using the laser was successful, the features did not survive the process required to assemble the microfluidic device, the microdfluidic device did prove successful at delivering the polyelectrolytes and nanoparticles to the surface in a layer-by-layer fashion. Overall, chapter 3 showed that assembly of 3D structures on patterned surfaces such as those in chapter 2 was easily achievable.

Chapter 4 was based on searching for other, more rapid ways of depositing the polyelectrolyte and nanoparticle materials already examined. The layer-by-layer methodology used in chapter 3, although simple, still suffered from the down-side of the long time *(1 hour)* required for assembly of the gold nanoparticles on the preceding layer. The first aim was to demonstrate that a commercially available inkjet printing system could be used to sequentially print the polyelectrolytes and

nanoparticles to glass surfaces in order to form microstructured polyelectrolyte/nanoparticle structures. The printing system was able to successfully deposit the polyelectrolyte to glass surfaces forming a range of film morphologies, from discrete features to a complete film. By modifying the surface chemistry of the glass to make it more hydrophobic, the lateral sizes of the polyelectrolyte features could be reduced. The technique, however, was not viable for deposition of the nanoparticles also from the same printer, as the nanoparticles aggregated in the print head. The printed polyelectrolyte structures could be used to direct the deposition of the nanoparticles from solution. The second aim of the chapter was to take the printed strctures and further define features within them using the sharp tip of an AFM to mechanical scratch away material. The AFM tip was able to easily displace the polyelectrolyte and nanoparticle structures, defining square and channel features within the printed structures. Overall, inkjet printing proved to be a highly viable technique for delivering materials, such as polyelectrolytes, to surfaces of differing chemistries. If a second, clean printer was utilised, the deposition of nanoparticles would be achievable on the polyelectrolyte foundations.

Chapter 5, rather than fabricating a structured surface, introduces a topographically pre-structured substrate recovered from gold-coated CD-R data disks and uses a novel technique conceived for the work presented, to deposit the hierarchical biological material collagen to the topographically structured surfaces. The first aim of the chapter is to carry out the removal of the structured gold surface from the CD-R disks and transfer it to silicon and glass surfaces. The gold structured surfaces are easily transferred to the new substrates. AFM confirmed that the structure was retained and XPS confirmed that there was an exposed gold surface. The second aim of the chapter is to deposit collagen with controlled directionality on the gold surfaces. Collagen was deposited to the surfaces with controlled directionality, with

both fibres and fibrils showing directionality on the structured surfaces, as seen with AFM. Collagen was observed to be suspended over some of the 'valleys' of the substrate. The third aim of the chapter was to examine the mechanical properties of the collagen deposited. By virtue of the collagen being suspended over the valleys of the surface, the downward displacement of the collagen into the valleys was measured and compared against the collagen diameter and length. Overall, the recovery of the structured gold surfaces from CD-R disks showed that the topographically structured substrates gave to rise readily and cheaply available substrates for use by experimental scientists. The deposition technique used proved to be successful in controlling the directionality of material, which could prove useful in the future for depositing other materials of interest such as nanotubes.

Finally, **Chapter 6** took another material, synthetic DNA oligonucloetides based upon the naturally occurring chemistry of DNA and combined it with photolithography to provide a route to 3D structuring of surfaces, exploiting the self-assembling properties of DNA. The first aim of the chapter was to chemically derivatise silicon surfaces with synthetic hairpin oligonucleotides carrying a photolabile group at the apex. The derivatisation methodology was successful in attaching the oligonucleotides to the silicon surfaces and was followed via a combination of contact angle, ellipsometry, AFM and XPS analysis. The second aim of the chapter was to carry out photolithography on the surface bound oligonucleotides and leave a single stranded oligonucleotide which can direct the deposition of a molecular dye and gold nanoparticles carrying a complementary oligonucleotide strand. The photolithography step left the single stranded oligonucleotide and allowed patterning of silicon substrates with the dye and gold nanoparticles. Overall, a semiconductor material was interfaced with biological based material, showing that future devices where the interface of biological materials and

electronics are a realistic possibility. Exploiting the natural self-assembling properties of the material to form 3D structured surfaces demonstrates that naturally occurring self-assembly processes are useful to the experimental scientist.

The thesis overall shows how the combination of existing fabrication techniques with novel materials or techniques can be used to develop the range of micro- and nanostructred surfaces that can be fabricated. These structured surfaces could be the basis of the technology in devices, sensors and electronics of the future, whereby nanolithography and self-assembly of nanomaterials are integrated, which is representing a paradigm shift in the manufacturing process.